DIFFRACTION STUDIES OF DISORDERED MATERIALS

A THESIS SUBMITTED TO

THE UNIVERSITY OF KENT AT CANTERBURY

IN THE SUBJECT OF PHYSICS

FOR THE DEGREE

OF DOCTOR OF PHILOSOPHY.

By

David W Huxley

November 1991

Abstract

A new method of collecting X-ray diffraction data which eliminates 90% of the Compton scattering component has been developed. The subsequent data analysis is described in detail with specific reference being made to the analysis of liquid carbon tetrachloride.

X-ray diffraction measurements have been made on two samples of amorphous phosphorus. The obtained radial distribution functions have been analysed via the fitting of Gaussian curves and the results compared to the local correlations obtained by other studies and from the crystalline allotropes of phosphorus. The results show a marked difference in the degree of crystalline order present in the samples and the inability of current models to describe the observed structure.

Neutron diffraction measurements have been made on liquid antimony pentafluoride at a variety of temperatures between 5 and 80°C. The obtained radial distribution functions have been described in terms of a cis-bridged molecular chain. Little alteration in the structure was observed in the temperature difference results.

Neutron diffraction measurements have been made on carbon and germanium tetrabromide. The results were analysed using a molecular form-factor which yielded bond lengths in good agreement with those obtained by other investigators. The intermolecular distribution functions obtained for the two samples compare favourably with those obtained from a RISM analysis.

Acknowledgements

I would like to thank my supervisor, John Dore for his help and guidance. I would like to acknowledge the assistance of Graham Bushnel-Wye and Jacky Turner of Birkbeck College, and John Finney of the Rutherford Appleton Laboratory, who collaborated with me on the experimental side of the X-ray work. My thanks also go to Pierre Chieux for his help with the experiments carried out at the Institut Laue-Langevin, Grenoble, France.

My thanks are extended to all member of the UKC neutron and X-ray scattering group, both past and present, for their support and friendship. I would also like to acknowledge the support of my other friends, both within the physics laboratory and elsewhere.

I would like to take this opportunity to thank my parents, William Anthony and Grace Elizabeth Huxley for their continual support and encouragement throughout my university career.

My eternal gratitude must go to Margaret for being with me and supporting me during the writing of this thesis.

Finally I would like to acknowledge the SERC, who provided financial support for this project.

Contents

List of Tables

List of Figures

Chapter 1

The Theory of X-ray and Thermal Neutron Diffraction

1.1 Introduction

This thesis presents development work on the use of X-ray diffraction at the Synchrotron Radiation Source at the Daresbury Laboratory as a means of studying the 'structure' of molecular liquids and amorphous solids. Also presented are the structural studies of two molecular liquids using thermal neutron scattering. This first chapter is therefore devoted to an outline of the basic theory behind the techniques used. General information on X-ray diffraction is contained in many standard texts [1-5] and reviews of its application to molecular liquids and amorphous solids are given in [6-10] . Similarly for neutron scattering standard texts [11-17] and review articles [18-22] are available.

When considering molecular liquids it is not possible to define a 'structure' comparable to a crystal structure. In liquids the positions of the molecules (or

atoms in the case of monatomic fluids) are continually changing and any local configuration will last for only a short time with a small possibility that an identical structure containing the same atoms will occur at some later time. The 'structure' of the liquid is therefore a time-averaged property which represents the probability of finding an atom or molecule at a given distance from the chosen origin. Since atoms and molecules have both size and shape there will be some spatial ordering around them. This local ordering will be short range (typically < 20 Å) and will be influenced by interatomic and intermolecular forces. Diffraction techniques allow a time averaged spatial distribution curve which describes the average positions of the atoms with respects to an arbitrary origin to be obtain. It would appear therefore that experimental diffraction studies can provide fundamental information linking the basic interaction forces to the properties of the liquid. Unfortunately due to the complexity of the forces involved it is generally not possible to extract this information. However in the case of simple molecules (i.e. systems of up to five or six atoms) it is possible to obtain a limited amount of information on the positions of the molecules in the liquid, which contributes to a basic understanding of the system.

The scattering of radiation by condensed matter can be used to give information on the distribution of atomic positions if the wavelength of the radiation is of the same order as the interatomic spacing. Given this condition the waves coherently scattered by different atoms will have similar amplitudes and fixed phase relations and will thus interfere with each other. The scattering vector $\mathbf{k}$[1] may be defined as the difference in the incident wave vector $\mathbf{k}_i$ and the scattered wave vector $\mathbf{k}_s$ (figure 1). For elastic scattering (i.e. where the scattered radiation suffers no loss

[1]In most cases where a difference between X-ray and neutron symbolism arises the X-rays notation has been adopted. Thus the scattering vector is represented by k rather than Q.

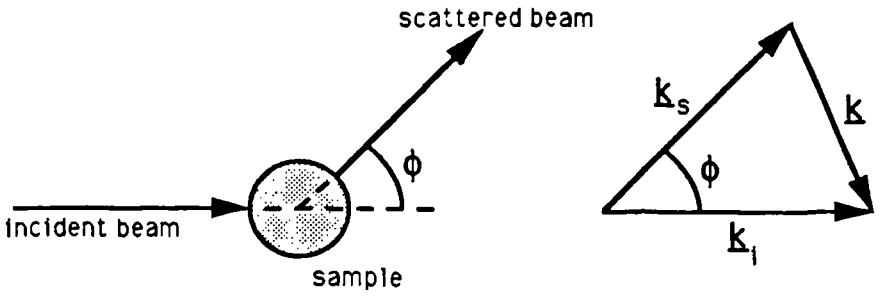

Figure 1: The definition of the scattering vector k

in energy) the incident and scattered wave vectors will have the same magnitude and the scattering vector **k** is given by

$$k = \frac{4\pi}{\lambda}\sin(\phi/2) \tag{1}$$

where λ is the wavelength of the incident radiation and ϕ is the angle between the incident and scattered beam. Thus in a diffraction experiment it is possible to record the intensity of scattered radiation as a function of k by keeping the wavelength at a particular value and varying ϕ or keeping ϕ fixed and varying the wavelength. From this spectra the structure factor can be extracted (as discused later).

Elastic scattering experiments on simple amorphous solids yield a structure factor which can be converted to give the one dimensional, real-space, representation of the sample. If the system being studied is a molecular liquid or a molecular amorphous solid (e.g. amorphous ice) the measured structure factor may be separated into two components representing the intra- and inter-molecular components of the scattering. The intra-molecular contribution arises from correlations within the molecule and can be represented by the molecular form factor. This function

is essentially a model containing the known information on the conformation of the molecule. After removing the molecular contribution from the structure factor the residual curve contains all of the inter-molecular information. This curve when converted to real-space gives the inter-molecular pair-correlation function which is the weighted sum of a series of partial pair-correlation functions, between atoms on separate molecules. Thus from the inter-molecular pair correlation function information on the 'structure' of the sample can be extracted.

1.2 The Structure Factor for Monatomic Systems

In the following sections it has been assumed that the collected experimental data may be corrected for all incoherent scattering of radiation and any absorption and experimentally related factor that are present, thus leaving only the elastic scattering cross section $\frac{\mathrm{d}\sigma}{\mathrm{d}\Omega}(\phi,\lambda)$. The extraction of $\frac{\mathrm{d}\sigma}{\mathrm{d}\Omega}(\phi,\lambda)$ from the collected data will be dealt with in later sections.

1.2.1 Neutron Scattering

In the case of neutrons the cross-section $\frac{\mathrm{d}\sigma}{\mathrm{d}\Omega}$ for a system of N identical atoms is given by the equation [11]

$$\frac{\mathrm{d}\sigma}{\mathrm{d}\Omega} = \left\langle \left| \sum_{j=1}^{N} b_j \exp(i\mathbf{k}.\mathbf{r}_j) \right|^2 \right\rangle \qquad (2)$$

Where <> denotes the ensemble average, $\mathbf{r}_j$, is the position of the j^{th} atom and b_j is its bound coherent scattering length. The neutron scattering length for an electron is small [23] provided no magnetic effects are present and thus electron scattering is totally overshadowed by nuclear scattering. The scattering length is therefore a

characteristic value of the neutron-nucleus interaction. It depends on the particular nucleus and on the spin state of the nucleus-neutron system [24]. The values of b vary irregularly for isotope to isotope and from one nucleus to the next in the periodic table. The scattering length is in general a complex quantity but provided that absorption is small the imaginary part is negligible and so the scattering length tends to be treated as a real number. Due to the small size of the nuclei compared neutron wavelengths b is independent of $\mathbf{k}$; figure 2 shows an illustration of elastic neutron scattering from an isolated atom.

Equation 2 may be expanded to give

$$\frac{\mathrm{d}\sigma}{\mathrm{d}\Omega} = \sum_{n,m}^{N} b_n b_m \exp(i\mathbf{k}.\mathbf{r}_{nm}) \tag{3}$$

$$= \sum_{n}^{N} b_n^2 + \sum_{n\neq m}^{N} b_n b_m \exp(i\mathbf{k}.\mathbf{r}_{nm}) \tag{4}$$

Where $\mathbf{r}_{nm} = \mathbf{r}_n - \mathbf{r}_m$. Assuming that there is no correlation between the scattering lengths of the different nuclei [12], the first term ($n = m$) becomes $N < b_n^2 >= N\overline{b^2}$, where $\overline{b^2}$ is the average value of b_n^2 and in the second term ($n \neq m$) $< b_n b_m >= \bar{b}^2$:

$$< b_n b_m >=< b_n >< b_m >=< b >^2 = \bar{b}^2 \text{ for } n \neq m \tag{5}$$

and

$$< b_n b_m >=< b_n^2 >=< b^2 >= \overline{b^2} \text{ for } n = m \tag{6}$$

Applying these relationships to equation 4 allows the cross-section to be reduced to two components

$$\frac{\mathrm{d}\sigma}{\mathrm{d}\Omega}^{self}_{n=m} = N\overline{b^2} \tag{7}$$

and

$$\frac{\mathrm{d}\sigma}{\mathrm{d}\Omega}^{int}_{n\neq m} = N\bar{b}^2 \sum_{n\neq m}^{N} \exp(i\mathbf{k}.\mathbf{r}_{nm}) \tag{8}$$

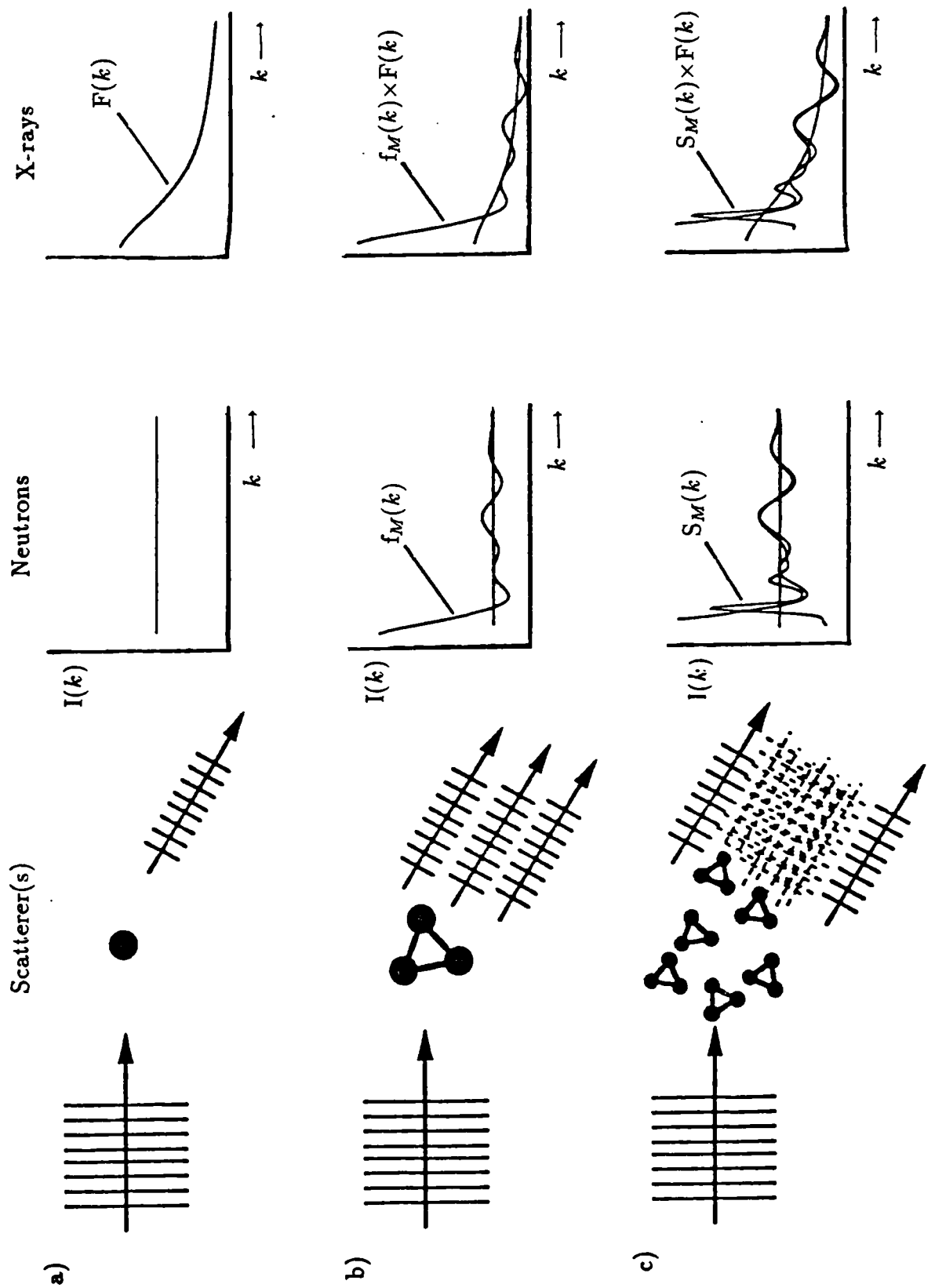

Figure 2: A schematic illustration of X-ray and elastic neutron scattering and the corresponding diffraction form of; a) an isolated atom; b) an isolated molecule and c) an assemble of molecules [19]

$$= N\bar{b}^2 \sum_{n=m}^{N} \exp(i\mathbf{k}.\mathbf{r}_{nm}) - N\bar{b}^2 \quad (9)$$

Here the 'self' component is caused by the interference of waves scattered by the same atom and thus yields a featureless curve equivalent to the scattering from an isolated atom (figure 2). The interference term with subscript 'int' arises from the interference of radiation scattered by pairs of atoms and contains information on the relative phase of the outgoing waves. It is the interference term which yields all of the available structural information about the system.

Recombining equations 7 and 9 gives an alternative expression for the cross-section

$$\frac{d\sigma}{d\Omega} = N\left(\overline{b^2} - \bar{b}^2\right) + N\bar{b}^2 \left|\sum_{n}^{N} \exp(i\mathbf{k}.\mathbf{r}_n)\right|^2 \quad (10)$$

$$= \frac{d\sigma}{d\Omega}^{inc} + \frac{d\sigma}{d\Omega}^{coh} \quad (11)$$

Where $\frac{d\sigma}{d\Omega}^{inc}$ and $\frac{d\sigma}{d\Omega}^{coh}$ are the incoherent and the coherent differential scattering cross-sections. The incoherent term arises because of the variation in scattering length from one nucleus to another. This variation is due to the differences in b according to the spin state of the neutron-nucleus interaction and from the presence of isotopes in the system. The deviation of the scattering lengths from the mean is a random distribution and because of this if the scattering is within the static approximation (see later) the incoherent elastic scattering is isotropic within the centre of mass coordinate system of the nucleus and provides no information on the structure.

The coherent differential cross-section is the scattering the system of atoms would give if all the scattering lengths were identical. In this case the scattering length would be $\bar{b}$ and the phase shifts occurring during the scattering process will all be equal, hence the scattering is coherent [15,16]. Thus the phase shifts which cause

interference effects arise from the relative positions of the nuclei with respects to each other. It is due to this that all the structural information about the scattering system is contained in this term.

For a homonuclear system we may write

$$\frac{\mathrm{d}\sigma}{\mathrm{d}\Omega} = b^2 \left\langle \sum_n^N \sum_m^N \exp(i\mathbf{k}.\mathbf{r}_{nm}) \right\rangle \tag{12}$$

and define the structure factor $S(k)$ by the relationship

$$\frac{\mathrm{d}\sigma}{\mathrm{d}\Omega} = Nb^2 S(k) \tag{13}$$

Hence

$$S(k) = \frac{1}{N} \left\langle \sum_n^N \sum_m^N \exp(i\mathbf{k}.\mathbf{r}_{nm}) \right\rangle \tag{14}$$

Applying equation 13 to equations 7 and 9 gives the self and interference terms of the structure factor

$$S(k)^{self} = \frac{\overline{b^2}}{\overline{b}^2} \tag{15}$$

$$S(k)^{int} = \frac{\overline{b^2}}{N\overline{b}^2} \left\langle \sum_{n \neq m}^N \exp(i\mathbf{k}.\mathbf{r}_{nm}) \right\rangle \tag{16}$$

For a homonuclear system $\overline{b^2} = \overline{b}^2$ and $S(k)^{self} = 1$.

Taking an orientational average over all of the scattering centres in a disordered material it is generally found that there is no preferential orientation of $\mathbf{r}_{nm}$ (i.e. the material is isotropic) and hence it is only the magnitude of $\mathbf{r}_{nm}$ that is important. It is now possible to replace the ensemble average over the phase factors in $S(k)^{int}$ giving

$$S(k) = 1 + \frac{1}{N} \sum_n^N \sum_{n \neq m}^N \frac{\sin(kr_{nm})}{kr_{nm}} \tag{17}$$

It is now useful to introduce $\rho(r)$ as the number density distribution of atoms around the origin atom. Integrating over the entire sample volume noting that the

sum over n is simply N gives

$$S(k) = 1 + \int \rho(r) \frac{\sin(kr)}{kr} \, \mathrm{d}V \tag{18}$$

In disordered solids $\rho(r)$ will in general be spherically symmetric for the ensemble average over all atoms, thus making the substitution $\mathrm{d}V = 4\pi r^2 \mathrm{d}r$ we have

$$S(k) = 1 + 4\pi \int_0^\infty r^2 \left[\rho(r) - \rho_0\right] \frac{\sin(kr)}{kr} \, \mathrm{d}r + 4\pi \int_0^\infty r^2 \rho_0 \frac{\sin(kr)}{kr} \, \mathrm{d}r \tag{19}$$

where ρ_0 is the average number density of the sample. The third term in this equation is zero for all but very small values of k and very small samples and may therefore be neglected under normal experimental conditions. We may now define the pair-correlation function $g(r)$ as

$$g(r) = \frac{\rho(r)}{\rho_0} \tag{20}$$

The function $g(r)$ expresses the probability of finding an atom at a distance r from the origin atom, thus it shows the distribution of particles in the system. At large distances $g(r)$ tends to one as there is a uniform probability of finding a particle. Departures of $g(r)$ from one indicate the extent and range of any order present in the sample. Deconvolution of $g(r)$ into a set of Gaussian peaks yields a series of co-ordination numbers for the origin atom. A co-ordination number is the number of atoms which lie in a shell around the centre particle at a given distance, r, and is obtained from the area under the fitted peak. This technique is of particular importance in the analysis of amorphous solids.

The pair correlation function is related to the structure factor by the equation

$$S(k) = 1 + 4\pi\rho_0 \int_0^\infty r^2 \left[g(r) - 1\right] \frac{\sin(kr)}{kr} \, \mathrm{d}r \tag{21}$$

Finally Fourier inversion of this gives $g(r)$ as

$$g(r) = 1 + \frac{1}{2\pi^2\rho_0} \int_0^\infty k \left[S(k) - 1\right] \frac{\sin(kr)}{kr} \, \mathrm{d}k \tag{22}$$

It is often convenient to define $g(r)$ in terms of the radial distribution function $d(r)$ defined as

$$d(r) = 4\pi r\rho_0 [g(r) - 1] \quad (23)$$

$$= \frac{2}{\pi}\int_0^\infty k [S(k) - 1] \sin(kr)\, \mathrm{d}k \quad (24)$$

which tends to zero at large r. The advantage of $d(r)$ is that a precise knowledge of ρ_0 is not required. The value of ρ_0 may be measured from the initial slope of $d(r)$ and this allows the subsequent calculation of $g(r)$. A comparison of $g(r)$ and $d(r)$ is shown in figure 3. Another commonly used way of describing the spatial distribution of the atoms in the sample is the radial distribution function $J(r)$ defined as

$$J(r) = 4\pi r^2\rho(r) = 4\pi r^2\rho_0 g(r) \quad (25)$$

The Static Approximation and Placzek Corrections

When considering neutrons the relationship between the measured cross section and the scattering function, $S(k)$, derived above is only true for the static approximation which assumes that all of the nuclei are rigidly bound in which case there is negligible energy transfer from the neutron to the nucleus during the scattering process. In a liquid a particular nucleus may only be considered as bound if its mass (or the effective mass of the molecule for molecular systems) is very large compared to the mass of the neutron and if any energy transfer involved in the system is small compared to the initial energy of the neutron. If these conditions are not satisfied it is necessary to make corrections to compensate for the departure from the static approximation. Placzek [25] derived corrections to the measured differential scattering cross section for monatomic systems using the static approximation as a best first approximation. These corrections were later extended to cover molecules [18,21]. In

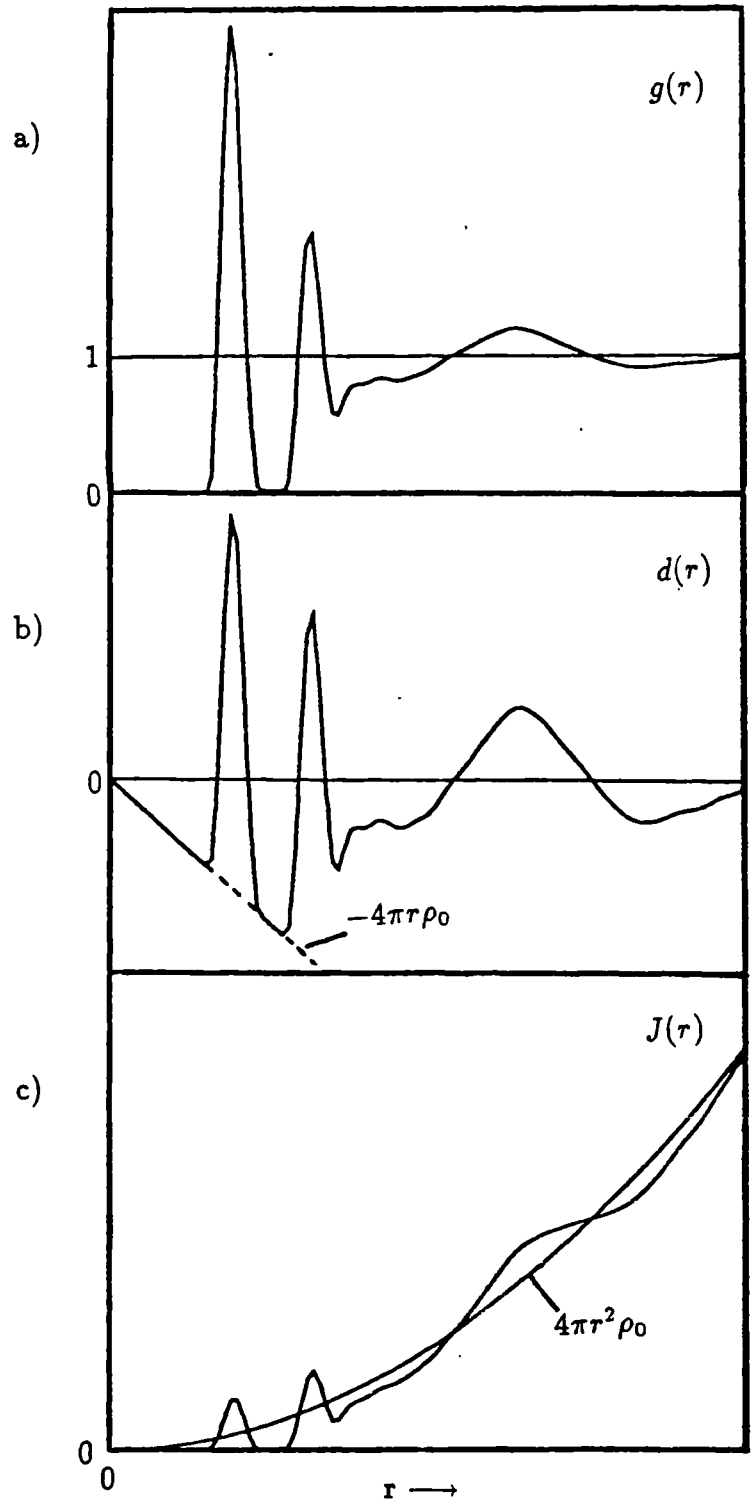

Figure 3: Various pair-wise spatial correlation functions: a) the pair correlation function $g(r)$ b) the pair distribution function $d(r)$ and c) the radial distribution function $J(r)$

general the corrections are complex and involve a detailed knowledge of the detector efficiency function, α_d. For a molecular liquid the first order correction to the self term is given by

$$\frac{\mathrm{d}\sigma}{\mathrm{d}\Omega}^{self} = \sum_i N\overline{b_i^2}\left[1 - \alpha_d\left(\frac{m_n}{M_i}\right)\sin^2\phi/2\right] \tag{26}$$

where m_n and M_i are the effective masses of the neutron and the nucleus respectively. The first order correction to the interference term may be shown to be zero and the second term is assumed to be small this is very important as it means that the interference effects are independent of the inelasticity of the scattering process.

In general the first order Placzek corrected self term may be expressed as

$$\frac{\mathrm{d}\sigma}{\mathrm{d}\Omega_{corr}}^{self} = \frac{\mathrm{d}\sigma}{\mathrm{d}\Omega}^{self}\left(1 - Ak^2\right) \tag{27}$$

Where A is a constant dependent on the detector law and inversely proportional to the effective mass of the scatterer. As the mass of the nucleus decreases this first order approximation becomes less accurate and it is found to be necessary to calculate higher correction terms. An alternative is to use an empirical approach to obtain the self scattering contribution. The empirical approach is preferable for all but very simple molecules and a correction term given by

$$\frac{\mathrm{d}\sigma}{\mathrm{d}\Omega_{corr}}^{self} = \frac{\mathrm{d}\sigma}{\mathrm{d}\Omega}^{self}\left(1 - Ak^2 + Bk^4\right) \tag{28}$$

has been found to be satisfactory for a variety of molecular liquids such as the liquid alcohols [26].

1.2.2 X-Ray Scattering

The final equations derived for X-ray scattering from a system of atoms are very similar to those obtained in the neutron case and so only a brief outline will be

presented here. Before proceeding, however, it is useful to consider the scattering of X-rays by a free electron and a single atom.

Coherent Scattering by a Free Electron

Consider an X-ray beam with a waveform given by

$$\mathbf{E} = \mathbf{E}_0 \exp i(kx - \omega t) \tag{29}$$

(ω is the angular frequency) incident on a free electron at the origin of the coordinate system shown in figure 4. The electron will be subject to an acceleration γ given by

$$\gamma = \frac{e}{m}\mathbf{E} \tag{30}$$

where e is the electron charge (-1.6×10^{-19} C) and m is its mass (9.1×10^{-31} kg). This acceleration will be oscillatory in nature and will thus cause the electron to oscillate. As an accelerating charge emits radiation the electron will radiate an electromagnetic wave of the same frequency as the incident wave, however due to the negative charge on the electron the emitted wave will be π radians out of phase.

The intensity of the emitted X-ray at the point P in figure 4 is given by classical electrodynamics [4] to be

$$I_s = I_0 \left(\frac{\mu_o}{4\pi}\right)^2 \left(\frac{e^4}{m^2 R^2}\right) \sin^2 \phi_z \tag{31}$$

where I_o is the incident X-ray intensity, R is the modulus of the position vector R of point P, which makes an angle ϕ_z with the z-axis and μ_o is the permeability of free space ($4\pi \times 10^{-7}$ Hm^{-1}).

If the incident X-ray beam is unpolarized it is necessary to resolve the electric vector into two perpendicular components. If the point P is used to define the plane

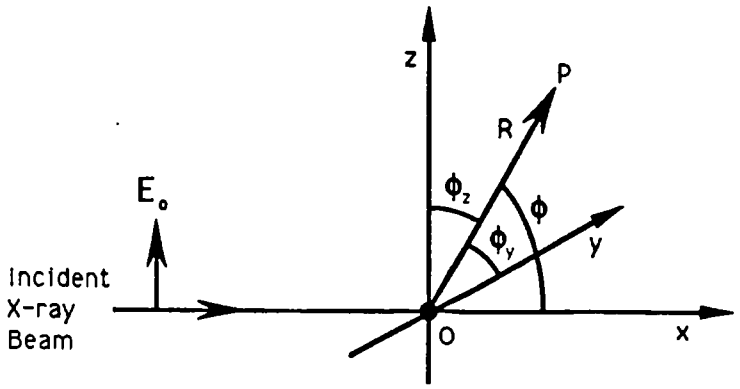

Figure 4: Polarized X-ray incident on a free electron

of scatter (i.e. to define the z direction such that P lies in the XZ plane) the electric vector may be resolved into components perpendicular and parallel to this plane. This gives

$$I_{\parallel} = I_0 \left(\frac{\mu_o}{4\pi}\right)^2 \left(\frac{e^4}{m^2 R^2}\right) \sin^2 \phi_z \tag{32}$$

$$I_{\perp} = I_0 \left(\frac{\mu_o}{4\pi}\right)^2 \left(\frac{e^4}{m^2 R^2}\right) \sin^2 \phi_y \tag{33}$$

As the point P is in the XZ plane, $\phi_y = 90°$. It may also be noted that $\sin^2 \phi_z = \cos^2 \phi$ where ϕ is the angle between the scattered and incident beams. Thus summing the two components yields

$$I_s = I_0 \left(\frac{\mu_o}{4\pi}\right)^2 \left(\frac{e^4}{m^2 R^2}\right) \left(p_{\perp} + p_{\parallel} \cos^2 \phi\right) \tag{34}$$

where $p_{\perp}$ and $p_{\parallel}$ are the fractions of the incident beam polarized perpendicular and parallel to the scattering plane. The term $\left(\frac{\mu_o}{4\pi}\right) \frac{e^2}{m}$ is the classical radius of the electron ($r_e = 2.8 \times 10^{-15}$ m). For an unpolarized beam $p_{\perp} = p_{\parallel} = 1/2$ and this

gives the well known *Thompson formula*

$$I_s = I_0 \frac{r_e^2}{R^2} \frac{(1 + \cos^2 \phi)}{2} \tag{35}$$

or in general

$$I_s = I_0 \frac{r_e^2}{R^2} P(\phi) \tag{36}$$

where $P(\phi)$ is called the polarization factor and the value of $\frac{r_e^2}{R^2}$ is a constant for most systems.

Incoherent (Compton) Scattering

In 1926, Compton found that part of the spectra scattered by an object has a longer wavelength than that of the incident beam. To explain this it is necessary to adopt the corpuscular model of radiation and treat the incident X-ray beam as a stream of photons each of which act as a particle of energy $h\nu$, h being Plancks constant (6.6×10^{-34} Js) and ν the incident frequency. It is now possible to apply the laws of conservation of energy and momentum. From conservation of energy we have

$$h\nu = h\nu' + mc^2 \left(\frac{1}{\sqrt{1 - \beta^2}} - 1 \right) \tag{37}$$

where ν' is the scattered frequency, m is the mass of the electron and c is the velocity of light. The quantity β is v/c where v is the recoil velocity of the electron and the term in which it is included corrects the electron mass for relativistic effects.

The principle of conservation of momentum yields two equations:

$$\frac{h\nu}{c} = \frac{h\nu'}{c} \cos \phi + \frac{m\beta c}{\sqrt{1 - \beta^2}} \cos \theta \quad \text{(X component)} \tag{38}$$

$$\frac{h\nu}{c} = \frac{h\nu'}{c} \sin \phi + \frac{m\beta c}{\sqrt{1 - \beta^2}} \sin \theta \quad \text{(Z component)} \tag{39}$$

where θ is the angle of scatter of the electron with respects to the primary photon direction. For a known scattering angle ϕ we now have three equations in three

unknowns (ν' β and θ) and thus the equations may be solved. The quantity of most interest is the wavelength of the scattered photon ($\lambda' = c/\nu'$) solution for this yields

$$\lambda' = \lambda + \frac{h}{mc}(1 - \cos\phi) \tag{40}$$

or as the quantity h/mc is a constant (0.0234 Å)

$$\delta\lambda = \lambda' - \lambda = 0.0234(1 - \cos\phi) \tag{41}$$

Thus it may be seen that the change in the wavelength upon scattering increases with the scattering angle but is independent of the incident wavelength of the photon and is the same for all substances.

Scatter by an Atomic Electron

It is found in experiment that the scatter by atomic electrons is a mixture of both coherent and incoherent scattering. As a starting point one considers the simplest instance where the atom contains only one electron (i.e. hydrogen). It can be shown using wave mechanics that this electron may occupy any of a series of energy states. If after the scattering event the electron is in the same state as it was before there can have been no energy transfer from the photon. This means that the scattering must have been coherent and that the incident and emergent wavelengths of the photon will be identical. If after the scattering event the electron is in a different energy state, the energy for this change must have come from the photon. This will mean that the wavelength of the photon will be changed and the scattering will be incoherent. The difference in the incident and scattered wavelengths will in general not be that given by equation 41 but will lie somewhere in a distribution centred on this mean value. The variation in the scattered wavelengths arises from the motion

of the scattering electron and due to this the resultant distribution has a definite width.

To calculate the scattering from an electron bound to an atom it is necessary to replace the point charge electron of the preceding sections with the wave mechanical model of a smooth distribution of electrical charge. The scattering factor of the electron may then be expressed as

$$f_e = \int_0^\infty U(r) \frac{\sin kr}{kr} \, \mathrm{d}r \tag{42}$$

The quantity $U(r)\ \mathrm{d}r$ is related to the charge density distribution and may be calculated using wave mechanics. The scattering power of the electron is then given by f_e^2, thus the coherent scattered intensity is

$$I_{coh} = I_e f_e^2 \tag{43}$$

where I_e is the scattered intensity given by the Thompson formula. As the total intensity scattered by the electron is I_e that proportion scattered as incoherent radiation is

$$I_{inc} = I_e - I_{coh} = I_e(1 - f_e^2) \tag{44}$$

The scattering factor f_e is always one at $\phi = 0°$ and decreases as ϕ increases. The rate of decrease of the scattering factor varies inversely with the extent of the electron cloud. Compton scattering however is always zero at $\phi = 0°$ and will increase with the angle ϕ being proportional to $\sin^2 \phi/2$ for small ϕ. These two effects mean that for weakly bound electrons the coherent scattering predominates close to the primary beam direction and at larger angles the scattering is mainly incoherent. In the limit of a free electron only incoherent scattering will be observed. If the electron is tightly bound (i.e. where the electron cloud is much closer to the nuclei) the coherent scatter will predominate to much larger angles.

The Atomic Scattering Factor

In the case of an atom with more than one electron the scattering factor will be related to the total electron density of the atom. To calculate this it is generally assumed that the total electron density is the sum of the individual electron densities. In this case the amplitude of the scattered waves at a given point will simply add. The intensity of the coherent scatter from an atom of Z electrons is thus given by

$$I_{coh} = f^2 I_e = \left(\sum_{j=1}^{Z} f_{ej} \right)^2 I_e \tag{45}$$

where f_{ej} is the scattering factor of the j^{th} electron as given in equation 42. The function f is called the *atomic scattering factor.*

In the case of incoherently scattered radiation there will be no interference between the waves scattered by the electrons due to the lack of any phase relationship and the total intensity will be given by the sum of the individual electron scattering intensities.

$$I_{inc} = \sum_{j=1}^{Z} (1 - f_{ej}^2) I_e \tag{46}$$

A more exact value for the incoherent scattering is obtained by taking into account the Pauli exclusion principle which states that only transitions to either unoccupied states or to states occupied by an electron of opposite spin are allowed. The effect of this is to introduce a correction term into the last equation to give

$$I_{inc} = I_e (Z - \sum_j f_{ej}^2 - \sum_j \sum_k f_{ejk}) \tag{47}$$

where the summations are over all Z electrons. In general the correction term is very small and may be ignored. The calculation of atomic scattering factors using wave mechanics has been carried out by a number of people and the results have been tabulated for both coherent [27,28] and incoherent [29-32] scattering.

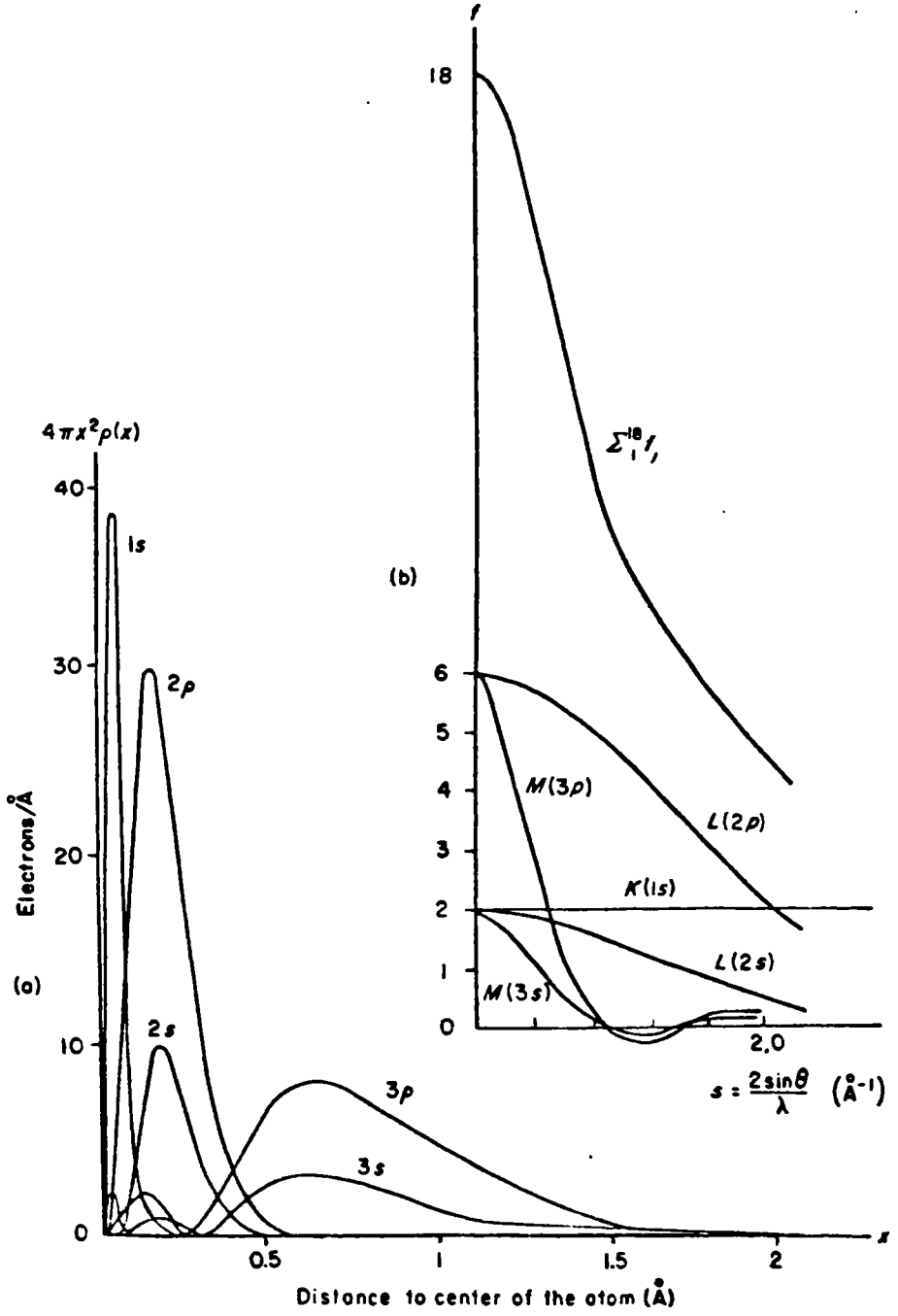

Figure 5: a) Radial electron densities for the various shells of the k^+ ion. b) Scattering factors for the individual electrons and the total scattering factor for the k^+ ion [33]

The equations above are only valid if the incident radiation has a large frequency compared to that of any absorption discontinuities in the atom. When the angular frequency of the incident X-ray is comparable to that of a particular type of electron in the atom (e.g. $1S$ or $2P$) resonance effects will occur that will alter the scattering from the electron and thus modify the atomic scattering factor. The most important electrons in these effects are those which are strongly bound and especially those associated with the K shell. Due to this the dispersion anomaly is most important when the incident wavelength is close to that of the K discontinuity of the scatterer. The K edge effect will also be evident for all wavelengths above that associated with the K discontinuity as the K electrons will be weakly excited by the radiation.

To correct for the anomalous scattering the atomic scattering factor is modified to give

$$f = f_0 + \Delta f' + i\Delta f'' \tag{48}$$

where f_0 is the uncorrected atomic scattering factor and $\Delta f'$ and $\Delta f''$ are the real and imaginary terms of the anomalous scattering. The amplitude of the scattered wave is determined by the modulus of f thus

$$|f| = \left[(f_0 + \Delta f')^2 + \Delta f''^2\right]^{1/2} \tag{49}$$

provided that $\Delta f''$ is small the value of $|f|$ is given by the expansion

$$|f| = f_0 + \Delta f' + \frac{\Delta f''^2}{2(f_0 + \Delta f')} \tag{50}$$

In the case of normal scattering the phase shift is π radians, for anomalous scattering that is modified to $\pi - \psi$ where

$$\psi = \tan^{-1} \frac{\Delta f''}{f_0 + \Delta f'} \tag{51}$$

The values of $\Delta f'$ and $\Delta f''$ are tabulated in the *International Tables of X-ray Crystallography* [27]. Unlike f_0 they are independent of the scattering angle as the electrons producing the effect are bound closely to the nucleus. They are, however, dependent on the incident wavelength and on the atomic number of the scatterer. If the incident wavelength is above the L or M absorption edge the effect of anomalous scattering on the atomic scattering factor are even more complicated and theoretical calculations for these cases tend to be unreliable. It is important to note that for light atoms and low X-ray wavelengths the anomalous scattering corrections make little difference and may be neglected.

Scattering by a Monatomic System.

Early work on X-ray scattering by Debye [34] showed that the coherently scattered waves from two atoms interfere with one another and that as a result of this an interference pattern is produced which is dependent on the separation of the two atoms. Zernicke and Prins [35] suggested a distribution function which would facilitate the prediction of the X-ray pattern produced by a substance. Conversely given a known X-ray spectra the distribution function could be found. Debye and Menke [36] completed the analysis for this reverse procedure and applied it to liquid mercury in 1931. An alternative version of this analysis was presented by Warren and Gingrich [6,37,38] and it is this method that will be followed in this section.

Consider an X-ray beam of amplitude E_0 incident on two atoms, one at the origin, O, of a coordinate system and the other at a point Q with the position vector $\mathbf{r}_{nm}$ (figure 6). If the incident wave is polarized perpendicular to the scattering plane the amplitude, at a point P, of the wave scattered by the atom at O will be given

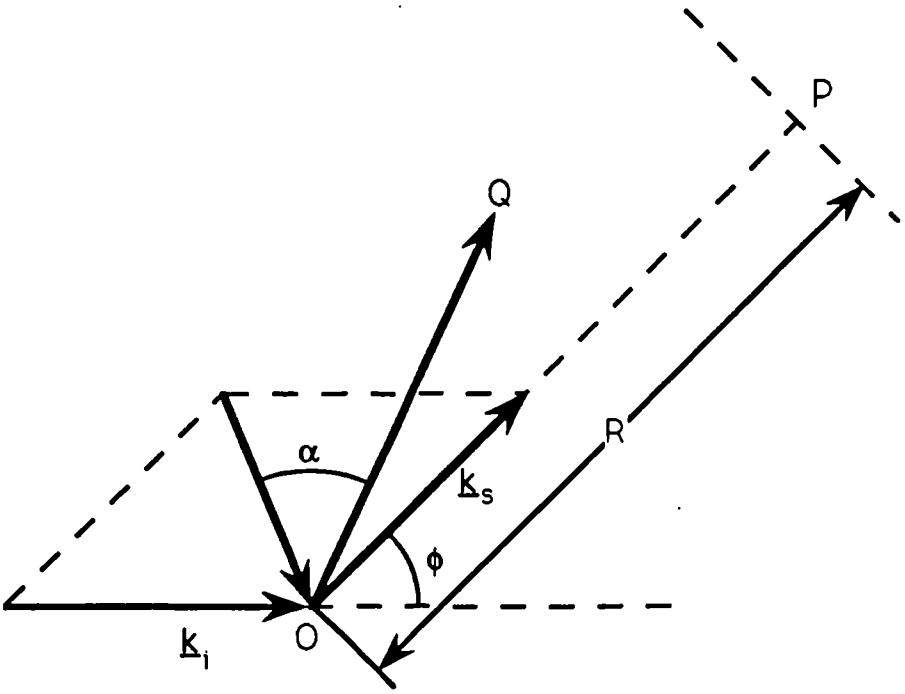

Figure 6: Scattering from a pair of atoms at positions O and Q

by

$$E_P = E_O f_n \left(\frac{e^2}{mR}\right)\left(\frac{\mu_0}{4\pi}\right) \tag{52}$$

(cf equation 33). The phase of the radiation scattered by atom n at position Q relative to the origin is $(\mathbf{r}_n.\mathbf{k}_i - \mathbf{r}_n.\mathbf{k}_s)$ where $\mathbf{k}_i$ and $\mathbf{k}_s$ are the initial and final wave vectors of the scattered radiation. Thus if the incident wave has the form $E = E_0 \exp(2\pi i\nu t)$ then the scattered wave from atom n is given by

$$E = E_0 \frac{r_e}{R} f_n \exp i(2\pi\nu t - \mathbf{r}_n.(\mathbf{k}_i - \mathbf{k}_s)) \tag{53}$$

where as before $r_e = (e^2/m)(\mu_0/4\pi)$, the classical radius of the electron. The total amplitude at the point P will be the sum of the individual amplitudes thus

$$E_P = E_0 \frac{r_e}{R} \sum_n f_n \exp i\,(\mathbf{k}.\mathbf{r}_n) \tag{54}$$

where $\mathbf{k} = \mathbf{k}_i - \mathbf{k}_s = \frac{4\pi}{\lambda}\sin\phi/2$ (cf equation 1). Thus the intensity of the scattered radiation at P is given by

$$I = E_P^2 = I_0\frac{r_e^2}{R^2}\left[\sum_n f_n \exp i\,(\mathbf{k}.\mathbf{r}_n)\right]\left[\sum_m f_m \exp i\,(\mathbf{k}.\mathbf{r}_m)\right] \quad (55)$$

$$= I_0\frac{r_e^2}{R^2}\left[\sum_{nm} f_n f_m \exp i\,(\mathbf{k}.\mathbf{r}_{nm})\right] \quad (56)$$

where $\mathbf{r}_{nm} = \mathbf{r}_n - \mathbf{r}_m$. Defining the angle between $\mathbf{r}_{nm}$ and $\mathbf{k}$ to be α and representing the observed intensity in electron units as $I_{eu} = I/I_e$ where I_e is the intensity given by the Thompson formula gives

$$I_{eu} = \sum_{nm} f_n f_m \exp[ikr_{nm}\cos\alpha] \quad (57)$$

As during the summation the vector $\mathbf{r}_{nm}$ takes on all positions in space, α will take on all angles; thus averaging the exponential function over all solid angle gives

$$\frac{\int_0^{4\pi}\exp[ikr_{nm}\cos\alpha]\,\mathrm{d}\Omega}{\int_0^{4\pi}\mathrm{d}\Omega} = \int_0^{\pi}\exp[ikr_{nm}\cos\alpha]2\pi\frac{\sin\alpha\,\mathrm{d}\alpha}{4\pi} \quad (58)$$

$$= \frac{\sin kr_{nm}}{kr_{nm}} \quad (59)$$

Substituting this into the previous equation gives the *Debye equation*

$$I_{eu} = \sum_{n,m} f_n f_m \frac{\sin kr_{nm}}{kr_{nm}} \quad (60)$$

It may be seen from the last equation that the intensity of scatter is dependent on the atomic scattering factors for the atoms in the system, the wavelength of the incident radiation and the scattering angle (via the scattering factor k). It is also dependent on the atomic separation of the component atoms. For a monatomic system $f_n = f_m = f$ and thus $f_n f_m = f^2$.

Performing the summation over all of the N atoms in the system leads to the equation

$$I_{eu} = Nf^2\left[1 + \sum_{n\neq m}\left(\frac{\sin kr_{nm}}{kr_{nm}}\right)\right] \quad (61)$$

Here the first term is due to the summation of atoms with respect to themselves, where in the limit $r_{nm} \rightarrow 0, \sin kr_{nm}/kr_{nm} \rightarrow 1$. This term is just the sum of the individual atomic scattering and contains no structural information (cf equation 4 of the neutron case). The second term contains the information on the interference between waves scattered by different atoms and thus contains all of the structural information on the system. As in the neutron case we may now introduce the microscopic atomic number density, $\rho(r)$ and summing over all of the atoms in the system gives

$$I_{eu} = Nf^2 \left[1 + \int_0^R 4\pi r^2 \rho(r) \frac{\sin kr}{kr} \, \mathrm{d}r\right] \tag{62}$$

where $4\pi r^2 \rho(r) \, \mathrm{d}r$ is the number of atoms in a shell of thickness $\mathrm{d}r$ at a distance r from the origin atom and R is the radius of the sample. If we now introduce the average atomic number density ρ_0 equation 62 may be written as

$$I_{eu} = Nf^2 \left[1 + \int_0^R 4\pi r^2 (\rho(r) - \rho_0) \frac{\sin kr}{kr} \, \mathrm{d}r + \int_0^R 4\pi r^2 \rho_0 \frac{\sin kr}{kr} \, \mathrm{d}r\right] \tag{63}$$

The second integral may be taken to be zero as

$$\int_0^R 4\pi r^2 \rho_0 \frac{\sin kr}{kr} \, \mathrm{d}r = \left[\left(\frac{4\pi r^3}{3}\right) \rho_0 \left(\frac{3}{kr^2}\right) \left(\frac{\sin kr}{kr} - \cos kr\right)\right]_{r=0}^{r=R} \tag{64}$$

For $r = 0$ this term is zero and for $r = R$ when R is large (i.e. of the dimensions of the sample) the integral will be zero for all but very small values of k.

As in the neutron case we may define the structure factor, $S(k)$ as

$$I_{eu} = Nf^2 S(k) \tag{65}$$

and the pair correlation function $g(r)$ as

$$g(r) = \frac{\rho(r)}{\rho_0} \tag{66}$$

Substituting these two equations into equation 63 and letting the upper limit tend to infinity gives

$$S(k) = \frac{I_{eu}}{Nf^2} = 1 + 4\pi\rho_0 \int_0^\infty r^2 \left(g(r) - 1\right) \frac{\sin kr}{kr} \, \mathrm{d}r \tag{67}$$

and Fourier inversion leads to

$$g(r) = 1 + \frac{1}{2\pi^2\rho_0} \int_0^\infty k \left(S(k) - 1\right) \frac{\sin kr}{kr} \, \mathrm{d}k \tag{68}$$

For a fuller description of the function $g(r)$ see section 1.2.1.

It can be seen that the resulting equations for $S(k)$ and $g(r)$ for both neutron and X-ray scattering (equations 21, 22, 67 and 68) are identical except that the neutron coherent scattering length, $\bar{b}$ in equation 13 is replaced by the atomic scattering factor, f in equation 65. The derivation of the X-ray scattering equations assumes that there is no transfer or share of electrons between atoms (e.g. ionic or covalent bonding). If the substance under examination is ionically bonded the atomic scattering factor needs to be recalculated to allow for the change in the number of electrons. The case of covalent bonding is more complicated in that there is a delocalization of the electron cloud around the atoms involved. It is generally assumed that this has little effect on the results and that the pair correlation function produced is directly comparable to that produced in the neutron case if the relative weighting of the scattering for neutrons and X-rays is taken into account (this is only important if more than one atom type is present in the sample). It should be noted that according to Wright [9] the change in X-ray scattering from light elements involved in strongly covalently bonded systems (i.e. where the electron cloud is highly distorted) from the predicted scattering from the equivalent free atoms may lead to an excessive sharpening of the peaks produced in the associated pair correlation function.

The differences in the coherent bound neutron scattering length and the X-ray atomic scattering factor mean that X-ray and neutron scattering may be used as complementary techniques. This is especially true when investigating systems involving mixtures of light elements, such as hydrogen and carbon, where the X-ray scattering from the lightest elements are weaker and have a correspondingly lower presence in the $g(r)$ curve. The neutron scattering intensity is not however dictated by the atomic number and thus often the light elements have an equivalent bound scattering length to the heavier elements and so show equally strongly in the $g(r)$ curve. These changes can help in the analysis of the $g(r)$ curve.

1.3 Scattering by a Molecular System

When considering scattering from a monatomic system in the last section, the system as a whole was treateded as a collection of discrete atoms. In a similar way it is useful to consider the scattering from a molecular system in terms of a set of discrete molecules. In the monatomic case the starting point was to explain the scattering by a single atom and similarly here the starting point is to consider the scattering by an isolated rigid molecule. From equation 3 it can be deduced that the scattering cross-section for a molecule is given by

$$\frac{d\sigma}{d\Omega}^{coh}_{mol} = \sum_{i,j}^{n} \overline{b_i}\,\overline{b_j} \exp(i\mathbf{k}.\mathbf{r}_{ij}) \tag{69}$$

Where n is the number of atoms in the molecule and $\overline{b_i}$ is the mean coherent scattering length of atom i. If it is assumed that there is no preferred orientation for the molecule (i.e. that the molecule occurs in all spatial orientations with equal

probability) the last equation becomes

$$\frac{d\sigma}{d\Omega}^{coh}_{mol} = \sum_{i,j}^{n} \overline{b_i}\,\overline{b_j} \frac{\sin kr_{ij}}{kr_{ij}} \tag{70}$$

In a similar way to the splitting of the scattering for the monatomic system into a 'self' and an interference term it is possible to subdivide the scatter from a molecule.

$$\frac{d\sigma}{d\Omega}^{coh}_{mol} = \sum_{i}^{n} \overline{b_i}^2 + \sum_{i \neq j}^{n} \overline{b_i}\,\overline{b_j} \frac{\sin kr_{ij}}{kr_{ij}} \tag{71}$$

The first term in this equation is the self term and arises from the $i = j$ components of the previous equation (when $i = j, r_{ij} = 0$ and $\sin(kr_{ij})/kr_{ij} = 1$).The self term arises from interference of waves scattered by the same atom and as such is a featureless curve. The second term is caused by the interference of waves scattered by different atoms within the molecule and contains information on all of the intramolecular distances (i.e. the spatial arrangement of the atoms in the molecule).

In general an molecule will not be rigid as there will be thermal vibration of the component atoms. The effect of the vibrations is that the atom separations, r_{ij}, will no longer be discrete distances but will be composed of Gaussian distributions centred around r_{ij}. It is necessary to take this into account to fully reproduce the scattering by the single molecule and to do this we introduce the Debye–Waller factor [18]. Equation 71 now becomes

$$\frac{d\sigma}{d\Omega}^{coh}_{mol} = \sum_{i}^{n} \overline{b_i}^2 + \sum_{i \neq j}^{n} \overline{b_i}\,\overline{b_j} \frac{\sin kr_{ij}}{kr_{ij}} \exp\left(\frac{-1}{2}\left\langle u_{ij}^2 \right\rangle k^2\right) \tag{72}$$

where $\left\langle u_{ij}^2 \right\rangle$ is the mean square amplitude of the thermal vibration of the atom pair.

The structure factor for the molecule, $F_M(k)$ may now be defined in an analogous way to the definition of the structure factor, $S_M(k)$, for the monatomic system

(equation 13).

$$\frac{d\sigma}{d\Omega}^{coh}_{mol} = \left(\sum_i^n b_i\right)^2 F_M(k) \tag{73}$$

Hence substitution in equation 72 gives

$$F_M(k) = \frac{\sum_i^n \overline{b_i}^2}{\left(\sum_i^n \overline{b_i}\right)^2} + \frac{1}{\left(\sum_i^n \overline{b_i}\right)^2} \sum_{i \neq j}^n \overline{b_i}\,\overline{b_j} \frac{\sin kr_{ij}}{kr_{ij}} \exp\left(\frac{-1}{2}\left\langle u_{ij}^2 \right\rangle k^2\right) \tag{74}$$

The function $F_M(k)$ is commonly known as the molecular form factor.[2]

If the system is now expanded to become an ensemble of N molecules it is possible to represent the molecular liquid structure factor, $S_M(k)$, as the sum of the scattering from the individual molecules and the interference contribution from the pair of atoms in separate molecules. The second of these contributions is represented by the intermolecular structure factor, $D_M(k)$. Thus

$$S_M(k) = F_M(k) + D_M(k) \tag{75}$$

This equation contains all of the structural information about the liquid.

The pair distribution function, $d(r)$, may now be derived in the same manner as before (equation 24) and yields

$$d(r) = 4\pi r \rho_M \left(g(r) - 1\right) \tag{76}$$

$$= \frac{2}{\pi} \int_0^\infty k \left(S_M(k) - \frac{\sum_i \overline{b_i}^2}{\left(\sum_i \overline{b_i}\right)^2} \right) \sin kr \; \mathrm{d}k \tag{77}$$

Where ρ_M is the molecular number density.

The function $d(r)$ contains information on the relative positions of all atoms in the system. If the conformation of the molecule is well known it is often more

[2]The molecular form factor is normally represented by the notation $f_1(k)$ this has been altered to $F_M(k)$ to avoid confusion with the X-ray scattering factors f_e and f for the electron and atom respectively

informative to consider only the intermolecular correlations. To do this the intermolecular distribution function, $d_L(r)$ is defined as

$$d_L(r) = 4\pi r \rho_M \left(g_L(r) - 1\right) \quad (78)$$

$$= \frac{2}{\pi} \int_0^\infty k D_M(k) \sin kr \; \mathrm{d}k \quad (79)$$

Where $g_L(r)$ is the intermolecular pair correlation function. The function $d_L(r)$ describes the intermolecular structure of the system and is often the most important distribution curve involved in the analysis of diffraction data. The function $D_M(k)$ is obtained by subtracting the theoretical molecular form factor from the measured liquid structure factor and because of this it is often difficult to determine $d_L(r)$ accurately.

For X-rays an identical argument may be followed and the end results are the same apart from the replacement of the neutron coherent bound scattering length, $\overline{b}_i$ with the atomic scattering factor f_i.

Chapter 2

Experimental Instrumentation

2.1 Introduction

Two types of radiation were used in the diffraction measurements performed on the samples, these being, neutrons produced at the high flux reactor at the Institut Laue Langevin (ILL), Grenoble, France and X-rays produced at the Synchrotron Radiation Source (SRS), Daresbury, England. The following sections describe the instrumentation and experimental procedures used.

2.2 The I.L.L. High Flux Reactor

The nuclear reactor at the Institut Laue-Langevin is a steady-state reactor which operates at a power of 57 MW. Fission neutrons produced within the enriched U^{235} core of the reactor are slowed to thermal equilibrium in a D_2O moderator at 300 K. The resultant thermal neutrons have a Maxwellian energy distribution which has a peak at an energy corresponding to a neutron wavelength of 1.2 Å. These neutrons are extracted in the form of a "white" neutron beam via ports in the reactor and

the neutron energy desired for the experiment is selected using Bragg reflection from a suitably chosen single crystal monochromator. The monochromatic neutron beam is collimated by a set of slits formed of a highly absorbing material, normally cadmium or boron. The flux of the resultant collimated beam is then measured using a transmission detector and the beam is passed into the sample vessel (see below).

In the study of molecular liquids it is necessary to obtain measurements of the flux of the diffracted neutron beam over a wide range of k values, (often to a k of 16 $Å^{-1}$ or more). This may be achieved by using neutrons of short wavelength, however, due to the shape of the neutron energy distribution, reduction of the chosen incident wavelength, to values significantly away from the peak of the distribution, leads to a large drop in the neutron flux. To overcome this the ILL reactor contains a "Hot Source", which consists of a 0.01 m^3 block of graphite at ~2400 K. The use of the Hot Source broadens the neutron energy distribution and shifts its peak towards higher energies giving an enhanced neutron intensity in the wavelength range $0.4 < \lambda < 0.8$ Å.

2.2.1 The Two-Axis Diffractometer, D4B

The D4B diffractometer has been specifically designed for the study of liquids, amorphous materials and gases. It is situated on the beam port H8 which supplies neutrons from the Hot Source. A Cu(220) or Cu(200) single crystal monochromator is used to select incident neutron wavelengths of 0.5 Å or 0.7 Å respectively. The flux of this beam at the sample position is 4 x 10^7 n cm^{-2} s^{-1} at $\lambda = 0.7$ Å. For $\lambda = 0.5$ Å this is reduced by a factor of about 2.5.

The incident beam is collimated by a series of four horizontal and vertical slits

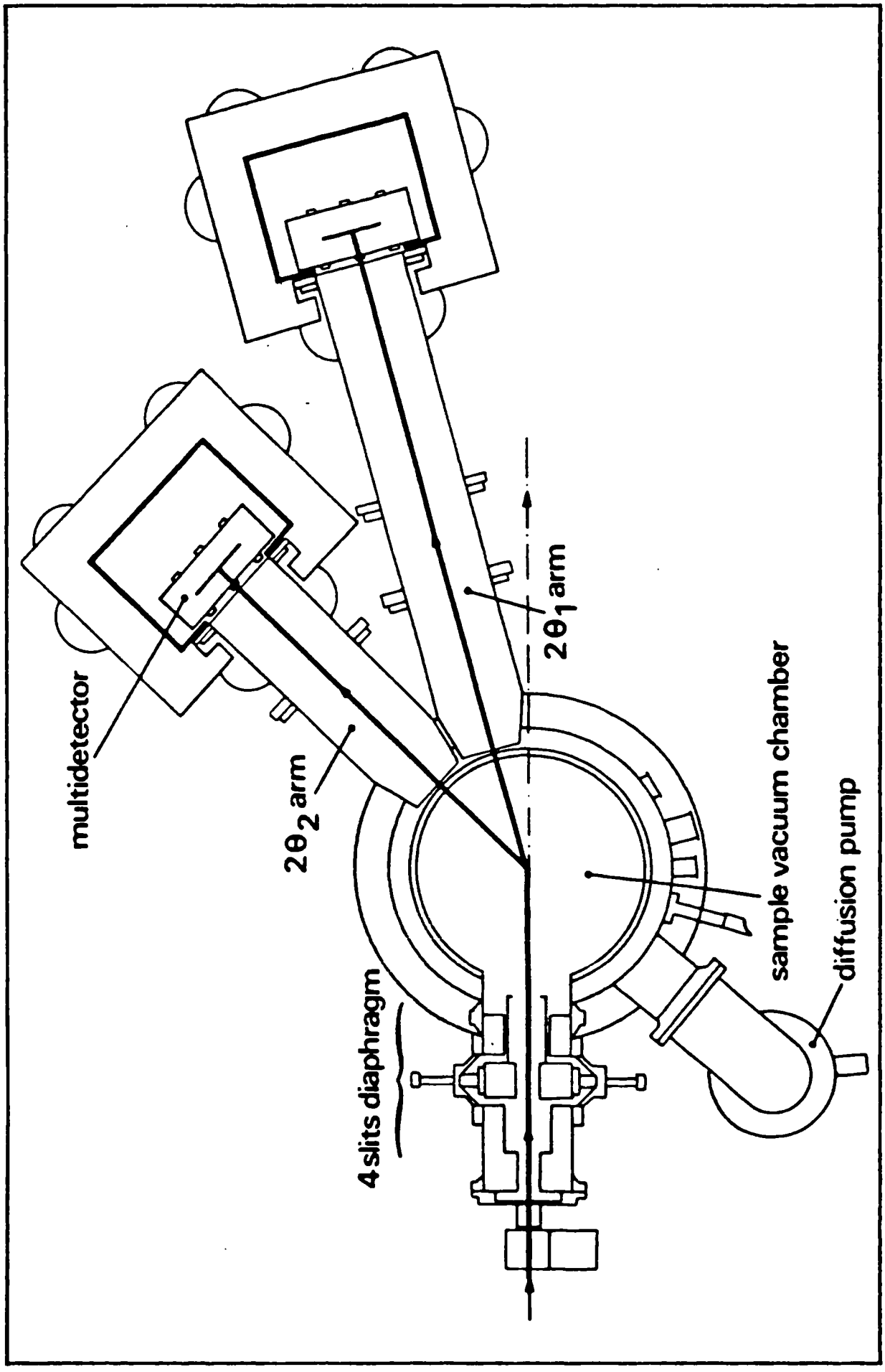

Figure 7: Schematic view of the liquids diffractometer D4B (plan view)

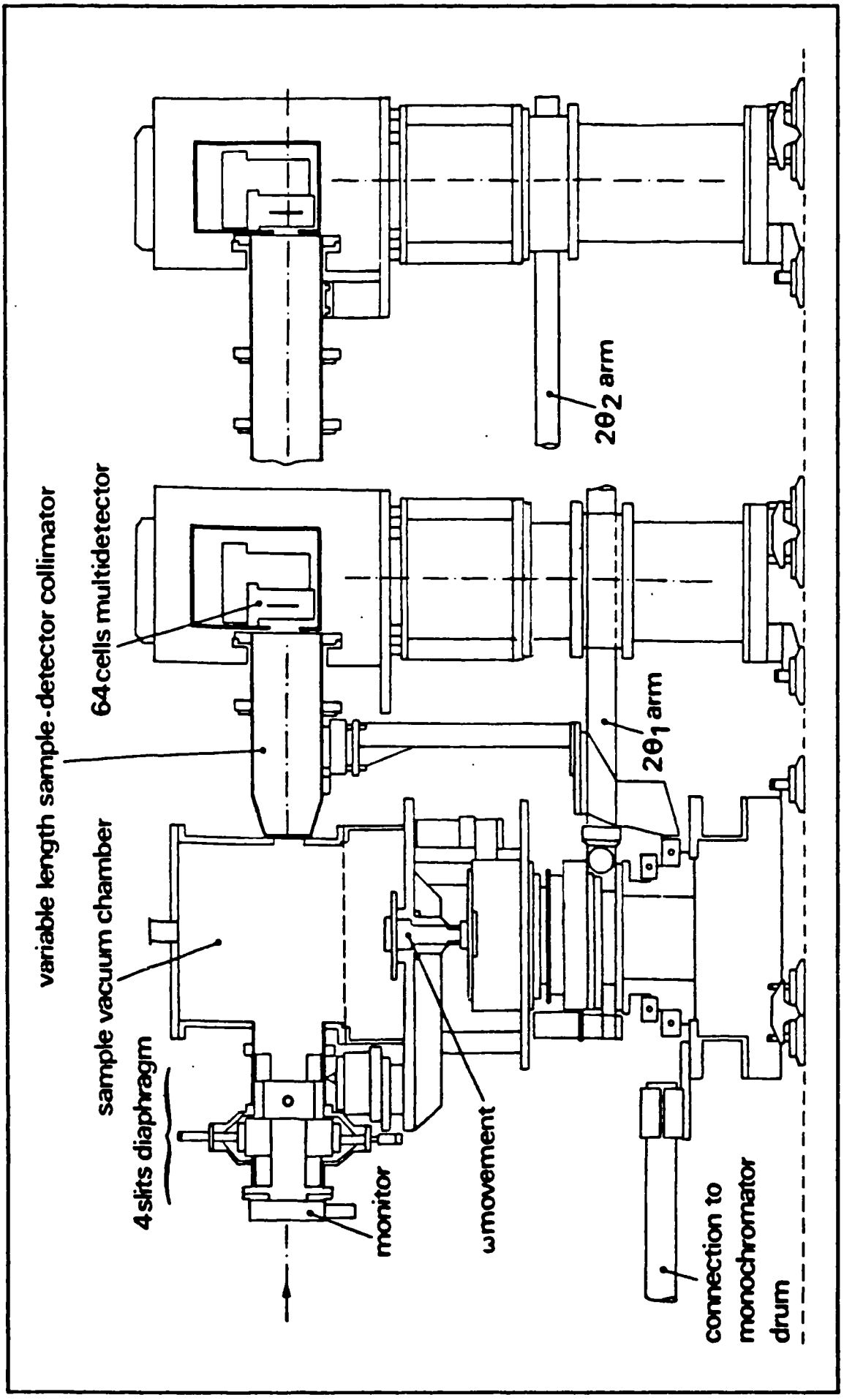

Figure 8: Schematic view of the liquids diffractometer D4B (front view)

giving a variable beam profile with a maximum size, at the sample, of 2 cm wide by 7 cm high. The sample is contained in a thin walled vanadium tube with a diameter of ~6 mm and height of ~100 mm which is mounted vertically in the centre of a large cylindrical sample chamber. The sample chamber is evacuated for the duration of the experiment to minimise air scatter and thus reduce the background count.

The diffractometer has two ^{3}He multidetectors each consisting of 64 cells filled to a gas pressure of 15 bars, allowing a reasonable detection efficiency even at low wavelengths. The cells have an angular spacing of 0.1° at 1.5 m from the sample. Each multidetector is connected to a movable arm outside of the sample chamber and the motion of the arm is under computer control. One detector is mounted at a distance of 1.5 m from the sample and moves over an angular range of 1.8° – 67.7° to collect the low angle part of the scattering spectrum. The second multidetector is mounted at 0.75 m from the sample and covers the range 42.2° – 131.6°. The large angular overlap is provided to allow accurate normalisation of the two collected spectra to each other. The collected scattering spectrum corresponds to momentum transfers in the range $0.3 < k < 16.3$ Å^{-1} for 0.7 Å neutrons or $0.4 < k < 22.9$ Å^{-1} for 0.5 Å neutrons.

The scattering spectrum is collected under computer control and the counts from the individual detector cells are combined to give a final data set for each detector. This data set is made up of a list of angular steps and for each step a corresponding neutron count and the statistical error in this count. The count and error are normalised to a monitor count of 10000 using the monitor count recorded by the transmission detector in the incident neutron beam.

2.2.2 The High Flux Two-Axis Diffractometer, D20

The D20 diffractometer is sited on the thermal neutron beam port H11. A choice of pyrolitic graphite (PG(002)), Cu(200) and Ge(511) monochromators allows neutrons of wavelength 0.87, 1.17, 1.35, 1.54 or 2.51 Å to be selected, of these the 0.87 Å wavelength is most suited to liquid studies as it yields the largest k range. Collimation of the neutron beam provides a beam size at the sample of 50 x 30 mm. The sample is contained in a thin-walled vanadium container with a diameter of ~6 mm and a height of ~100 mm which is mounted at the centre of a large cylindrical sample vessel. This sample vessel is evacuated for the course of an experiment to reduce background scattering.

The diffractometer has a single position sensitive gas detector at a distance of 1.45 m from the sample. The detector is mounted on a movable arm which can be scanned, under computer control, over a range of 0° to 120°. This gives a corresponding k range of 0 to 12.5 $Å^{-1}$ for a neutron wavelength of 0.87 Å. The detector consists of 126 cells filled with a mixture of ^3He and C_3H_8 gases at a pressure of 4 bars and 1 bar respectively. The cells are arranged to give the detector an angular aperture of 12.6° and a vertical aperture of 150 mm.

The scattering spectrum is collected under computer control and processed in the same way as those obtained on D4B.

2.3 The Synchrotron Radiation Source

When a charged particle is accelerated in a circular orbital path it emits a smooth continuous spectrum of electromagnetic radiation. This emission is called synchrotron radiation, taking its name from the General Electric Synchrotron where it

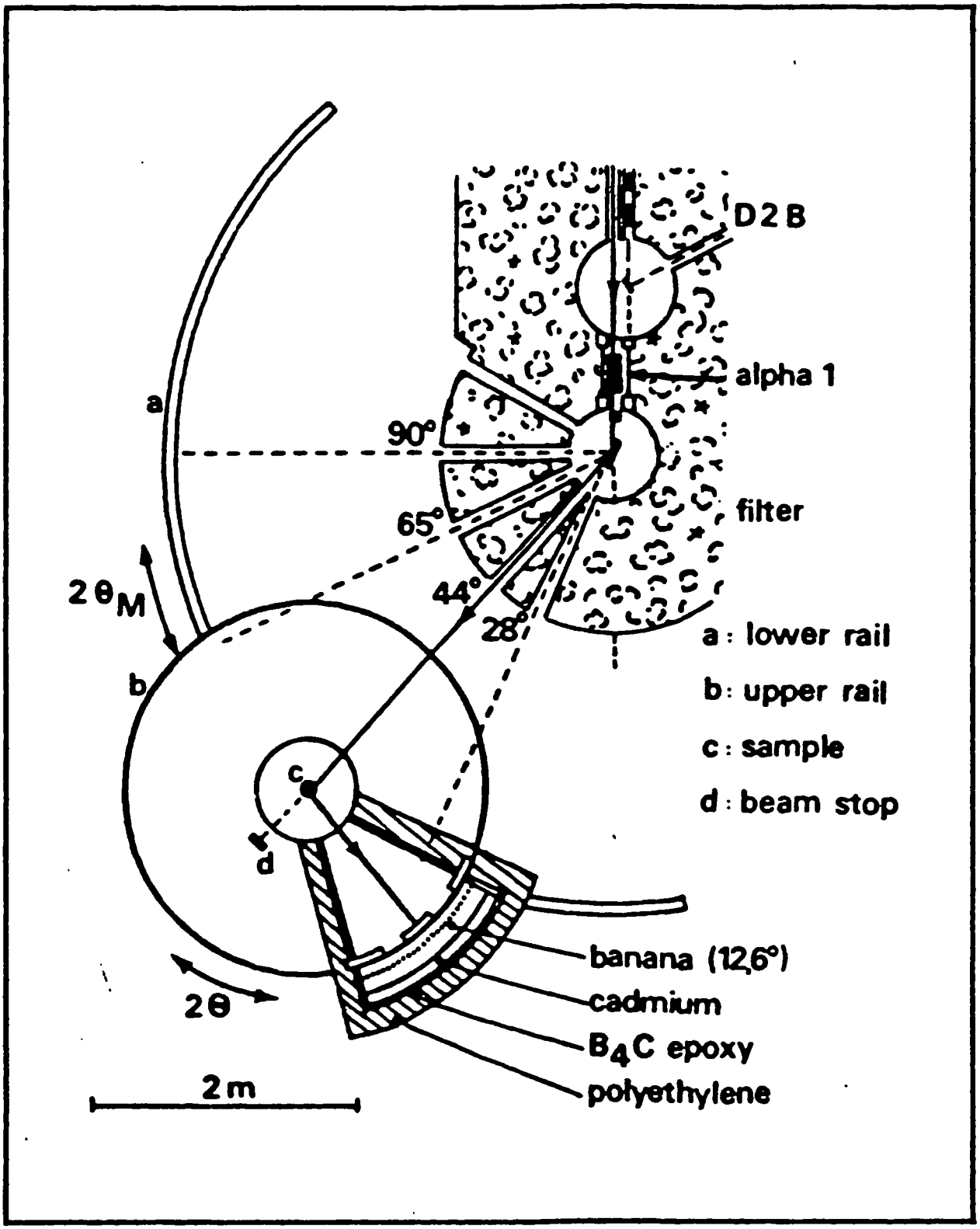

Figure 9: Schematic view of D20

it was first directly observed in 1947 [39]. If the accelerated particles are high energy electrons (i.e. electrons travelling at relativistic velocities) the spread of emitted radiation stretches from X-rays through into the far infra-red. Synchrotron radiation is unique in having a high intensity over a wide range of photon energies and producing a highly polarized, collimated beam tangential to the orbital path of the electrons and in the forward direction. It is for this reason that the synchrotron provides an ideal source of radiation for all kinds of experimental work.

At the Synchrotron Radiation Source (SRS) at Daresbury Laboratory, electrons are initially produced by emission from a hot cathode. These electrons are accelerated to an energy of 12 MeV in a linear accelerator (linac) prior to transfer to a booster synchrotron. Here the electrons undergo a second acceleration to an energy of 600 MeV and are then injected into the main synchrotron storage ring. The storage ring contains a series of rf cavities, connected to a klystron, and it is these that are used to accelerate the electron beam up to its final peak energy of 2 GeV. The rf accelerating system is also used to replenish the energy emitted by the electrons as synchrotron radiation, this allows the electrons to be stored for many hours.A second effect of the rf cavities is to produce 'bunching' of the electrons. This imposes a time structure on the emitted radiation causing it to appear at the experimental stations as a rapid succession of discrete pulses.

The SRS storage ring (figure 10) has a circumference of 96 m. Around the circumference of the ring 16, 1.2 Tesla dipole magnets are arranged, each responsible for bending the electron beam through a radius of $\sim$5 m. It is these magnets that provide the radial acceleration required to cause the electrons to emit a pulse of electromagnetic radiation. The 16 bending magnets are connected via straight sections that house pairs of quadrupole magnets which focus the electron beam,

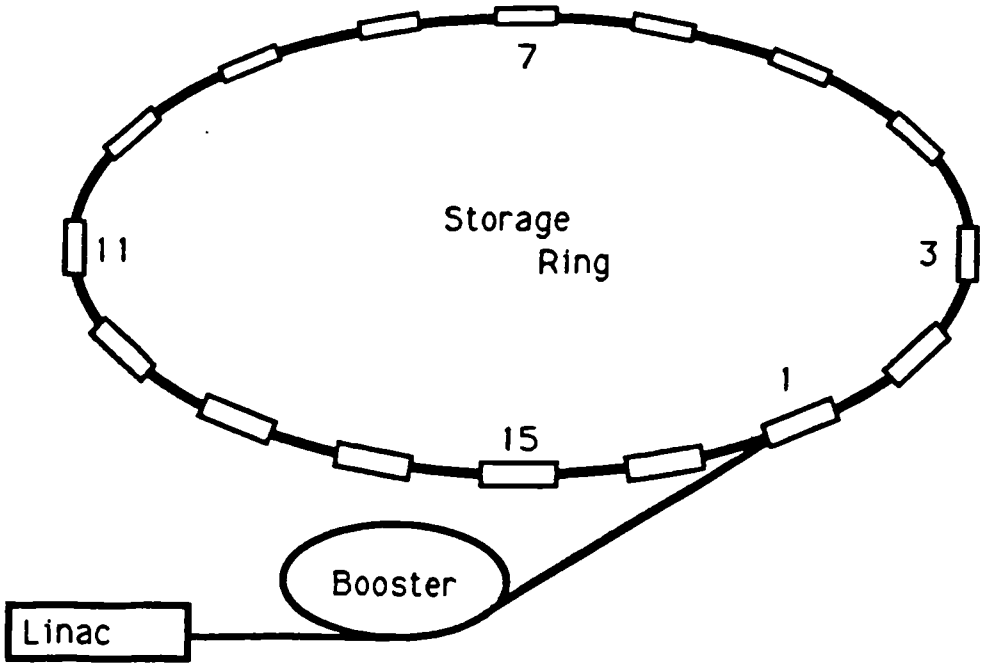

Figure 10: Schematic view of the SRS storage ring.

thus maintaining it in its orbital path. To prevent the electrons being scattered out of their orbits, the whole of the beam path is kept under ultra-high vacuum (10^{-12} – 10^{-13} bar). The maximum beam current obtainable at the SRS is 375 mA, however, the normal operating range (within which all of the experiments were carried out) is 250 mA to 150 mA.

The synchrotron radiation generated in the storage ring is extracted through evacuated beampipes which lead from 'ports' on the storage ring. There is a port situated at each of the bending magnets, the ports and beamlines being numbered to match the bending magnet to which they are attached. The beamlines guide the X-rays to the individual experimental stations and their associated beamline optics.

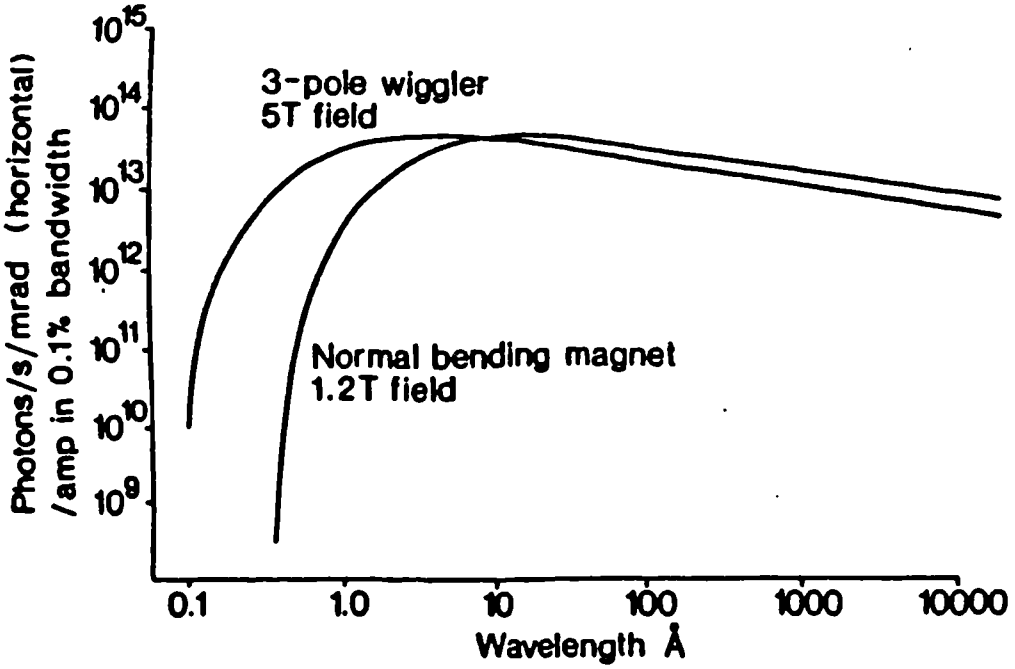

Figure 11: Comparison of the radiation spectra from wiggler and dipole bending magnets at the SRS.

A 5 Tesla superconducting 'wiggler' magnet has been added to the SRS storage ring which imparts an additional oscillation to the electron beam. The effect of this oscillation is to shift the peak in the 'white' electromagnetic continuum to a shorter wavelength (figure 11) making hard X-rays of wavelengths down to ~0.1 Å accessible to stations attached to beamport 9. Opposing magnetic fields before and after the wiggler ensure that no nett translational displacement of the beam occurs.

2.3.1 The Powder Diffractometer Station 9.1

Station 9.1 has been specifically designed for high resolution powder diffraction studies. It is, however, ideally suited as the basis for the development of a liquids

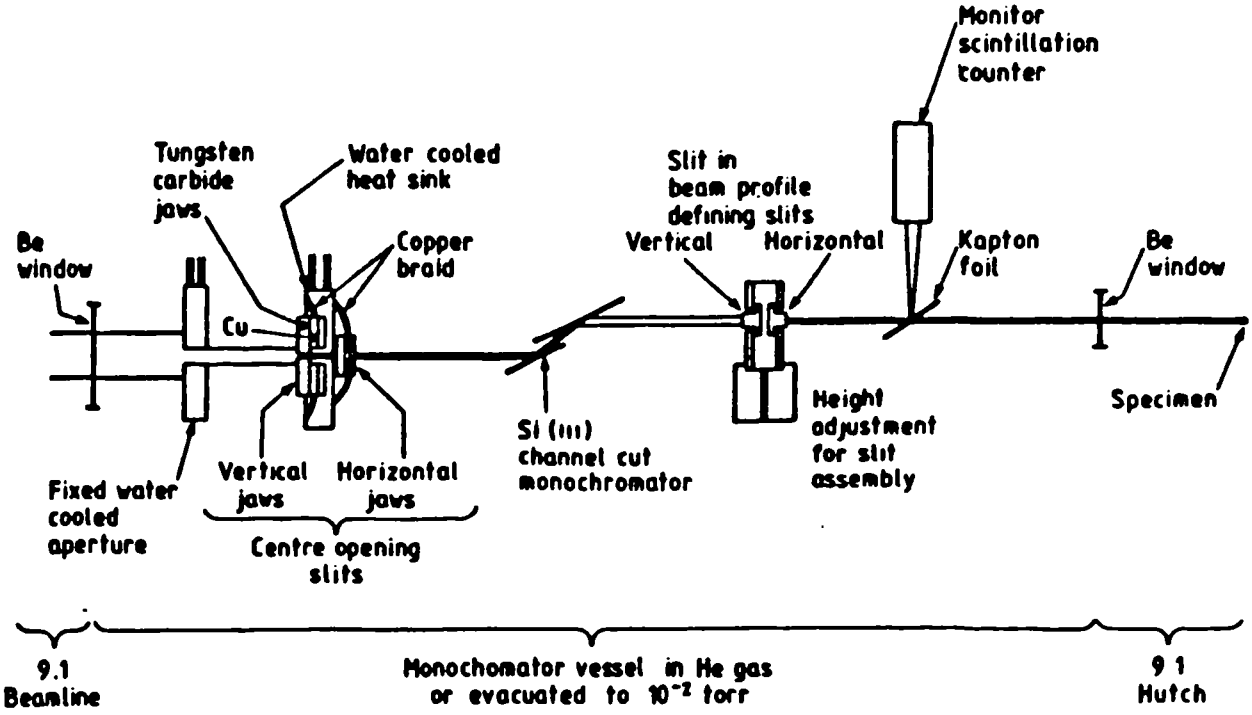

Figure 12: Schematic diagram of the front end assemble of SRS station 9.1

diffractometer from both the point of view of its basic design and the fact that, being situated on beamport 9, it has access to a tunable, short wavelength, high intensity X-ray beam.

A schematic diagram of the front end assemble of 9.1 is shown in figure 12. The X-ray beam arriving from the synchrotron is reduced to a size of 25 x 5 mm by a tungsten carbide fixed aperture. The beam profile may be further reduced by a set of centre-opening horizontal and vertical slits. Both the fixed and variable slits are cooled to prevent excessive beam heating. The beam then falls on a Si(111) channel-cut monochromator. This monochromator is pivoted so that its angle to the incident beam can be altered to select the desired wavelength of X-rays extracted from the white beam in accordance to Braggs law:

$$n\lambda = 2d\sin\theta \tag{80}$$

Where n will be 1 for the principle wavelength and d is the distance separating the Si(111) planes in the crystal (3.138 Å).

The polychromatic beam, which passes straight through the monochromator, is collected in a backstop, whilst the monochromatic beam is reduced to its final size by the beam profile definition slits. The monochromatic beam is monitored by a scintillation counter which observes the scatter from a thin piece of kapton foil. The whole of the front end assemble is enclosed in an evacuated chamber (at $\sim 10^{-2}$ torr). The X-ray beam enters the monochromator chamber through a beryllium window, that separates the chamber from the beamline vacuum, and leaves through a second Be window set close to the sample.

The sample holder consists of two flat plates, made of either brass or perspex, with a 10 mm square aperture in each. These apertures are formed into windows by attaching mica (chosen for its rigidity) to the inside of each plate and the two halves of the sample cell are held apart by a gasket of suitable thickness made from either neoprene or teflon (figure 13). The sample liquid is contained in the central hole of the gasket between the two windows. The sample is mounted on a flat plate attached to the diffractometer. This plate has a large central hole to allow the X-ray beam to pass unobstructed, and is free to rotate about the diffractometer axis so that the sample may be aligned at any desired angle to the incoming beam.

The scattering spectrum is observed through a double slit assemble (with a slit separation of ~230 mm) using a high resolution scintillation counter (figure 14), mounted such that it rotates about the sample in the vertical plane. This orientation is chosen as the incident X-ray beam is almost entirely vertically polarized. Two

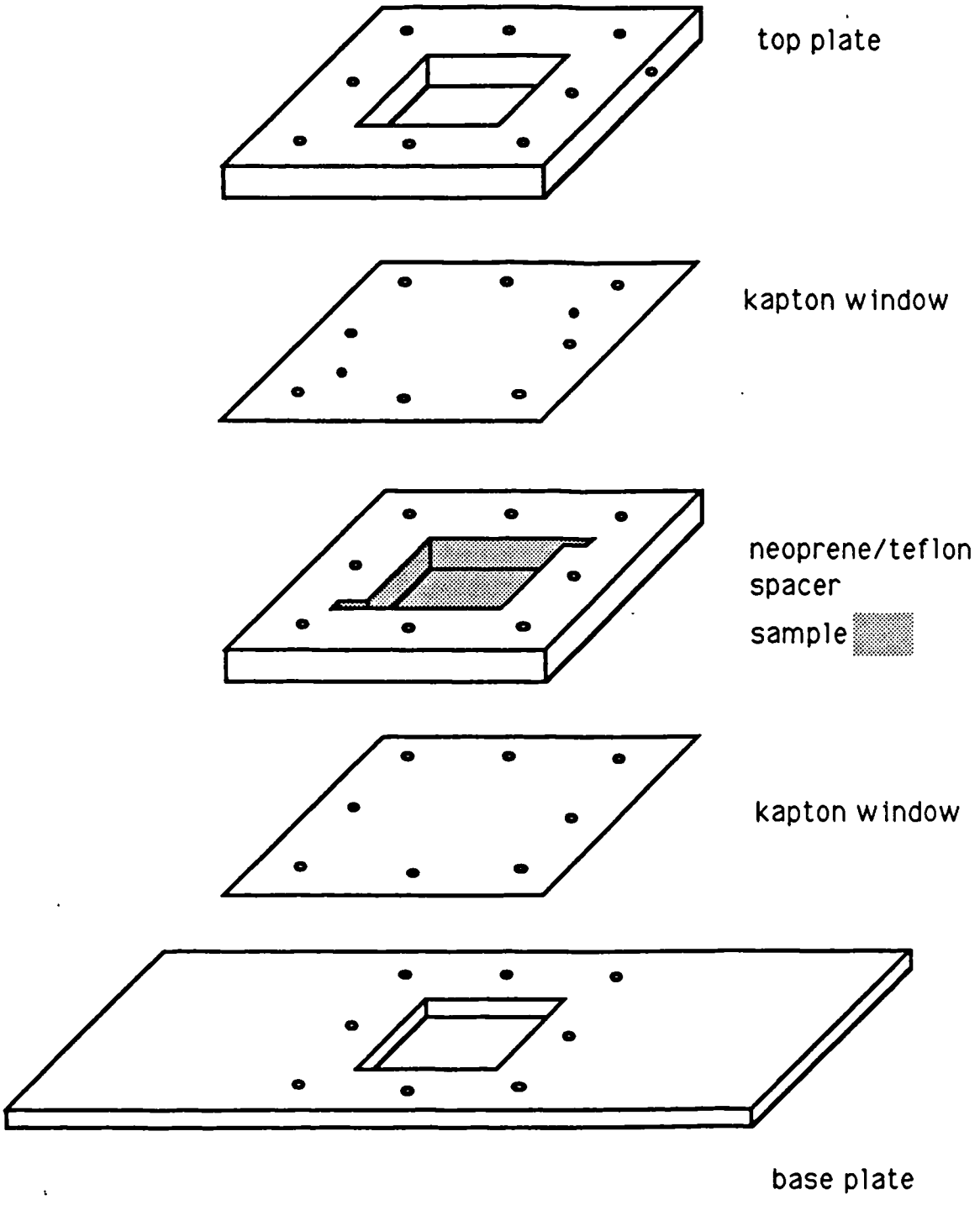

Figure 13: The sample holder used on the 9.1 diffractometer.

detector arrangements were used. In the 'normal' mode the detector is attached directly to the end of the slit assemble. In the second, or 'Warren-Mavel', mode [40], the detector is set at an angle to the line of the slits and used to observe fluorescence scattering from a suitable chosen thin foil which is placed in the scattered beam (see section 3.2). In both arrangements the slit assemble and the detector are mounted on an arm that is free to rotate about the diffractometer axis. Both the diffractometer arm and the sample rotation are under computer control allowing both to be moved during the scan.

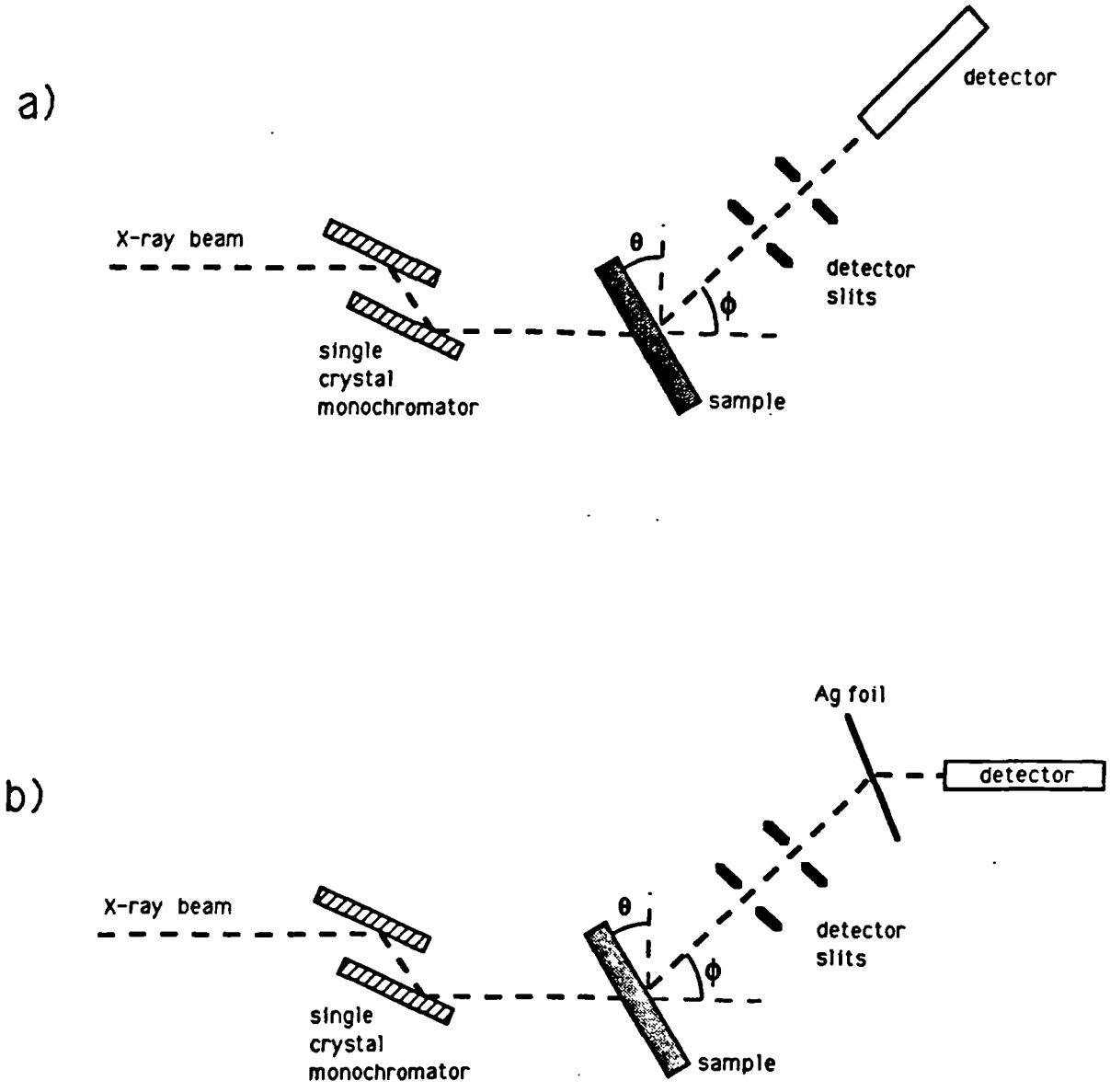

Figure 14: Schematic diagram of the detector arrangement in a) Normal and b) Warren-Mavel mode, as used on station 9.1.

Chapter 3

Elimination of the Compton Component from X-ray Diffraction Experiments

3.1 Introduction

The present chapter explains the procedures developed for the collection and analysis of X-ray diffraction data. Detailed reference will be made to the analysis of carbon tetrachloride (CCl_4) which was used as a standard sample during the development phase of the work. Carbon tetrachloride was chosen because it is a liquid at room temperatures and has a simple molecular structure giving rise to long range oscillations in the recorded diffraction pattern. It also exhibits a high degree of intermediate-range order producing corresponding peaks at comparatively large distances in the pair correlation function. Additionally, there is a wealth of previous results available in the literature allowing detailed comparison to be made between the

between the new results and those from former X-ray diffraction studies [41-48] and from other experimental techniques [49-54] . The datasets used to illustrate the correction procedure have been smoothed prior to the production of the graphs, this smoothing has only been used to improve the clarity of the diagrams and is not part of the analysis of the data.

3.2 The Experiment

All of the experiments described were carried out at the Daresbury Laboratory Synchrotron Radiation Source (SRS) on instrument 9.1 (see section 2.3). Two experimental techniques were used on carbon tetrachloride, the first was a conventional transmission experiment and the second a related technique involving the observation of fluorescence radiation using a method first developed by Warren and Mavel [40]. The following sections outline the two experimental systems and the selection of the experimental parameters used.

3.2.1 The Conventional Transmission Mode

The basic arrangement of the equipment used for the conventional experiments is shown in figure 14a. A beam of monochromatic X-rays falls onto the sample and the diffracted beam was measured using a high flux scintillation counter. The intensity of the diffracted beam was measured as a function of the detector angle, ϕ, and the sample angle, θ. For the purposes of this experiment the sample angle was continually varied such that it was always half of the detector angle ($\phi = 2\theta$). This arrangement is termed the $\theta/2\theta$ mode. The $\theta/2\theta$ arrangement was used primarily because the total pathlength of all the X-rays scattered into the detector will be

the same thus simplifying the correction of the scattering intensity for absorption in the sample. A secondary advantage is that the entire spectrum may be collected in a single experiment whereas if θ is kept at a constant value a number of smaller scans are required to collect the scattering over the complete range required (see below).

Over a period of time the intensity of the X-ray beam from the synchrotron falls and to help compensate for this effect it was decided to measure the low intensity part of the spectrum first (thus getting the highest available flux in this region). Hence all scans were performed by scanning the detector from high angle to low angle with a constant angular step and a constant counting time at each position. For a typical scan the detector angle was varied from 120° down to 0.8° in 0.2° steps. The upper limit is determined by the physical arrangement of the equipment and the lower limit by the point at which the collected intensity starts to rise due to proximity to the non-diffracted beam. Measurement of the background was carried out by recording the scattering spectrum from the empty sample cell using the same scanning arrangement.

3.2.2 The Warren-Mavel Mode

The main disadvantage of the conventional transmission mode described above is that it measures all of the X-rays scattered by the sample and thus includes the contribution from the Compton scattering (see page 15). The Compton or inelastically scattered X-rays contain no information on the structure of the sample and must be subtracted from the collected data before analysis of the spectra may be carried out. Unfortunately, an exact determination of the Compton profile is difficult due to the variation in absorption arising from the wavelength shift of the

scattered X-rays and also because the greater change in energy at large scattering angles often means that part of the spectrum is excluded by the energy acceptance windows set on the detector.

The energy shift of the Compton-scattered photons provides the key to differentiating between coherent and incoherent scattering during the experimental data collection thus reducing the problem of correcting for the Compton scattering contribution inherent in the total scattering mode. The technique used for this differentiation was first developed by Warren and Mavel [40] in 1965.

When a low energy X-ray is incident on an atom it may be scattered either coherently or incoherently as shown in chapter 1. As the energy of the X-ray increases it will reach a point where it will have enough energy to excite an electron from its bound state in the atom to a free state. If the X-ray has more than the required energy the excess is taken by the electron in the form of kinetic energy. The atom will now de-excite by an electron falling from a higher energy level to the vacant state and this process will emit radiation in the form of an X-ray of lower energy than the incident one. These secondary X-rays are called fluorescent radiation. The energy required by an X-ray to excite an electron into a free state is known as the absorption edge of the atom. An atom will have a series of absorption edges associated with it corresponding to each different initial electron state. This absorption edge effect was made use of in the experiment by placing a foil in the scattered beam path (figure 14b) and arranging for the energy of the X-rays incident on the sample to correspond to the absorption edge of the foil. Any X-rays coherently-scattered by the sample will have sufficient energy to excite fluorescence in the foil. Incoherently-scattered radiation, because of the energy lost in the scattering process, will not be able to excite fluorescence and will pass through the foil although

Scan	Sample angle (θ)	Scan range (ϕ)
1	50°	120°– 80°
2	40°	100°– 60°
3	25°	70°– 30°
4	10°	40°– 2°

Table 1: Values of the sample angles and the detector scanning ranges used in the fixed theta geometry.

a small amount of Compton radiation will undergo scattering into the detector. By arranging the detector at an angle to the scattered beam it will only observe the fluorescent radiation and hence it is possible to collect the coherent scattering spectrum with only a small Compton contribution arising from scattering by the foil.

In the Warren-Mavel (WM) mode two sets of experiments were carried out. The first set used the $\theta/2\theta$ geometry described above. The second set consisted of a series of scans with the sample angle (θ) held constant during each scan. This is of particular use for samples were the continuous variation in the scattering volume caused by the rotation of the sample is not a well-defined function. One example of this is when the sample is a powder where voids in the packing of the sample may lead to unpredictable variations in the scattering volumes. The fixed theta geometry is also superior if the walls of the sample cell are distorted (e.g. by bowing). The individual scan ranges used are shown in table 1, each scan being performed with a detector step of 0.2°. The four separate scans were later combined to give data for the full angular range.

3.2.3 Experimental Parameters

Wavelength and Fluorescent Foil

To obtain a diffraction pattern, the incident wavelength of the X-ray beam needs to be of a similar order to the atomic separations in the sample. For most solids and liquids the bonds are of about 1 to 3 Å long and spatial correlations of the order of 1 to 5 Å or more, are present, thus a wavelength of 0.1 to 1 Å is ideally suited to diffraction studies. The choice of wavelengths in this range is further supported by the associated reduction in sample absorption achieved. This reduction is especially important in cases where the choice of a low wavelength will moved the incident beam energy below an absorption edge. From the definition of the scattering vector k (equation 1) it can be seen that k is inversely proportional to the wavelength, hence for a detector with a fixed angular scanning range the corresponding k range increases as the wavelength decreases. Selection of a short wavelength has the effect of moving the diffraction pattern to smaller angles and reducing their angular widths, however, the width of the peaks obtained for most molecular liquids are broad enough that this effect is of little consequence. A further consideration is the wavelength spectrum available on the experimental instrument. On station 9.1 the incident X-ray flux is at a maximum at ~0.6 Å. At wavelengths below 0.6 Å the flux falls off rapidly and the minimum available wavelength is about 0.35 Å. To maximise the k range of the recorded spectrum whilst also maintaining a relatively high X-ray flux it was decided to work at a wavelength between 0.5 and 0.7 Å.

Exact selection of the wavelength is dependent upon which element is used as the fluorescent foil in the Warren-Mavel mode experiment as the same wavelength is used in the conventional mode to ensure that the two data sets are fully comparable. Three foils were readily available in the wavelength range required, these being,

silver λ(Ag K edge) = 0.486 Å, Molybdenum λ(Mo K edge) = 0.560 Å and zirconium λ(Zr K edge) = 0.698 Å. Of these three, silver was chosen as it provides the widest k range (for the maximum detector angle (120°) the corresponding values of k are approximately 22, 19.5 and 15.8 $Å^{-1}$ for Ag, Mo and Zr respectively).

Having selected the fluorescent foil the next stage was to match the incident wavelength to it. Although in theory the absorption edge is a step function and the incident wavelength is totally monochromatic in actuality both have a finite width (figure 15) and because of this the incident wavelength is set to be slightly below the actual edge wavelength so as to minimise the amount of fluorescence produced by the tail of the Compton spectrum. To set the incident wavelength, an Ag foil was placed in the X-ray beam and the intensity of the transmitted beam was measured as a function of wavelength (by adjusting the monochromator angle). The monochromator crystal was then set to an angle which yielded an intensity of slightly above the mid-point of the intensities below and above the edge 16. The wavelength when measured using a crystalline, silicon powder standard was found to be 0.485 Å.

After the foil material and incident wavelength had been selected the fluorescent yield of the foil was optimised. The fluorescent intensity was estimated by placing a sample in the diffractometer and positioning the detector such that it recorded the scattered intensity at the centre of a broad diffraction peak. The choice of a broad peak is essential as it reduces the change in recorded intensity caused by movement of the peak when the incident wavelength is changed by a small amount. The diffracted intensity was measured at the chosen wavelength and the monochromator was then rotated to give an incident wavelength just below the absorption edge so that the scattered beam could not excite fluorescence, this measures the intensity

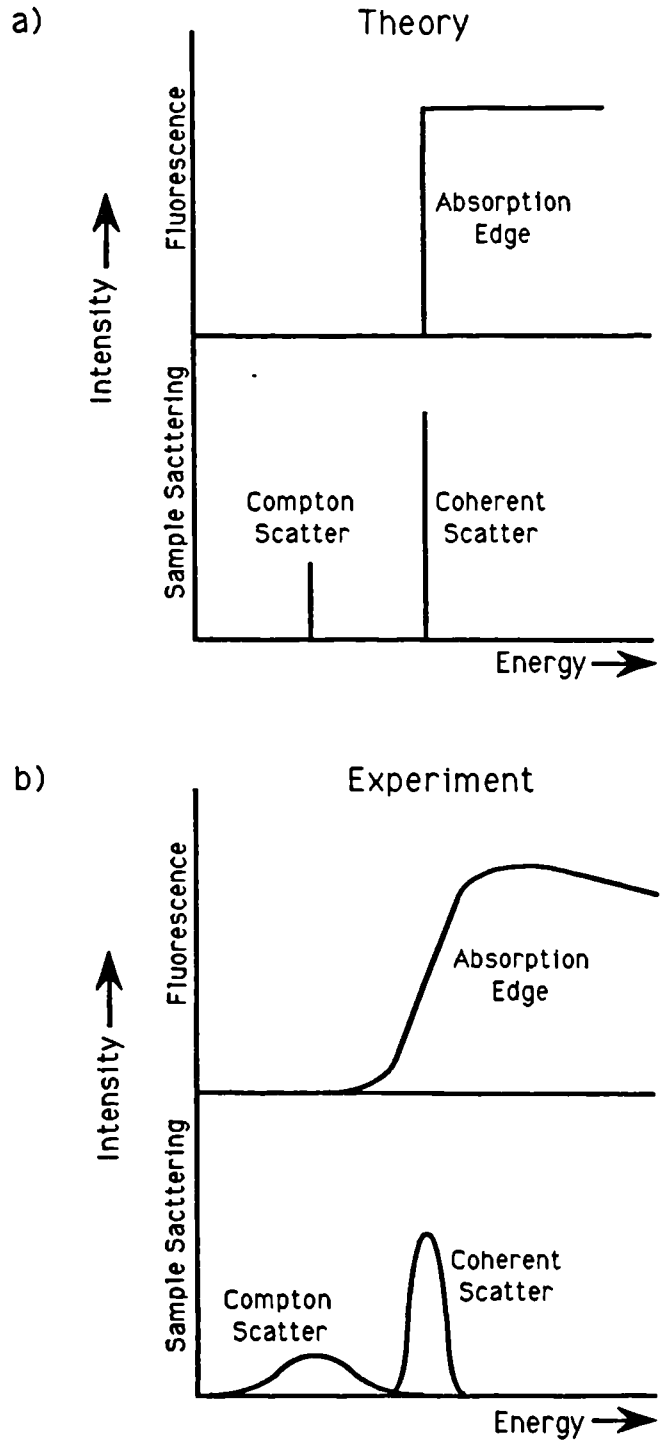

Figure 15: The sample scattering and foil fluorescence profiles in a) theory and b) experiment.

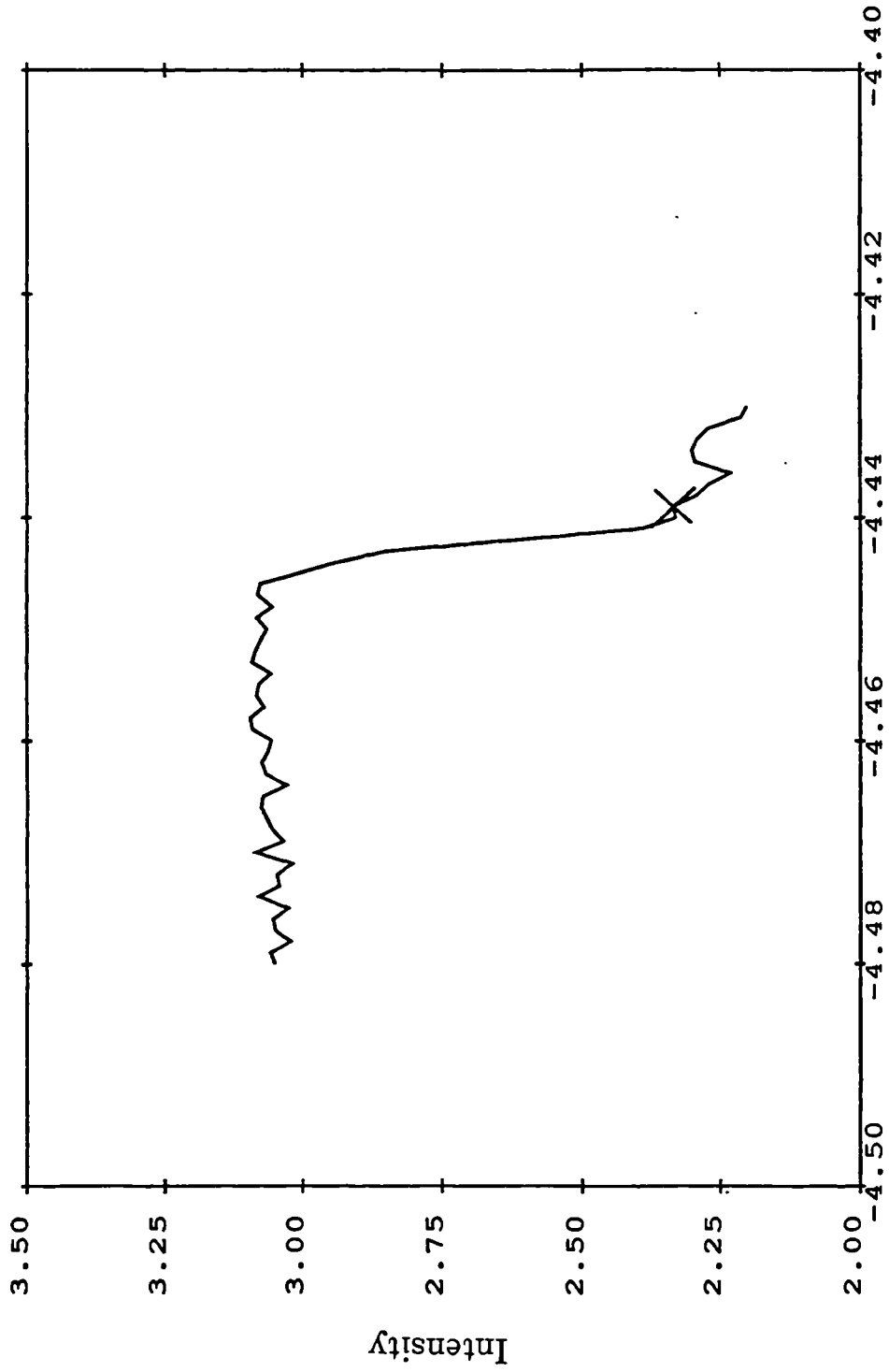

Figure 16: Scan of the Ag k-edge used to set the incident wavelength. The cross indicates the point used to select the monochromator angle.

of the beam scattered by the Ag foil and is about 10% of the intensity recorded at the fluorescent wavelength. The actual intensity of the scattered beam will be dependent on the angle of the detector with respect to the beam incident on the foil. In an ideal situation the detector would be at a high angle as the back scattered intensity is low. Unfortunately, due to the limitations in the diffractometer, the largest angle available was 45° to the beam and hence this was used. The difference in these two intensities was taken to be the fluorescent yield. The thickness of the foil was then varied, by placing a variety of foils in the beam, until the measured fluorescent intensity was a maximum. To further increase the count rate the detector was positioned as closely as possible to the foil so as to subtend the greatest possible solid angle without intercepting the straight-through beam.

Incident Beam Cross Section and Detector Slit Settings

The cross-section of the incident X-ray beam will determine both the scattering volume of the sample and the cross section of the scattered beam as seen by the detector (otherwise known as the footprint). To maintain a large count rate a large scattering volume is required which as the sample thickness is necessarily low (see above) means that a large incident cross section is required. However it is also necessary to collect all of the scattered beam at all detector angles to both maintain the count rate and more importantly to prevent the need for a further analytical calculation to correct the collected intensity for the lost scattering. To ensure collection of the entire scattering a narrow scattered beam is preferable. Having a narrow diffracted beam also improves the angular resolution of the system as it allows small detector slits to be used.

The incident beam, on this experimental station, has a rectangular cross section

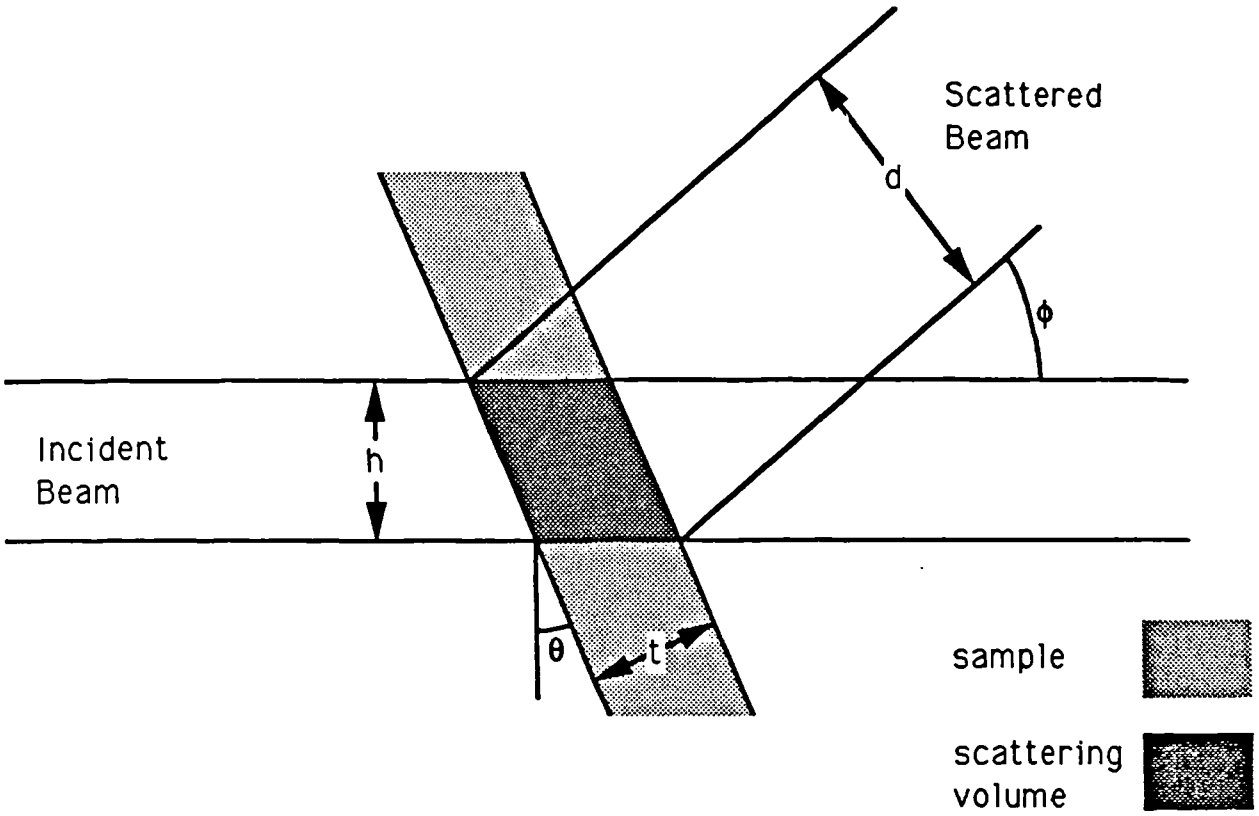

Figure 17: Cross section of the sample showing the scattering volume and the 'footprint' width of the scattered beam.

whose height and width may be adjusted by means of replaceable pairs of tungsten nickel slits. The width of the beam is defined parallel to the horizontal axis of the diffractometer and because of this, the width of the scattered beam will have no angular dependence and hence no effect upon the angular resolution of the diffractometer. The height, h, of the incident beam is defined vertically in the scattering plane and thus the height of the scattered beam, d, (see figure 17) is dependent on the height of the incident beam, the sample thickness, t, the sample angle, θ, and the detector angle, ϕ. The height of the scattered beam is given by the equation

$$d = t\frac{sin\phi}{\cos\theta} + h\frac{\cos(\theta - \phi)}{\cos\theta} \tag{81}$$

The detector slits are set so as to receive the entire scattered beam at all angles,

their width being chosen to be slightly above the beam width and their height being set to be the same as the maximum scattered beam height. To satisfy the conditions that the cross section of the incident beam be as large as viable and the beam height as small as possible a set of slits were chosen to give a beam width of 6 mm and a beam height of 0.6 mm. The detector slits were chosen to be larger than the beam width and to be slightly greater than the size of the maximum beam height. For the $\theta/2\theta$ mode the maximum scattered beam height occurs when the sample and detector are at their maximum angle, giving a beam height in this case of 2.35 mm. For the fixed-theta mode the detector angle corresponding to the maximum height is given by

$$\phi = \tan^{-1}\left(\frac{t + h\sin\theta}{h\cos\theta}\right) \tag{82}$$

Of the four different fixed-theta scans the maximum height is for the $\theta = 50°$ scan and corresponds to a detector angle of 75.3°thus giving a height of 2.36 mm. As before, to maintain comparability between the collected data sets the setting for the two experimental geometries were set to the same value and a detector slit height of 2.5 mm was chosen. The angular acceptance of the detector is determined by the height of the detector slits (h_d) and the distance between the two pairs of slits (l). It is given by the equation

$$\phi \pm \delta\phi = \phi \pm \tan^{-1}\frac{h_d}{l} \tag{83}$$

For the detector slit setting chosen $h_d = 2.5$ mm, $l = 230$ mm) the angular acceptance was $\phi\pm$ 0.6°. Reduction of the angular acceptance by reducing the detector slit height or increasing the separation of the two slits, will increase the resolution of the system.

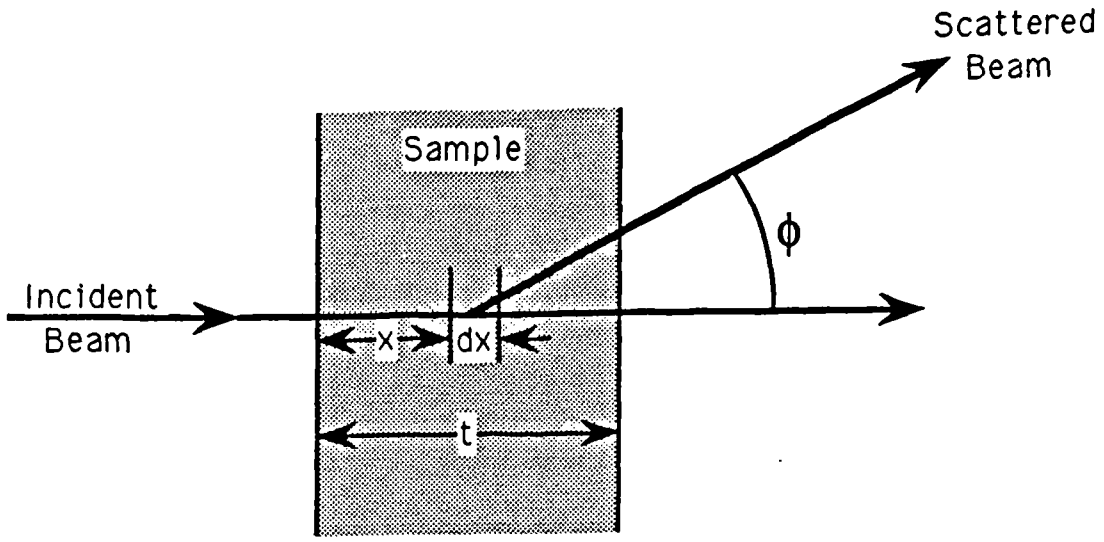

Figure 18: Definition of the symbols used in the derivation of the optimum sample thickness.

Sample Size

When considering scattering by a flat plate perpendicular to the incident beam (figure 18) it is possible to calculate an optimum sample thickness. The optimum thickness arises because if the cell is too thin there will be insufficient scattering material in the beam path and if the thickness is too great the scattered beam will be attenuated too strongly. Considering the case of a flat plate sample of thickness, t, with a linear absorption coefficient, μ, and an incident beam intensity of I_0. Then the contribution to the scattering by an element of thickness $\mathrm{d}x$, at a depth x, will be $\mathrm{d}I_\phi$ where

$$\mathrm{d}I_\phi = [cI_0 \exp(-\mu x)\ \mathrm{d}x] \left[\exp\left(\frac{-\mu(t-x)}{\cos\phi}\right)\right] \tag{84}$$

The first term on the right-hand side represents the intensity scattered by the element $\mathrm{d}x$ after the incident beam as been absorbed in traversing the path x.

The second term is the absorption of the scattered beam as it travels out of the sample. Integration yields

$$I_\phi = K\left[\exp\left(-\mu t\right) - \exp\left(\frac{-\mu t}{\cos\phi}\right)\right] \tag{85}$$

where

$$K = \frac{cI_0\cos\phi}{\mu\left(1-\cos\phi\right)} \tag{86}$$

The optimum thickness is determined by the point at which I_ϕ reaches a maximum intensity and thus is the value of t for which the differential of I_ϕ with respect to t is zero:

$$\frac{\mathrm{d}I_\phi}{\mathrm{d}t} = K\left[-\mu\exp\left(-\mu t_0\right) + \left(\frac{\mu}{\cos\phi}\right)\exp\left(\frac{-\mu t_0}{\cos\phi}\right)\right] = 0 \tag{87}$$

and hence

$$t_0 = \frac{1}{\mu}\left[\frac{-\cos\phi\log\left(\cos\phi\right)}{1-\cos\phi}\right] \tag{88}$$

in the limit as ϕ approaches 0 ($\cos\phi \rightarrow 1$) this yields $t_0 = 1/\mu$. Thus for scattering at small angles the optimum thickness is the reciprocal of the linear absorption coefficient, but as ϕ rises and the total pathlength increases so the optimal thickness will become less. Another point in favour of having $\mu t < 1$ is the effect this has on multiple scattering. When an X-ray photon is scattered two or more times it is said to have been multiply-scattered and because of the second scattering event it will have lost its phase relationship to the photons scattered into the same angle by a single scattering event. Multiply-scattered X-rays contribute an additional component to the collected spectra. It is possible to carry out 'Monte Carlo' calculations which enable this contribution to be subtracted and redistributed to the parts of the spectra at which they would have occurred if they had undergone a single scattering event (note that this is only possible for X-rays that undergo two or more coherent scattering events, if the photon is incoherently scattered at any point in

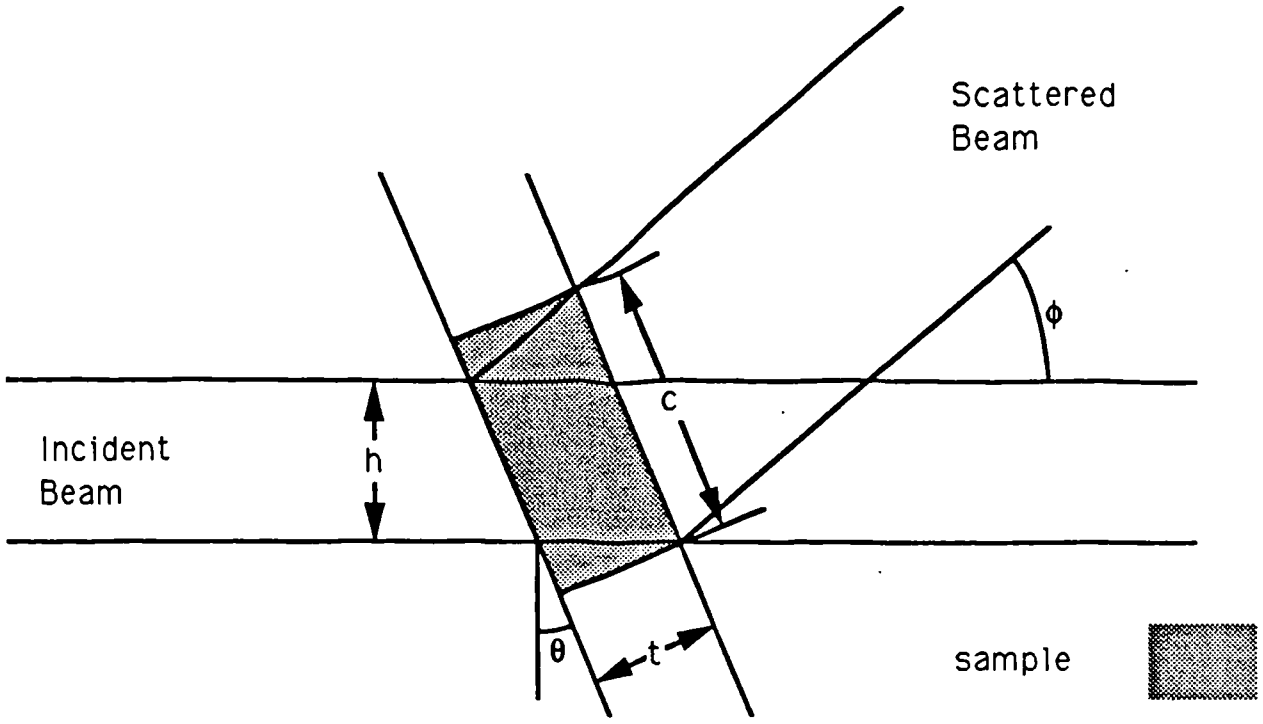

Figure 19: Definition of the symbols used in the determination of the minimum sample height.

its path it will contribute only to the incoherent part of the spectra). It has been shown by a number of workers (e.g. Dwiggins [55,56]) that the use of a low value of μt reduces the level of multiple scattering present. To reduce the multiple scattering to a level which will hopefully be low enough to exclude the need for multiple scattering corrections we chose a sample thickness of 1.01 mm giving a value of μt for the experiment of 0.224 (for CCl_4, $\mu = 2.22\ cm^{-1}$). Any errors arising from the omission of the multiple scattering correction will appear as a reduction of the peak heights of the corrected spectra.

Choice of a smaller sample thickness than the optimum, allowed the cross-sectional area of the sample cell to be reduced. This is because the thickness of the sample, t, and the maximum angle to which the sample needs to be rotated, θ_m, combine together with the incident beam height, h, and maximum detector angle,

ϕ_m to define a minimum height for the cell, c. The absolute minimum value of c is defined when the bottom of the incident beam just passes the bottom edge of the cell and the top edge of the scattered beam just passes the top of the cell (see figure 19). This height is given by the equation:

$$c = \frac{t \sin \phi}{\cos(\phi - \theta) \cos \theta} + \frac{h}{\cos \theta} \tag{89}$$

Reducing the thickness of the cell reduces the minimum height and thus the sample size. The advantage of using a smaller cell is that the window is reduced in size and therefore less prone to bowing thus providing better definition of the sample volume. The minimum height determined by the above equation for a beam height of 0.6 mm and sample thickness of 1 mm for the $\theta/2\theta$ mode is 4.7 mm. If the thickness of the cell is increased to 1.6 mm (a requirement for some of the other samples that were to be used) the minimum cell height is increased to 6.8 mm. To allow a for error in the mounting of the cell on the diffractometer a cell height of 10 mm was chosen. For the sample width the only requirement is that it is wider than the incident beam, as a beam width of up to 8 mm was required, a sample width of 10 mm was chosen to again allow some freedom in the mounting of the sample.

The Sample Cell

The sample was contained in the sample holder shown in figure 13. The construction of the cell is such that only the gasket and windows of the cell come into contact with the sample and thus the material used to make the body of the cell, provided that it is rigid, has no effect upon the experiment. The thickness of the sample could be altered by variation of the gasket thickness. Carbon tetrachloride is a very strong solvent and it was necessary to choose gasket and window materials with which it

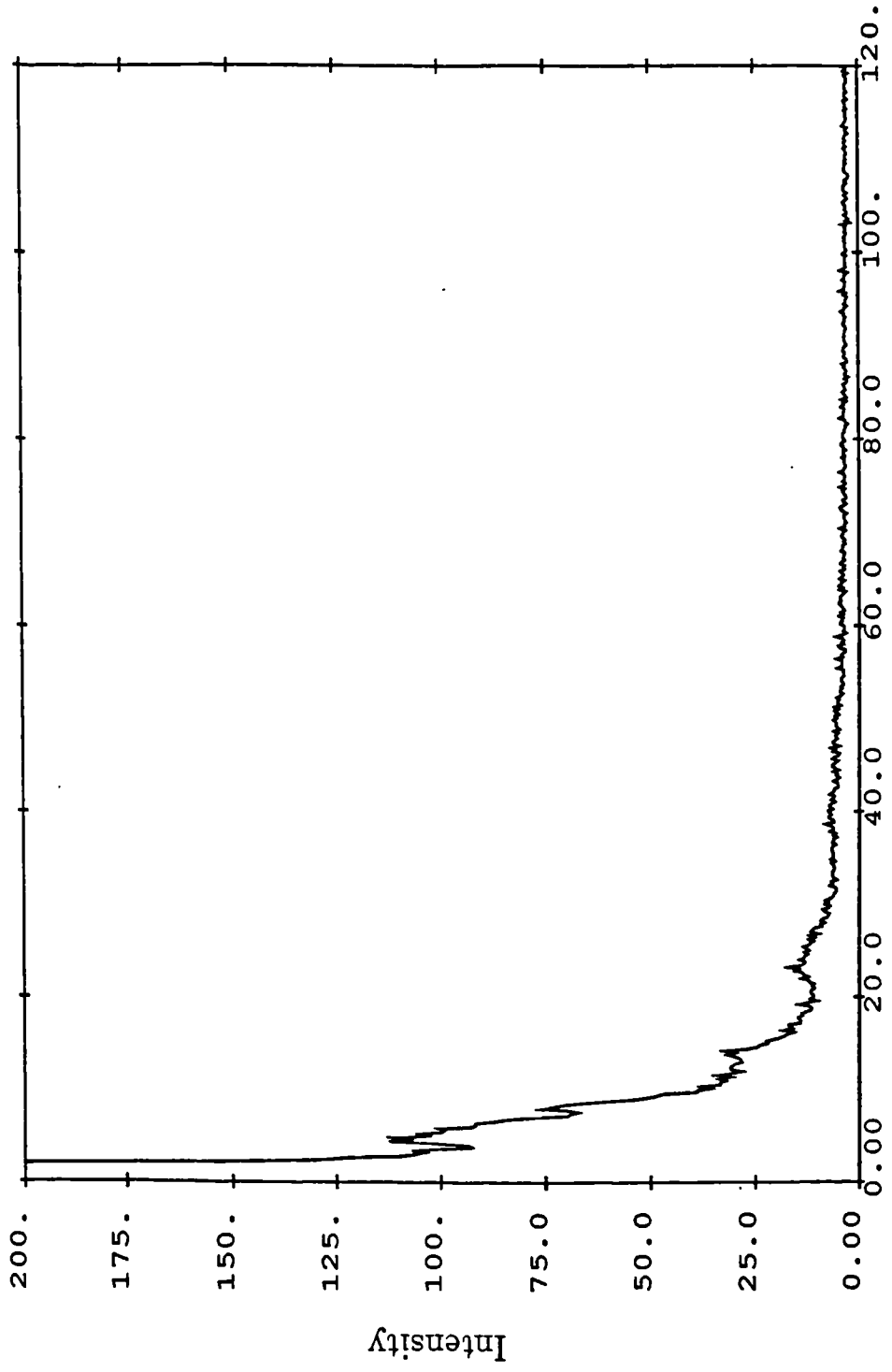

Figure 20: A typical background diffraction pattern obtained from an empty cell with kapton-windows. The spectra was recorded using a conventional transmission mode experiment.

would not react, for this reason it was decided to use teflon as the gasket material though in general it is preferable to use a softer material, such as neoprene as then a better seal is formed between the gasket and the window. After trying several different windows mica was chosen for the first experiments as it is inert, gives a fairly rigid window even for thin sheets (for the experiment a thickness of 20 μm was used) and produces only a low intensity scattering profile. Measurement of the absorption of the X-ray beam by mica showed a negligible amount of absorption by the windows, thus the use of mica has the advantage that it is unnecessary to carry out any corrections for absorption of X-rays by the cell. It was found however that the spectra recorded from the mica windows contained a number of very sharp spurious peaks of unknown origin whose position in the spectra was unpredictable. Due to the random variation of the positions and intensities of these peaks it was not possible to remove them from the sample spectrum using a normal background subtraction and hence they had to be removed by interpolating the height of the scattered spectrum below them from the data on either side of the peaks. For this reason in latter experiments kapton was used as a window material. Kapton has a more complicated scattering profile and although its slightly lower rigidity meant that thicker windows were required ($\sim$50 μm) it still demonstrates a similarly low absorption of the X-ray beam. Figure 20 shows a typical background spectrum collected from the kapton-windowed cell.

3.3 Data Correction Procedures

The following sections detail the procedure developed for the analysis of data collected using the experimental techniques outlined above. The analysis has been divided into two sections, the first section covering corrections that arise from the

experimental conditions and the second those concerning the sample itself.

3.3.1 Sample-Independent Corrections

The following are the first set of corrections applied to the data. All are independent of the sample and simply correct for factors arising from the equipment used to perform the experiment. As such all of the parameters will be constant and the application of these corrections may thus be carried out using a computer program to preprocess the data.

Dead Time

The dead time (τ) of the detector is the period of time between two resolvable counting events. If two photons fall on the detector within τ seconds of each other the detector will not have returned to a state where it can record the second event and thus the second photon will go uncounted. The dead time of the detector used was measured during the experiment by observation of the attenuation of the diffracted beam by a series of Zr foils [57]. The incident photon flux was then set to give count rates well below the point where significant dead time effects where observed. For completeness of the preprocessing program a dead time correction was carried out upon the data using the measured dead time, τ, of ~ 1 μS and the formula

$$I_t = \frac{I_{obs}}{1 - \tau I_{obs}} \tag{90}$$

where I_{obs} is the observed count rate per second and I_t is the true number of photons incident on the detector.

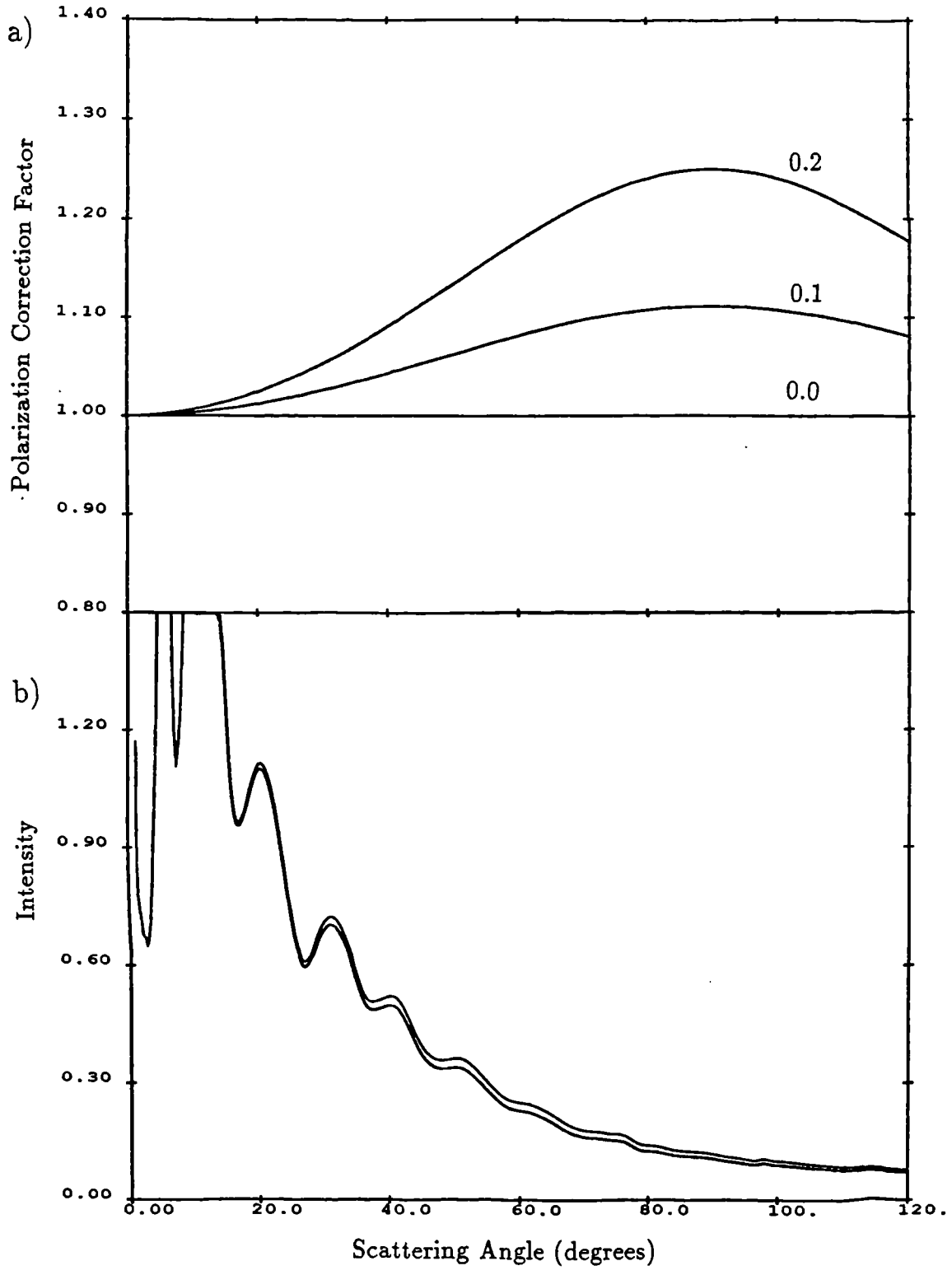

Figure 21: a) The multiplicative polarization correction factor for $p_{\|} = 0$, 0.1 and 0.2 and b) the corresponding change in the CCl_4 upon application of the correction (the upper curve is the corrected data).

Polarization Factor

In X-ray diffraction, the intensity of the diffracted beam is dependent on the polarization of the incident beam. For X-rays whose electric vectors are polarized parallel to the scattering plane, the intensity is dependent on the scattering angle, but for X-rays which are perpendicularly polarized the scattered intensity is angle independent. For a beam of unspecified polarization the scattering intensity may be decomposed into the scattering from two separate beams giving, from equation 34

$$\begin{aligned} I_{\perp} &\propto I_0 \\ I_{\parallel} &\propto I_0 \cos^2 \phi \end{aligned} \tag{91}$$

where I_0 is the incident beam intensity and $I_{\perp}$ and $I_{\parallel}$ are the intensities scattered from the perpendicular and parallel polarized X-ray beams. If the resolved beams are in the proportions $p_{\parallel}$ and $p_{\perp}$ for the parallel and perpendicular beams respectively we have

$$I_t \propto I_0 \left(p_{\perp} + p_{\parallel} \cos^2 \phi \right) \tag{92}$$

Where I_t is the experimentally observed intensity after dead-time correction. On instrument 9.1 approximately 10% of the incident beam is polarized parallel to the scattering plane. Figure 21 shows the multiplicative polarization correction factor and the change in the CCl_4 data resulting from applying the correction. The effect of the polarization correction is greatest at 90° corresponding to $k = 18.3$ Å^{-1} for $\lambda = 0.485$ Å. As it can be seen from the graph the main effect of the correction is a rise in the general level of the spectrum above $k = 6$ Å ($\phi \approx 27°$) and because of this, can lead to errors in the corrections for Compton scattering and sample absorption (see below).

Normalization of Data

During the course of the experiment the flux of the incident beam at the sample varies and it is necessary to correct for this change before further analysis may proceed. To record the variations in the incident beam a monitor counter is installed on the instrument and its count rate is recorded in the file containing the diffraction data. Calculating the number of counts per second corresponding to a constant flux of M_c monitor counts is simply a case of dividing the diffraction count rate by the monitor count rate and multiplying by M_c. As the monitor count rate tends to be large compared to the scattered count rate the constant M_c was set at 10 000 to give a normalized diffraction pattern with a magnitude large enough to prevent rounding errors occurring on the computer. It should be noted that the choice of M_c is purely arbitrary and its effect on the magnitude of the data is totally removed upon normalization of the diffracted data to the atomic scattering factor (see below).

3.3.2 Sample-dependent Corrections

When the X-ray beam interacts with the sample a number of undesirable features are introduced into the collected spectrum. The following corrections are carried out to remove these factors and gain the coherent scattering profile.

Background

When the scattering pattern is collected it contains not only photons scattered by the sample but also those scattered by the sample container and by the air around the sample. These two sets of scattering contributions may be divided into container scattering (I_c) and background scattering (I_b) due to the air scattering and

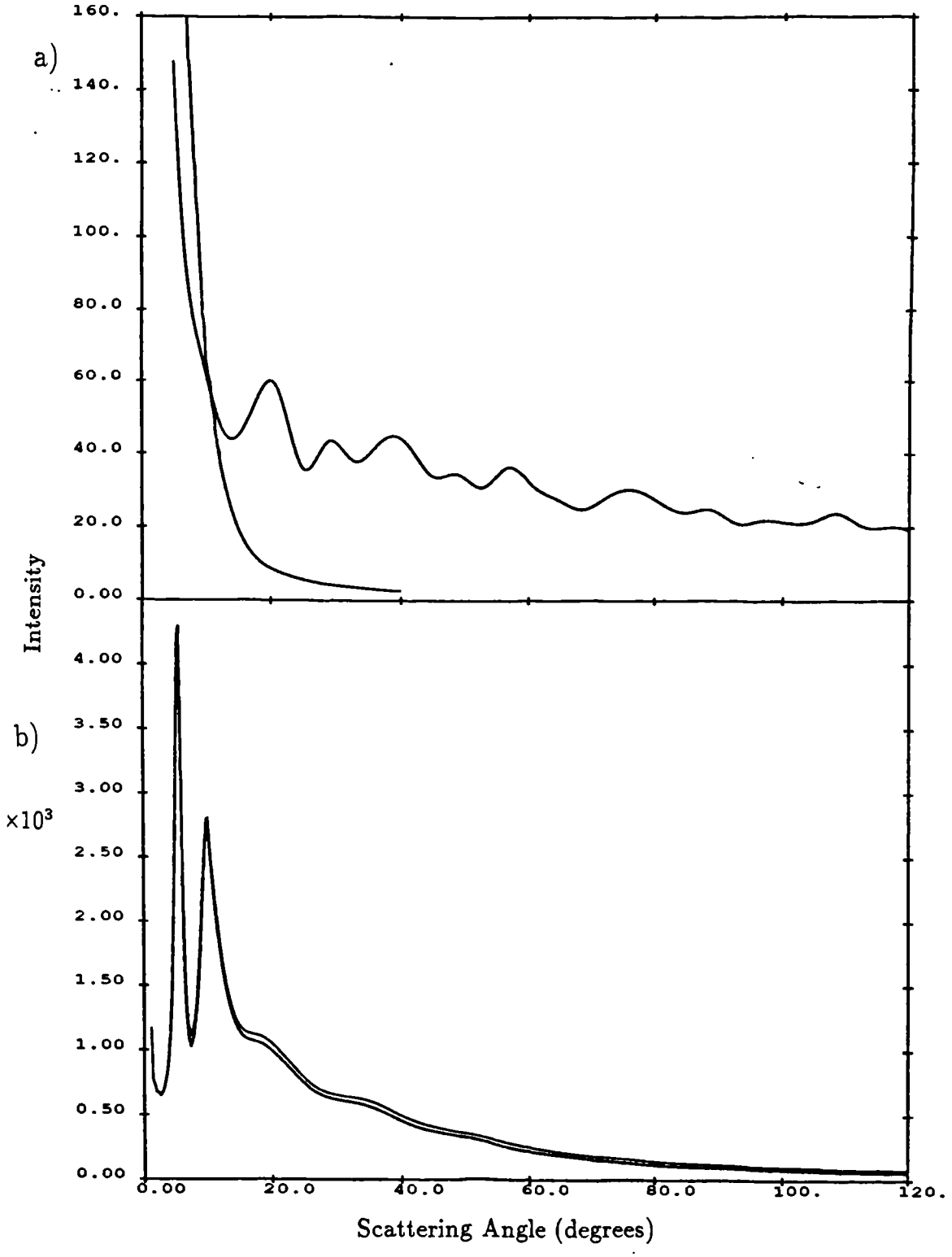

Figure 22: a) The background and kapton container scattering spectra and b) the collected CCl_4 spectra before (upper) and after (lower) the background corrections. (All data collected using the WM mode, $\theta/2\theta$ experiment).

noise in the detector electronics. Two sets of spectra where collected to measure this scattering. The first was a run carried out with no sample cell mounted on the diffractometer and hence the only counts recorded arose from air scatter and detector noise. This spectrum was found to be negligible for all but small angles, showing that the air scatter is insignificant apart from angles close to the main beam and that the detector noise is negligible (see figure 22). The second spectrum consisted of the scattering due to the empty sample cell and is a measure of the scattering spectrum from the cell windows (I_c). This scan will also include the background contribution (I_b). To perform the subtraction of the background and container scattering from the spectrum it is necessary to first subtract the background count from the collected sample count (I_{s+c+b}) and from the collected cell scattering (I_{c+b}) and then subtract the cell scattering from the sample spectra.

$$I_s = (I_{s+c+b} - I_b) - f\,(I_{c+b} - I_b) \tag{93}$$

where f is a multiplicative factor included to make allowance for the alterations in the beam intensity at the second window and the absorption of scattering from the first window caused by the presence of the sample. The value of f may be calculated using the formalism developed by Paalman and Ping [58]. It should be noted that all of the sample-independent corrections carried out upon the sample scattering before the subtraction of the background must also be carried out upon the container and background spectra.

Compton Scattering

Having obtained the scattering from the sample only, it is necessary to remove any incoherent scattering contribution. A number of methods are available to do this and of these the best is probably to calculate the theoretical Compton scattering

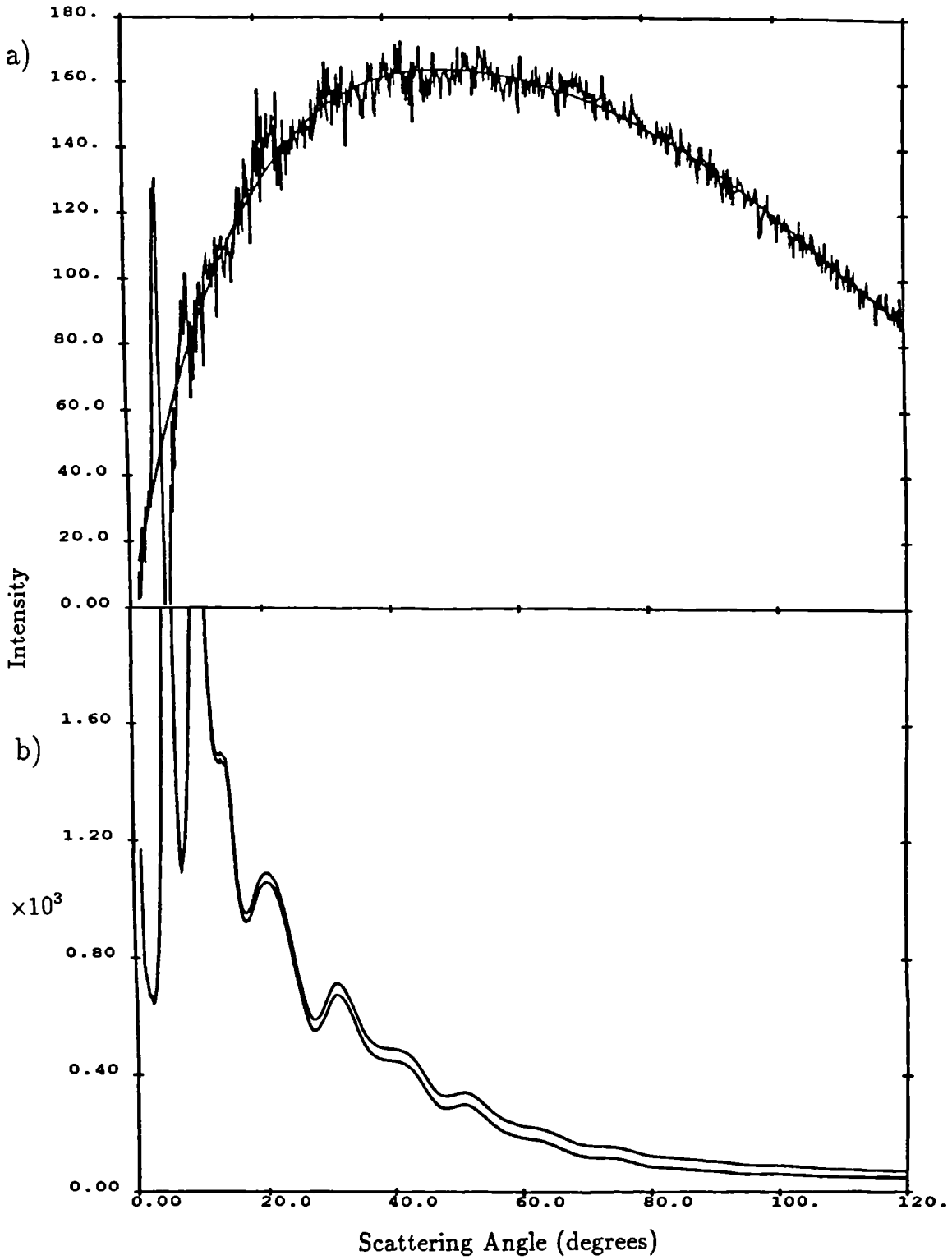

Figure 23: a) The Compton profile obtained from the difference of the conventional and WM data sets and b) the WM data set before and after Compton correction.

from the sample by the use of tables [29-31]. Having calculated this spectrum it is then necessary to adjust it to get the scattering expected from the sample. These additional adjustments include correction of the spectrum for absorption of the incoherent scatter by the sample and for the proportion of the Compton spectrum excluded by the incoherent scattering excluded by the energy setting of the detector windows. The absorption correction is dependent on the wavelength of the scattering and thus dependent on the scattering angle (equation 40). This is complicated as the Compton wavelength of the scattered photons is spread in a distribution about the theoretical wavelength (see figure 15). The correction for the detector windows is specific to the instrument used, window settings chosen and the wavelength profile of the Compton scattering and as such is usually difficult to determine. It is because of the problems involved in these corrections that the Warren-Mavel technique was adopted in order to eliminate most of the Compton component as the data was collected, however even using this method about 10% of the original Compton scattering reaches the detector via elastic scattering from the Ag foil. To overcome this problem, the two analysis techniques outlined below were used. It should be noted at this stage that correction for the Compton scattering and for the absorption of the coherent scattering by the sample (see below) was carried out as an iterative process and the Compton subtraction yielding the best final result was adopted.

The first technique for Compton subtraction was developed for data sets collected under identical conditions in both experimental modes. This is the ideal case however and it was necessary to develop a second approach for samples where limited access to the diffractometer allowed time only for the collection of data using the Warren-Mavel mode experiment. When data from both experimental

modes are available it is possible to obtain the profile of the Compton scattering excluded by the WM mode. After both data sets had been corrected for sample-independent factors and background as outlined above, the conventional data, I_{cnv}, was multiplied by a constant to bring it to the same order as the WM data, I_{WM}, thus compensating for the loss of recorded intensity inherent in the WM technique. Next the WM data were subtracted form the conventional data to yield the profile of the 90% of the Compton scattering I_{cmp} excluded by the WM technique.

$$I_{cmp} = CI_{cnv} - I_{WM} \tag{94}$$

The normalization constant, C, was then adjusted to obtain a difference profile which went to zero at the origin and was free from any residual oscillations which would indicate the presence of residual coherent scattering. Having obtained the incoherent scattering a quintic function was fitted to it to recover the smooth Compton profile, free from any random noise (figure 23). It was assumed that the curve thus obtained was a true representation of the complete Compton profile entering the detector and that by taking a constant fraction, A, of this curve the residual Compton component in the WM data could be subtracted.

$$I_{nocmp} = I_{WM} - AI_{cmp} \tag{95}$$

When only the WM-mode pattern is available it is necessary to correct for the Compton scattering using some other method. The full correction of the theoretical Compton profile to yield the actual Compton scattering distribution produced by the sample is complicated and basically involves adjusting the correction factors used to produce the profile until the curve thus obtained creates the required results in the sample spectrum. It was felt therefore that it would be as efficient and accurate to start with a quintic equation as an approximation to the required curve

and then to adjust this until the final result of correcting the data appeared correct (i.e. the sample spectrum oscillated about the atomic form factor). As a double check the data were analysed without the subtraction of any Compton component and a smooth curve fitted to the data. The difference between this curve and the atomic form factor was then back-corrected (that is the effects of the absorption correction and the scattering volume correction were reversed) and the Compton profile thus obtained was compared to the fitted quintic. The Compton subtraction and absorption correction were accepted if these two curves were in reasonable agreement.

Failure to properly subtract the residual Compton scattering may lead to an error in the amount of absorption correction applied. This in turn leads to an increase in the amplitude of the diffraction peaks at all but low angle and thus to some distortion of the peaks in the $d_L(r)$ curve. This affects any coordination numbers obtained from the radial distribution curves but will have little effect upon the determination of the inter-atomic distances. A second effect of an incorrect Compton subtraction is to produce a long range oscillation in the diffraction pattern which will show up in the $d_L(r)$ curve as a peak corresponding to a very short interatomic distance (i.e. below about 0.75 Å). This peak is at a distance below that expected for any bond distance and thus is easily seen as spurious and as such does not affect the interpretation of the data.

Absorption Correction

As the X-ray beam passes through the sample, a proportion of it will be lost by absorption. The amount of this absorption will be determined by the pathlength of the X-rays in the sample and its absorption coefficient. To calculate the absorption

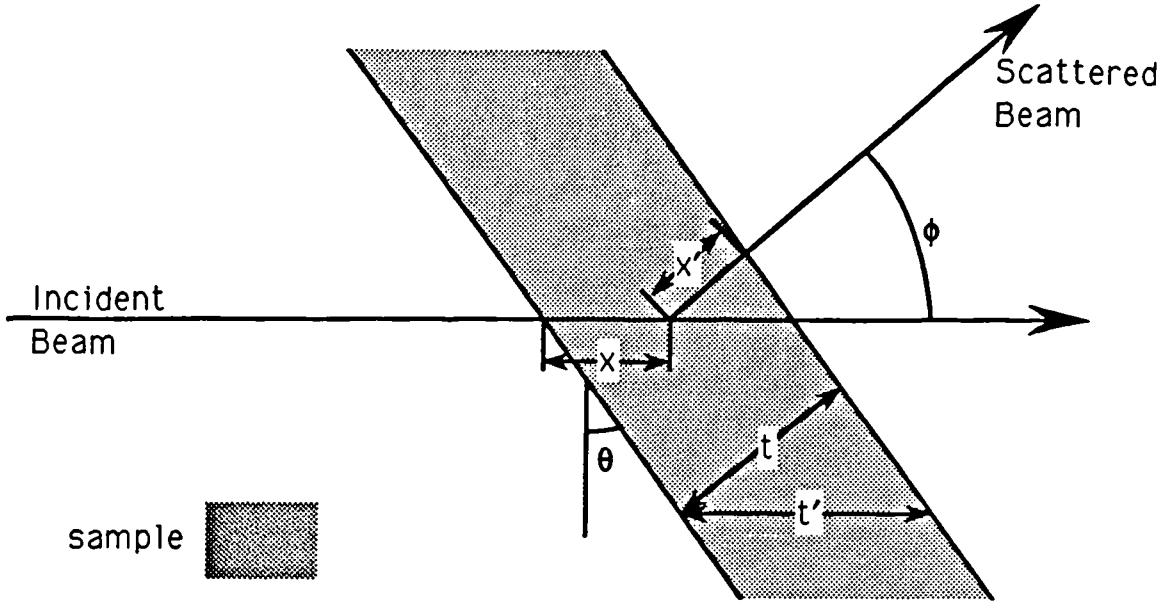

Figure 24: Definition of symbols used in the derivation of the absorption coefficient

correction for a flat plate sample in transmission geometry it is necessary to calculate the ratio of the scattering intensity with and without absorption for all angles, ϕ. Consider a beam of intensity I_0 incident on a flat plate sample of thickness t (figure 24). The intensity of the beam at a depth x into the sample will be

$$I_x = I_0 \exp(-k\sigma_a x) \tag{96}$$

where ϕ_a is the absorption cross section and $k = \rho/A$ (where ρ is the sample density and A is the atomic mass of the absorber). The intensity after scatter from an element Δx at position x is

$$I_x(\phi)\Delta x = I_x k\sigma_s(\phi)\Delta x \tag{97}$$

where $\sigma_s(\phi)$ is the scattering cross section and $k\sigma_s(\phi)$ is therefore the probability of a photon being scattered at an angle ϕ. Thus the intensity of the beam emergent from the sample is

$$\begin{aligned} I_{x'}(\phi)\Delta x &= I_x(\phi)\exp(-k\sigma_a x')\Delta x \\ &= I_0 k\sigma_s(\phi)\exp(-k\sigma_a x)\exp(-k\sigma_a x')\Delta x \end{aligned} \tag{98}$$

Thus the total intensity, $I(\phi)$, for a single scattering event with absorption is given by the integral of equation 99 over the thickness of the sample, t'. Substitution for x' and t' gives

$$I(\phi) = I_0 k\sigma_s(\phi)\int_0^{t/\cos\theta} \exp\left\{-k\sigma_a\left[x + \frac{t - x\cos\theta}{\cos(\phi-\theta)}\right]\right\}\,\mathrm{d}x \tag{99}$$

Evaluation of this yields

$$I(\phi) = \frac{I_0\sigma_s(\phi)}{\sigma_a}\left\{\frac{\cos(\phi-\theta)}{\cos(\phi-\theta)-\cos\theta}\right\}\left[\exp\left\{\frac{-k\sigma_a t}{\cos(\phi-\theta)}\right\}\exp\left\{\frac{-k\sigma_a t}{\cos\theta}\right\}\right] \tag{100}$$

with no absorption ($\sigma_a \rightarrow 0$) expanding the exponential terms as a power series and discarding all terms above order 2 as negligible yields

$$I^{noabs}(\phi) = \frac{I_0\sigma_s(\phi)kt}{\cos\theta} \tag{101}$$

As one would expect this is simply the probability of scattering per unit path length multiplied by the pathlength of the incident beam in going straight through the sample. We may now define an absorption correction factor $R(\theta,\phi)$ as the ratio of equations 100 and 101. Thus

$$\begin{aligned} R(\theta,\phi) &= \frac{I^{abs}(\phi)}{I^{noabs}(\phi)} \\ &= \frac{1}{kt\sigma_a}\left\{\frac{\cos(\phi-\theta)\cos\theta}{\cos(\phi-\theta)-\cos\theta}\right\}\left[\exp\left\{\frac{-\sigma_a kt}{\cos(\phi-\theta)}\right\} - \exp\left\{\frac{-\sigma_a kt}{\cos\theta}\right\}\right] \end{aligned} \tag{102}$$

If however $\phi = 2\theta$ (as is the case for the $\theta/2\theta$ experiments) a special case exists as all of the scattering pathlengths are the same and equal to t'. This gives the scattered intensity with absorption as

$$I_s(\phi) = \frac{I_0 k \sigma_s(\phi) t}{\cos\theta} \exp\left\{\frac{-h\sigma_a t}{\cos\theta}\right\} \tag{103}$$

and the absorption correction reduces to

$$R(\theta, 2\theta) = \exp\left\{\frac{-k\sigma_a t}{\cos\theta}\right\} \tag{104}$$

Comparison of the two absorption correction equations (equations 102 and 104) shows the major advantage of the use of the $\theta/2\theta$ scattering geometry which is the simplicity of the absorption correction compared to the fixed θ arrangement. To correct the collected spectrum for absorption the recorded count is divided by the correction factor, $R(\theta, \phi)$.

In the above equations the factor $k\sigma_a$ may be replaced by the linear absorption coefficient, μ. The values of μ and μ/ρ, the mass absorption coefficient, are available in tabulated form [59] for all elements at a variety of wavelengths and may be found for any specific wavelength by interpolation. To calculate the linear absorption coefficient of a molecule of formula $X_a Y_b$ the following formula is used

$$\mu_{X_a Y_b} = \left\{\frac{a\left(\frac{\mu}{\rho}\right)_X M_X + b\left(\frac{\mu}{\rho}\right)_Y M_Y}{M_{X_a Y_b}}\right\} \rho_{X_a Y_b} \tag{105}$$

where M_i is the atomic weight of element (or molecule) i and $\left(\frac{\mu}{\rho}\right)$is its mass absorption coefficient. It is the linear absorption coefficient ($\mu_{X_a Y_b}$) thus obtained which is also used in the calculation of the optimum sample thickness (see page 57). For CCl_4 at a wavelength of 0.485 Å $\left(\frac{\mu}{\rho}\right)_C = 0.321$ cm^{2}g^{-1} and $\left(\frac{\mu}{\rho}\right)_{Cl} = 3.79$ cm^{2}g^{-1} thus giving $\left(\frac{\mu}{\rho}\right)_{CCl_4} = 3.52$ cm^{2}g^{-1} and for room temperature, $\mu_{CCl_4} = 2.22$ cm^{-1}.

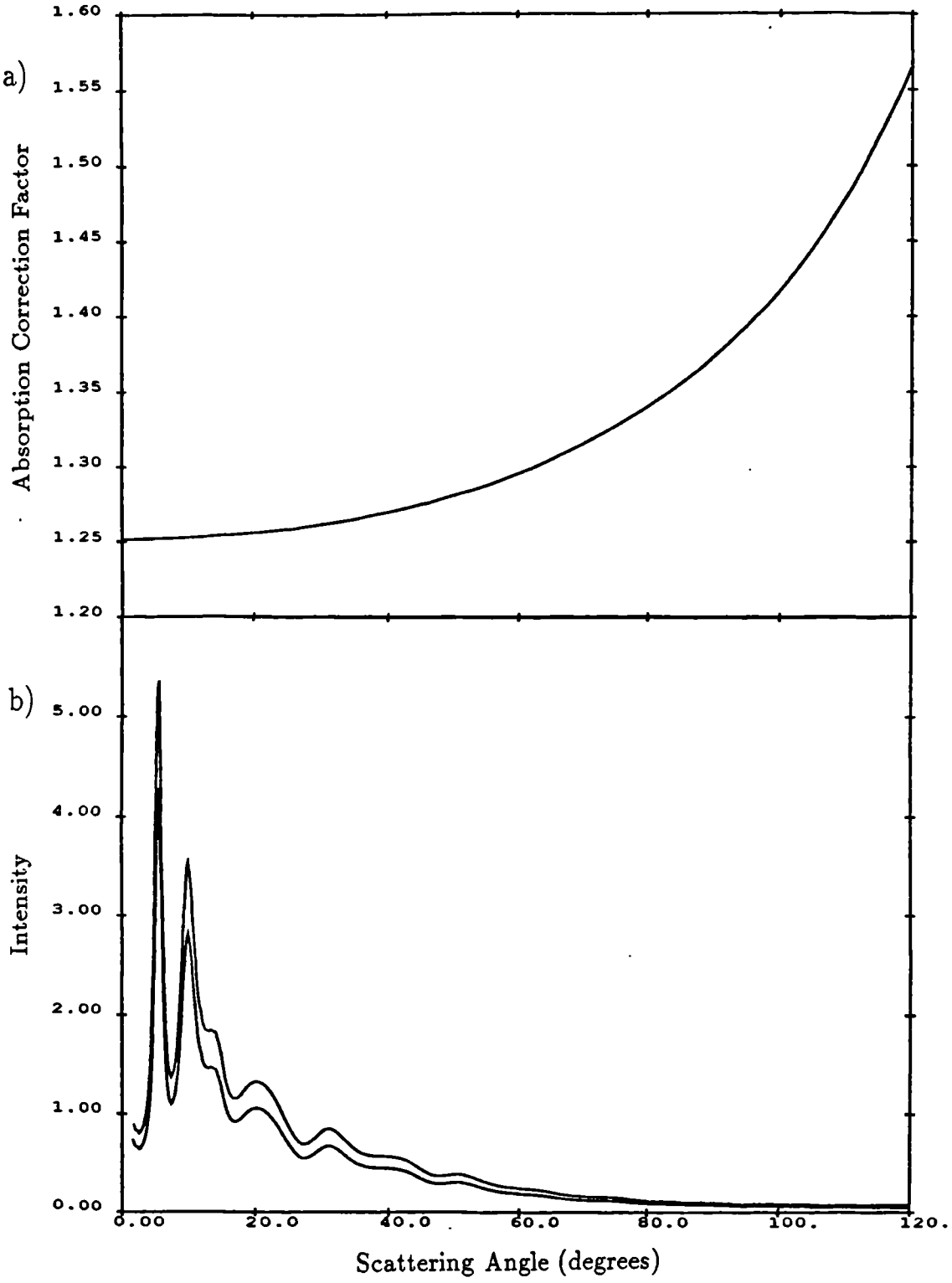

Figure 25: a) The multiplicative absorption correction for the CCl_4 $\theta/2\theta$ experiment and b) the corresponding CCl_4 spectra before and after correction.

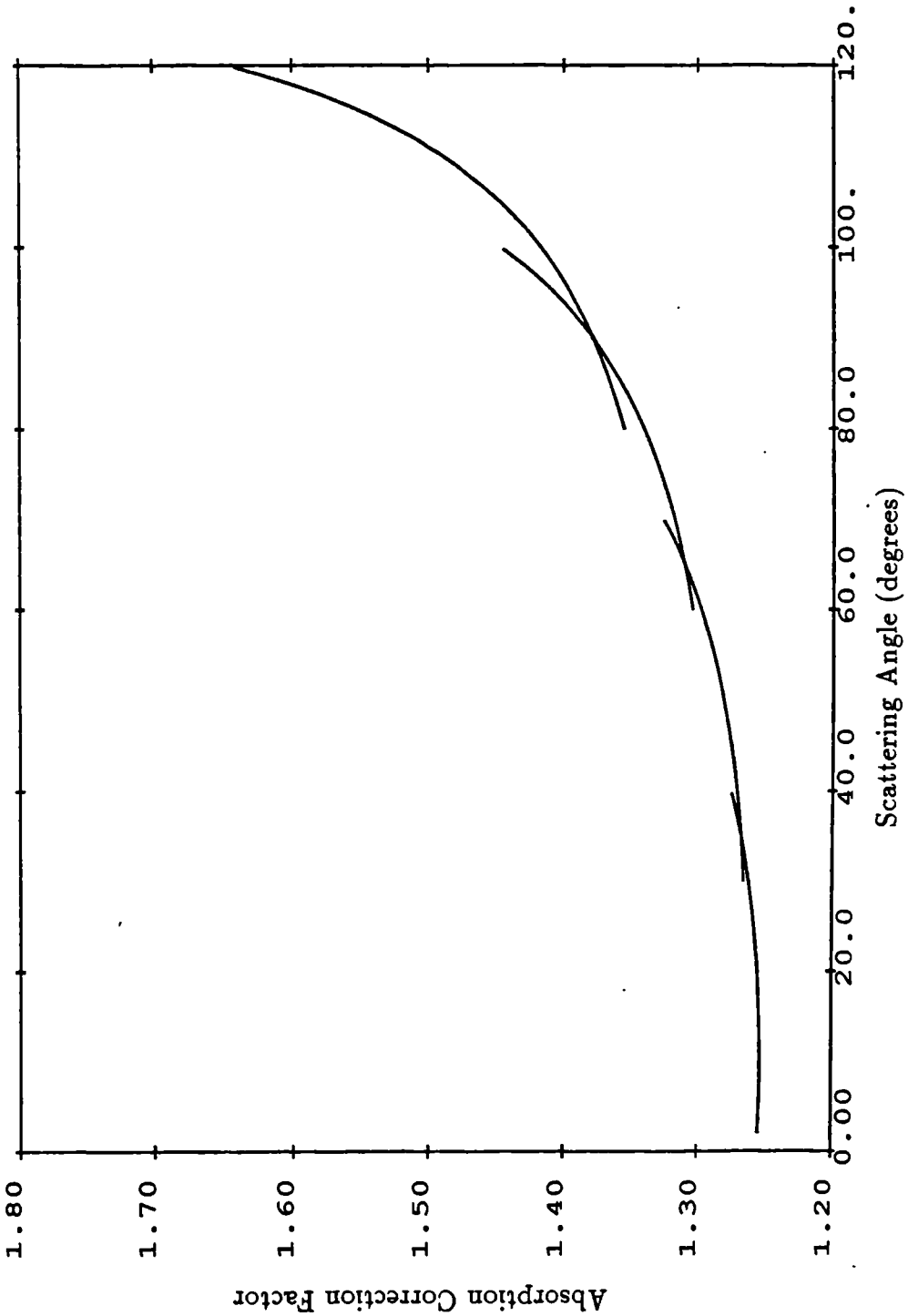

Figure 26: The four multiplicative absorption correction factors for the CCl_4 fixed theta experiment.

Figure 25 shows the multiplicative absorption correction ($1/\mathrm{R}(\theta/2\theta)$) and its effects on the CCl_4 data. Figure 26 shows the four correction curves associated with the fixed-theta experiment. It can be clearly seen from these curves that the general trend of the corrections is the same for both experimental geometries and as is to be expected the largest corrections occur at high angles. The four curves in the fixed theta case are each steeper than the corresponding section of the $\theta/2\theta$ case due to the greater pathlength variations inherent in the fixed-theta geometry and in general the corresponding corrections are larger.

Scattering Volume

The intensity of the scattered beam is dependent on the scattering volume illuminated by the incident beam (figure 17) and it is therefore necessary to normalize the recorded spectra to the scattering from a constant volume. Assuming that the sample is of thickness t and has flat parallel sides the normalized intensity, I_{cv}, is given by

$$I_{cv} = \frac{I_s \cos\theta}{t} \tag{106}$$

This equation is only strictly true for 'slab' samples but it is a very good approximation however for samples with a small amount of bowing of the cell windows. If the sample shows a significant degree of window curvature or is a powder which has a very uneven packing, the correction becomes much more complicated and it is better to use a series of scans at fixed θ with sufficient overlap between each to allow the spectra's intensity to be normalized to each other. This approach removes the need to know how the scattering volume changes with sample angle.

Binning

The next stage was to convert the data from a function of scattering angle to a function of the scattering vector k. To do this the equivalent scattering vector was calculated for each data point using equation 1.

$$k = \frac{4\pi}{\lambda} \sin \phi/2 \tag{107}$$

It can be seen from this equation that the points will be unevenly distributed in k space, being more concentrated at high angles. To make the k space consistent the data was binned. To do this, k space was divided into a set of equal regions each 0.05 Å^{-1} wide and the equivalent number of data points in each region is calculated from the collected spectra. Besides making the data evenly spaced, binning performs two other important functions. Firstly it may be used as means of reducing the number of data points in the spectrum thus speeding calculations based on the separate points in the spectrum. Secondly it increases the statistical accuracy in the high angle (low count rate) part of the spectrum. As stated above the equivalent points in k space become closer together as the angle increases. This has the inverse effect that each successive k-bin covers an increasingly large angular range and thus contains a proportionately larger number of points in the spectrum. Thus, as more points are summed together at higher angles, so the relative statistics of these points are improved.

The binning of the data has to be left until after the corrections are carried out because it is both wavelength and angle dependent. If the binning is done before the Compton subtraction, difficulties arise, caused by the wavelength shift of the incoherent scattering. this leads to the Compton scattering being binned into a higher k-bin than it should. The effect of this to alter the normalization of the conventional spectrum to the WM spectrum such that the Compton spectrum obtained

by subtraction of the binned curves is lower at high angles than that obtained from the subtraction of the unbinned data. This error makes it impossible to perform the Compton correction using the binned data. Similarly, the absorption correction is angle-dependent and thus needs to be performed before binning. Binning the data before the correction leads to errors because, it is necessary to convert from k back to angle, but, this process yields the average angle of the set of data points which combined to form the corresponding k point. Using the average angle of a number of point leads to only an average path length and thus a greater error in the correction especially in the high angle region where the angular range corresponding to each k-space point is greatest.

3.4 Data Analysis

After correction of the data as outlined above, the intensity, $I(k)$, may be expressed as

$$I(k) = \left(\sum_{\alpha} f_{\alpha}(k)\right)^2 S_M(k) \tag{108}$$

where the molecular structure factor, $S_M(k)$, may be expressed as the sum of three components, (equation 75).

$$S_M(k) = F_M(k) + D_M(k) \tag{109}$$

$$= F_M^{self}(k) + F_M^{int}(k) + D_M(k) \tag{110}$$

where $F_M^{self}k$ and $F_M^{int}(k)$ are the 'self' and 'interference' parts of the molecular form-factor and $D_M(k)$ is the intermolecular structure factor. The following sections discuss each of these terms in detail.

Element		1	2	3	4
C	a [Å^{-1}]	2.3100	1.0200	1.5886	0.8650
	b [Å^2]	20.8439	10.2075	0.5687	51.6512
	c [Å^{-1}]	0.2156	—	—	—
Cl	a [Å^{-1}]	11.4604	7.1946	6.2556	1.6455
	b [Å^2]	0.0104	1.1662	18.5194	47.7784
	c [Å^{-1}]	-9.5574	—	—	—

Table 2: Constants used in the calculation of the atomic scattering factors of carbon and chlorine.

3.4.1 Self-Scattering

The self-scattering is the contribution to the coherent scattering arising from the interference of photons scattered by the electron density distribution of the individual atoms. As such it gives no information on the atomic structure of the sample and may be subtracted from the coherent scattering to obtain a reduced intensity, $i(k)$, which contains the structurally-dependent part of the molecular structure factor. In the independent atom approximation the self-scattering is dependent only on the atomic scattering factors of the elements forming the molecule and therefore may be easily calculated if the individual scattering factors of the elements are known. The atomic scattering factors, f, are tabulated for all atoms and selected ions in the *International Tables for X-ray Crystallography* [27]. Also available is an analytical approximation to the atomic scattering factor which gives good agreement over the k range of interest. This approximation takes the form:

$$f\left(\lambda^{-1}\sin\phi\right) = \sum_{i=1}^{4} a_i \exp\left(\frac{-b_i \sin^2\phi}{\lambda^2}\right) + c \qquad (111)$$

where a_i,b_i and c are constants listed in the *International Tables* [28]. The values of the constants for carbon and chlorine are given in table 2 and the corresponding atomic scattering factors are shown in figure 27.

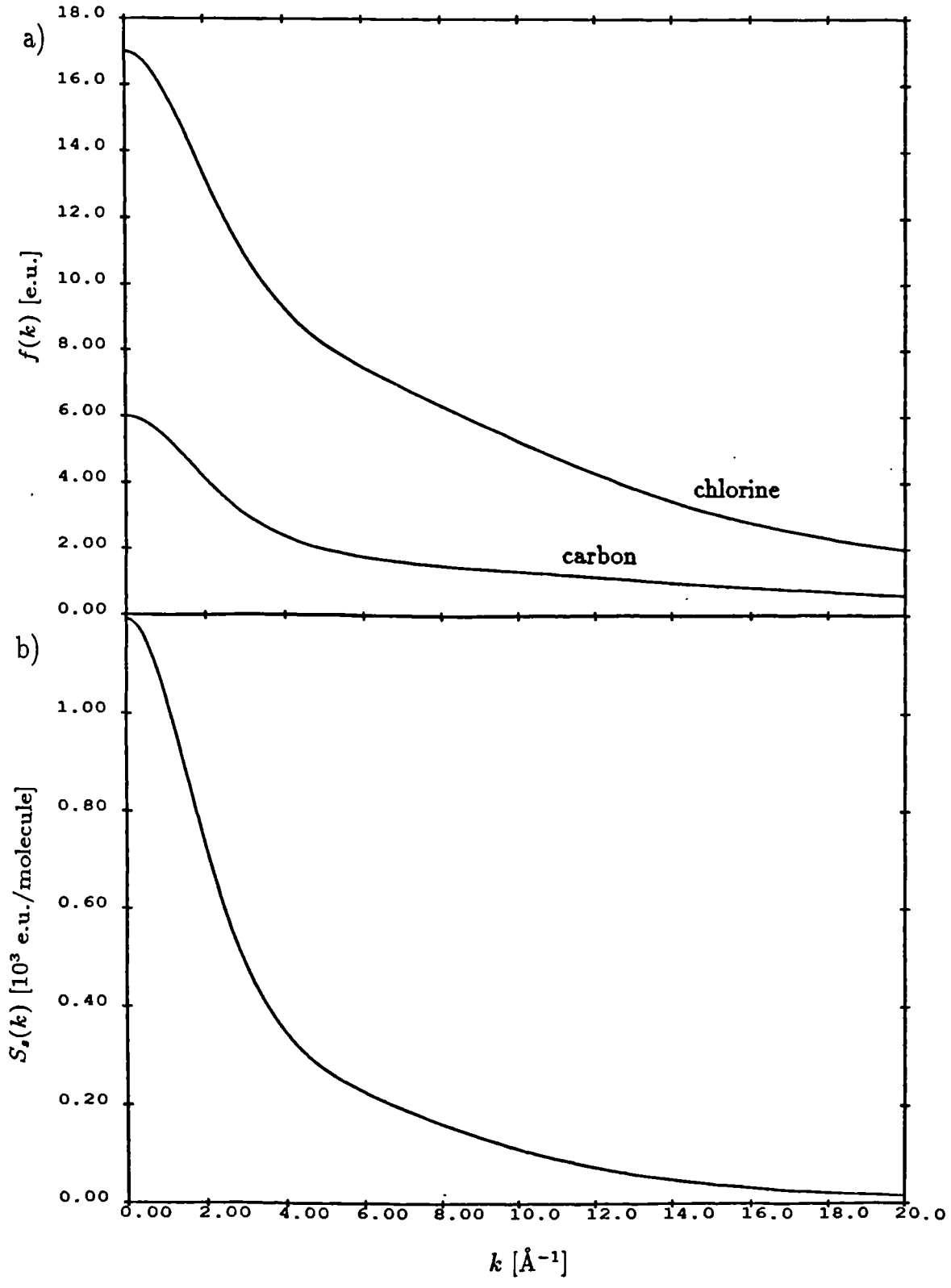

Figure 27: a) The atomic scattering factors for carbon and chlorine and b) the self-scattering from carbon tetrachloride

Having calculated the individual atomic scattering factors for carbon and chlorine, it is now necessary to calculate the self-scattering from the molecule. The self-scattering, $S_s(k)$, is purely dependent on the atomic scattering factors and is given by

$$S_s(k) = \sum_\alpha f_\alpha^2(k) = f_C^2(k) + 4f_{Cl}^2(k) \tag{112}$$

where the sum over α is for all atoms in the molecule and $f_\alpha(k)$ is the atomic scattering factor of the atom α. The calculated self-scattering will be in electron units (e.u.) and to normalize the data to e.u. they are multiplied by a normalization constant such that the resultant spectra oscillates around the self-scattering (see figure 28). This normalization also provides a check on the validity of the preceding corrections. Errors show up as a deviation of the corrected data away from the self-scattering curve and such errors were eliminated by refinement of the constants involved in the Compton, absorption and related corrections.

Subtraction of the self-scattering from the normalized structure factor yields the reduced intensity, $i(k)$, which represents the structurally sensitive part of the structure factor, in electron units.

$$i(k) = \left(\sum_\alpha f(k)\right)^2 S_M(k) - \sum_\alpha f_\alpha^2(k) \tag{113}$$

where the summations are over all of the atoms in the molecular unit.

3.4.2 The Interference Terms

The reduced intensity obtained by the subtraction of the self-scattering is composed of two terms. From equation 110

$$i(k) = \left(\sum_\alpha f(k)\right)^2 \left\{F_M^{int}(k) + D_M(k)\right\} \tag{114}$$

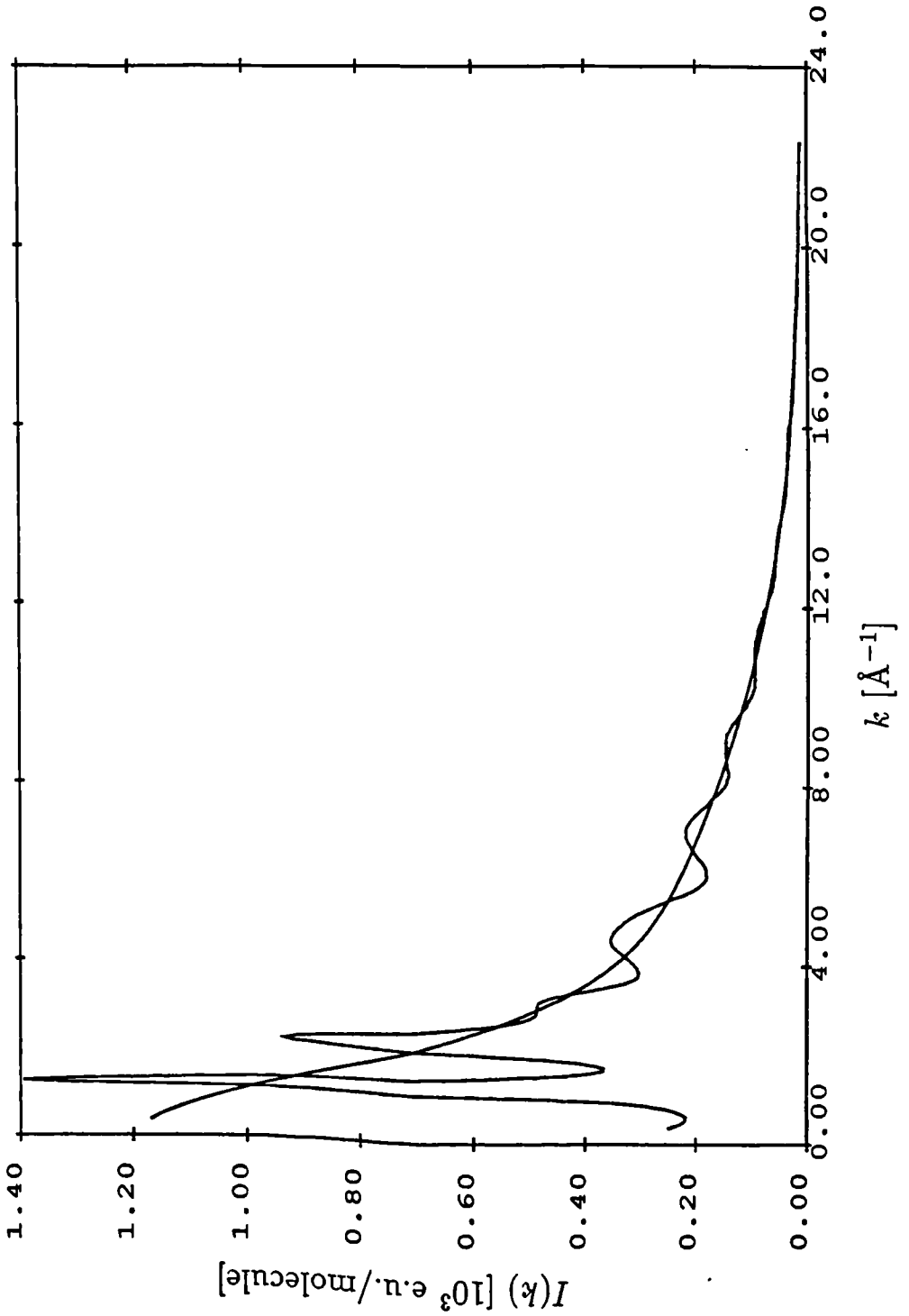

Figure 28: The self-scattering curve and the scattering intensity from CCl_4 after correction and normalization to electron units.

where $F_M(k)$ is the intra-molecular term and contains all of the information about the conformation of the molecule and $D_M(k)$ is the inter-molecular contribution to the interference term and contains information on the inter-molecular correlations. It can be seen from the above equation that if the intra-molecular correlations are accurately known the inter-molecular correlations may be found. For the purposes of this section of the work, however, only the reduced intensity, $i(k)$, the conformation of the molecule and the total radial distribution function are required to allow comparisons to be made with previously published work.

The Molecular Form-Factor

The conformation of the CCl_4 molecule may be obtained by fitting a molecular form-factor to the data. The form-factor used to fit the data was

$$F_M(k) = \frac{1}{(f_C(k)+4f_{Cl}(k))^2}\left[8f_C(k)f_{Cl}(k)j_0\{ak\}\exp\left\{-\gamma_{CCl}k^2\right\}\right. \quad (115)$$
$$\left.+12f_{Cl}^2(k)j_0\{bk\}\exp\left\{-\gamma_{ClCl}k^2\right\}\right]$$

were $j_0(x)$ is the zero order Bessel function and is given by

$$j_0(x) = \frac{\sin x}{x} \quad (116)$$

the distances a and b refer to the C–Cl and Cl–Cl separations in the molecule and the γ_{ij} terms are the damping factors due to molecular motion.

The molecular form-factor was fitted to the data using a least-squares-fit algorithm. The fit was made from k = 6.6 Å^{-1} to k = 17.8 Å. A lower limit of 6.6 Å^{-1} was selected because above this point only the short-range intra-molecular correlations should be present in the interference function. The upper limit was set because above this point the data become very noisy due to the low counting statistics combined with the multiplying effect caused by the division of the data

Method	Authors		Reference	State	Bond length/Å
Electron	Bartell *et al.*	(1955)	[49]	vapour	1.769±0.005
diffraction	Morino *et al.*	(1960)	[50]	vapour	1.765±0.002
Neutron	van Tricht *et al.*	(1977)	[60]	liquid	1.770±0.002
diffraction	Clarke *et al.*	(1979)	[52]	liquid	1.766±0.002
	Bermejo *et al.*	(1988)	[54]	liquid	1.766±0.005
				liquid	1.769±0.003
X-ray	Bray *et al.*	(1943)	[41]	liquid	1.74
diffraction	Eisenstein	(1943)	[42]	liquid	1.85
	Grubel *et al.*	(1967)	[43]	liquid	1.8
	Narten *et al.*	(1967)	[61]	liquid	1.773±0.003
	Reichelt *et al.*	(1974)	[44]	liquid	1.767±0.003
	Narten	(1976)	[45]	liquid	1.766±0.003
	Nishikawa *et al.*	(1979)	[47]	liquid	1.768±0.006
	This Work			liquid	1.766±0.004

Table 3: A comparison of the values for the CCl bond length in carbon tetrachloride obtained from different experimental measurements.

by the square of the sum of the atomic scattering factors. The fit yielded a bond length of 1.766 Å for the C–Cl bond and a value of 2.884 Å for the Cl–Cl separation. These in turn give a Cl–C–Cl bond angle of 109.48° which is in excellent agreement with the expected tetrahedral angle of 109.47°. The values obtained for the Debye-Waller factors are, $\gamma_{CCl} = 0.0013$ and $\gamma_{ClCl} = 0.0038$. The fit obtained is shown in figure 29. Table 3 shows a comparison of the C–Cl bond length found by previous authors.

Figure 29 illustrates the need to collect data at high-k for a longer period of time and thus to maximise the statistical accuracy in this region. Although data were collected to approximately 23 Å^{-1} the lack of statistical accuracy above ~18 Å^{-1} makes this part of the data redundant for fitting purposes and also if Fourier transformed would lead to a large increase in noise in the obtained radial distribution function. In this figure there is also a discrepancy between the fit and the data at

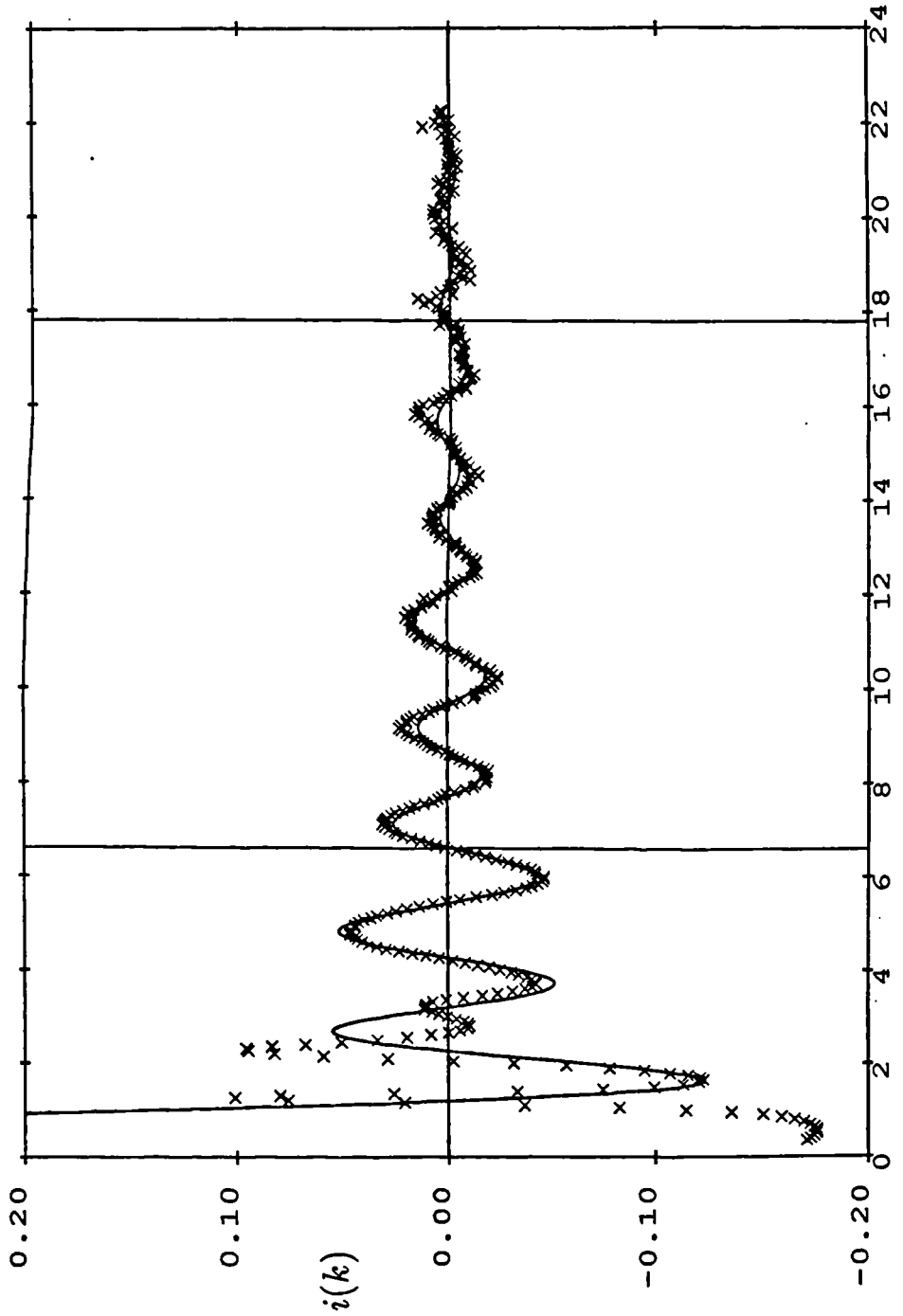

Figure 29: The reduced intensity, $i(k)$, for CCl_4 ($\times\times\times$) and the calculated molecular form-factor (—). The vertical lines show the lower and upper bounds of the window within which the molecular form-factor was fitted.

about 16 $Å^{-1}$, this actually matches the position of the highest angle mica spike found in this dataset and suggests that this has not been removed properly, thus emphasising the need for a better window material. However, despite these problems the fit obtained is in excellent agreement with those of previous authors.

A comparison has been made between the weighted structure function, $kS(k)$, obtained from this analysis with those obtained by Narten [45] and Nishikawa [47]. The Narten dataset was obtained from a table of values printed in the paper whereas the Nishikawa dataset was obtained by tracing the published plots using a digitising pad connected to a computer. After digitisation the Nishikawa data was interpolated to give even k spacing and then divided by the normalization factor, $1/(\sum_\alpha f_\alpha(k))^2$, as this had not been done in his illustration. Examination of these curves again shows the spurious peak at about 16 Å. The presence of a discrepancy in the minima just above 14 Å will also be noted, no explanation for this could be found. The peak just below 14 Å shows good agreement between the current data and that of Nishikawa, but a significant drop in the height of Narten's data, indicating an error in his data, which is as severe as that occurring in the next minima of the current data. The only other major difference in the three datasets is for the third peak. Figure 28 shows that this peak is originally present as a shoulder on the side of the second peak in the total intensity plot. The differences arising in this peak are shown, by a comparison of the equivalent plots in the two papers, to arise from the way in which the self-scattering passes through this shoulder. From these curves it can concluded that the present data correction method may be used as an alternative to previous theoretical methods for the removal of the Compton component, with a similar accuracy in the final results.

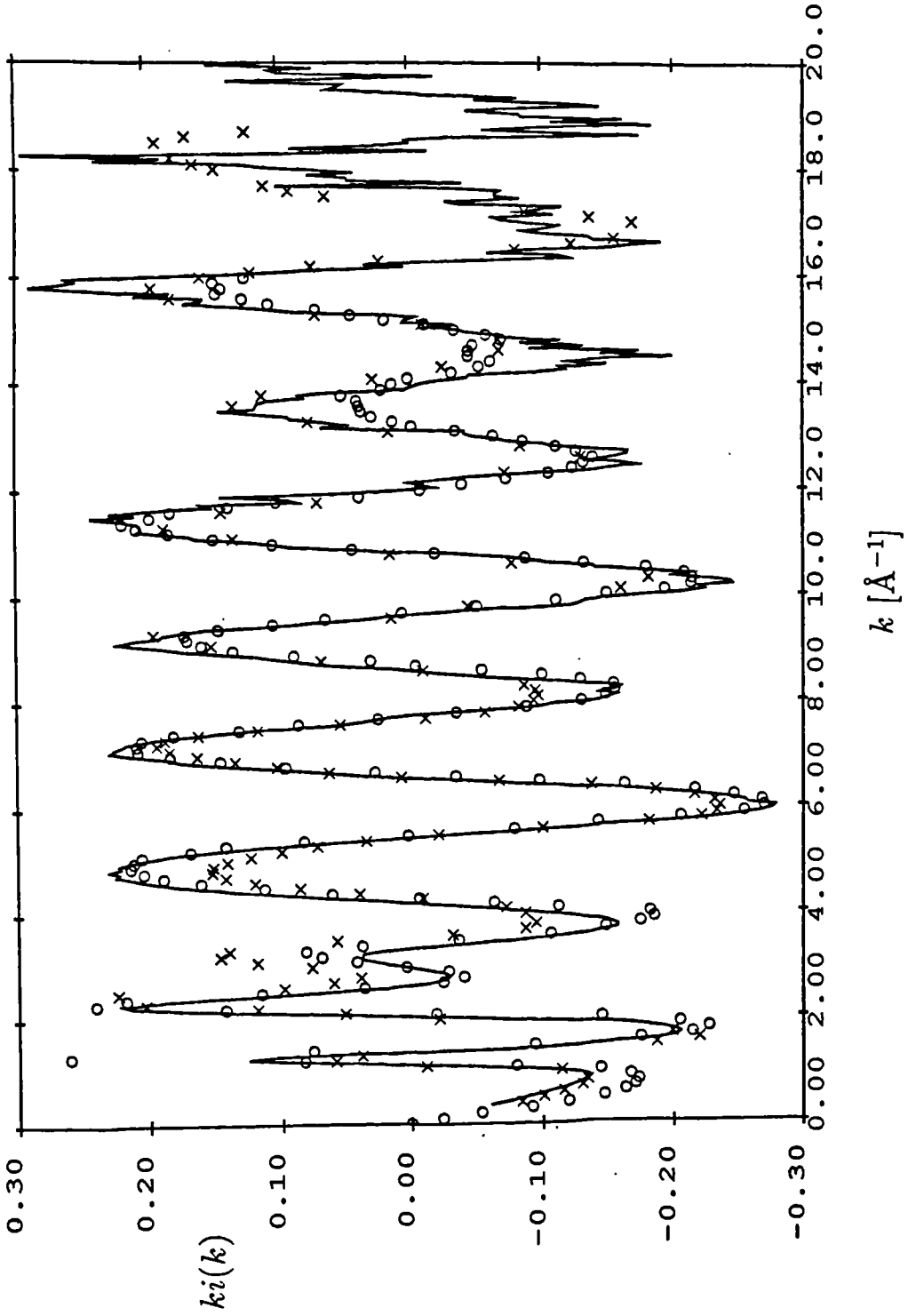

Figure 30: The weighted structure function, $kS(k)$, for CCl_4 (—) compared to the equivalent curves obtained by Narten [45] (o o o) and Nishikawa [47] (× × ×).

3.4.3 The Pair Distribution Function

From the reduced intensity, the pair distribution function, $d(r)$, may be obtained via the Fourier inversion

$$d(r) = \frac{2}{\pi}\int_0^{k_{max}} kS(k)M(k)\sin kr \; \mathrm{d}k \tag{117}$$

$$= \frac{2}{\pi}\int_0^{k_{max}} k\frac{i(k)}{\left(\sum_\alpha f_\alpha(k)\right)^2}M(k)\sin kr \; \mathrm{d}k \tag{118}$$

where $M(k)$ is a modification function which is introduced to reduce termination ripple [62] by ensuring that the transformed function goes smoothly to zero at the maximum range of the data. The modification function chosen has the form

$$M(k) = \frac{\sin(\pi k/k_{max})}{\pi k/k_{max}} \tag{119}$$

The result of the transform is shown in figure 31. This curve shows two very sharp peaks corresponding to the C–Cl and Cl–Cl distances within the molecule. At high-r there is a large amount of ripple in the transform which probably arises from the large amount of noise in the weighted structure function ($ki(k)$). The rest of the peaks are in reasonable agreement with other authors provided allowance is made for the ripple effects. The small peak just below 4 Å corresponds to the closest separation of chlorine atoms on different molecules and the broad peak at ~6 Å corresponds to the separation of the centres of the CCl_4 molecules.

3.5 Conclusions

An experimental technique has been developed, based on the work of Warren and Mavel [40], which allows coherent diffraction data to be collected in an X-ray diffraction experiment whilst excluding a large proportion (~ 90%) of the Compton scattering. Subsequently, a method of analysis has been developed which eliminates

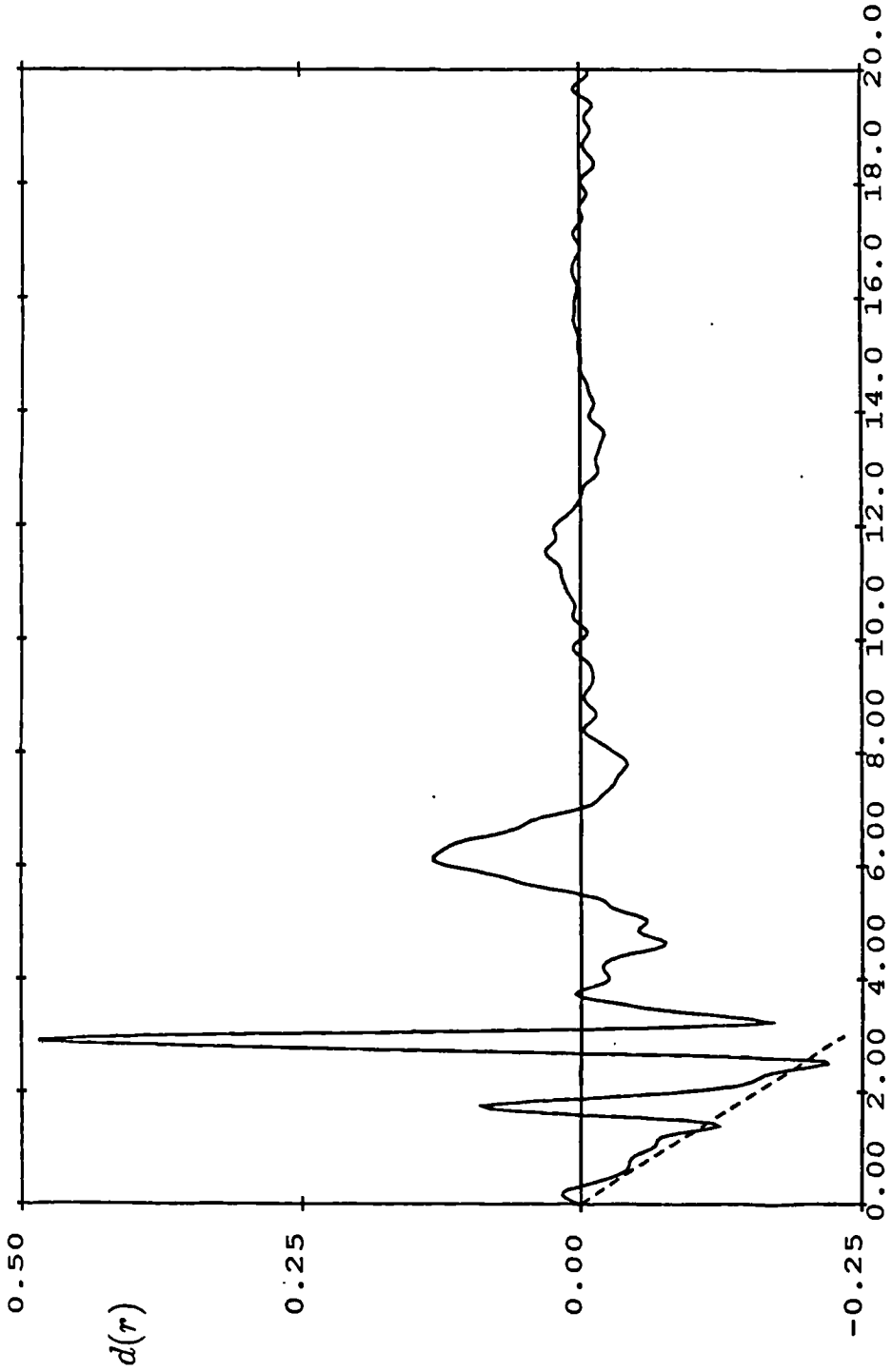

Figure 31: The radial distribution function, $d(r)$ obtained for liquid CCl_4. The dashed line is the density line ($-4\pi\rho r$).

the final 10% of the Compton scattering present in the data. The experimental technique and data correction has been carried out upon a sample of liquid carbon tetrachloride. The results of this procedure were shown to be in good agreement with those obtained by other authors who used corrections based on theoretical calculation of the Compton profile.

The major problem with the technique outlined is that it requires experiments to be carried out in both the conventional and WM modes. A better method would be to eliminate the last 10% of the Compton scattering during the experiment. A method was suggested for this by Warren [40] which involved the use of a second foil. This foil is placed in front of the detector and chosen such that it absorbs the Compton component, whilst allowing the fluorescence to pass. This is possible because the fluorescent radiation is wavelength shifted from the coherent scattered wavelength by such an amount, that it will be on the other side of the Compton wavelength. This system reduces the choice of available foils as it is necessary to select a matched pair of foils rather than a single foil but, this inconvenience will be far outweighed by the advantages. Two suitable pairs of foils are Ag K_{α_1} with an Ru sheet, (λ (K_{α_1}) = 0.5594 Å, λ (Ru K edge) = 0.5605 Å), or Mo K with a Zr sheet, (λ (Mo K edge) = 0.615 Å, λ (Zr K edge) = 0.689 Å. Use of this method should make the remaining Compton component negligibly small and should, therefore, provide a fruitful line of further inquiry as it will remove the need for the use of the two different experimental modes. This final developement will mean that the Warren-Mavel technique can be used in place of all conventional X-ray diffraction experiments carried out upon synchrotron sources and provide data which no longer contains the problems arising from Compton scattering.

Chapter 4

An X-ray diffraction Study of Amorphous Phosphorus.

4.1 Introduction

The study of amorphous systems using diffractions techniques has always proved difficult because the interpretation of the scattering data is not straight forward. This is especially true for multicomponent systems, where the measured scattering intensity is the weighted sum of the contributions from the various inter-atomic contributions present. Obviously the interpretational problems are minimised for a single component system. Amorphous phosphorus (a-P) provides just such an elemental system and, as such, is an ideal candidate for study.

The following chapter presents an X-ray diffraction study of a-P. Amorphous red phosphorus is of interest both as an elemental amorphous solid and because a variety of different amorphous systems seem to occur none of which has been fully characterised. Of particular interest, is whether the intermediate-range order ($\sim$ 5

to 15 Å) of the amorphous system demonstrates structural characteristics similar to any of the crystalline allotropes.

Phosphorus exists in many forms of which three are easily recognizable, these are red, white and black. When heated all three sublime to a vapour composed of P_4 molecules, which when recondensed yields white phosphorus. White phosphorus is easily changed to red by the action of heat, light or X-rays. Under a pressure of 12000 atmospheres and a temperature of 200°C, it changes to black phosphorus. Black phosphorus changes to red when heated to a temperature of 550°C. All of these changes are irreversible. Some information on the structure of each of these forms is outlined below.

White phosphorus exists as transparent crystals. It is a molecular solid consisting of aggregates of P_4 molecules which are bonded together by van der Waals forces. It has a bond length of 2.21 Å and a bond angle of 60°.

Black phosphorus when ground resembles graphite. It exists in three forms, orthorhombic, (o-P), rhombohedral, (r-P), and cubic, (c-P). The more common orthorhombic form consists of puckered double layers of identical six-fold rings [63]. It has bond lengths of 2.22 and 2.24 Å and bond angles of 96° and 102°. The rhombohedral modification also consists of identical six-fold rings but this time they form a sheet structure with a bond length of 2.13 Å and a bond angle of 105°. Finally the cubic form has a simple cubic structure with a coordination number of 6 and a bond length of 2.38 Å.

Violet phosphorus, or monoclinic phosphorus (m-P) has 84 atoms in its unit cell and consists of layers of parallel tubes of pentagonal cross-section containing P_8 and P_9 clusters. The tubes in adjacent layers are approximately perpendicular. There is no fixed bond length instead they range from 2.18 to 2.30 Å and similarly the

bond angles are in the range 85 - 116°.

Red phosphorus is the amorphous form which is of interest in this study. Red phosphorus has been investigated extensively using a number of different techniques [64-75] . From this work two models for a-P have been formed. In the first, based on the X-ray diffraction work of Beyeler [67], comparisons were made between the total radial distribution functions, $J(r)$ of a-P and o-P paying special attention to the small third peak. Further support is obtained from a comparison of o- and a-P performed using X-ray spectroscopy [75], from ^{31}P NMR [66] and from vibrational measurements [69,70]. The second model is also based on X-ray diffraction work [64,65]. In this model a-P is formed of pentagonal tubes as found in m-P. This theory is supported by work carried out using Raman-scattering [71,72]. The following chapter presents the first part of an investigation into a-P being carried out using both neutron and X-ray diffraction.

4.2 The Experiment

Two samples of amorphous phosphorus were used in this study. The samples were obtained from *Mining and Chemical Products Ltd*, Alperton, Wembley, U.K. where they were made by thermal conversion from white phosphorus. The two samples were distinguishable by a notable difference in their colour, sample 1 being dark red and sample 2 being dark violet. The powdered samples were packed into the sample cell shown in figure 13. This cell was made of perspex and had a 1.6 mm neoprene spacer inserted between the plates to define the sample thickness. The windows were constructed of 50 μm kapton.

The X-ray diffraction experiments were performed on station 9.1 at the Daresbury Laboratory (see chapter 2). The experimental technique used was the same

Scan	Sample angle (θ)	Scan range (ϕ)
1	50°	120°– 80°
2	40°	100°– 60°
3	25°	70°– 30°
4	10°	40°– 2°

Table 4: Values of the sample angles and the detector scanning ranges used in the collection of the a-P data.

as that outlined in chapter 3 for the Warren-Mavel fixed-theta mode experiment. Datasets were collected over the scan ranges shown in table 4, with a detector step size of 0.2°. The data were collected in the order shown, with the data for each point being collected until the detector count reached 10000 counts. This corresponds to an error of 1% in the count at each data point. The collected diffraction spectra, after normalization to a monitor count of 10000, are shown in figures 32 and 33. These figures also show the normalized 'background plus container' count. It is clear from these figure that there is a greater recorded intensity from sample 2. This is probably caused by differences in the amount of powder exposed to the beam, arising from differences in the thickness of the sample and in their packing fractions. This later supposition is supported by the visual appearance of the samples, sample two being of smaller grain size than sample 1, thus allowing closer packing.

4.3 Data Analysis

After collection, the data were corrected for the background and container scattering, polarization effects, Compton scattering and sample absorption as described in chapter 3. The data, after these corrections have been applied, are shown in figure 34. This figure illustrates more clearly the differences in the intensity scattered

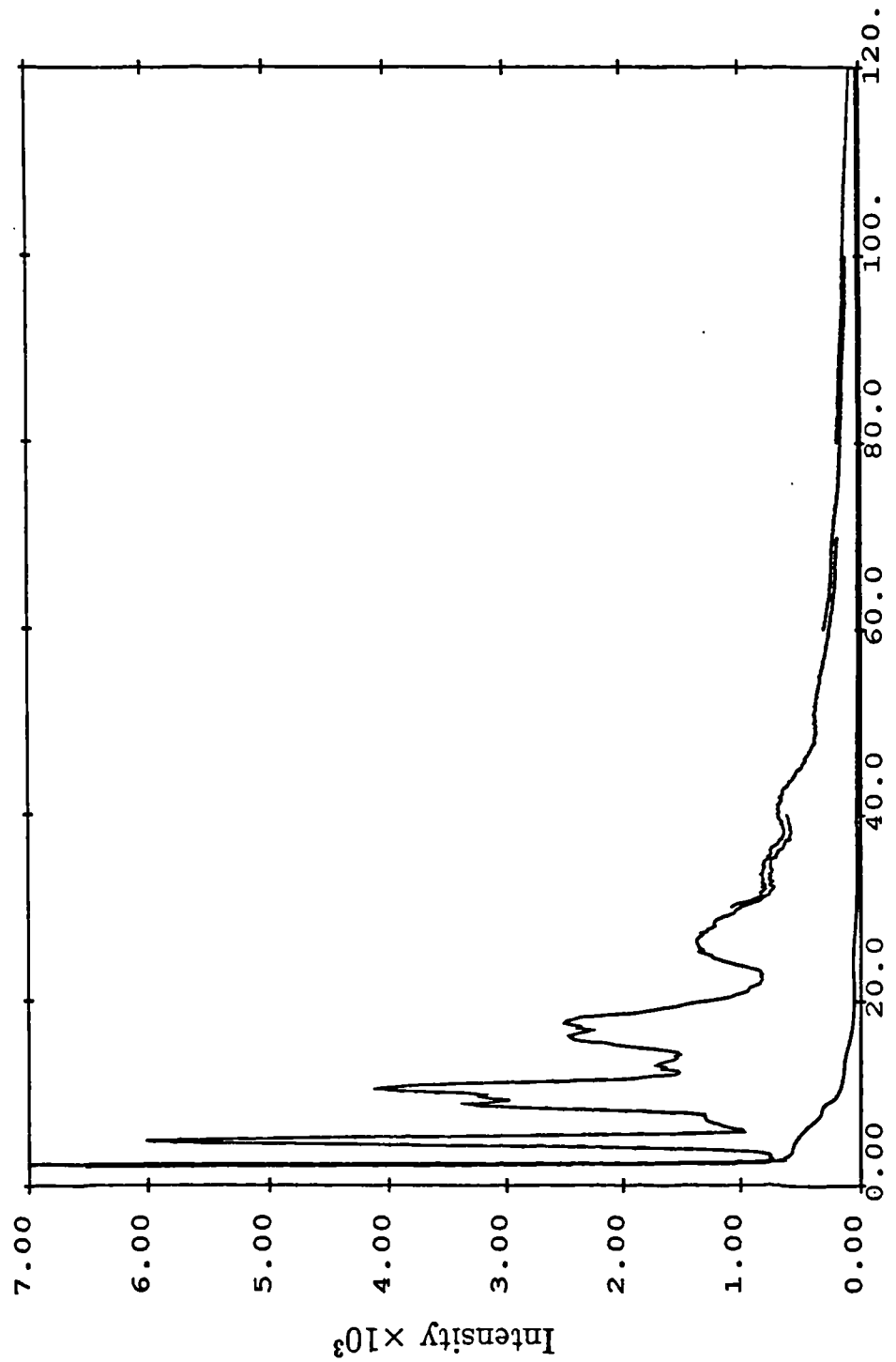

Figure 32: The normalized data collected from a-P sample one.

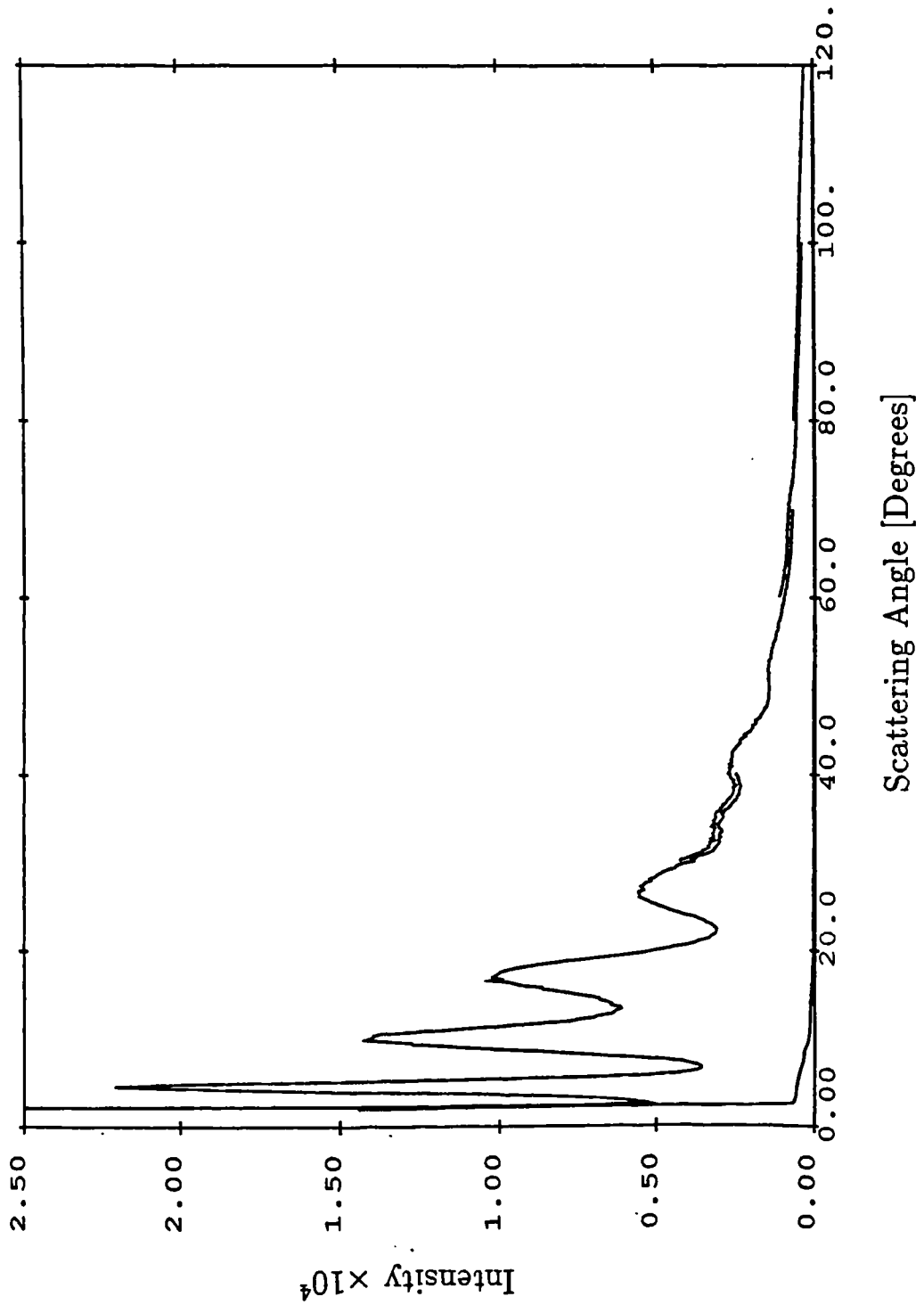

Figure 33: The normalized data collected from a-P sample two.

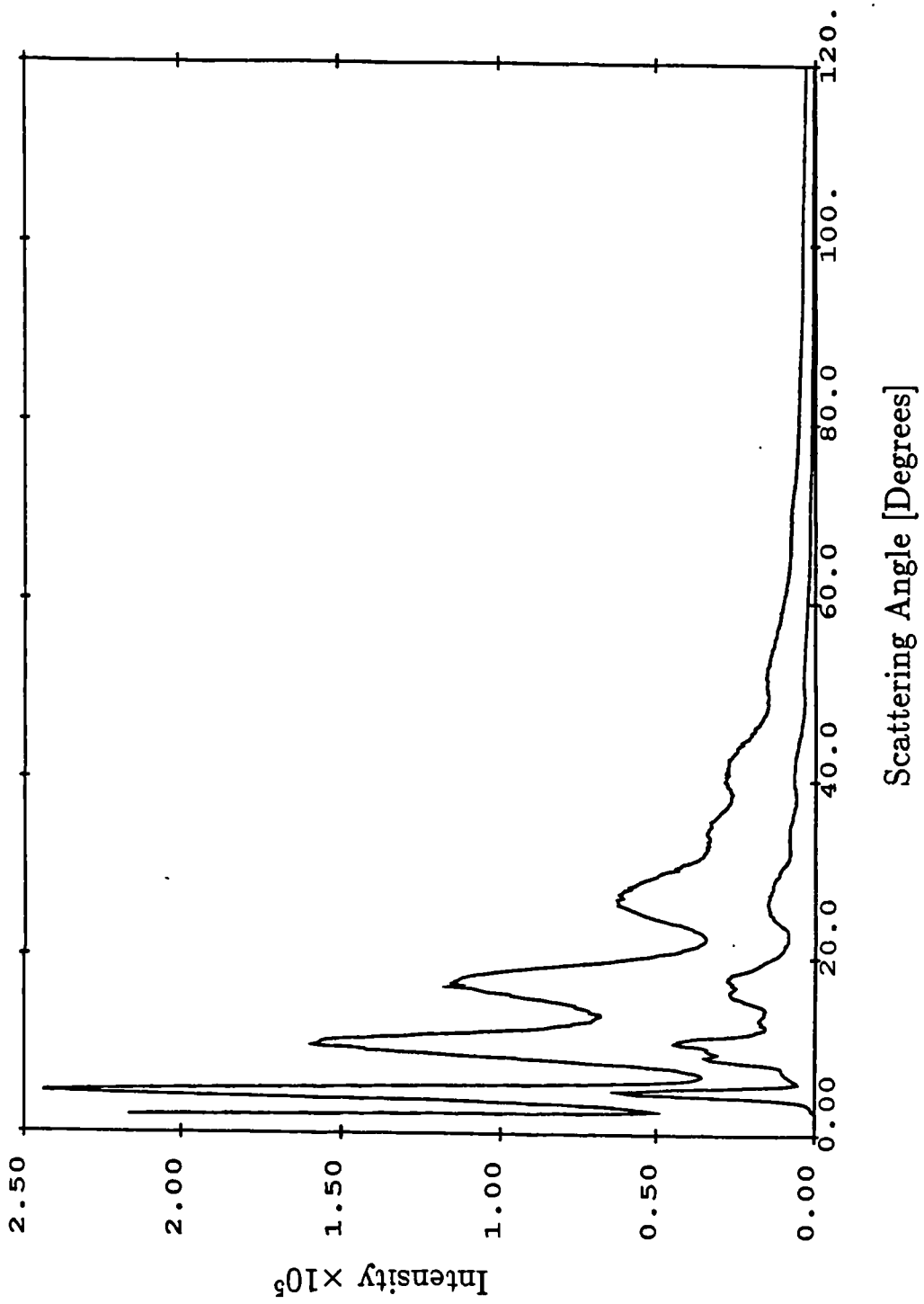

Figure 34: The corrected scattering intensities for the two a-P samples.

	1	2	3	4
a [Å^{-1}]	6.4345	4.1791	1.7800	1.4908
b [Å^2]	1.9067	27.1570	0.5260	68.1645
c [Å^{-1}]	1.1149	—	—	—

Table 5: Constants used in the calculation of the atomic scattering factor of phosphorus

by the two samples. It can also be seen from this figure that the overlapping regions of the separate datasets have been correctly matched indicating that the corrections applied to the data are valid. This check is especially useful as the agreement of the curves depends very heavily upon the absorption corrections applied, which in turn are dependent on the thickness of the sample. This check, therefore, supplies a consistency check of the amount of powder exposed to the X-ray beam. The differences in the low-k peak shapes of the two curves indicate a difference in the atomic structure of the samples.

After correction the data were placed into k bins of 0.05 Å^{-1} width and normalized to the self-scattering curve to give the total scattering intensity $I(k)$ as outlined in chapter 3. The structurally dependent component of the scattering is contained in the reduced structure factor (see chapter 3) which may be expressed in terms of the observed intensity as

$$S(k) = \frac{1}{f_P^2(k)} \left(N_c I(k) - f_P^2(k) \right) \tag{120}$$

where N_C is a normalisation constant chosen to make the observed intensity oscillate around the atomic scattering factor curve ($f_P^2(k)$). The atomic scattering factor was obtained using the analytical approximation [28]

$$f(\lambda^{-1} \sin\phi) = \sum_{i=1}^{4} a_i \exp\left(\frac{-b_i \sin^2\phi}{\lambda^2} \right) + c \tag{121}$$

where a_i, b_i and c are constants with the values given in table 5. This expression

yields a good approximation to the atomic scattering factor of a free atom. Its use here assumes that this expression is still valid. If, however, strong delocalization of the electron cloud occurs this will change the atomic scattering factor and will led to discrepancies in the analysis. Such effects have not been noted by previous authors.

The two reduced structure factor curves obtained for the phosphorus samples are shown in figure 35. These two curves show clear differences at low-k. Sample 1 shows has a number of small peaks associated with the main peaks shown by sample 2. The first peak in sample 1 also appears to be sharper than the corresponding peak in sample 2. These differences appear to indicate that sample 1 contains a higher degree of crystalline order than sample 2. Above approximately 6 Å the two curves are exhibit very similar features.

The Fourier transform of the reduced structure factor yields the radial distribution function, $d(r)$. To reduce the termination ripple present in the $d(r)$ functions a modification function, $M(k)$, was introduced into the transform. Thus we have

$$d(r) = \frac{2}{\pi} \int_0^{k_{max}} kS(k)M(k) \sin kr \; \mathrm{d}r \tag{122}$$

The modification function chosen has the form

$$M(k) = \frac{\sin \pi k/k_{max}}{\pi k/k_{max}} \tag{123}$$

The resultant $d(r)$ curves are shown in figure 36. The high-r region of these curves show a large amount of noise. This noise is due to transforming the noise in the high-k region of the $S(k)$ curve. The noise in the high-k region arises from statistical fluctuations in the recorded scattering profiles. Due to the use of the WM technique these fluctuations are smaller than those normally present in the $S(k)$ curve after the removal of the Compton component, they do however still pose a problem. To

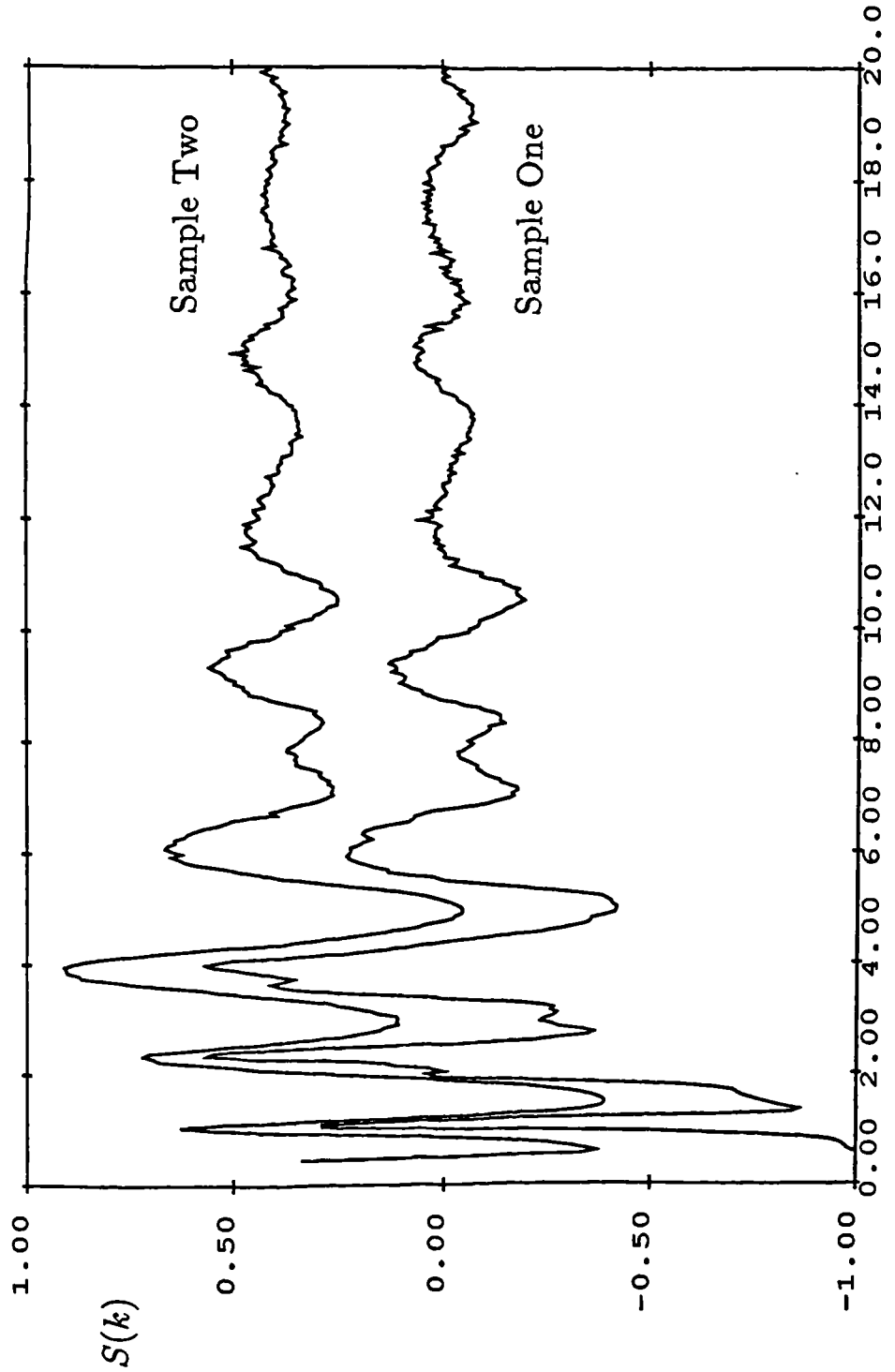

Figure 35: The two reduced structure functions obtained from the a-P samples. The curve obtained for sample two has been offset for clarity.

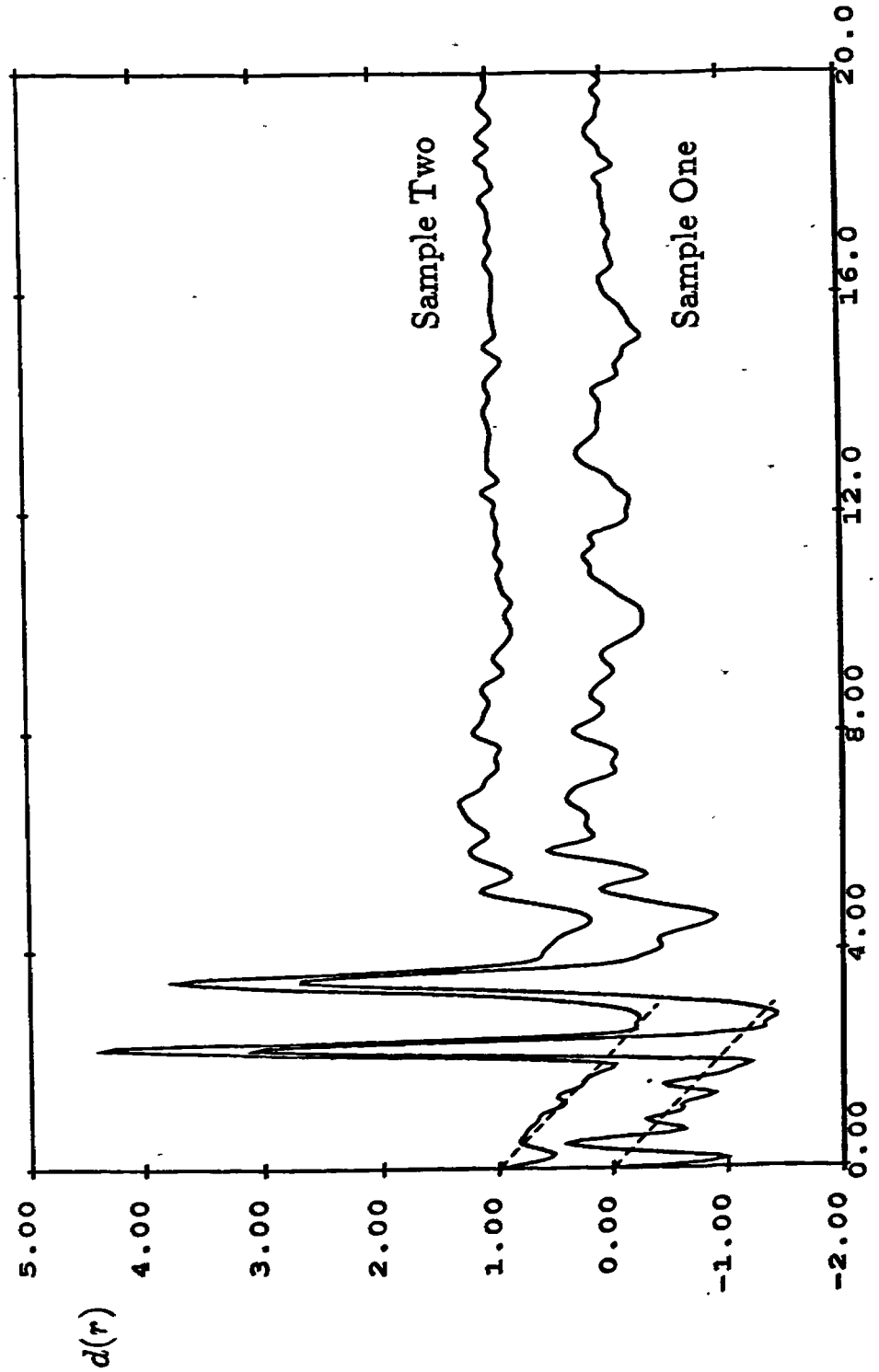

Figure 36: The radial distribution function, $d(r)$, obtained for the two a-P samples. The dashed line is the density line ($-4\pi\rho r$). Sample two has been offset for clarity.

reduce this noise, the $S(k)$ curve was smoothed using a cubic spline routine. This smoothing was carried out from 6 $Å^{-1}$ upward. The lower limit of the smoothing was chosen so that the low-k peaks were not altered, as smoothing these would led to a reduction of their heights. Care was also taken to ensure that the smoothing did not severely affect the resolution of the low-r part of the $d(r)$ spectra. The $d(r)$ curves obtained from the smoothed data are plotted in figure 37. This figure shows a great reduction in the noise at high-r without significant change in the general shape of the curves. There is, however, a slight drop in the height and a corresponding broadening of the two main peaks. For this reason the unsmoothed $d(r)$ shown in figure 36 have been used for all position and coordination number calculations (see below).

The two curves show very different degrees of crystallisation. In sample one correlations can be seen extending over the entire range of the transform, whereas, sample 2 only shows significant structure as far as 10 Å. This is indicative that sample 1 has a much higher degree of intermediate range crystalline order than sample 2. This is probably caused by differing degrees of polymerisation, of the P_4 molecules in the white phosphorus, occurring during the fabrication of the samples. Another apparent difference is found by examining the density line, in both cases the number density was taken as 0.037. This line gives a good fit for sample 2, but for sample 1 the line appears to be slightly high. This suggests that the microscopic number density is higher in sample 1 than it is in sample 2, which in turn indicates a reduction occurring in the density of the sample as its crystallinity is reduced.

The next stage in the analysis was to obtain the positions and sizes of the peaks appearing in the radial distribution function. To aid this, the $d(r)$ curves were

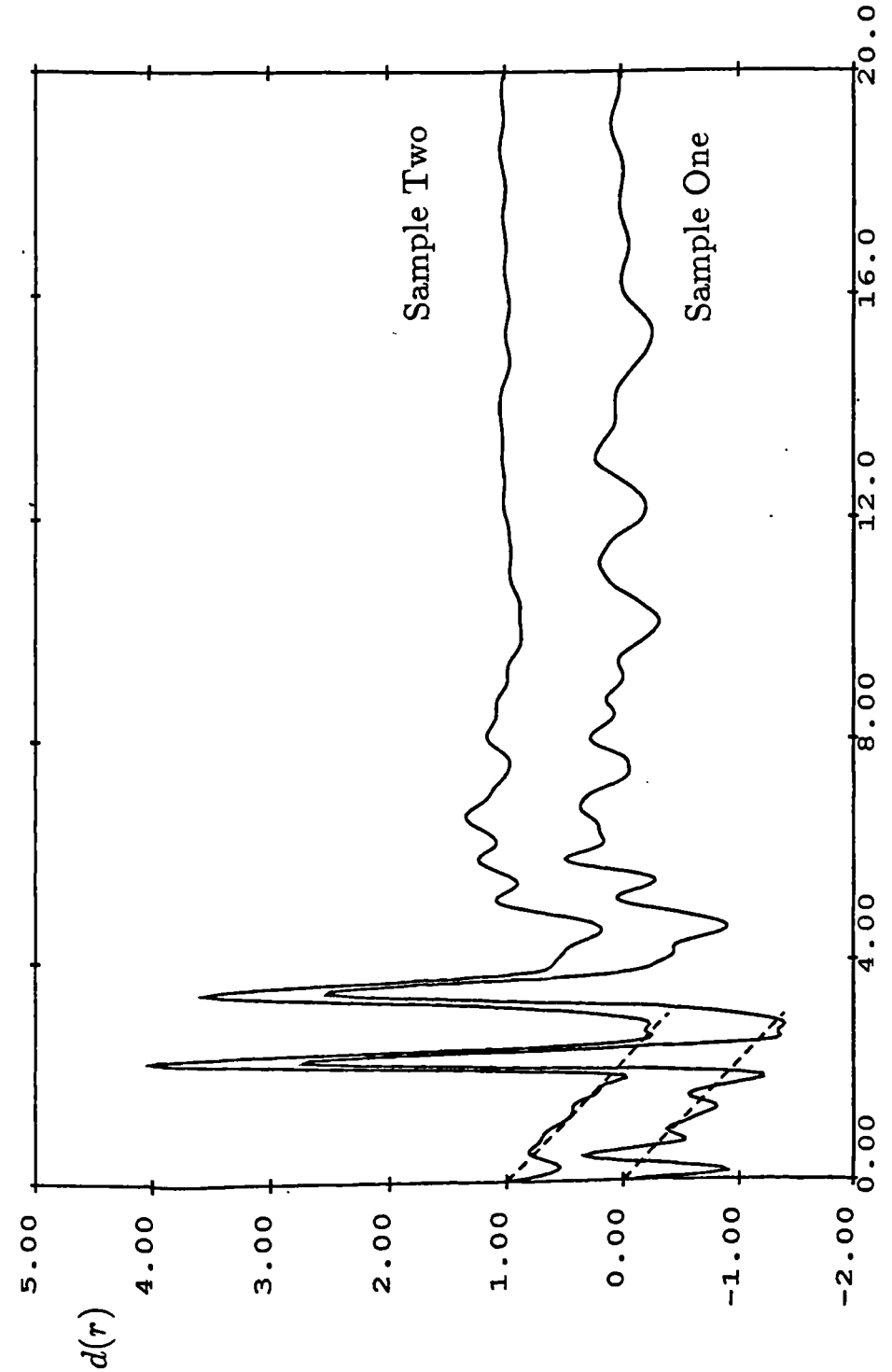

Figure 37: The radial distribution function, $d(r)$, obtained after smoothing of the two a-P reduced structure factors. The dashed line is the density line ($-4\pi\rho r$). Sample two has been offset for clarity.

Peak	Sample 1			Sample 2		
	Position [Å]	width [Å]	Area [atoms]	Position [Å]	width [Å]	Area [atoms]
1	2.228	0.112	2.8	2.227	0.111	2.9
2	3.477	0.205	7.6	3.456	0.197	7.0
3	4.184	0.276	4.7	4.172	0.294	4.8
4	5.157	0.358	12.1	5.105	0.341	10.4
5	5.908	0.251	12.0	5.920	0.336	13.5

Table 6: Gaussian parameters used to fit the first five peaks in a-P.

converted to give the total radial distribution functions, $J(r)$, using the equation

$$J(r) = rd(r) + 4\pi r^2 \rho \tag{124}$$

It is evident from this equation that the resultant distribution will be heavily depend upon on the number density of the sample. As shown in figure 36 the number density of sample 1 is not equal to that used to calculate the density line. For this reason a new number density was calculated for sample 1, such that the density line cut the minimum between the first and second peaks in a similar manner to that demonstrated in sample two. This new number density was 0.040. The results of the conversion to $J(r)$ are shown in figures 38 and 39. Comparison of the $d(r)$ and $J(r)$ curves shows that the shoulder on the side of the second peak in the $d(r)$ curve becomes a peak in the $J(r)$ curve. There is also a clear broadening of this peak in sample 2 when compared to the other sample. This is yet another indication that sample 2 is of a more amorphous nature. A lowering of the fourth peak is also visible in the second sample.

To find the peak positions and coordination numbers of the low-r peaks in the two samples, they were fitted with a series of Gaussian curves. These peaks had the form

$$f(r) = \frac{C_N}{\sigma\sqrt{2\pi}} \exp\left\{-\frac{1}{2}\left(\frac{r-d}{\sigma}\right)^2\right\} \tag{125}$$

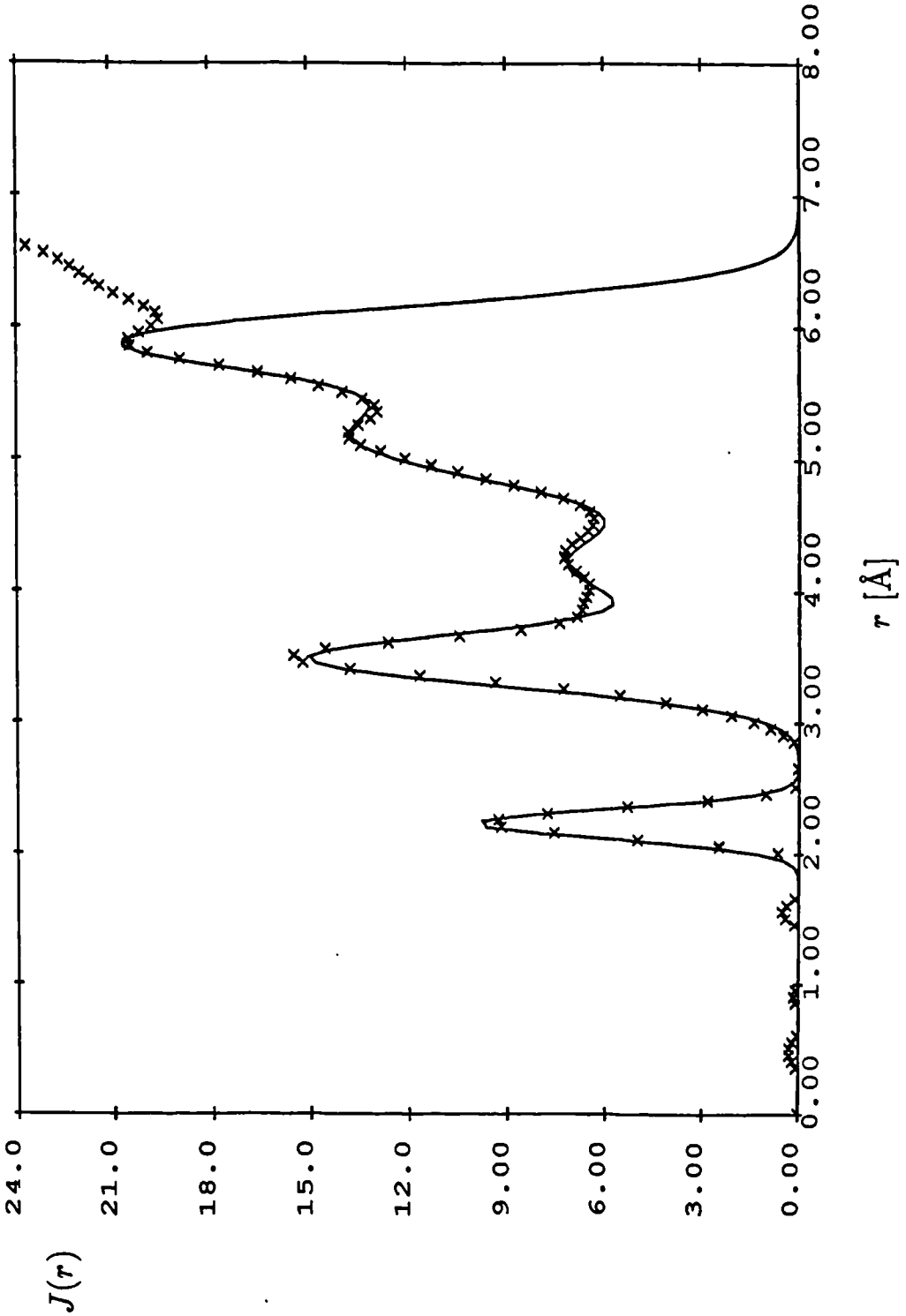

Figure 38: The total radial distribution function, $J(r)$, for sample one ($\times\times\times$) and the Gaussian fit to this curve (—).

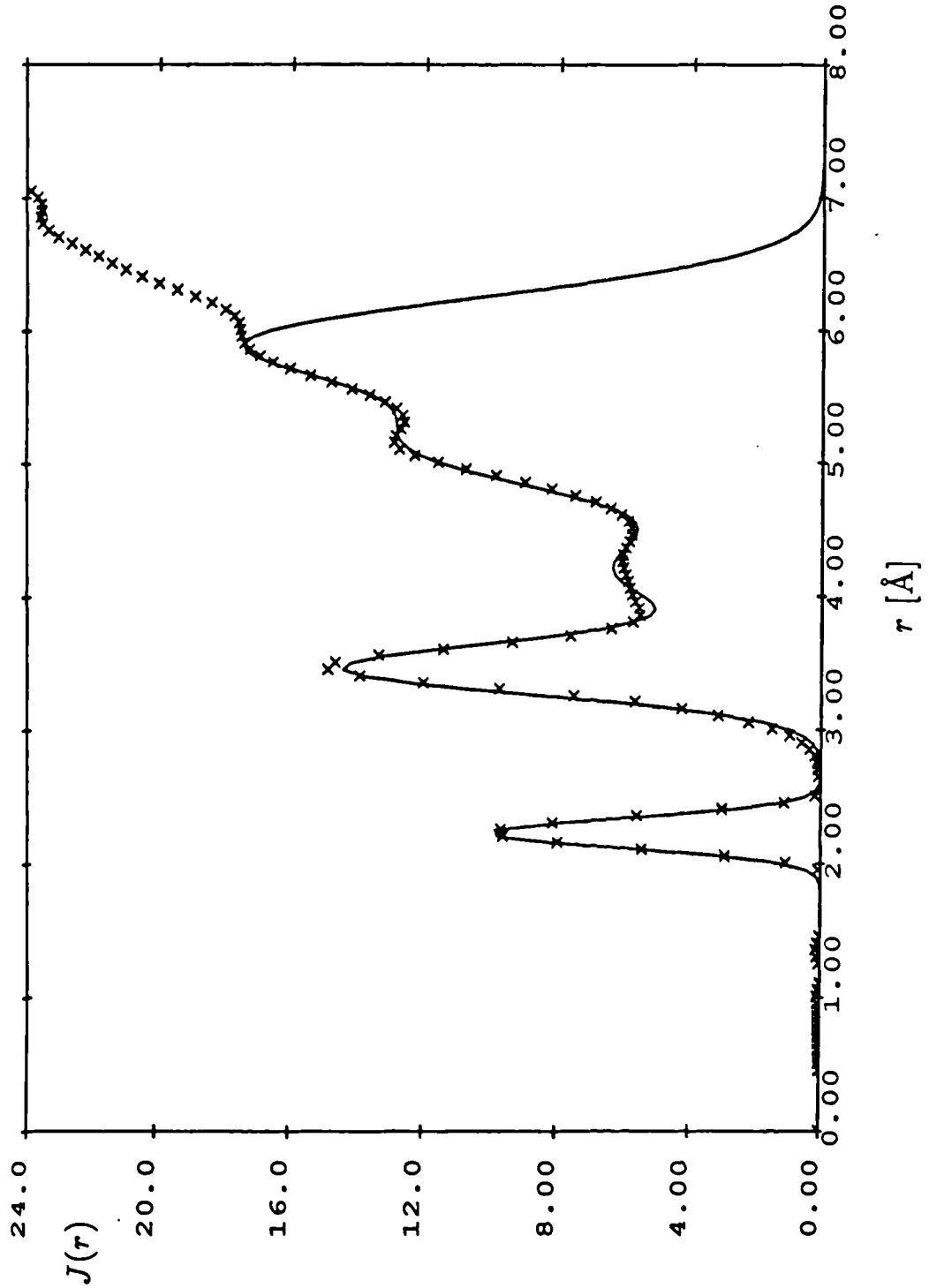

Figure 39: The total radial distribution function, $J(r)$, for sample two ($\times\times\times$) and the Gaussian fit to this curve (—).

where C_N is the area under the Gaussian curve and corresponds to the coordination number of the peak, d is its mean (or centre) and σ is its standard deviation (width). The fitting was carried out using a least-squared-fit algorithm. The results obtained from the fitting procedure are shown in table 6. It was possible in both samples to fit the first peak with a single Gaussian. For the next peaks a series of Gaussians had to be used as the peaks overlap. To obtain reasonable estimates of the positions of the second and third peaks a series of four Gaussians was calculated, thus fitting the curve to the top of the fifth peak. Of these four Gaussians, only the first two are useful as the effects of excluding higher peaks will be small. The third Gaussian in the series will be moderately influenced and the fourth Gaussian heavily influenced by the higher peaks but have been included in table 6 for comparison purposes. The corresponding fits are shown in figures 38 and 39. The curve, for sample one, indicates that a good fit was obtained for the first peak. In the second fitted peak the Gaussian has a slightly lower amplitude indicating a higher coordination number than that found and the position of the third peak appears to be shifted towards low-r. The fit of the fourth and fifth peaks is good indicating that their influence on the third peak has been reasonable well described although, due to the lack of fitting to higher peaks, the obtained coordination numbers and to a certain extent the peak centres obtained for these peaks are clearly incorrect. In sample 2 the second peak fit is again low and the shallowness of the third peak could not be achieved. A reasonable fit was again obtained for the fourth and fifth peaks. Both figures demonstrate the difficulty of fitting a single peak function to the third peak of the distribution. It is possible that this difficulty arises because, either this peak is not Gaussian in form or, this is not actually a single but a composite peak. Examination of the sample 1 curve seems to indicate that there may be a small

Peak	Beyeler [67]	Elliott [74]	Krebs [64]	Sample 1	Sample 2
1	2.32 (4.5)	2.224 (3.2)	2.24 (2.97)	2.228 (2.8)	2.227 (2.9)
2	3.52 (11.6)	3.49	3.48 (7.7)	3.48 (7.6)	3.46 (7.0)
3	4.15 (2.9)	4.3	—	4.18 (4.7)	4.17 (4.8)

Table 7: Comparison of the peak positions (in Å) from this work and those obtained by other authors. The corresponding coordination numbers are given in parentheses where available.

peak between the second and third peaks, at approximately 3.9 Å (i.e. the position of the minima in the fit) which would account for the flatness of this region. It was felt, however, that there was not enough detail in the curves to justify the inclusion of an extra peak at this position.

Comparison of the fits for the first three peaks of the two samples shows good agreement especially for the first peak. These results show that the samples are effectively identical in their local correlations (<5 Å) and that the structural differences arise in the intermediate range (5–15 Å).

4.4 Discussion

Table 7 shows a comparison of the first three peak positions obtained by Beyeler [67], Elliott [74] and Krebs [64] and the coordination numbers where available. This table shows the lack of consistency amongst the previous results. The most major discrepancy is that of the coordination numbers of the peaks found by Beyeler, who assumed an arbitrary background level to obtain his peak heights. In the discussion section of his paper he then scales all of his coordination numbers to give the first peak a coordination number of three, whilst making allowance for alterations in the experimental uncertainty. Having carried this out, he obtains coordination numbers of 3, 8 to 11 and 2 to 3. From a comparative graph in the Elliott paper it may be seen

Peak	r-P [63]	o-P [63]	m-P [65]	Sample 1	Sample 2
1	2.13 (3.0)	2.23 (3)	2.22 (3)	2.228 (2.8)	2.227 (2.9)
2	3.34 (3+6)	3.40 (8) 3.70(4)	3.46 (8.24)	3.48 (7.6)	3.46 (7.0)
3	—	3.99,4.25,4.38	3.97,4.13,4.50	4.18 (4.7)	4.17 (4.8)

Table 8: Comparison of the peak positions (in Å) for a-P from this work and those found in crystalline r-, o-, and m-P. The corresponding coordination numbers are given in parentheses where available.

that the second peak of Krebs and that of Elliott are very similar, suggesting that Elliott's second peak also has a coordination number of around 8. It is important to note that the samples used in the previous experiments were made using different methods and this is probably a major factor in the differences shown. The results from this study are closest to those obtained by Elliott. The samples used for this study were from the same source as those used in Elliott's study and this may be the main reason for this similarity. The coordination number of the second peak is an important feature of these results. It was suggested by Elloitt it may be possible to explain the structure of a-P in terms of a three-fold continuous random network. This network predicts a second coordination number of 6 for a fully bonded network or $\sim$5 for a network with a first coordination number of 2.8. The results of all of the studies find a coordination number higher than this which indicates that there are both atoms connected to the origin atom via two bonds and atoms which are connected by a greater number than two bond (or not connected at all if the network is not continuous) at the second neighbour distance. This effect must be explained by any model proposed for a-P.

Table 8 show comparisons between the results of this analysis and those obtained from the crystalline r-, o-, and m-P states. It is clear from this table that a-P contains little or no r-P structure. The o-P and m-P crystalline allotropes are both very similar in their first three peaks and both could explain the structure seen in the

two samples. It could be argued, that of the two possibilities, the samples studied tend to be closer in nature to the m-P structure. It is more likely, however, that the local-order in the a-P samples is not the same as that found in the crystalline allotropes.

Recent work by Hohl and Jones [76,77] has suggested that a-P is made up of a network of P_n clusters, using a molecular dynamics/density functional method they obtained peak positions of 2.27, 3.55, 4.4 and 5.33 Å and coordination numbers of 3, 10.8, ~2 and ~20 respectively, for the first four peaks. At first sight the peak positions are all higher than those found in this study, however, there is a shift in the peak positions of the model of 1-2% due to the use of s-nonlocality in the pseudo-potential. Taking this into account, the first two peaks are in reasonable agreement. The third peak fitted to the experimental spectra for sample 1, appeared to be at too low an r-value (see above). Allowing for this effect and the reduction in the peak position of the model brings these two peaks into agreement. The coordination number of the second and third peaks do not agree, although the sum of the two coordination numbers are reasonably close, indicating that the same total number of atoms lie beneath the two peaks. In the cluster model, the second peak is very wide (~twice the width of the experimental curve) and the third peak is very flattened, see figure 40, this is probably due to a much wider distribution of atom separations occurring in the model than in the real data. This in turn leads to greater difficulty in defining the peaks and their corresponding coordination numbers. The model also fails to produce the characteristic series of three peaks (peaks 4,5,6) seen in the data though this is probably due to the limited size of the cell, and number of atoms (124) used in the MD/DF calculations.

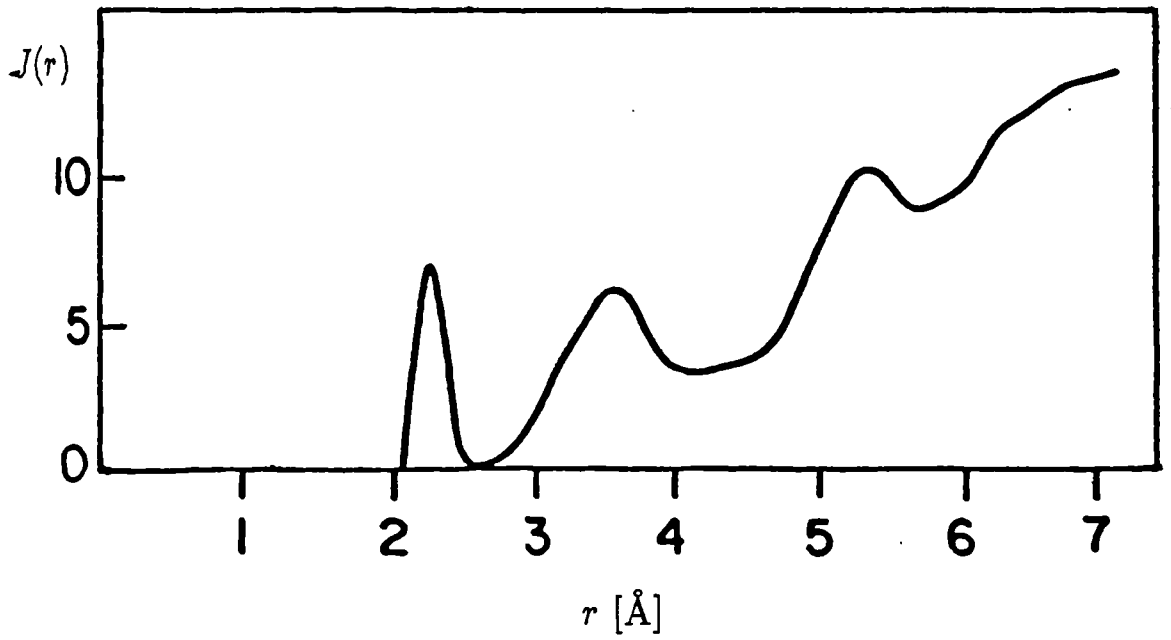

Figure 40: The radial distribution function obtained by Hohl [77] from an MD/DF simulation study of a model based on a network of P_n clusters.

also fails to produce the characteristic series of three peaks (peaks 4,5,6) seen in the data though this is probably due to the limited size of the cell, and number of atoms (124) used in the MD/DF calculations.

4.5 Conclusions

An experimental study has been carried out on two samples of a-P produced by thermal conversion of white P_4. The data obtained for the two samples shows a marked difference in the intermediate range order present, indicating differing degrees in the amount of polymerisation present. The experimental data have been used to calculate the total radial distribution function curves, $J(r)$, for the two samples. From these curves the peak positions and coordination numbers of the first three peaks were found. These peak positions have been compared to those

the sample. Despite the presence of these variations, all of the a-P samples show a similar degree of sharpness in the low-r peaks and a characteristic series of three peaks between 5 and 7Å. The comparison of the data with the crystalline allotropes of P shows that both the o-P and m-P forms have similar low-r features but, despite this similarity to a-P they do not explain all of the features found. The same is also true of the P_n cluster model. In this model the low-r features do not exhibit the sharpness found in the experimental data, indicating that it does not have the required degree of short-range order. The loss of intermediate-range order found between sample 1 and 2, whilst the short-range order was maintained, suggests that the differences found between the model and the samples cannot be explained in terms of the variations found within the samples. It has been suggested [77] that the quenching of the system in the molecular dynamics calculation is too fast and that a slower rate of quenching may develop the sharper peaks seen in the experimental data. Another field of interest is the changes which occur during the production of a-P from white P_4 and better understanding of a-P may well be found in a detailed investigation of this process.

Chapter 5

Neutron Scattering Studies of Antimony Pentafluoride

5.1 Introduction

The study of molecular liquids using neutron and X-ray diffraction provides a means of gaining detailed information on both the conformation of the molecule itself and on the spatial distribution of the molecules in the liquid phase. Interest in the structural properties of simple molecular systems has generally involved the study of either systems which interact via a well defined site-site potential (e.g. the tetrachlorides and tetrabromides) or in systems which show strong associative properties. Interest in the later class of liquids has been mainly concerned with those liquids which demonstrate hydrogen-bonding effects (e.g. water and the alcohols). In these liquids, the orientation of the molecules caused by the bonding plays a major role in the determination of the liquids properties. There are, however, other systems in which a simple molecule is involved in molecular association and of these

systems the phenomenon of fluorine-bridging offers an interesting field of inquiry. Antimony pentafluoride (SbF_5) is well suited for use in the investigation of fluorine-bridging using neutron diffraction techniques.

In the vapour phase the SbF_5 molecule has a bipyrimidical structure [78,79], figure 41a. In the liquid, it is thought that the planar triangle opens out to give a square structure corresponding to an octahedral unit, figure 41b. The ^{19}F NMR spectra of supercooled SbF_5 [80] and the vibrational spectra studies [81,82] suggest that the molecules are associated through cis-Sb–F–Sb bridges where the bridging fluorines are on adjacent corners of the square, rather than trans-bridging where the bridge-fluorines are on opposite corners of the square. For the molecule illustrated in figure 41b the atom F_{1a} corresponds to the fluorine bridging atom in the cis-bridged case and the atom F_1, the trans-bridging case. Other evidence for the association of the SbF_5 molecules is the high viscosity of the liquid (0.46 $N\,s\,m^{-1}$ at 20 °C). If the liquid consists of molecules, each of which is randomly associated with two more molecules, this high viscosity is presumably the result of the formation of chains of molecules of indeterminate length [81].

In the crystalline form (melting point 7°C) SbF_5 units have an octahedral co-ordination about the antimony atoms and are linked in cyclic tetramers via cis-bridging [83]. This form of structure has also been observed in NbF_5, TaF_5 and RuF_5 [84,85].

One previous neutron diffraction study of SbF_5 has been performed by M. S. Garawi [86]. This study analysed data collected with the sample at room temperature by comparing it to a variety of different models of SbF_5 in the liquid state and confirmed that the liquid is made up of cis-bridged chains. The following chapter continues this study by examining the temperature variation of the structure and

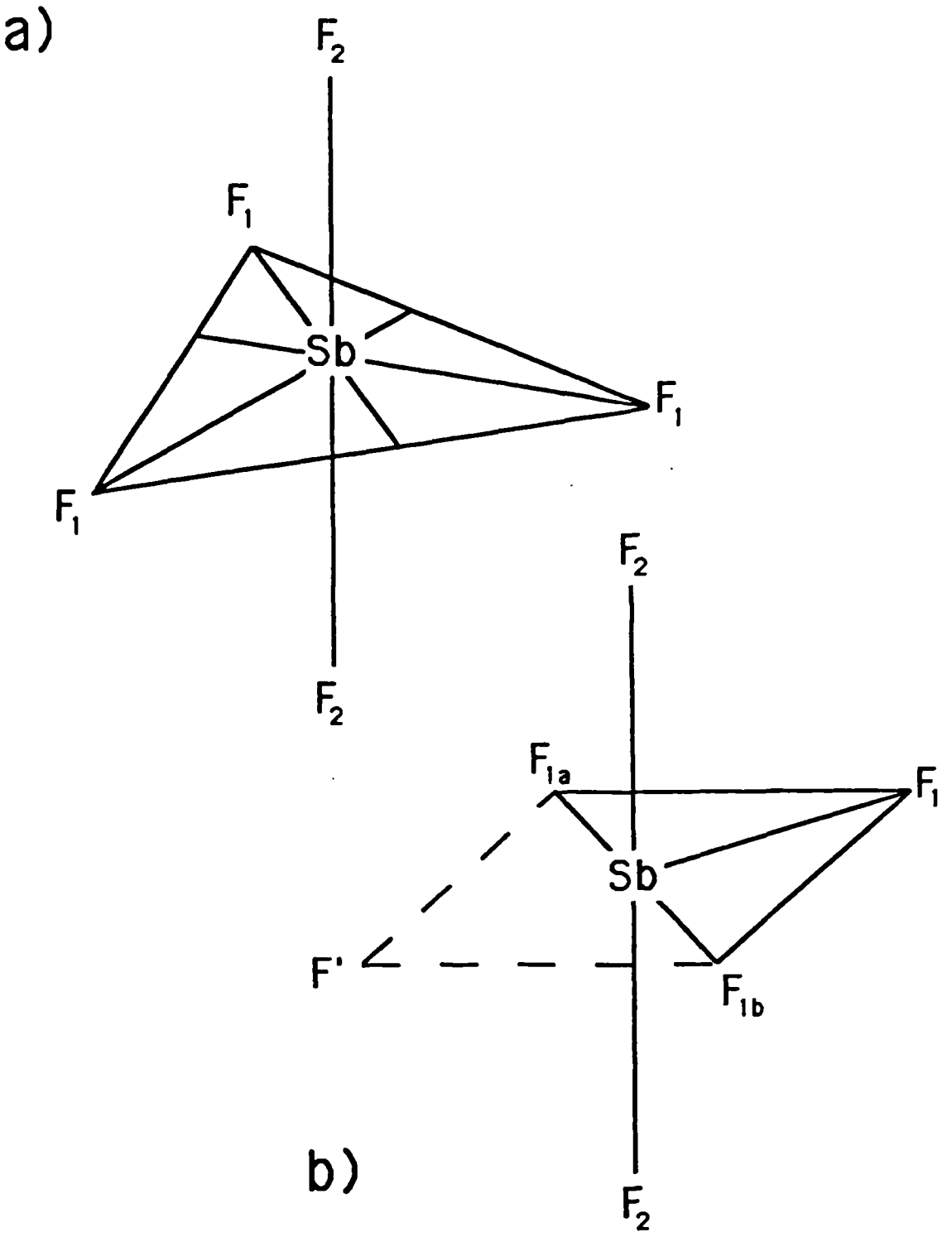

Figure 41: Conformation of the SbF_5 molecule in a) an isolated molecule the vapour state and b) after the molecule has opened out to form a fluorine bridge in the liquid state.

attempts to explain these changes in terms of the cis-bridged chain model. The data analysed here were originally collected by M. S. Garawi who kindly donated the raw data sets and experimental details.

5.2 The Experiment

Antimony pentafluoride is a highly reactive material and this makes the sample preparation and experiment particularly difficult. Due to the reactive nature of SbF_5 it is impossible to use either a metal or silica container. The presence of moisture in even minute quantities leads to the formation of HF and thus a container which is chemically inert to residual HF must be used. For these reasons the choice of container material is extremely limited and must by necessity be a fluorinated polymer. A fluorinated ethylene propylene copolymer (FEB-teflon) container was selected because it is readily available in the form of a suitable sized cylindrical tube whose ends are easily sealed by the application of heat and it demonstrates the required inertness and low porosity necessary to contain the sample.

The sample was prepared by Professor J. H. Holloway of the chemistry department of the University of Leicester. The Sb metal was fluorinated in a silica reactor and was purified by a trap-to-trap distillation in a dried and prefluorinated Pyrex apparatus and then placed in the sample container. This cell had an internal diameter of 4.0 mm and a wall thickness of 0.5 mm. The tube was sealed thus allowing the sample to be freely handled. The sample is a liquid at room temperatures, having a melting point of 7°C and a boiling point of 149.5°C.

The experiment was performed on the D4B diffractometer at the Institut Laue-Langevin (ILL), Grenoble, France (see Chapter 2). At the time of the experiment

the high theta arm of the instrument was out of commission and hence the measurements were taken using the low theta arm to scan the entire spectrum. Diffraction measurements were taken for the sample at temperatures of 5, 11, 20, 36, 55 and 80°C, for the sample cell at temperatures of 11 and 38°C and for the background at a temperature of 20°C. The 5°C dataset although it is 2°C below the melting point is still clearly liquid, this is possibly an error in the temperature measurement or may be due to a change in the melting point brought about by the presence of HF contamination. All measurements were made using an incident neutron wavelength of 0.695 ± 0.001 Å. The results were recorded in the form of the number of counts recorded in each cell of the detector bank as a function of angle. A program available at the instrument was then used to correct for the efficiency of each cell and group the data to form a single set of results which were corrected to a constant monitor count.

5.3 Data Reduction

The neutron counts from the sample were determined by subtracting the background count, I_b from the sample plus container count, I_{s+c+b}, and from the container count, I_{c+b} and then the container count was subtracted off of the 'sample plus container' count using the formalism developed by Paalman and Pings [58] which accounts for the self-shielding and absorption that occurs during the scattering process. After the application of the Paalman and Pings factors the resultant spectra was examined for any signs of residual peaks corresponding to peaks in the container spectra and the Paalman and Pings factors were refined to remove these. This small adjustment of the Paalman and Pings factors reflects the uncertainty in the parameters used to calculate the factors. Figure 42 shows the data before and after the subtraction

Material	Nuclear Mass / amu	b/fm	σ_{coh} / barns	σ_{incoh} / barns	σ_{abs} / barns
Sb	121.750	5.641	3.999	0.310	1.986
F	18.998	5.654	4.017	0.000	0.004
FEB – Teflon	—	—	24.918	80.832	0.143

Table 9: Neutron parameters for Sb, F and teflon (quoted for bound atoms [87,88]) at a wavelength of 0.7 Å.

of the container scattering. This figure also illustrates the effects arising from the dominant scattering contribution of the FEB-teflon container (see table 9).

The sample count was then converted from a function of the incident neutron wavelength, λ and scattering angle, ϕ, to a function of k using equation 1 and then k-binned into equal increments of 0.05 Å^{-1}.

5.4 Data Analysis

5.4.1 Correction for Departures from the Static Approximation

The total scattering must be corrected for departures from the static approximation and normalized to give the differential scattering cross section in units of barns/steradian/molecule. This is done by calculating the first order correction to the self term [25,18] and then multipling the data by a constant such that the resultant cross section oscillates about the calculated self term. The self term for SbF_5 , with the first order correction applied, is given by

$$\frac{d\sigma}{d\Omega}^{self}(k) = \left(b_{Sb}^2 + 5b_F^2\right)\left\{1 - \frac{\alpha_d}{M_{eff}}\left[\left(\frac{\lambda k}{4\pi}\right)^2 - \frac{k_B T}{2E_0}\left(1 + \beta_d\left(\frac{\lambda k}{4\pi}\right)^2\right)\right]\right\} \quad (126)$$

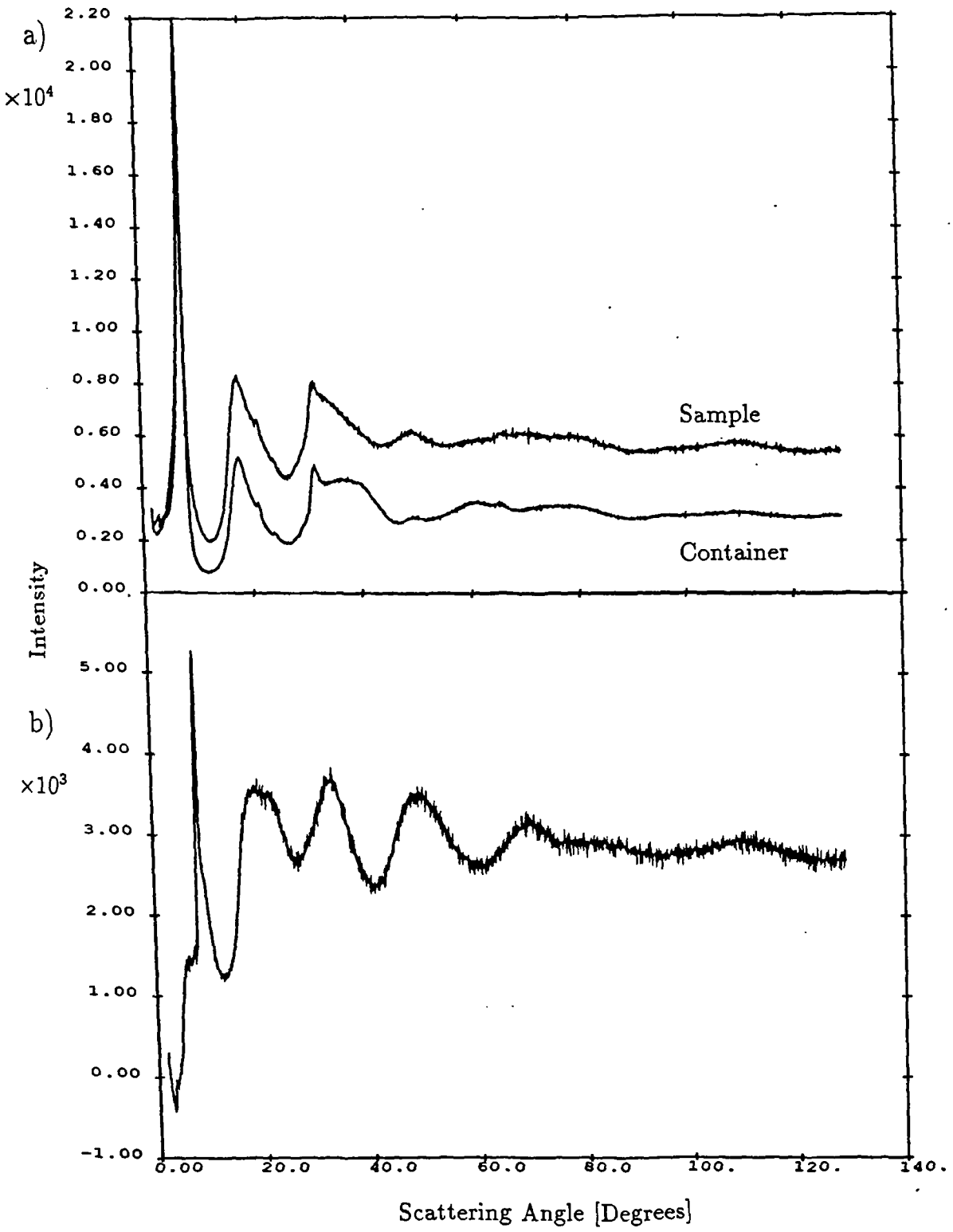

Figure 42: The scattering intensity recorded for liquid SbF_5 at a temperature of 20°C and an incident wavelength of 0.7 Å and the corresponding spectra after the subtraction of the teflon container scattering.

where b_{Sb} and b_F are the coherent scattering lengths of the antimony and fluorine nuclei, α_d and β_d are constants for the detector response and are equal to 3.54 and -1.5894 respectively and M_{eff} is the effective mass of the SbF_5 molecule, in the free atom limit, is given by

$$\frac{b_{Sb}^2 + 5b_F^2}{M_{eff}} = \frac{b_{Sb}^2}{M_{Sb}} + \frac{5b_F^2}{M_F} \tag{127}$$

where M_{Sb} and M_F are the nuclear masses of Sb and F respectively. This formula is only applicable to the pure liquid. In general some HF will be present in the sample and this will lead to a smaller effective mass being needed to calculate the self-scatter. The exact amount of HF present in the sample was unknown and to allow for the effects of its presence the parameter M_{eff} was varied during the fitting of the data to the molecular form-factor (see below) so as to obtain the best fit possible. At this stage a normalization constant was introduced such that after multiplication of the data by the constant the high k part of the data oscillated about the self-scattering. Figure 43 shows the 20°C data set and the fitted self-scattering.

5.4.2 The Molecular Form-Factor

After removal of the self-scattering from the collected spectra, only the interference term is left as the spectra do not need to be corrected for inelasticity effects because of the large mass of the molecule. The interference term is made up of two components, these being the intra-molecular component arising from pairs of atoms within the molecule and the inter-molecular component arising from pairs of atoms on separate molecules.

$$\frac{d\sigma}{d\Omega}^{int}_{obs}(k) = \frac{d\sigma}{d\Omega}^{int}_{intra} + \frac{d\sigma}{d\Omega}^{int}_{inter} \tag{128}$$

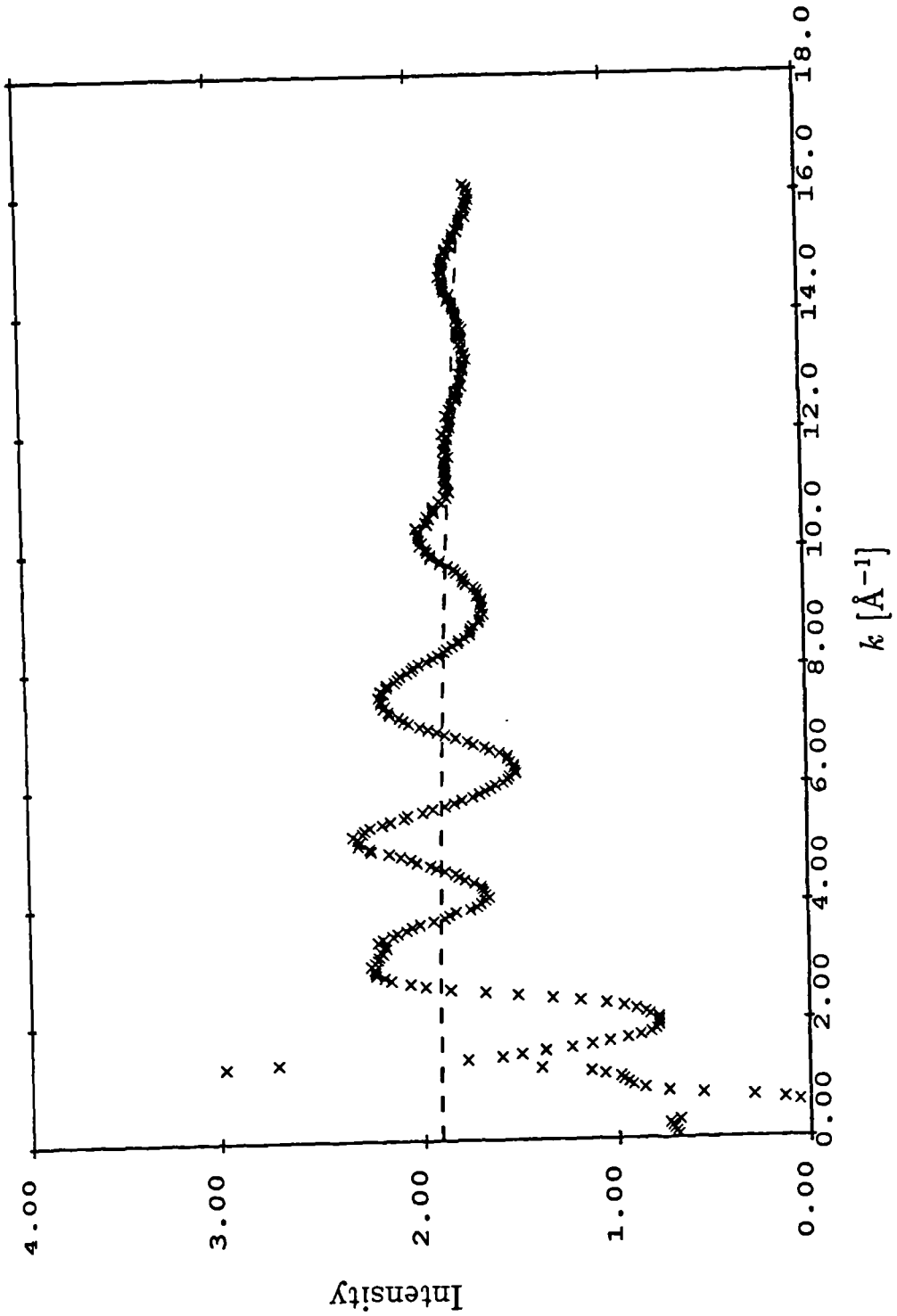

Figure 43: The normalized 20°C SbF_5 data set and the fitted self-scattering term.

From equations 73 and 72 it can be seen that the intra-molecular interference cross section is given by

$$\frac{d\sigma}{d\Omega}^{int}_{intra}(k) = \left(\sum_i b_i\right)^2 F_M(k) - \sum_i b_i^2 \tag{129}$$

where $F_M(k)$ is the molecular form-factor and the summations are for all atoms in the molecule. The second term in equation 128 is the intermolecular contribution to the interference term which may be expressed in terms of the function $D_M(k)$, thus giving

$$\frac{d\sigma}{d\Omega}^{int}_{obs}(k) = \left(\sum_i b_i\right)^2 \left[F_M(k) - \frac{\sum_i (b_i^2)}{(\sum_i b_i)^2} + D_M(k)\right] \tag{130}$$

Rearranging this equation yields

$$\left(\sum_i b_i\right)^2 D_M(k) = \frac{d\sigma}{d\Omega}^{int}_{obs}(k) - \left(\sum_i b_i\right)^2 \left[F_M(k) - \frac{\sum_i (b_i^2)}{(\sum_i b_i)^2}\right] \tag{131}$$

Thus the inter-molecular scattering may be obtained from the observed scattering provided the intra-molecular contribution is accurately known. A number of different molecular conformations was tried by Garawi and the form-factor resulting from each was fitted to the high-k region of the observed data (> 7 Å) where only short range correlations will be present i.e. those corresponding to intra-molecular distances. He found that to obtain a good fit to the observed data it was necessary to open out the planar atoms as shown in figure 41b and also to include the bridging fluorine of the next molecule into the form-factor as this lies at a similar distance, from the central Sb atom, to the molecules own bridging fluorine. It was also found that extending the bond lengths of the bridged fluorines and adopting a cis-bridged molecule as opposed to a trans-bridged molecule led to an improved fit. In the light of these results it was decided to adopt a similar model as a starting point for this investigation. The molecule used to obtain the form-factor is shown in figure 44.

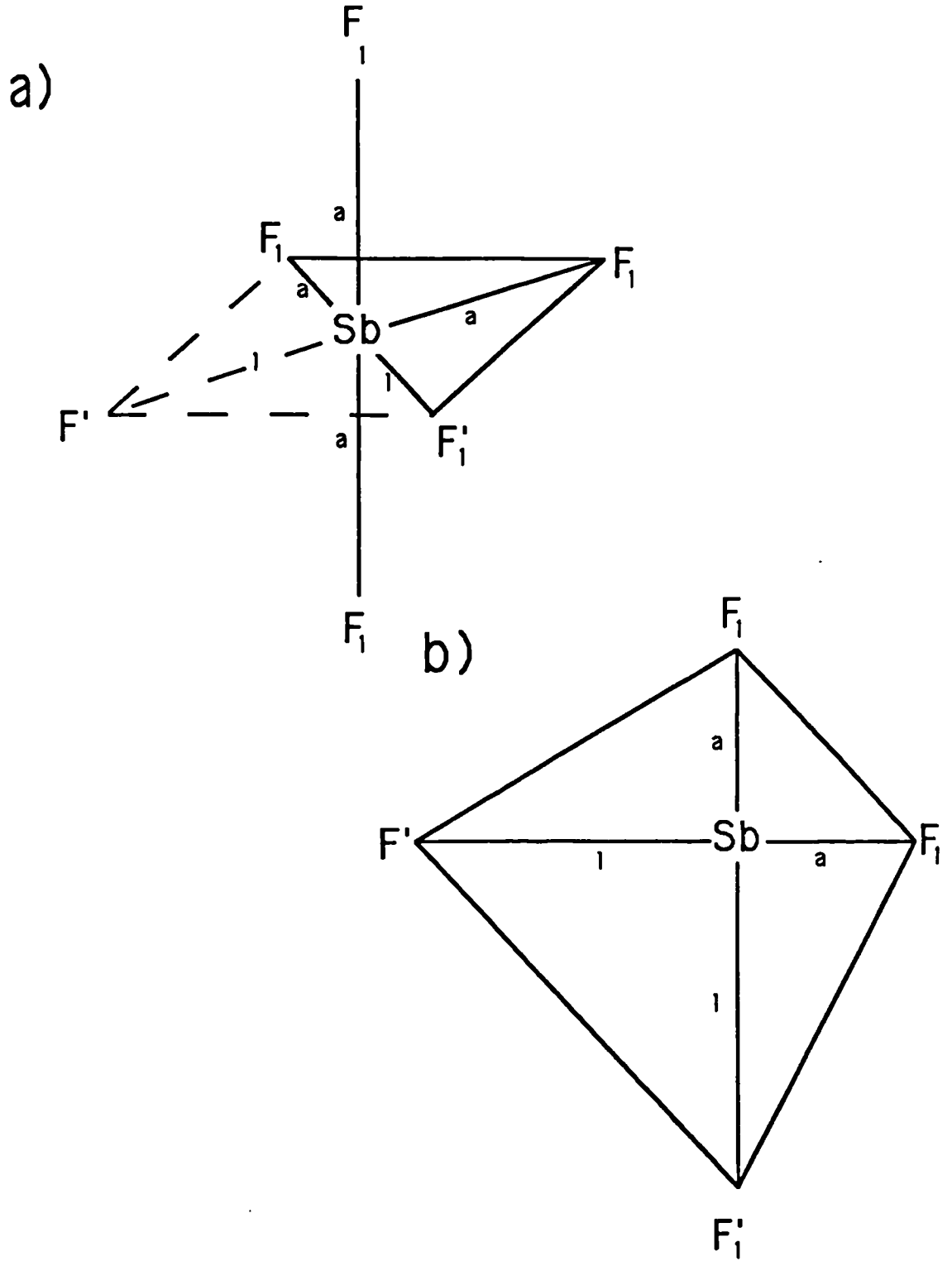

Figure 44: a) Conformation of the SbF_5 molecule used to calculate the form factor and b) plan view showing the distortion of the planer square caused by the extended bond lengths associated with the cis-bridging

In Garawi's study the bond lengths corresponding to the Sb-F_1 and Sb-F_2 bonds (figure 41a) were found to differ by less than 0.3% and hence it was decided to treat all non-bridged fluorine atoms as identical. The two bridging fluorines were initially treated entirely independently allowing the non-bonded fluorine (F′) to have a different distance from the Sb atom and different Debye-Waller damping factors to the bonded bridging atom. Fitting was also attempted using the same parameters for both bridging atoms and it was found that this did not significantly reduce the 'goodness' of the fit. Due to this, it was decided to treat both atoms as identical throughout the study thereby reducing the number of variables in the fitting routine and hence speeding the analysis. All of the primary bond angles were fixed at 90°. Thus the SbF_5 form-factor used to fit the data was

$$\begin{aligned} F_M(k) &= \frac{1}{(b_{Sb}+5b_F)^2}\Big[b_{Sb}^2+5b_F^2+8b_{Sb}b_F j_0\{ak\}\exp\left\{-\gamma_{SbF}k^2\right\} \\ &+ 4b_{Sb}b_F j_0\{lk\}\exp\left\{-\gamma_{SbF'}k^2\right\}+2b_F^2 j_0\{2ak\}\exp\left\{-\gamma_{FF}k^2\right\} \\ &+ 10b_F^2 j_0\left\{\sqrt{2}\,ak\right\}\exp\left\{-\gamma_{FF}k^2\right\}+4b_F^2 j_0\{(a+l)k\}\exp\left\{-\gamma_{FF'}k^2\right\} \\ &+ 12b_F^2 j_0\left\{\sqrt{a^2+l^2}\,k\right\}\exp\left\{-\gamma_{FF'}k^2\right\}+2b_F^2 j_0\left\{\sqrt{2}\,lk\right\}\exp\left\{-\gamma_{F'F'}k^2\right\}\Big] \end{aligned} \tag{132}$$

where $j_0(x)$ is the zero order spherical Bessel function and is given by

$$j_0(x)=\frac{\sin x}{x} \tag{133}$$

F represents the non-bridged fluorine at a distance a from the central Sb atom and F′the bridged fluorine at a distance l. The γ_{ij} terms are the damping factors due to molecular motion, and b_i is the bound coherent scattering length of the atom i (see table 9).

The six datasets were fitted using a least-squares-fit algorithm. The fit was made from $k = 7$ Å^{-1} to the full range of the data ($k = 16.15$ Å^{-1}). A lower limit of

Parameter	Temperature					
	5°C	11°C	20°C	36°C	55°C	80°C
Sb — F (Å)	1.836	1.838	1.837	1.837	1.836	1.837
Sb — F′ (Å)	2.071	2.072	2.070	2.074	2.065	2.067
M_{Eff} (amu)	14.65	15.16	15.42	14.41	14.92	14.94
γ_{Sb-F} ($\times 10^{-3}$ Å)	2.37	2.49	2.40	2.67	2.65	2.61
$\gamma_{Sb-F'}$ ($\times 10^{-3}$ Å)	6.46	6.46	6.46	6.46	6.46	6.46
γ_{F-F} ($\times 10^{-3}$ Å)	4.75	4.34	4.51	4.61	5.29	4.94
$\gamma_{F-F'}$ ($\times 10^{-3}$ Å)	8.07	8.85	9.18	9.18	8.90	9.34
$\gamma_{F'-F'}$ ($\times 10^{-3}$ Å)	10.65	10.65	10.65	10.65	10.65	10.65

Table 10: Parameter values used in the form-factor fit to the observed differential scattering cross-section for the various sample temperatures.

7 $Å^{-1}$ was selected because above this point only the short intramolecular distances should be present in the interference function. For all six datasets the same set of starting parameters and constraints were used. The results are shown in table 10. Fits for the 5°C, 20°C and 80°C data sets are shown in figures 45 to 47.

It is clearly seen from the results in table 10 that there is remarkably little variation in the antimony – fluorine bond lengths. This is especially true for the bond length of the non-bridged fluorine atoms. The results for the 20°C show good agreement with those obtained by Garawi (1.83 Å and 2.04 Å respectively for the non-bridged and bridged bonds) and those found by Edwards [83] for the solid tetramer (1.82 and 2.02 Å). In the solid, the SbF_5 molecules are found to form a tetramer ring structure with cis-bridging, but having non-linear bridges. These bridges have two distinct angles of 140°and 170°(see figure 48). Thus it would appear that the local geometry is relatively unchanged between the crystalline and the liquid states up to a temperature of at least 80°C. It is possible however that the increase in the Sb–F′ bond (2.02 for the tetramer, 2.07 in this study) is an indication that the tetramer has opened out to form a more loosely bonded chain

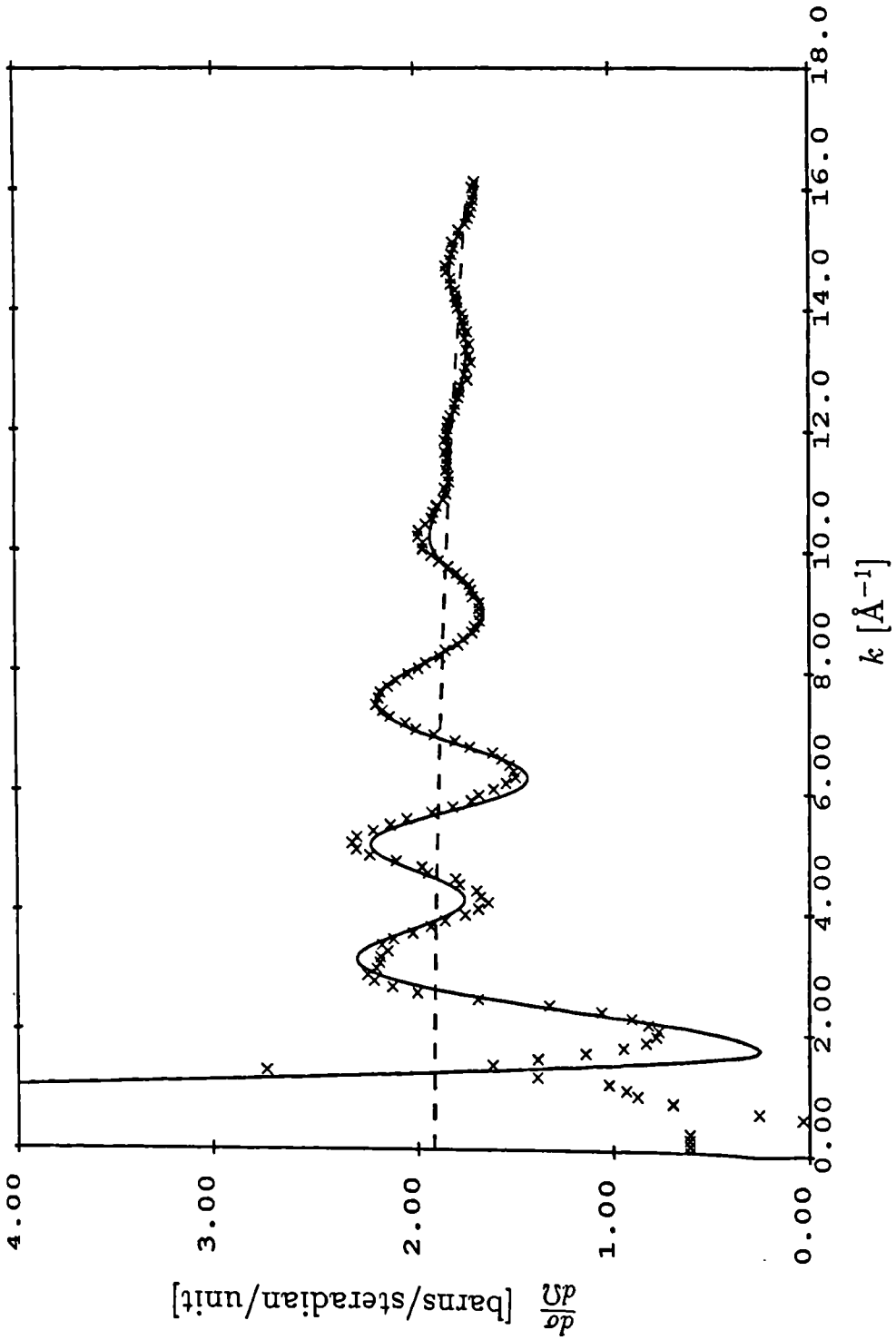

Figure 45: The observed differential cross-section for liquid SbF_5 at 5°C (×××), and the form-factor fit to the data (—) using the parameters listed in table 10. The dashed line is the differential self-scattering obtained using equation 128. For clarity only every other data point is displayed.

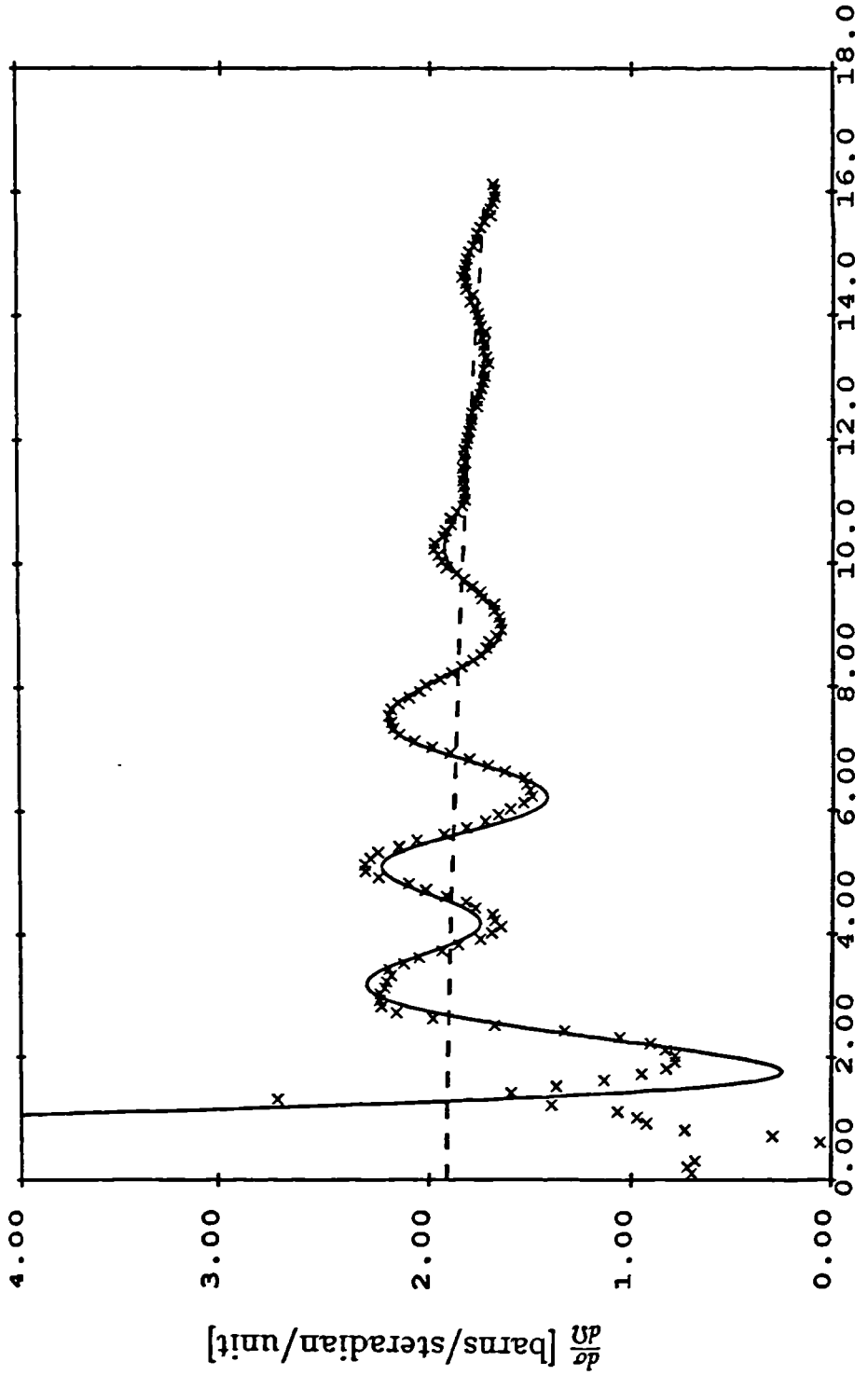

Figure 46: The observed differential cross-section for liquid SbF_5 at 20°C (×××), and the form-factor fit to the data (—) using the parameters listed in table 10. The dashed line is the differential self-scattering obtained using equation 128. For clarity only every other data point is displayed.

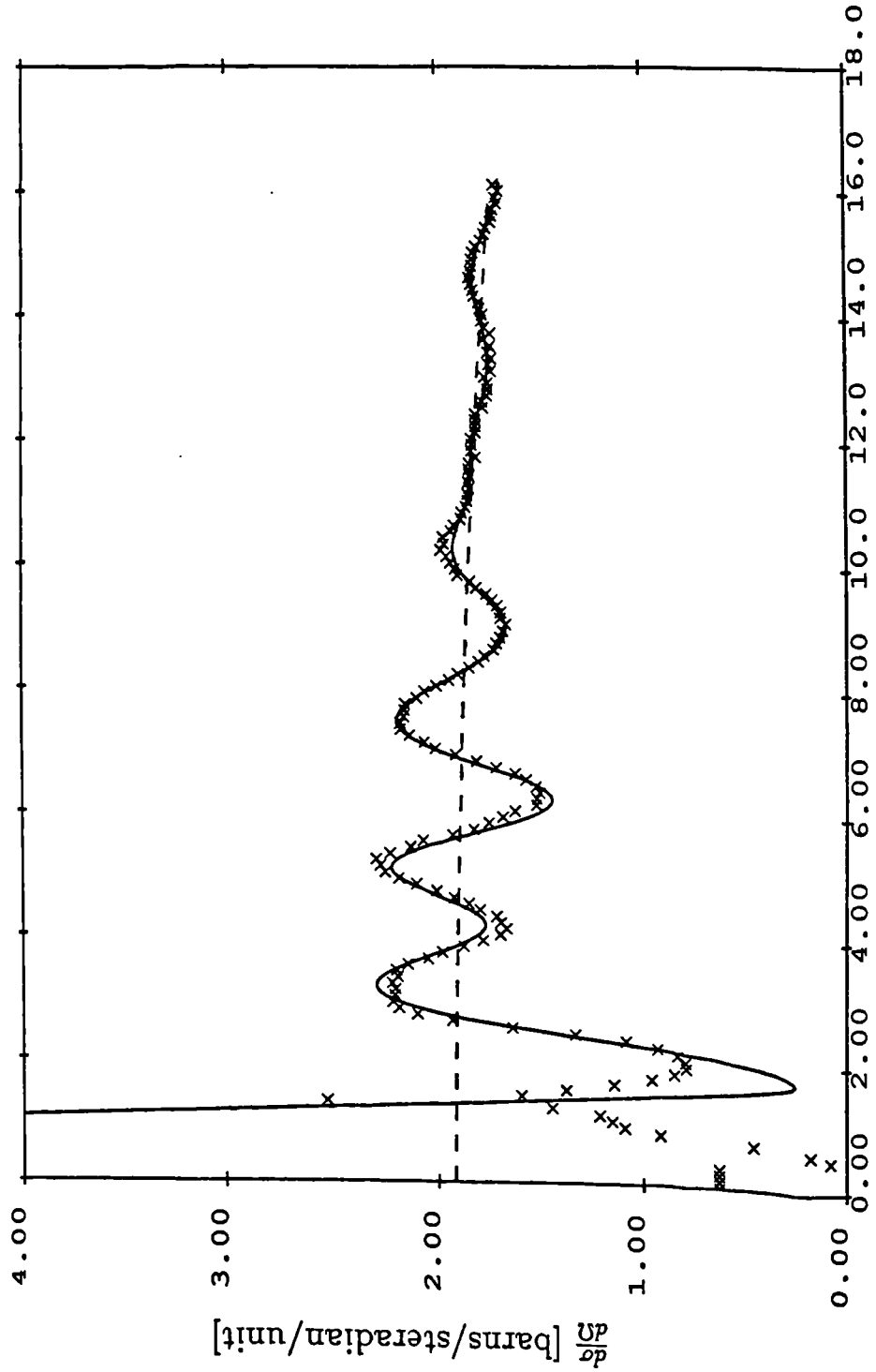

Figure 47: The observed differential cross-section for liquid SbF_5 at 80°C (×××), and the form-factor fit to the data (—) using the parameters listed in table 10. The dashed line is the differential self-scattering obtained using equation 128. For clarity only every other data point is displayed.

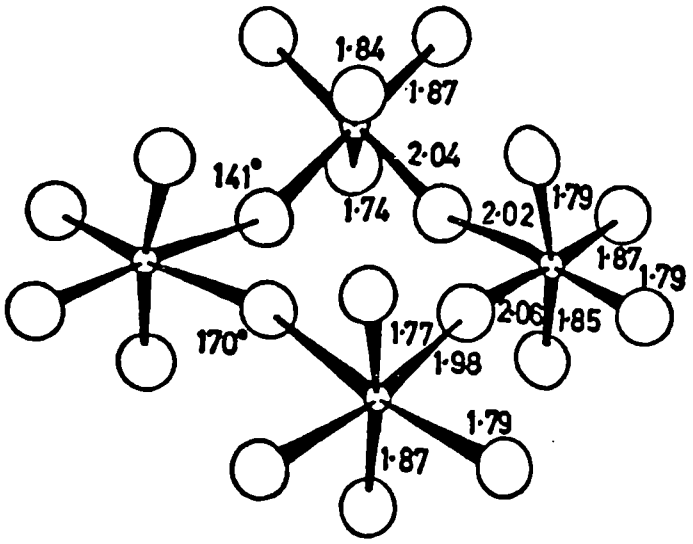

Figure 48: The inter-molecular structure for SbF_5 units showing the four-fold puckered cis-bridged tetramer form of the crystalline solid. The value of the distances are in ångstöm.

structure.

The effective masses found in the fit determine the fall off in the self scattering contribution. If the antimony and fluorine atoms are considered to be free during the neutron scattering process, the effective mass of each nucleus will be equivalent to it's nuclear mass and, from equation 129, the effective mass for the SbF_5 molecule is 21.2 amu. The result of the experiment is noticeably lower than this and surprisingly it is also lower than Garawi's result of 18.7 amu. Both his experiment and the present one were carried out on the same sample but were separated by at least a year. The difference in the effective mass may possibly be explained by an increase in the level of HF contamination in the sample. It is unclear how much HF is present but from the results obtained it would appear to be less than 0.5%.

The gamma factors are, as one would expect, smallest for the non-bridged fluorines. The large values associated with the bridged fluorine being related to the relative motion of the two molecules causing increased vibration of the bridging fluorine. The values of $\gamma_{SbF'}$ and $\gamma_{F'F'}$ are the same for all data sets because these values have floated to their upper limits in the course of the fit. Allowing the values of these two Debye-Waller factors to increase further led to no significant improvement in the χ^2-value for the fit and due to this the constrained values were accepted for the final fit.

5.4.3 Inter-molecular Correlation

The inter-molecular information is contained in the $D_M(k)$ function and was extracted from the data using equation 131. The $D_M(k)$ functions obtained for the 5°C, 20°C and 80°C data sets are shown in figure 49. It is seen from this picture that there is very little change in the $D_M(k)$ function with temperature and this is indicative of the presence of only very small changes in the inter-molecular structure of the liquid. The Fourier transform of the $D_M(k)$ function yields the inter-molecular distribution function, $d_L(r)$, which is given by equation 79 as

$$d_L(r) = 4\pi\rho_M r\,[g_L(r) - 1] \quad (134)$$

$$= \frac{2}{\pi}\int_0^\infty k D_M(k) \sin kr \; \mathrm{d}k \quad (135)$$

where ρ_M is the molecular number density, r is the distance from the origin atom and $g_L(r)$ is the inter-molecular pair-correlation function. The limits of the transformation are zero and infinity, however, the real data has a range of only 0 to $k_{max} = 16.15$ Å^{-1} which introduces an upper limit of k_max into the above integral.

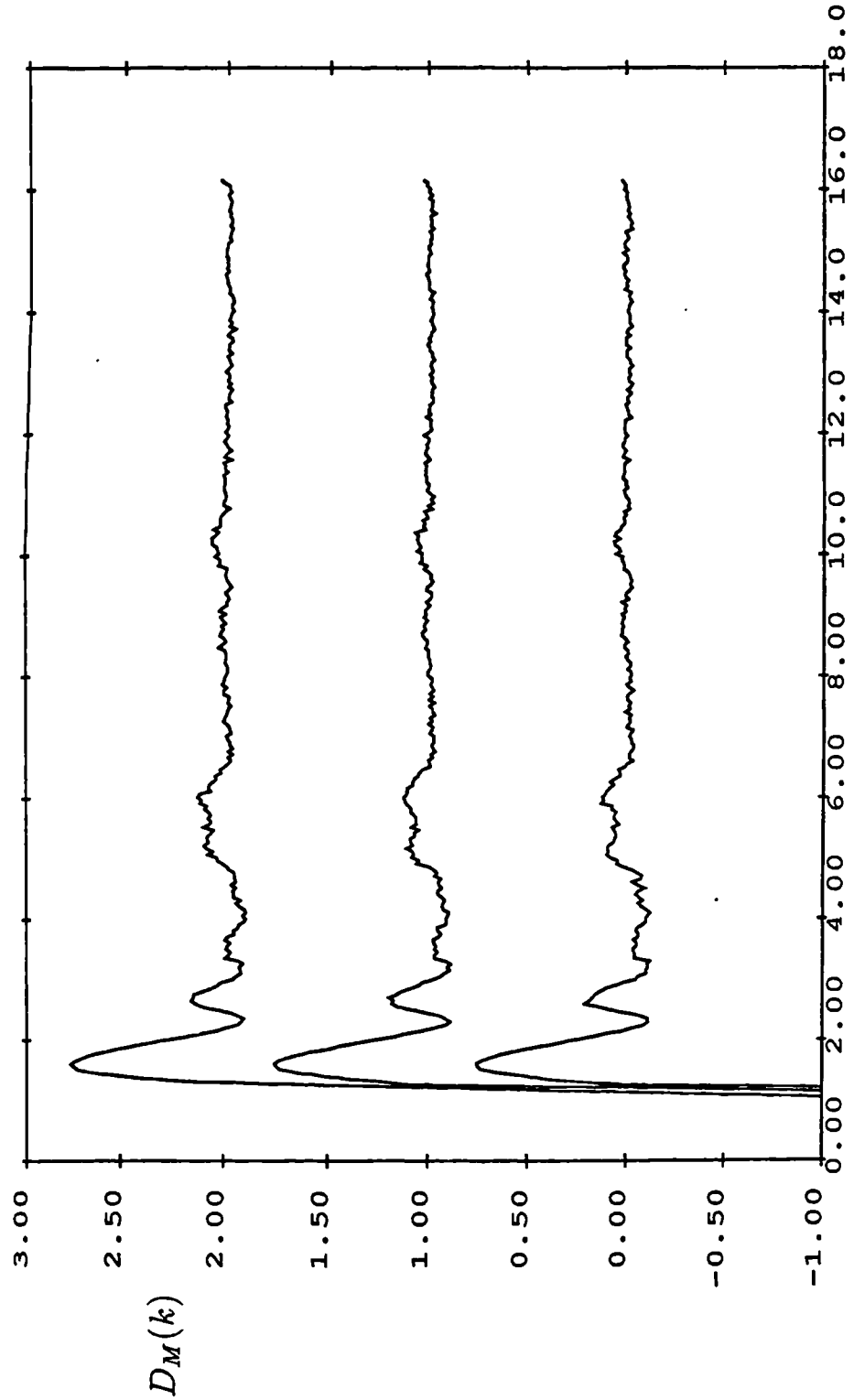

Figure 49: The inter-molecular function, $D_M(k)$, obtained for liquid SbF_5 at 5°C (bottom), 20°C (centre) and 80°C (top).

The effect of the imposition of a finite upper limit is generally to introduce 'truncation ripples' into the $d_L(r)$ function, these occur as small oscillations superimposed onto the actual $d_L(r)$ curve. To reduce the effect of these ripples a modification function, $M(k)$, is introduced into the transform. This function ensures that the data tend to zero as k tends to k_{max}. The function chosen was

$$\begin{aligned} M(k) = j_0\left(\tfrac{\pi k}{k_{max}}\right) \quad &\rightarrow 1 \quad \text{as} \quad k \rightarrow 0 \\ &\rightarrow 0 \quad \text{as} \quad k \rightarrow k_{max} \end{aligned} \tag{136}$$

Thus the $d_L(r)$ function becomes

$$d_L(r) = \frac{2}{\pi}\int_0^{k_{max}} kD_M(k)M(k)\sin kr \; \mathrm{d}k \tag{137}$$

The total radial distribution, $d(r)$, may be obtained by Fourier transforming the total interference pattern instead of only the interference term. The curve produced using this transform will contain both the intra- and inter-molecular distances occurring in the liquid. It is useful to compare the $d(r)$ and $d_L(r)$ curves as this gives an indication of the validity of the molecular form-factor fit. For a 'good' fit the sharp low r features of the total radial distribution will be absent in the $d_L(r)$ plot and in this region the resultant curve will follow the density line $(-4\pi r\rho_M)$ of the sample. The total and inter-molecular radial distribution functions for the 5°C, 20°C and 80°C data sets are shown in figures 50 to 52. It is clearly seen in these diagrams that the sharp features in the low-r region of the $d(r)$ curve have been removed with the exception of a peak at $\sim$ 1.25 Å and a second peak at $\sim$ 2.5Å. The shortest bond length in the SbF_5 molecule is the Sb–F distance of 1.83 Å which indicates that the 1.25 Å peak is spurious. The second peak at 2.6 Å is followed by a minimum at $\sim$2.9 Å, these features lie below the main peak in the $d(r)$ curve corresponding to the F–F bond length. This major peak is actually a composite peak

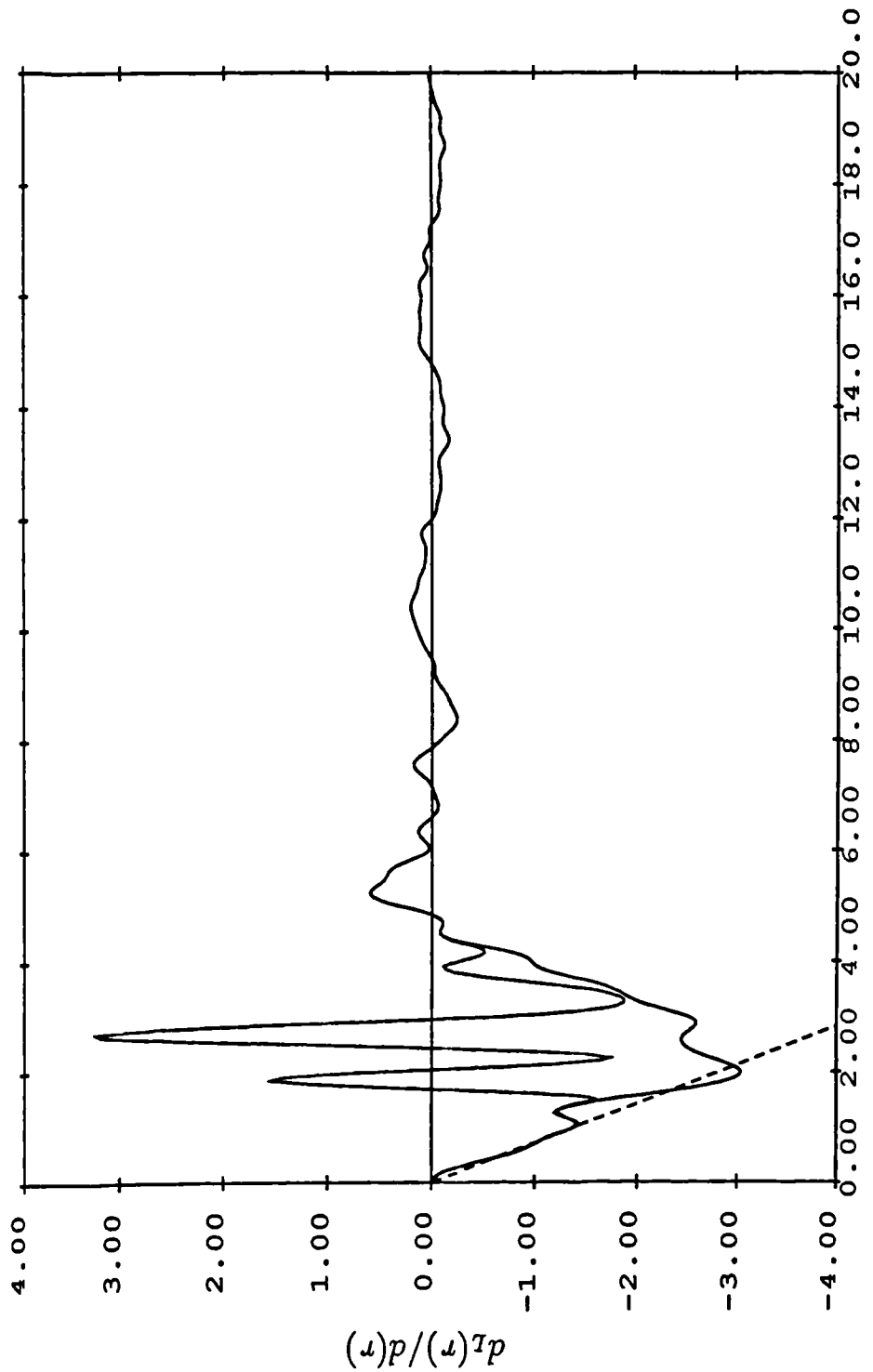

Figure 50: The total and inter-molecular radial distribution functions ($d(r)$ and $d_L(r)$ respectively) for liquid SbF_5 at 5°C. The dashed line represents the density line ($-4\pi r\rho_M$).

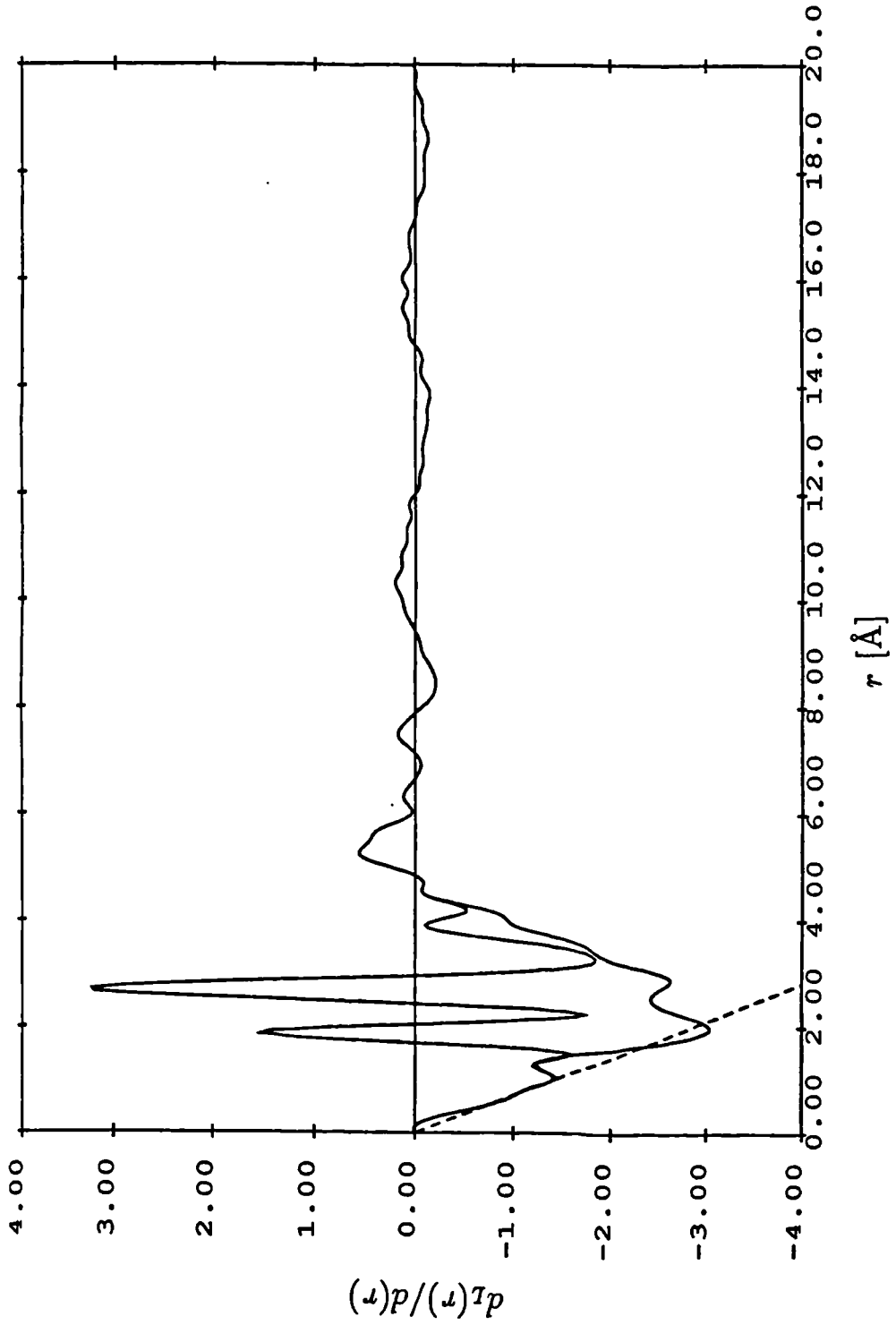

Figure 51: The total and inter-molecular radial distribution functions ($d(r)$ and $d_L(r)$ respectively) for liquid SbF_5 at 20°C. The dashed line represents the density line ($-4\pi r\rho_M$).

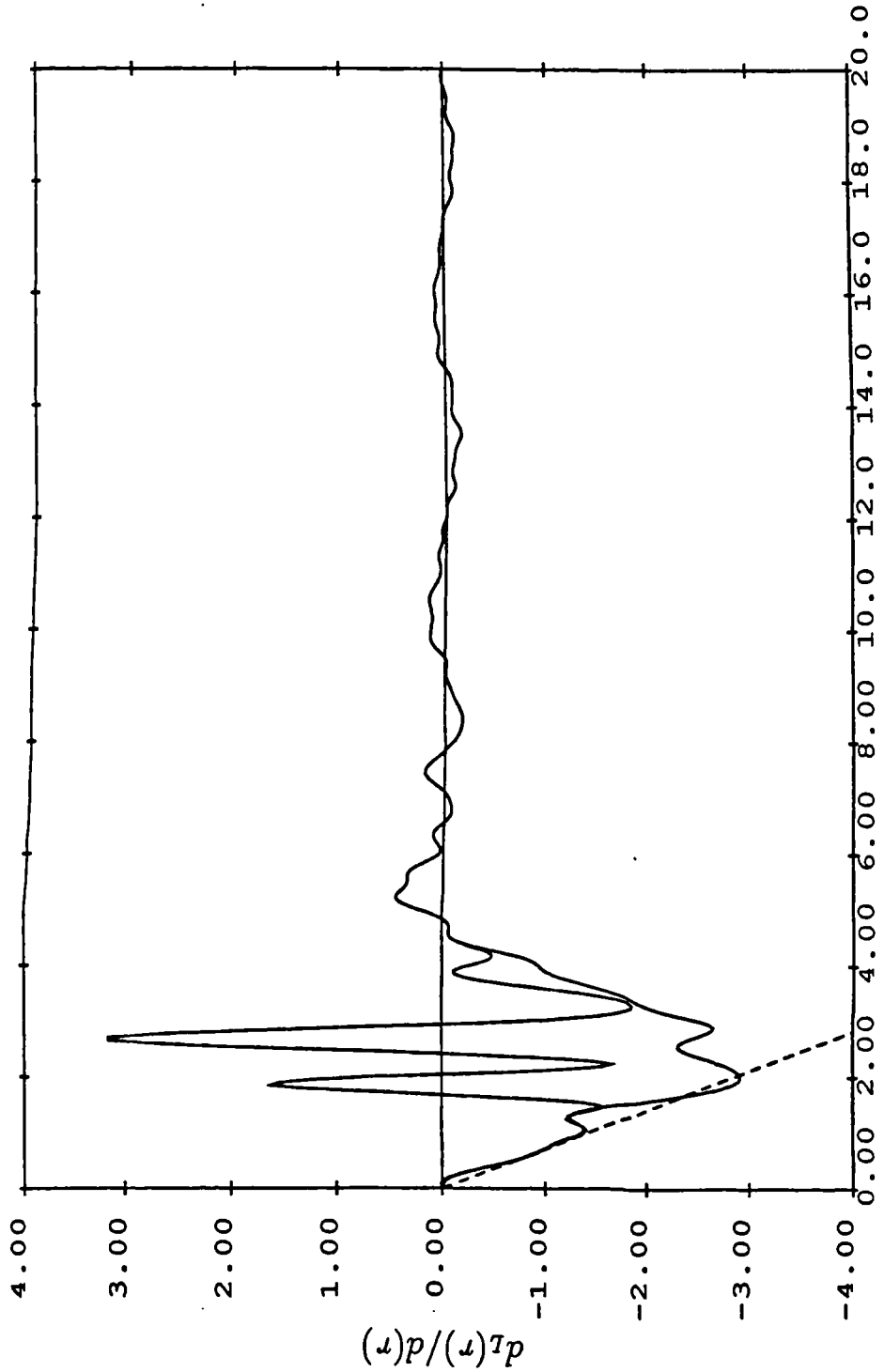

Figure 52: The total and inter-molecular radial distribution functions ($d(r)$ and $d_L(r)$ respectively) for liquid SbF_5 at 80°C. The dashed line represents the density line ($-4\pi r\rho_M$).

composed of the FF peak at 2.59 Å the FF′ peak at 2.7 Åand the F′F′ peak at 2.9 Å. In fitting the data the Debye-Waller factors for the F′F′ peak were constrained the effect of which is to constrain the width of the corresponding peak in real space. Broadening this peak has the effect of moving the composite peak position towards the left thus reducing the amplitudes of the minima and maxima occurring in the $d_L(r)$ curve in this region, this indicating that these effects are caused by errors in the fitted Debye-Waller factors. Reduction of the 2.6 Å maximum may also be produced by reducing the width of the FF peak. The constraint of the Sb–F′ Debye-Waller factor is the probable cause of the $d_L(r)$ curve dropping below the density line at $\sim$ 2 Å. The 2 Å peak in the $d(r)$ curve is a composite peak formed from the SbF and SbF′ peaks. Broadening of the SbF′ peak will reduce the composite peak height making the peak broader and moving its position very slightly to the left thus bringing the $d_L(r)$ curve closer to the density line.

5.4.4 A Molecular Model for Antimony Pentafluoride

Garawi produced a number of different models for SbF_5 using a variety of different chain structures; of these he concluded that a cis-bridged chain gave the closest correspondence between the position of the peaks in his data and the distances occurring in his model. To perform the comparison he used a histogram plot of the number of atom pairs against the pair separation. In continuing this work Garawi' final model was adopted as a starting point (figure 53) and a Gaussian width was calculated to give the resultant distribution an appearance which approximates that of the $d(r)$ function. To calculate this curve, firstly, the co-ordinates of each of the atoms in the model chain were calculated. To do this, the co-ordinates of a basic chain unit of three molecules were found and then a chain of the desired length (30

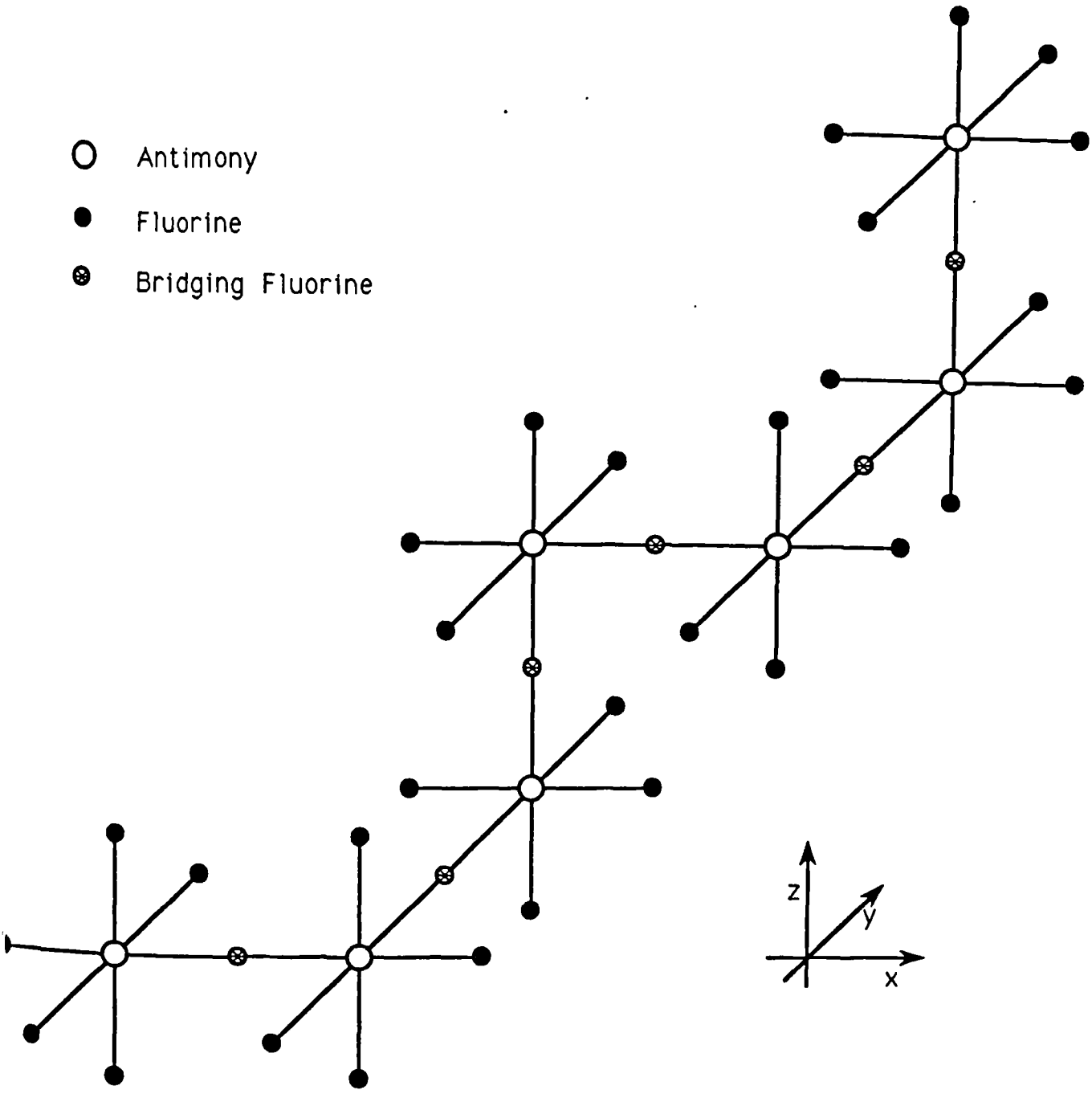

Figure 53: The starting model for the SbF_5 chain structure, showing six SbF_5 molecules linked in a cis-bridged helical spiral.

molecules in this case) was create by applying appropriate linear transformations to the basic unit. Following this, the distances from each atom in the end molecule, to every other atom in the chain were calculated and Gaussian peaks were calculated centred upon these distances. These peaks were then summed together to give the required distribution.

To calculate the Gauss distribution associated with a particular atom pair having a separation, d, the formula used was

$$f(r) = \frac{1}{\sigma\sqrt{2\pi}} \exp\left\{-\frac{1}{2}\left(\frac{r-d}{\sigma}\right)^2\right\} \tag{138}$$

where the separation, d, is the mean (or centre) of the distribution and σ is its standard deviation (width). For this model it was assumed that the width of the Gaussian was proportional to the atom pair separation. This is not strictly true as the width of the peak will depend upon which atoms constitute the pair, it should however give a reasonable approximation and will give a better indication of peak heights and positions, than that obtained from purely plotting the number of pairs occurring at each separation, because it allows for the convolution of adjacent peaks. The method chosen to scale the peak width was to simply multiply the pair separation by a constant, i.e.

$$\sigma = wd \tag{139}$$

where the scale factor w was chosen to be 0.05. Finally the calculated peak was multiplied by two to allow for the symmetry of the chain. This is because for each correlation appearing in the forward direction along the chain an equivalent correlation will occur in the opposite direction, provided that the chain is assumed to be semi-infinite (i.e. the effects of the ends of the chains are negligible).

The atom pair separation distribution, $N(r)$, is equal to the sum of the individual

Gaussian peaks and thus given by the equation

$$N(r) = \sum_{i=1}^{N_m} \sum_{j=i+1}^{N_c} \frac{2}{w d_{ij} \sqrt{2\pi}} \exp\left\{ -\frac{1}{2} \left(\frac{r - d_{ij}}{w d_{ij}} \right)^2 \right\} \tag{140}$$

where N_m is the number of atoms in a single molecule (6), N_c is the number of atoms in the chain and d_{ij} is the distance between atoms i and j. The calculated curve, $N(r)$ is analogous to the radial distribution function ($J(r) = 4\pi r^2 \rho_0 g(r)$) but only includes the correlations occurring within the chain. The function $N(r)$ may be transformed into the equivalent of a $d(r)$ curve, for the chain only, by using the relation

$$d_{ch}(r) = \frac{N(r)}{r} - 4\pi r \rho_0 \tag{141}$$

Unfortunately this relationship will scale both the intra- and inter- molecular contributions with respect to the density of the system whereas in actuality the intra-molecular terms are independent of the density, being only dependent on the conformation of the molecule, and as such should be unaltered. This leads to a distortion of the low r peaks which reduces the usefulness of the transform. Due to the lack of knowledge of the individual peak widths, it is only the peak positions which are of interest in this study, and for this reason all comparisons have been carried out using the $N(r)$ distribution. It should be noted that the $d_{ch}(r)$ curve has a $1/r$ dependence on the $N(r)$ curve and thus for all but the intra-molecular peaks, the peaks of the $N(r)$ curve will be r times the amplitude of the corresponding peaks in $d_{ch}(r)$.

Figure 54 shows the $N(r)$ function obtained from the cis-bridged chain shown in figure 53 and, for comparison, the $d(r)$ curve obtained from the 20°C dataset. As expected, there is exact agreement in the first two peak positions. The third peak should correspond to the SbSb distance and the related separations between

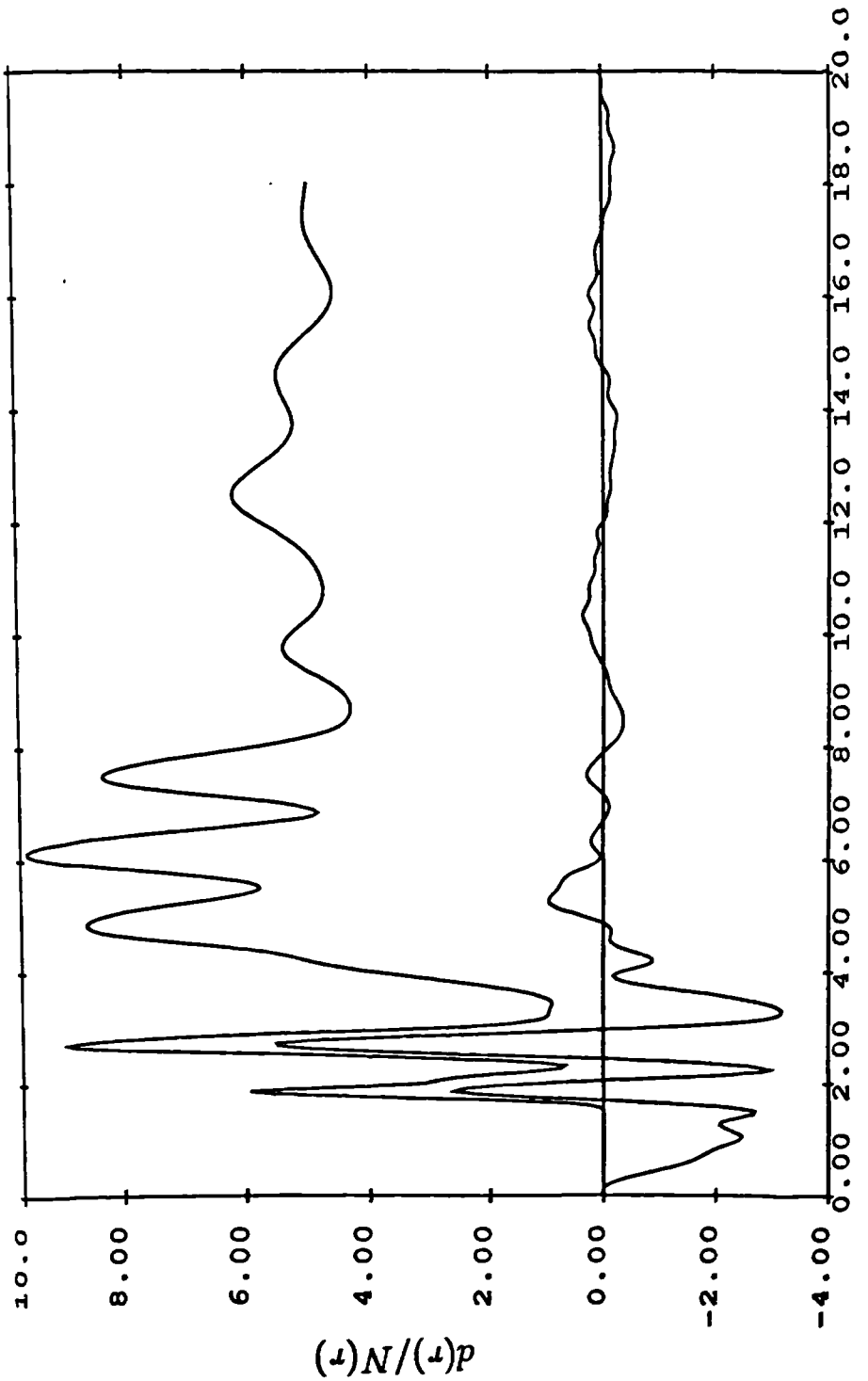

Figure 54: The $d(r)$ curve (lower) for SbF_5 and the $N(r)$ curve (upper) calculated for the basic SbF_5 cis-bridged chain

the atoms occurring in the two planes through the Sb atoms perpendicular to the bond. In the data, this peak occurs at 3.9 Å however, in the model it occurs at 4.8 Å. There is also no correlation between the third model peak and the fourth peak in the real data (5.25 Å) thus indicating that the model is significantly different from the real case and that the correlations that occur at higher-r are probably coincidental. From these results it can be concluded that Garawi's model is wrong even though it yielded the closest fit of any of the models he tried. As no other starting model could provide a better starting point it was decided to attempt to distort the chain and see if this could be used to move the peaks into a more agreeable position.

The 'Twisted' Chain

It is apparent from figure 53 that the cis-bridging produces a chain structure which is in the form of a helical spiral about the '111' axis. It may be further observed that it is possible to change the pitch of the spiral by introducing a series of rotations about the Sb–F′–Sb bonds. This rotation or 'twist' will either compress or stretch the chain. The twist is defined as shown in figure 55 such that when viewed along the bridge axis (SbF′Sb) from one molecule to the next in the chain a clockwise rotation is positive. Using this definition a positive rotation increases the helical pitch and thus, the length of the chain. In the limit, a twist of +90° changes the chain shown in figure 53 into a zig-zag chain with the central Sb atoms all lying in the xy plane. A negative rotation reduces the helical pitch and hence, shortens the chain. The limit in this case occurs when a rotation of -90° is applied to a chain of four atoms to generate a tetramer. A series of different twists were applied to the model and a selection of these from -40° to 40° in 10° steps are shown in figure 56. The vertical lines in this diagram indicate the positions of the peaks found in the

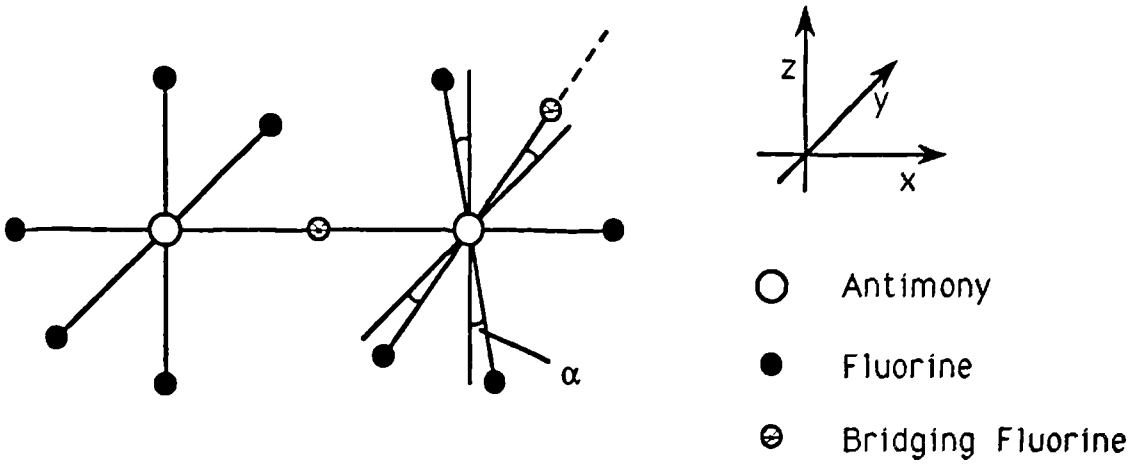

Figure 55: Two consecutive molecules in an SbF_5 chain showing the definition of the bond twist α

real data, for convenience these peaks will be referred to by the letters A to F. There is also a small peak occurring at 4.55 Å which has been omited from the graph as it is initially only the intention to explain the major peaks. This small peak will be referred to later.

From figure 56 it may be seen that applying a twist to the model does not effect the first two peaks. This is because these peaks are determined purely by the intra-molecular correlations, thus, the first peak of significance is the third peak in the distribution. It is clearly shown in the figure that applying either a positive or negative twist to the chain moves the third peak towards lower-r, however, this peak never moves low enough to reach the position of peak D. Simultaneously the fourth peak, in the model, moves outward and a smaller peak appears between the third and fourth peaks in approximately the position of peak D. Only in the non-twisted chain is there ever a peak at position F. These results show that at no twist angle

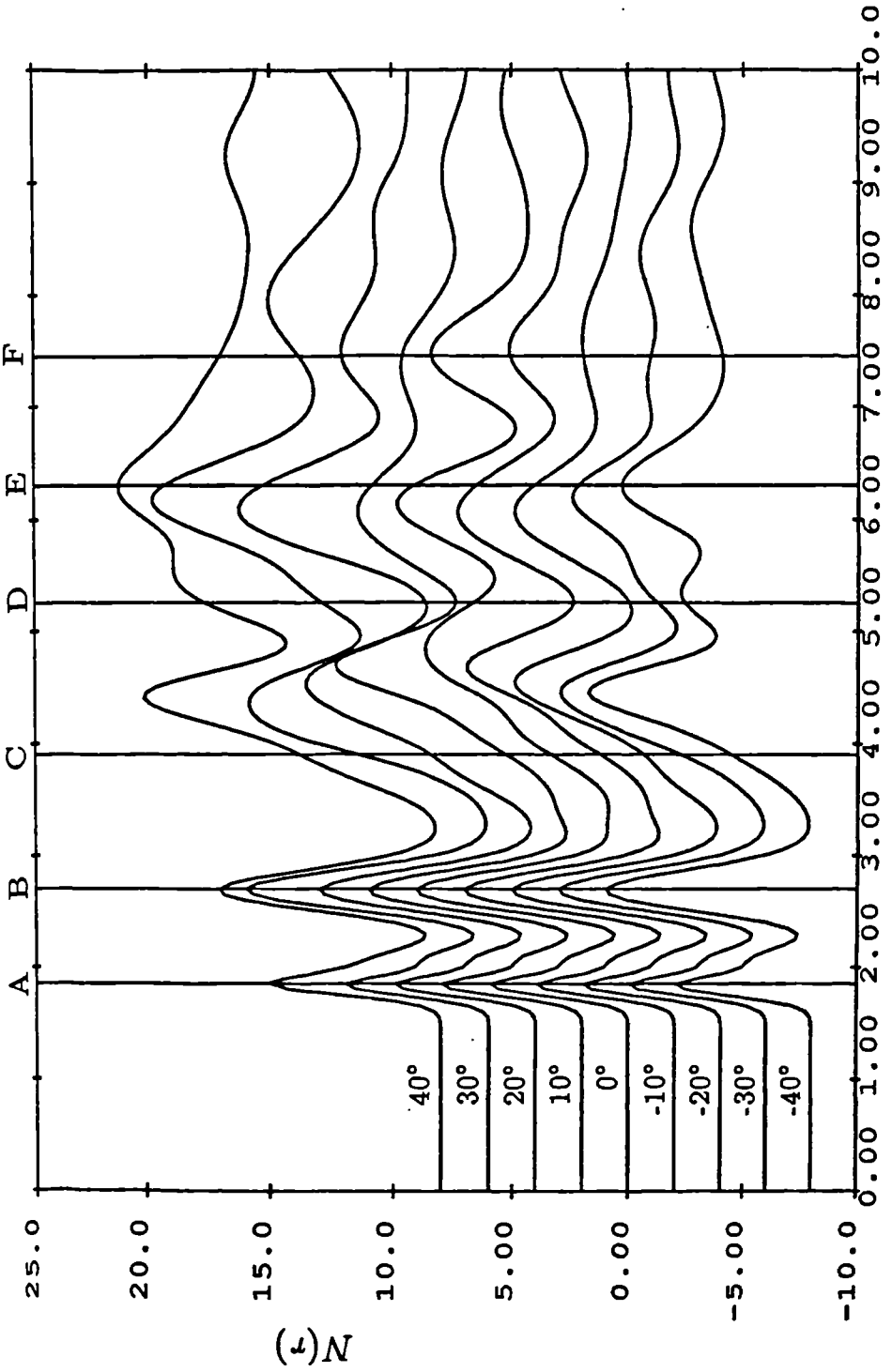

Figure 56: The variations occurring in the SbF_5 chain model upon the application of a series of different twists. The vertical lines correspond to the positions of the peaks observed in the $d(r)$ function. The data have been offset for clarity.

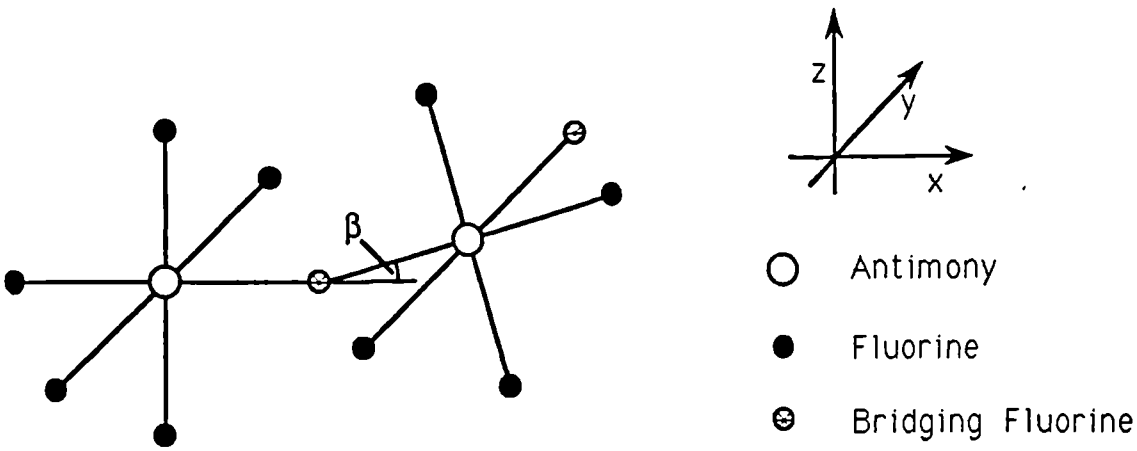

Figure 57: Two consecutive molecules in an SbF_5 chain showing the definition of the bond bend β

is there correlation, between the model and data, of more than two of the higher four peaks (C to F). This indicates that the inter-molecular correlations cannot be explained in terms of a twisted molecular chain.

The 'Bent-Bridge' Chain

In the solid phase, SbF_5 exists as tetramers in which the Sb–F'–Sb bridge is bent, two of the bonds having an angle of 170° and the other two being 140° (see figure 48). This suggests that modeling the SbF_5 chain in the liquid using linear bonds may be incorrect. In the 'bent-bridge' model, the atom positions in the chain were calculated using a bend angle defined as shown in figure 57. As in the twist model, adjusting the amount of bond-bending present alters the overall length of a finite chain. A positive bend, although it will bring the central Sb atoms of consecutive units closer together, will move the central Sb of second neighbour units further

apart and thus have the effect of lengthening the chain. Similarly, a negative bend moves the second neighbour units closer together and thus shortens the overall length of the chain. Figure 58 shows the effects upon the chain distribution of a selection of different bends between -40° and 40°. This graph shows the expected correlation between the first two model peaks and peaks A and B in the real data. The motion of the third peak is similar to the found in the twist model but, this time the third peak does move far enough down in r to correspond to peak C. The first major difference in the two models is the action of the fourth peak, whereas in the twist model this peak moved outward, on the bend model it moves to lower-r. Another notable feature is the peak at position F in the unbent chain which moves to slightly-higher r values when a positive bend is applied, but very markedly to lower-r upon application of a negative bend. This latter motion is so marked that for a -40° bend, it has moved down to about 6 Å. Of the peak shown closest correlation between the model and the real data occurs with bends of -40°and 40°. These angles are the same as the large bond bend that occurs in the solid. To further investigate this region and any improvement that may be gained by going to higher bond bends, datasets to either side of the ± 40° peaks where produced, figures 59 and 60

Figure 59 shows that for the negative bending case the closest agreement to the F peak occurs for a bond bend of -40°. For the D and E peaks no exact agreement occurs. The closest match to the E peak probably occurs at a bend of between -35° and -30°, however at these angles the agreement of the D peak is lost. From this it appears that agreement on three of the higher four peaks is the best which can be achieved for a negative bend.

Figure 60 shows a similar sequence of plots but this time for the positive bending

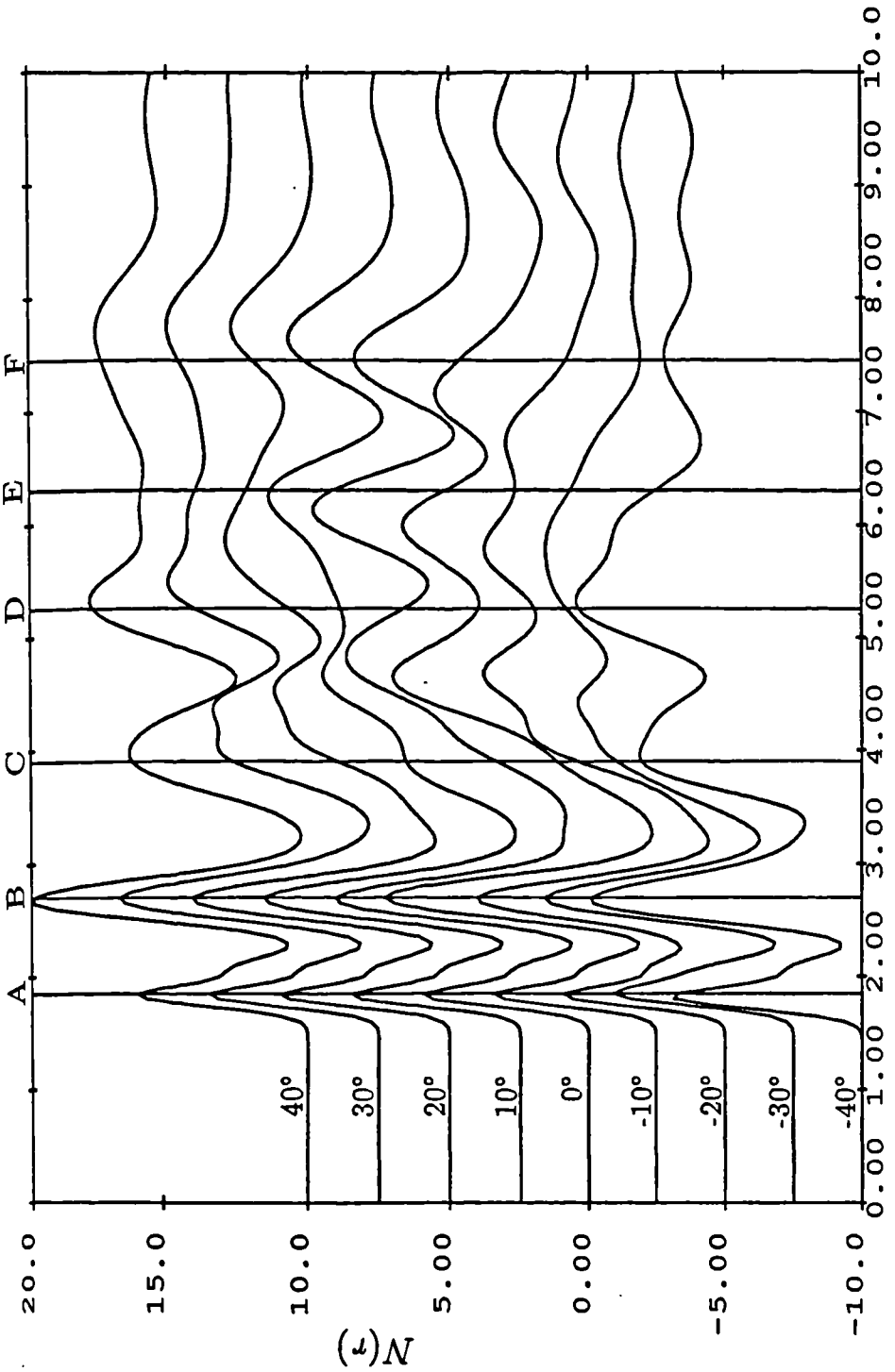

Figure 58: The variations occurring in the SbF_5 chain model upon the application of a series of different bends. The vertical lines correspond to the positions of the peaks observed in the $d(r)$ function. The data have been offset for clarity.

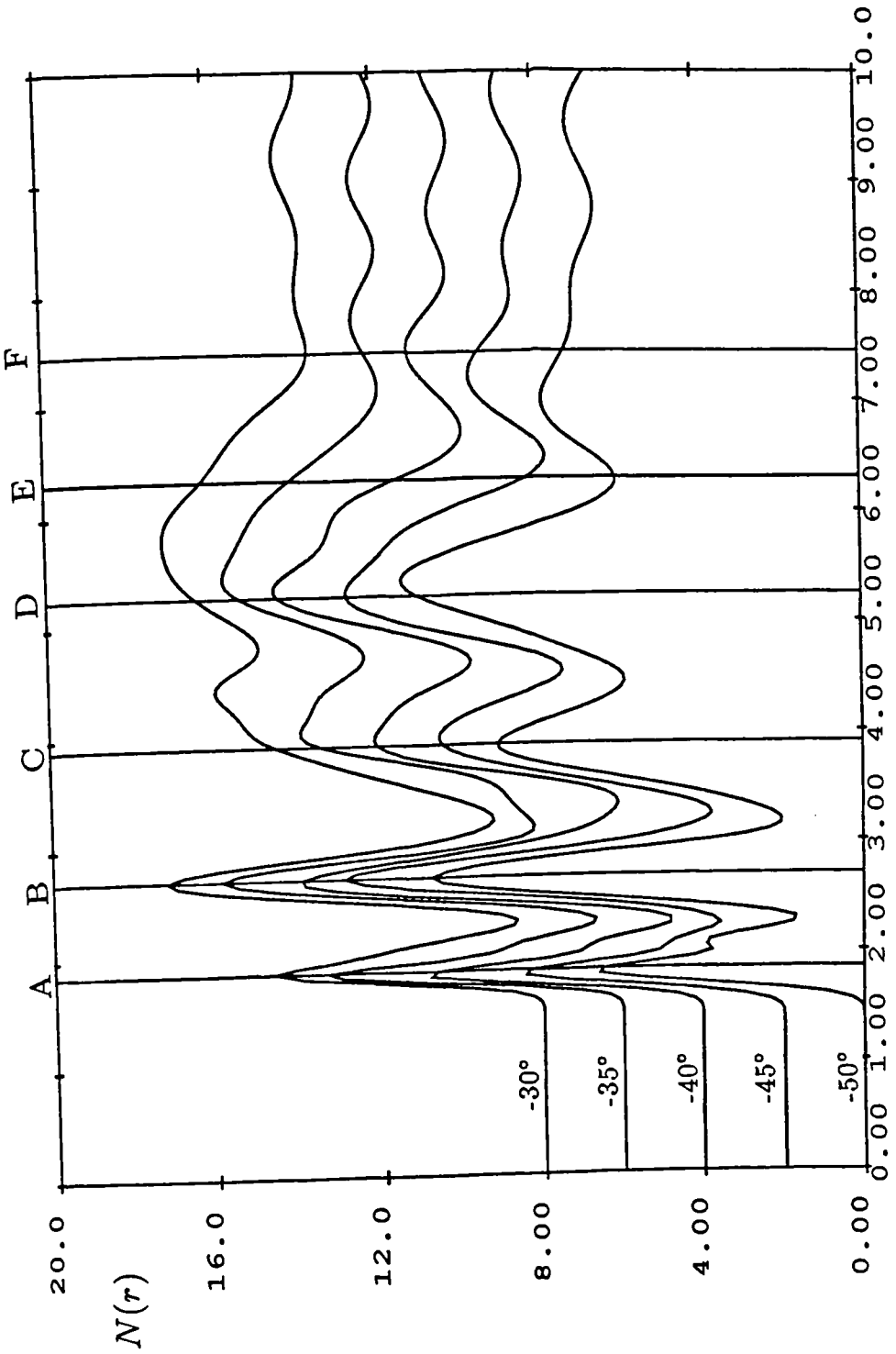

Figure 59: The variations occurring in the SbF_5 chain model upon the application of a series of different negative bends from 30° to 50°. The vertical lines correspond to the positions of the peaks observed in the $d(r)$ function. The data have been offset for clarity.

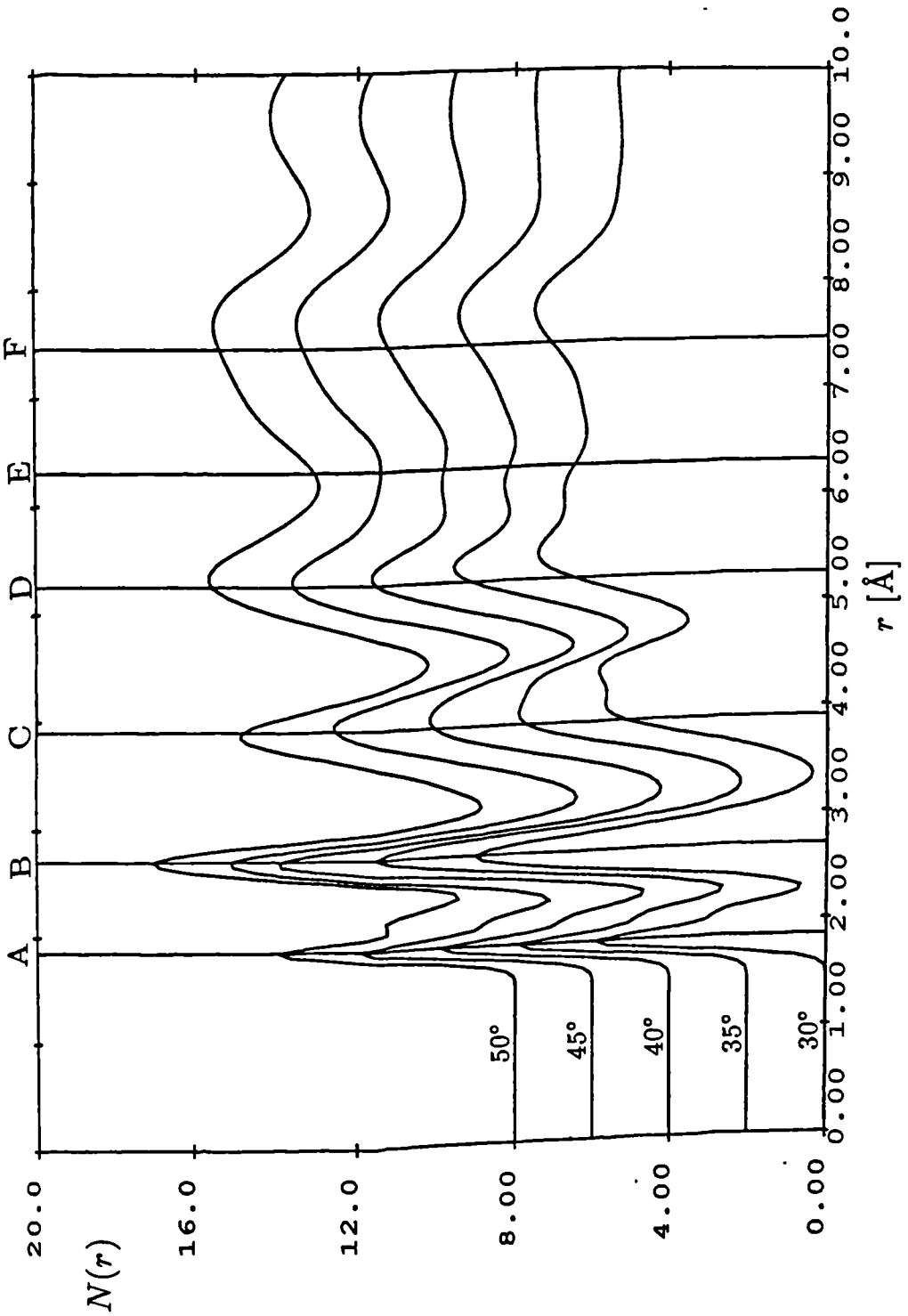

Figure 60: The variations occurring in the SbF_5 chain model upon the application of a series of different positive bends from 30° to 50°. The vertical lines correspond to the positions of the peaks observed in the $d(r)$ function. The data have been offset for clarity.

case. These curves show a remarkable lack of change in the peak positions when compared to the previous case. The main changes are a splitting of the C peak as the bend is reduced in angle and a reduction of the height of the peak just below position E with a possible motion of this peak towards higher-r. The best fit to the data seems to occur within the 40° and 45°dataset, by the time the bend reaches 50° the A peak has developed a noticeable side-peak. Thus the most apparent problem is the lack of a well developed peak in position E. The $d(r)$ curve in figure 51 shows that the E peak (at 6.3 Å) is smaller than the D and F peaks to either side of it and will thus be less visible than these two. The width of peaks used to determine the $N(r)$ curve has been scaled with respect to r (equation 139) and due to this, a small peak may become so wide that it has little amplitude in the $N(r)$ function. If, as in this case, the peak is placed between two larger peaks it presence may have little effect on the curve. To test this a new Gaussian broadening function was introduced to reduce the effect of the broadening. This function takes the form

$$\sigma = \sigma_0 + b\sqrt{r} \tag{142}$$

where σ_0 and b are both constants and where set equal to 0.05. A comparison of the two $N(r)$ plots obtained from the different broadening functions are shown in figure 61. In this figure a peak just below position E is clearly shown. The F peak has also been resolved into two peaks, whereas the actual data only shows one. A possible explanation for these effects is found by examining the origin of the peaks. The peak at E is due almost entirely to correlation between second neighbour molecules. The two peaks at F are caused by correlations in the third neighbour molecules with some second neighbour correlations in the lower of the two peaks. If it is assumed that the main cause of the Gaussian broadening is due to molecular vibrations, caused by the looseness of the fluorine bridge, it would be expected

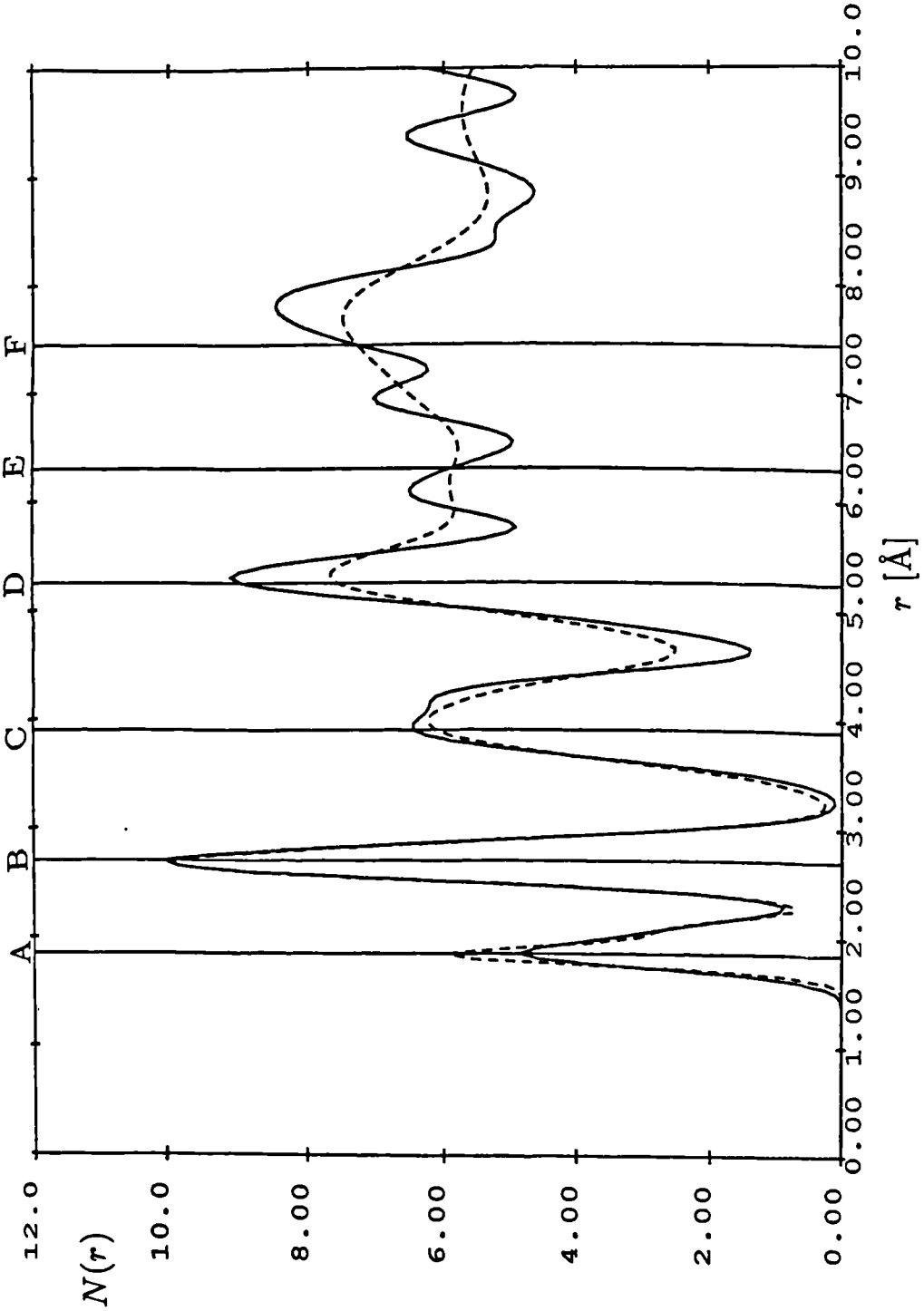

Figure 61: Comparison of the $N(r)$ curve obtained, for a SbF_5 chain with a 40° bend, using two different Gaussian broadening functions.

that those vibrations associated with the third neighbour correlations, will be much greater than those of the second neighbour. This effect will lead to a situation where the broadening will be more dependent on the molecules in which the atoms are situated, than the actual separation of the atoms. Correction of this error in the model would lead to the a relative sharpening of the E peak as produced by the second broadening function and broader peaks at position F leading to a composite peak as shown by the first function. Thus the only discrepancy left between the model and the real data is the small errors in the positions of the E and F peaks.

The Twisted Bent-Bridge Chain

In an attempt to explain the errors in the E and F peaks the first two models where combined, thus producing a chain in which the fluorine bridges where first bent and then the chain was twisted about the bond from the bridging fluorine to the lower antimony in the chain. The results of this analysis are shown, for a fixed bend of 40° and variable twist, in figure 62. This figure shows a clear peak shift for the F peak. For negative twists this peak moves to lower-r and at -20° its peak coincides exactly with the position of the F peak in the real data. The -20° data also shows an side-peak just above the C peak. Early in the discussion it was mentioned that a small peak occurs at 4.55 Å (position C1) in the real data and that due to its size it was not being considered as a major factor in fitting the peak positions. That small peak was in the region of the peak that has now appeared in the -20° data set. The only problem visible here is the slight shift of the C peak downwards in r. Of the other datasets the best fit appears to lie somewhere between the 0° and 10° set as here the E peak moves from one side of the required position to the other. These data do not however show signs of a peak at 4.55 Å. It

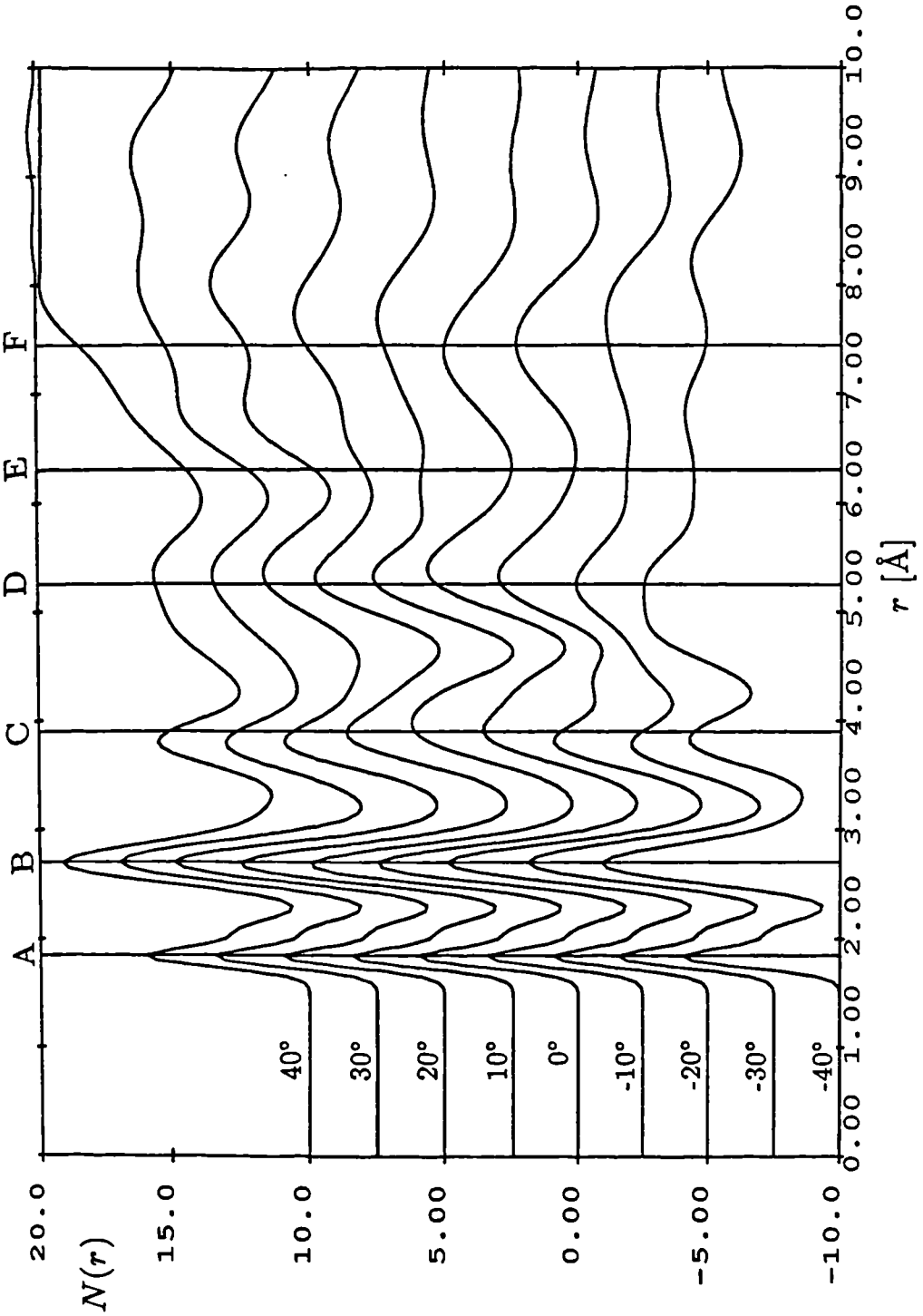

Figure 62: The variations occurring in the SbF_5 chain model upon the application of a series of different twists applied to a chain with an Sb–F′–Sb bond angle of 40°. The vertical lines correspond to the positions of the peaks observed in the $d(r)$ function. The data have been offset for clarity.

thus appears that to produce a good fit to the data a model with a twist of about -30° and a bridge-bend of around 40° is required. Further exploration of this region revealed the best fit to be obtained with values of -28° and 35° for the twist and bend respectively. A comparison of the model $N(r)$ produced using these parameters and the $d(r)$ curve is shown in figure 63. This combination of transformations moves the C peak back to the required position and gives good agreement for all peak positions and relative amplitudes apart from the F peak. This peak is a composite of two peaks (see above) of which the lower peak is a combination of correlations between atoms on the second and third neighbour molecules. The correlations for the second neighbour separations should have narrower peaks than those for the third neighbour separations (see above), thus meaning that the lower peak should be narrower and correspondingly higher, this will have the effect of moving the peak towards lower-r and give better agreement with the real data. It may, therefore, be concluded that the above model may be used to adequately describe all of the features present in the $d(r)$ curve.

5.5 Temperature Difference

To investigate the effects of temperature on liquid SbF_5 , data where collected at 6 different temperatures (5°, 11°, 20°, 36°, 55°and 80°C). These were independently analysed (see above) and then their $d_L(r)$ curves were compared. To perform this comparison the difference between each dataset and the 5°C set was taken, after the datasets had been corrected for variation in density. These results are shown in figure 64. A close examination of these curves, when superimposed on top of each other reveals three major features. Firstly, there is a decreasing peak occurring just above the position of the B peak, at approximately 3 Å. Next a second decreasing

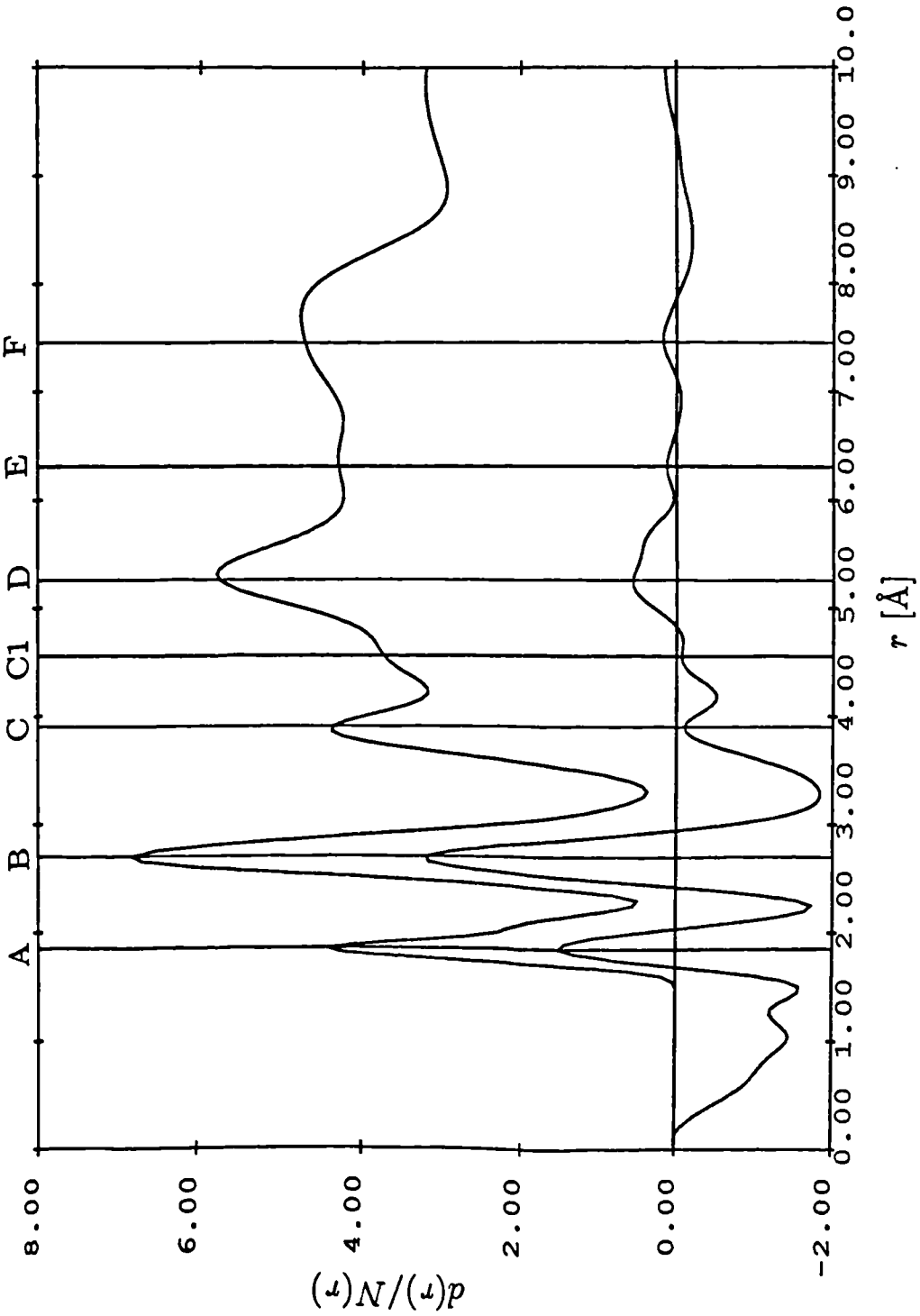

Figure 63: The $d(r)$ curve (lower) for SbF_5 and the $N(r)$ curve (upper) calculated an SbF_5 cis-bridged chain with a bridge-bend of 35° and a bond twist of -28°.

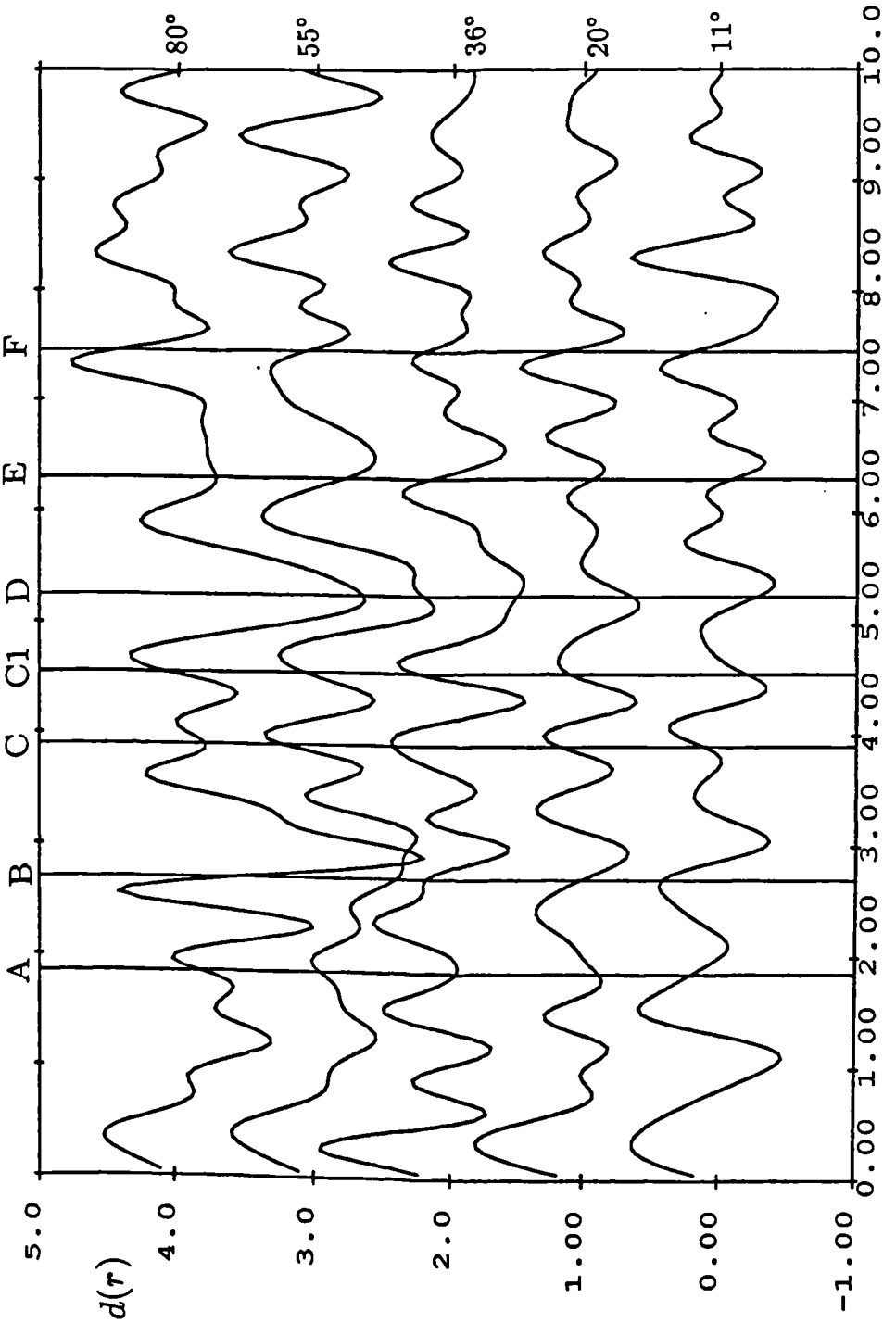

Figure 64: The temperature difference functions obtained by subtracting the 5°C $d(r)$ curve from each of the other $d(r)$ curves. The plots have been offset for clarity.

peak size is found at the D peak position and finally the peaks to either side of the F peak clearly indicate a shift in this peak toward lower-r. Other possible features are an increase in the size of the C_1 peak and a shift towards higher-r of the E peak. These features are, however, less clear than the other three listed. It has not been possible to exactly reproduce any of the difference functions by manipulation of the model. It is possible however, to produce many of the observed changes by altering the bend or twist angle of the model. Figure 62 shows a shift in the F peak in the desired direction as the twist angle is reduces. A difference plot of the datasets also reveals a decrease in the height of the right-hand side of the B peak similar to that shown in the difference plots. Small variations in the angle of the bond-bend produce corresponding changes in the height of the D peak with this peak decreasing as the bond angle is reduced. It would appear, therefore, that it should be possible to recreate the effects seen in the temperature variation plots by an appropriate combination of twisting and bond-bending. From the trends observed it would appear that the desired effects are achieved for both the twist and bend by a corresponding lengthening of the chain.

There are two reasons why it has not been possible to reproduce the exact changes occurring in the chain. The main reason is that due to the noise in the original datasets the $d(r)$ plots contain a large amount of noise at high r in the form of low amplitude ripples. Although this noise has only a small effect on the general shape of the $d(r)$ curves it is very noticeable in the difference function. This makes it very difficult to differentiate between real and spurious effects and may lead to the enhancement or reduction of the real effects. A second factor is that the effect of molecular vibrations has not been included in the model. It is probable that as the temperature increases the vibration of the molecules within the chain, with respects

to their neighbours, is increased and that this will lead to a general smearing out of the $d(r)$ curves especially at high-r. It should be possible to introduce a new Gaussian broadening function into the model, which will be dependent on not only the separation of the atoms, but also on the molecules containing the atoms. This would give a better representation of the actual $N(r)$ curve. Having done this the molecular vibration parameter may then be linked to the temperature of the sample to reproduce the temperature dependent broadening effects, in the hope of obtaining a more representative difference function. It may be possible to overcome the noise problem by smoothing the original data, although a better solution would be to repeat the experiment to obtain improved statistics.

5.6 Conclusions

Taking as a starting point, a basic cis-bridged chain the structure of liquid SbF_5 has been investigated. This chain consisted of molecular units which had opened out into octahedra to allow for the presence of a bridging fluorine from an adjacent molecular unit. The fluorine bridge-bond was found to be longer than the ordinary Sb–F bond length by about 0.2 Å. It has been found that the peak positions of the $d(r)$ curve and their relative amplitudes may be explained using this model if a rotation about, and a bending of, the fluorine bridge is introduced. The fluorine bridge shows a preference for a bond bend of 35°. This is similar to the bond angle found for two of the four bridges occurring in the tetramer form of SbF_5 found in the solid phase. Such a bending of the bond in the liquid was unexpected because of the simple nature of the fluorine atoms and has provided an interesting line for further inquiry. The high viscosity of the liquid is clearly a result of chain entanglement and indicates that the life-time of the fluorine bridge connection is long compared

to the molecular motion of the chain units. The temperature difference results are difficult to explain using the current model partly because the temperature difference function is very noisy and partly due to the simple model employed to calculate the width of the peaks associated with various atom separations. It is possible, however, that if a new Gaussian broadening function were introduced into the model to allow for inter-molecular vibrations within the chain, and if the noise in the difference function can be reduced, that the features observed in the temperature difference function may be explained by small changes in the twist and bend angles used to describe the chain.

Chapter 6

A Neutron Diffraction Study of Carbon and Germanium Tetrabromide

6.1 Introduction

The structural study of liquids composed of tetrahedral molecules has been carried out almost exclusively on the tetrachloride series (CCl_4 to $SnCl_4$). There have, however, been few studies of the tetrabromides. The main source of interest in liquids comprised of tetrahedral molecules concerns intermolecular correlations. Originally it was believed that the molecules possessed a great enough spherical symmetry for them to act as simple spheres in the liquid. If this were the case the molecular distribution function of the molecular centres would be similar to that of a liquid rare gas. This is not found to be the case and thus indicates that some form of short range order is present amongst the molecules in the liquid. A number of models

have been developed, to try to explain this order, with differing degrees of success. One model that has been used quite successfully with the tetrachlorides is reference interaction site model (RISM) [54,89,90,91]. This model describes the molecule as a cluster of hard spheres which define the surface contours of the molecule. The modelling of the molecular assembles thus, results in an integral equation which may be solved to give the intermolecular pair distribution function for the liquid.

Neutron diffraction experiments have been performed on two tetrabromide systems (carbon tetrabromide, CBr_4 , and germanium tetrabromide, $GeBr_4$) and RISM calculations for these systems have been performed by E. Enciso [92]. Carbon tetrabromide has been extensively studied in the plastic crystal phase [93-97]. Some neutron data have been made available [98] but these are of poor statistical accuracy and cover a limited k range. Germanium tetrabromide is another little studied liquid, anomalous X-ray scattering (AXS) studies have been published by Ludwig [99,100] and a neutron diffraction analysis has been carried out by Egelstaff [101].

6.2 The Experiment

The neutron diffraction experiments were performed on D4b diffractometer at the High Flux Reactor of the Institut Laue-Langevin (ILL), Grenoble, France (see chapter 2). The samples were contained in thin-walled vanadium cylinders with a outer diameter of 5.0 mm and a wall thickness of 0.1 mm. Both of the samples were heated. The CBr_4 (mp = 90.1°C, bp = 189.5°C) experiment was performed at a temperature of approximately 97°C and the $GeBr_4$ (mp = 26.1°C, bp = 186.5°C) experiment at approximately 30°C. Diffraction measurements were made for 'sample plus container',$I_{scb}(\theta)$, 'empty container',$I_{cb}(\theta)$ and background, $I_b(\theta)$ with an

incident neutron wavelength of 0.7049 Å. The collected data was in the form of a computer file containing the scattering angle and corresponding neutron counts for each cell in the detector array. This data was then corrected for the detector cell efficiency and normalized to the same monitor count using a program available on D4B. The corrected counts for each cell were then combined to yield the intensity profiles shown in figures 65 and 66 for CBr_4 and $GeBr_4$ respectively. Both of these figures show the typical tetrahedral pattern although there are obvious differences in the relative sizes of the first two peaks and an alteration in the peak spacing consistent with the larger size of the $GeBr_4$ molecule.

6.3 Data Correction

After collection the experimental data needs to be corrected for the container and background scattering and for absorption and multiple scattering of the beam in the sample. The following section deals with these corrections.

6.3.1 Background and Container Subtraction

To obtain the scattering contribution from the liquid, $I_s(\theta)$, the background and container contributions must be removed from $I_{scb}(\theta)$. To do this it is necessary to take into account the attenuation/absorption of the beam within the sample and container.

Paalman and Pings [58] presented a method of calculating the absorption corrections for X-ray diffraction from a liquid sample in a cylindrical cell. This formalism

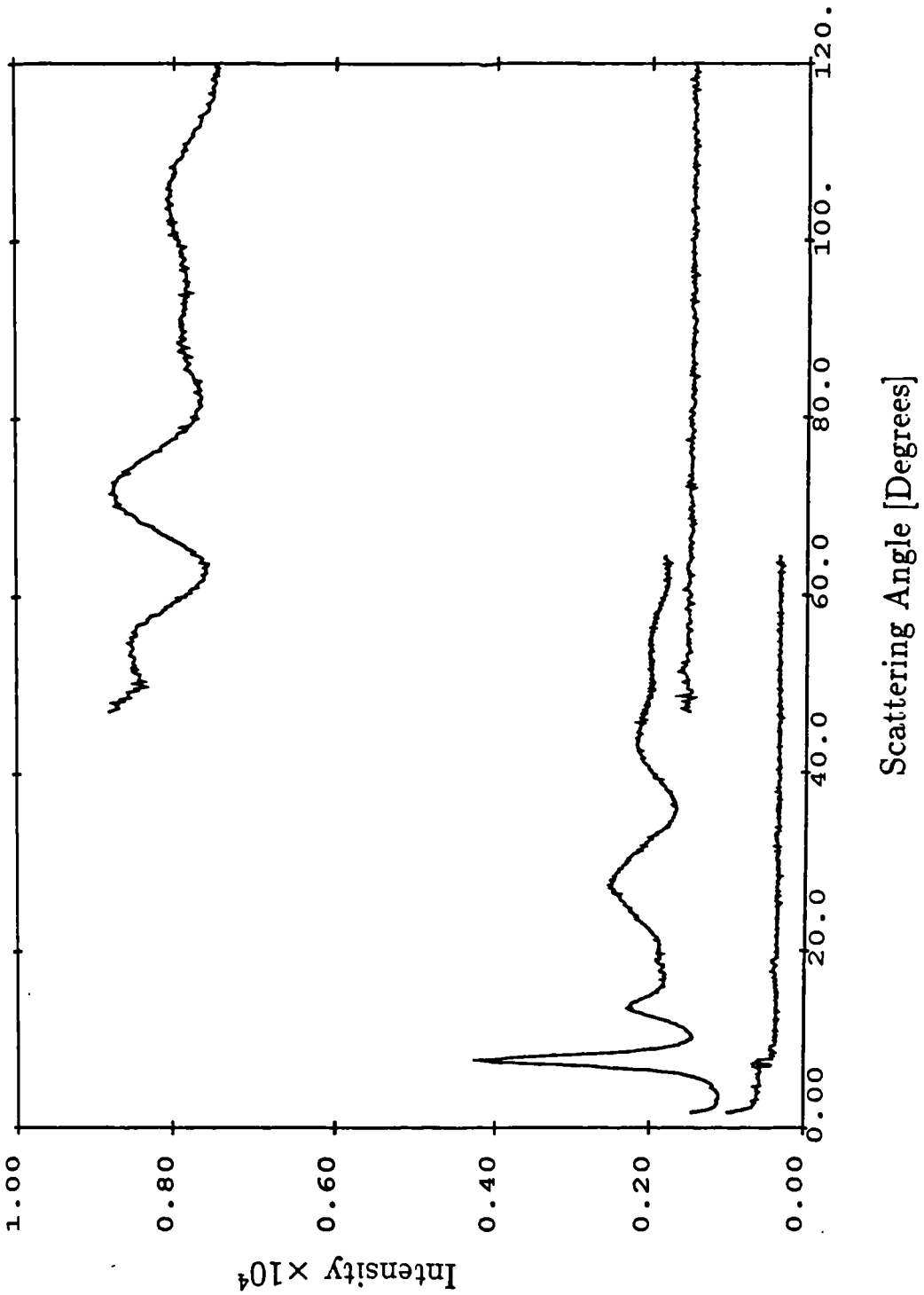

Figure 65: The scattered neutron intensity for liquid CBr_4 in a vanadium container at 97°C. The profiles were collected using two detectors.

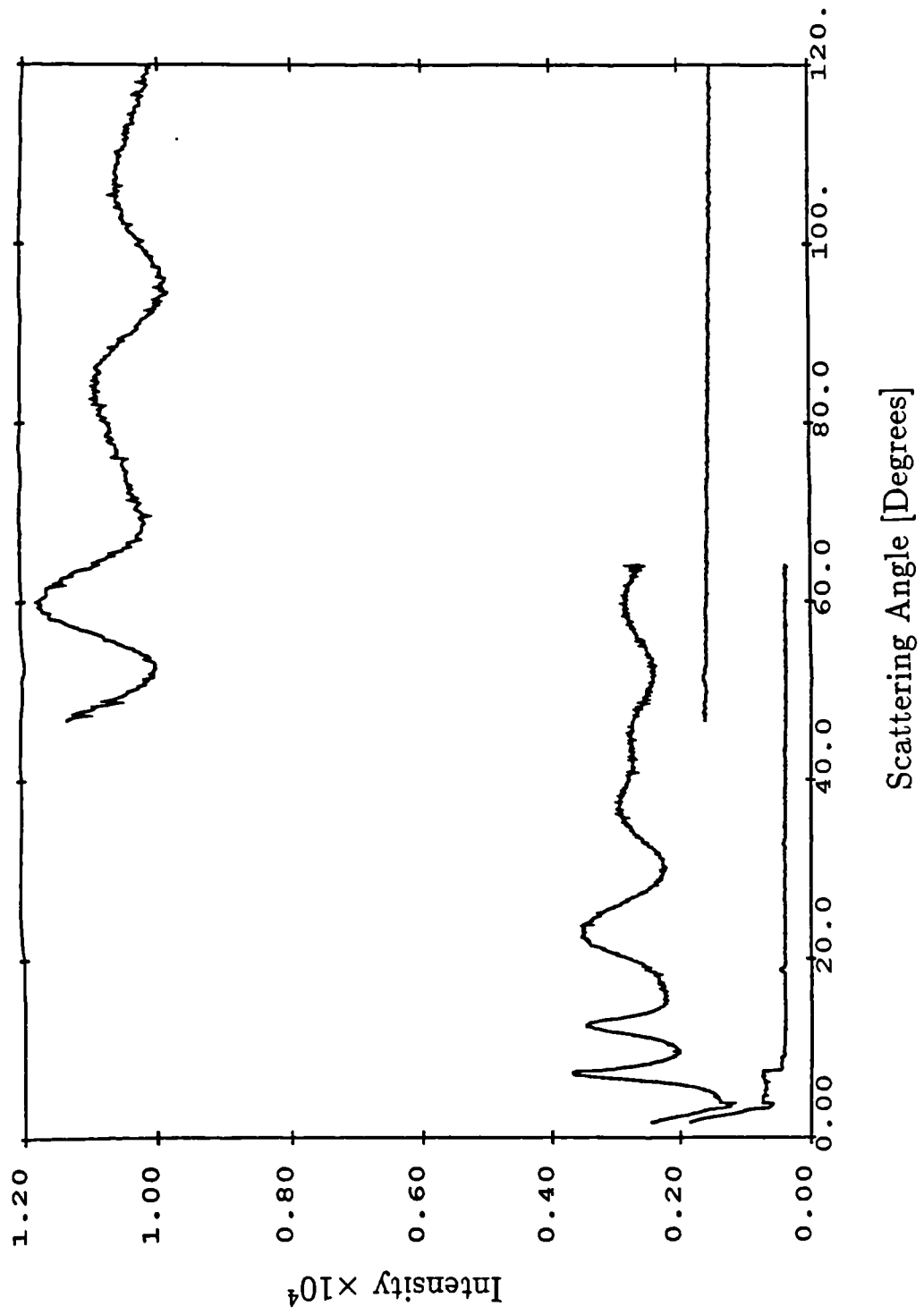

Figure 66: The scattered neutron intensity for liquid $GeBr_4$ in a vanadium container at 30°C. The profiles were collected using two detectors.

was adapted for use with neutrons in a program written by Page [102] which calculates f_{sc} and f_c such that

$$I_s(\theta) = f_{sc}(\theta)\{I_{scb}(\theta) - I_b(\theta)\} - f_c(\theta)\{I_{cb}(\theta) - I_b(\theta)\} \quad (143)$$

where $I_s(\theta)$ is the actual sample contribution of I_{scb} corrected for attenuation and scattering in the container, and absorption in the sample.

After the container and background subtraction, the data were placed into k bins of 0.05 Å^{-1}. The effect of this binning is to average the data without losing any significant resolution.

6.3.2 Multiple Scattering

Having obtained the sample counts, it is necessary to correct this intensity for multiple scattering and for absorption by the sample. This was done using the elastic multiple scattering program ELMS [103] obtained from Howells [104] at the Rutherford Appleton Laboratory. ELMS is a Monte Carlo type simulation which is made computer-efficient by forcing the neutrons into useful trajectories by use of statistical weights. The probability distribution, $Pr(k)$, for once-scattered neutrons is approximated by the normalised sample counts, $I_s(k)$. This is a good approximation when the multiple scattering component is small, or if the sample scattering is predominantly incoherent. Higher order ($\geq 2^{nd}$ order) scattering was not concidered as it is small and will have negligible effect. The result of applying the multiple-scattering corrections to the data is to obtain a corrected spectra, $I_s^{cor}(k)$.

6.4 Data Analysis

The following section outlines the analysis of the corrected intensity, $I_s^{cor}(k)$ which is the single scattered intensity, from the sample only, and with the sample absorption effects removed. This cross-section is described by the equation

$$\begin{aligned} \frac{d\sigma}{d\Omega_{obs}}(k) &= N_c I_s^{cor}(k) \\ &= \frac{d\sigma}{d\Omega_{self}}(k) + \frac{d\sigma}{d\Omega_{intra}}(k) + \frac{d\sigma}{d\Omega_{inter}}(k) \end{aligned} \tag{144}$$

where $\frac{d\sigma}{d\Omega_{self}}(k)$ is the self scattering, $\frac{d\sigma}{d\Omega_{intra}}(k)$ is the intramolecular interference term and $\frac{d\sigma}{d\Omega}inter(k)$ is the intermolecular interference term. Each of these terms is discussed below.

6.4.1 The self-scattering

It is necessary to normalise the data to the self term and to correct for departures from the static approximation. To do this, an empirical approach was used. The self-term is represented as

$$S_s(k) = \frac{1}{(\sum_i b_i)^2}\frac{d\sigma}{d\Omega_{self}}(k) = \frac{\sum_i b_i^2}{(\sum_i b_i)^2}\left(1 - Ak^2 + Bk^4\right) \tag{145}$$

where A and B are constants and b_i is the scattering length of atom i. The summations are over all of the atoms in the molecule. The scattering lengths used for C, Ge and Br are 6.648, 8.186 and 6.77 fm respectively. The self-term was fitted using a least-squares-fit algorithm which allowed the constants A and B to vary along with the normalization constant, N_c, which was used to reduce the observed intensity $I_s^{cor}(k)$ such that it oscillated about the self curve. The results of this fit are shown in figures 67 and 68.

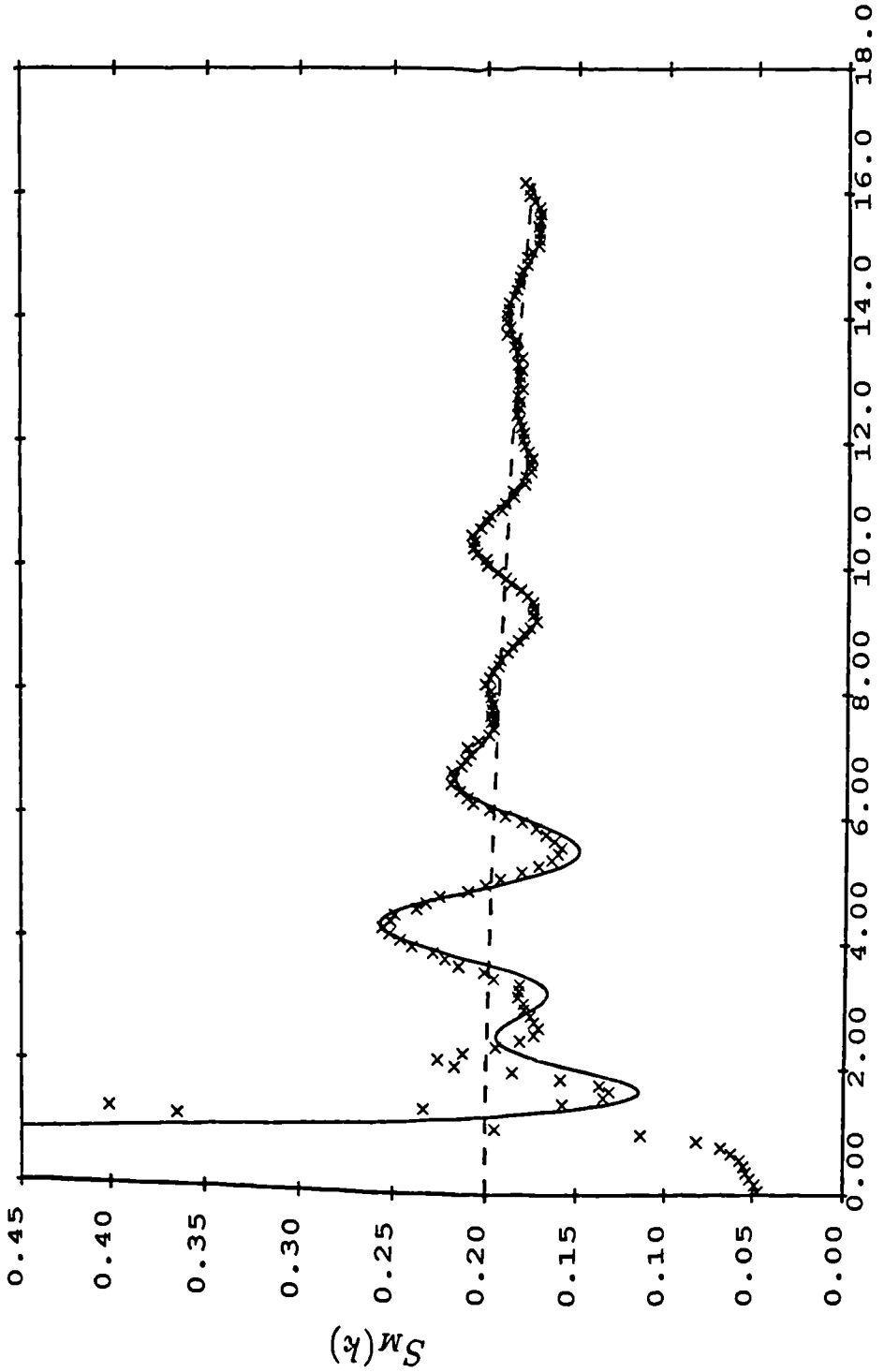

Figure 67: The observed structure factor, $S(k)$, for liquid CBr_4 at 97°C ($\times \times \times$) and the form-factor fit to the data (—) using the parameters listed in table 11. The self-scattering curve is shown as a dashed line. For clarity only every other data point is plotted.

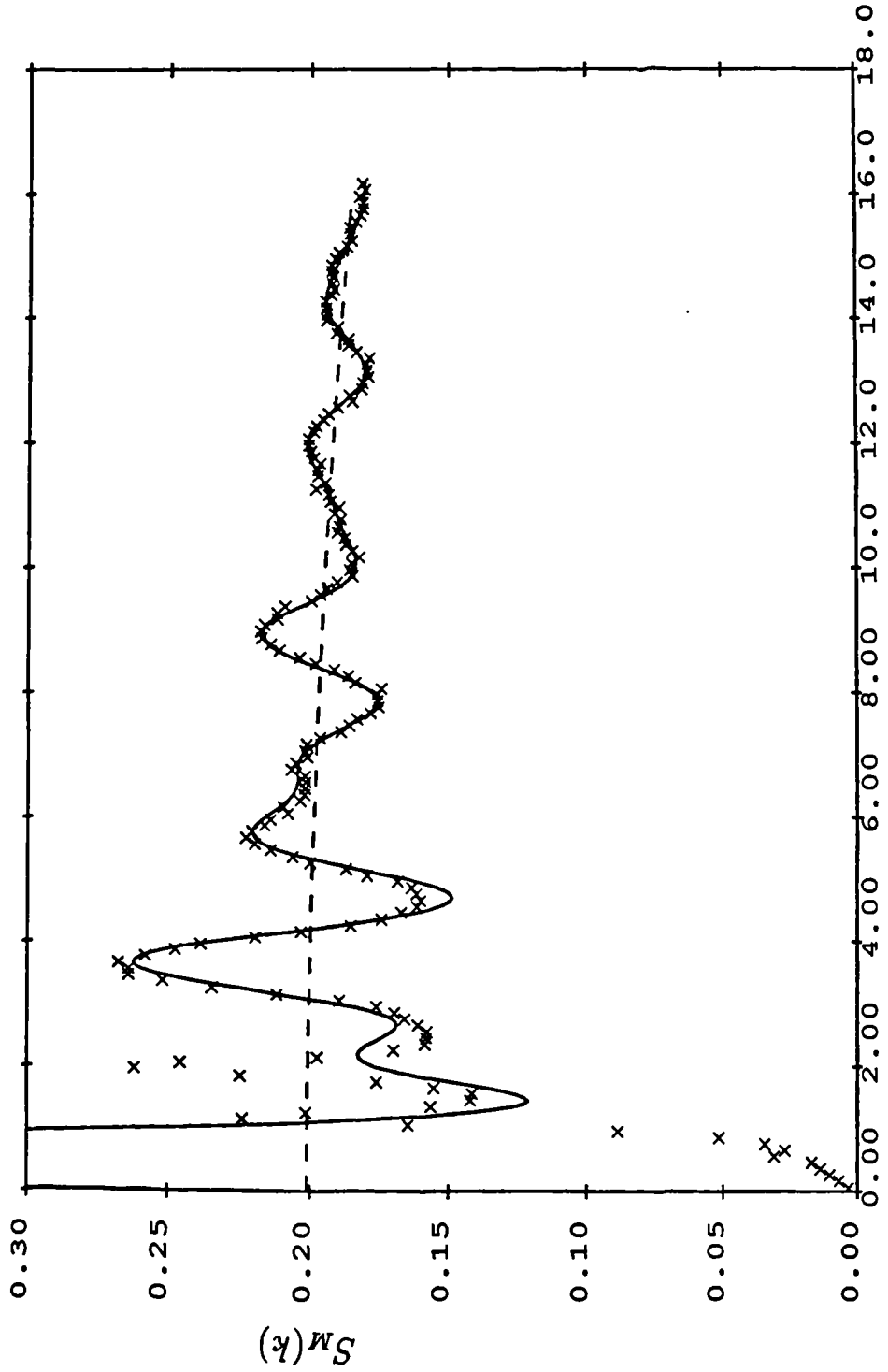

Figure 68: The observed structure factor, $S(k)$, for liquid $GeBr_4$ at 30°C ($\times \times \times$) and the form-factor fit to the data (—) using the parameters listed in table 11. The self-scattering curve is shown as a dashed line. For clarity only every other data point is plotted.

6.4.2 The Molecular Form-Factor

Having normalized the observed scattering to the calculated self term, the scattering curve obtained is equivalent to the molecular liquid structure factor, $S_M(k)$. This may in turn be divided into two components, the molecular form-factor, $F_M(k)$, and the intermolecular structure factor, $D_M(k)$

$$S_M(k) = F_M(k) + D_M(k) \tag{146}$$

where $F_M(k)$ is the sum of the scattering from the individual molecules and $D_M(k)$ is the interference contribution from pairs of atoms in separate molecules. The first of these terms may be further divided to give

$$F_M(k) = S_s(k) + S_i(k) \tag{147}$$

where $S_s(k)$ is the self term described above and $S_i(k)$ which is the intramolecular interference function. For a molecule of the form XY_4, $S_i(k)$ is given by

$$\begin{aligned} S_i(k) \;=\; & \frac{1}{(b_X + 4b_Y)^2}\Big[8b_X b_Y j_0\{r_{XY}k\}\exp\left\{-\gamma_{XY}k^2\right\} + \\ & 12b_Y^2 j_0\{r_{YY}k\}\exp\left\{-\gamma_{YY}k^2\right\}\Big] \end{aligned} \tag{148}$$

where b_i is the scattering length of atom i, r_{ij} is the separation of atoms i and j and γ_{ij} is their mean square vibrational amplitude. The function $j_0(x)$ is the zero order Bessel function and is given by

$$j_0(x) = \frac{\sin x}{x} \tag{149}$$

The molecular form-factor, as defined by equation 147, was fitted using a least-squares-fit algorithm. The fit was made from $k = 7.0$ Å^{-1} to the full range of the data. In the fitting of the intramolecular term the XY bond length and the two

XY_4	r_{XY} [Å]	r_{YY} [Å]	γ_{XY} [Å]	γ_{YY}[Å]	A [Å^2]	B [Å^4]
CBr_4	1.934	3.159	3.45×10^{-3}	6.25×10^{-3}	4.6×10^{-3}	0.9×10^{-9}
$GeBr_4$	2.270	3.707	2.56×10^{-3}	8.20×10^{-3}	3.0×10^{-3}	0.7×10^{-9}

Table 11: Parameters used in the form-factor fitting of the CBr_4 and $GeBr_4$ data.

Debye-Waller factors were allowed to vary freely. The YY separation was determined from the XY bond length by defining the tetrahedral angle (Y–X–Y) to be 109.5°. In the actual fitting routine, the fitting of the self term was also performed. This introduced three additional variable parameters i.e. the normalization constant, N_c, which adjusts the magnitude of the observed data and the two constants A and B (equation 145) which determine the magnitude of the fall-off in the self term. The results of the fitting of the molecular form-factor to each of the samples is shown in figures 67 and 68 and the final values of the variables are tabulated in table 11.

Both of the obtained fits are good and there are no obvious discrepancies between the form-factor above 7 Å and the observed data. The form-factor at low-k for the two systems shows the expected similarity. The primary bond length obtained for the CBr_4 molecule (1.93 Å) is in good agreement with that found by Dolling [98] of 1.91 Å investigations into the plastic crystal phase by More [96] also found a bond length of 1.91 Å. For $GeBr_4$ the bond length of 2.27 Å is in excellent agreement with that obtained by Ludwig (2.28 Å) [99] using AXS and by Finney (2.272 Å) [105] using electron diffraction. The result obtained by Egelstaff (2.36 Å) [101], for a liquid sample at 60°C, using neutron diffraction is in poor agreement, but it would appear that the error is in his work rather than the present study.

6.4.3 The Intermolecular Structure Factor

Subtraction of the molecular form factor, $F_M(k)$, from the observed molecular liquid structure factor, $S_M(k)$, yields the intermolecular structure factor, $D_M(k)$. This function contains all of the available information on the intermolecular structure of the sample. The two $D_M(k)$ curves are shown in figures 69 and 70. These curves very clearly show the two sharp peaks characteristic of liquids composed of tetrahedral molecules. The CBr_4 sample has a very sharp first peak and a much smaller second peak whereas for the $GeBr_4$ sample the two peaks are of a similar height. Also show in the figures is the RISM prediction obtained from E. Enciso [92]. In the RISM method [106] the interaction potential is represented by a hard sphere repulsion centred on each atomic site and therefore defines an effective hard core contour for the molecule. The resultant integral equation may be solved to yield the partial pair correlation functions and hence, the intermolecular structure factor for the system.

A comparison of the models with the observed $D_M(k)$ curves shows that the model yields a good prediction of the positions of the first two peaks although in both cases the height of the first peak in the model is lower than that of the data. The second peak in both cases is in excellent agreement. The third and fourth peaks for both samples are at lower k than the corresponding peaks in the models.

6.4.4 The Radial Distribution Functions

The total radial distribution function, $d(r)$, is obtained from the Fourier transform of the molecular liquid structure factor, $S_M(k)$, less the self-term by using the equation

$$d(r) = \frac{2}{\pi}\int_0^{k_{max}} k(S_M(k) - S_s(k))M(k)\sin(kr)\ \mathrm{d}r \qquad (150)$$

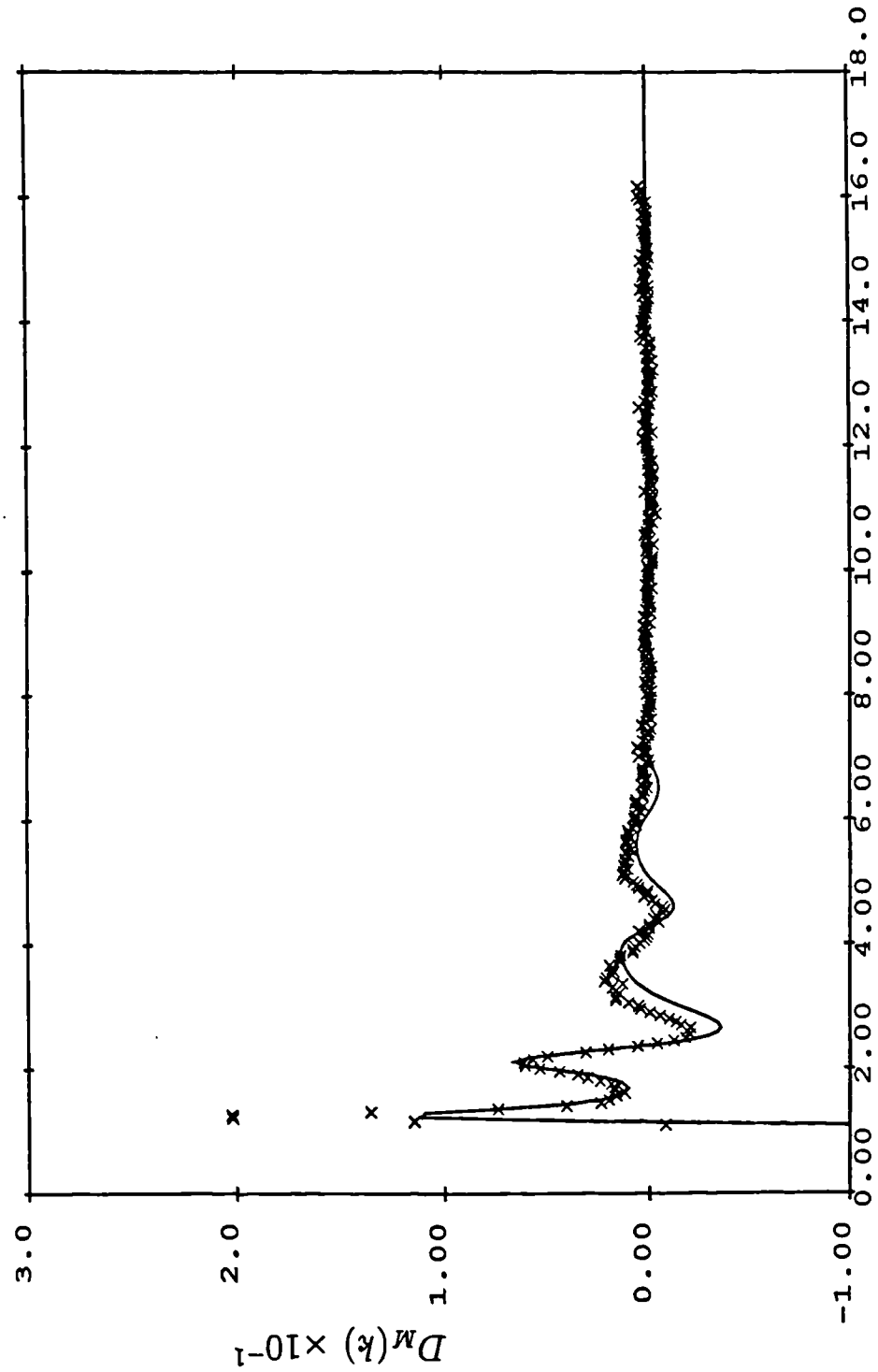

Figure 69: The intermolecular structure factor, $D_M(k)$, for liquid CBr_4 at 97°C (× × ×) and the corresponding RISM prediction (—).

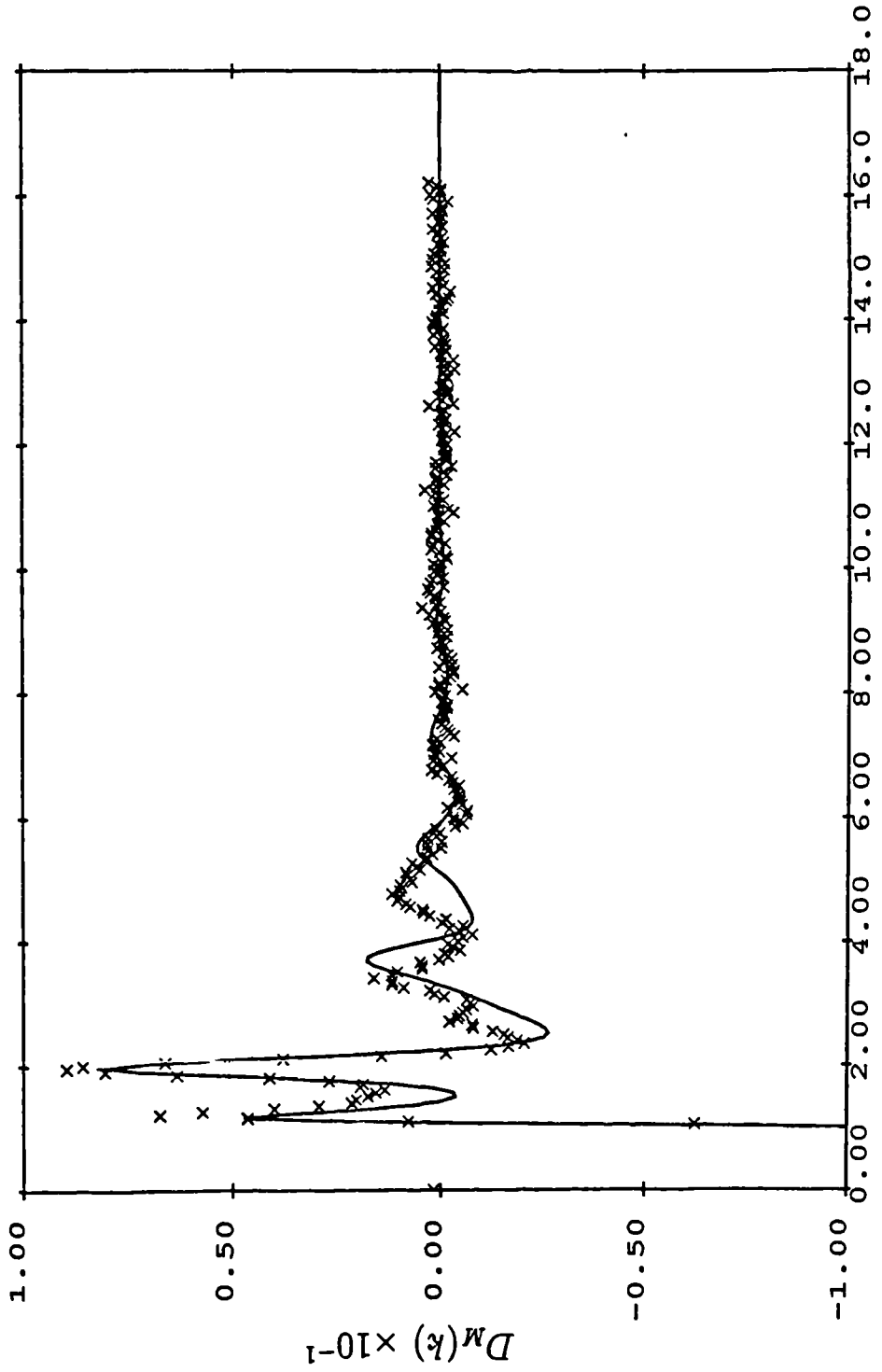

Figure 70: The intermolecular structure factor, $D_M(k)$, for liquid $GeBr_4$ at 30°C (× × ×) and the corresponding RISM prediction (—).

where $M(k)$ is a modification function introduced to reduce termination ripple and has the form

$$M(k) = j_0\left(\frac{\pi k}{k_{max}}\right) \begin{array}{ll} \rightarrow 1 & \text{as} \quad k \rightarrow 0 \\ \rightarrow 0 & \text{as} \quad k \rightarrow k_{max} \end{array} \tag{151}$$

Similarly the intermolecular radial distribution function, $d_L(r)$ is obtained from the Fourier transform of the intermolecular structure factor, $D_M(k)$. The $d(r)$ and $d_L(r)$ curves for the two samples are shown in figures 71 and 72. The curves obtained for both samples show the two very sharp peaks associated with the 'XY' and 'YY' separations in the molecule. The sharpness of these peaks is an indication of the rigidity of the conformation of the molecule. The intermolecular correlations (above ~5Å) for the two samples are quite different indicating differing degrees of intermediate range order. The CBr_4 sample shows three large broad peaks below 20 Å and these continue to higher-r indicating a long range order in the sample. The $GeBr_4$ sample does not show these large oscillations, instead the first intermolecular peak appears to have a shoulder on the low-r side possiblely indicating alignment of adjacent molecules. The spherical symmetry of a tetrahedral molecule may be defined by the anisotropy parameter [90], ξ which, for a molecule XY_4, is given by the ratio $r_{YY}/2r_C$, where r_{YY} is the YY distance occurring in the molecule and r_C is the external hard core radius, which is equivalent in this case to the atomic radius r_Y. The anisotropy parameter is a measure of the departure from spherical symmetry of the molecule. If r_{YY} is small compared with r_C there is a large overlap of the spheres and only a small deviation from spherical symmetry ($\xi \simeq 0$). As ξ increases the contours show further deviations from spherical symmetry and would therefore be expected to show enhanced orientational correlation. The anisotropy parameters for CBr_4 and $GeBr_4$, using a Br atomic radius of 1.89 Å, are 0.83 and 0.98 respectively thus indicating that $GeBr_4$ should show the highest degree of

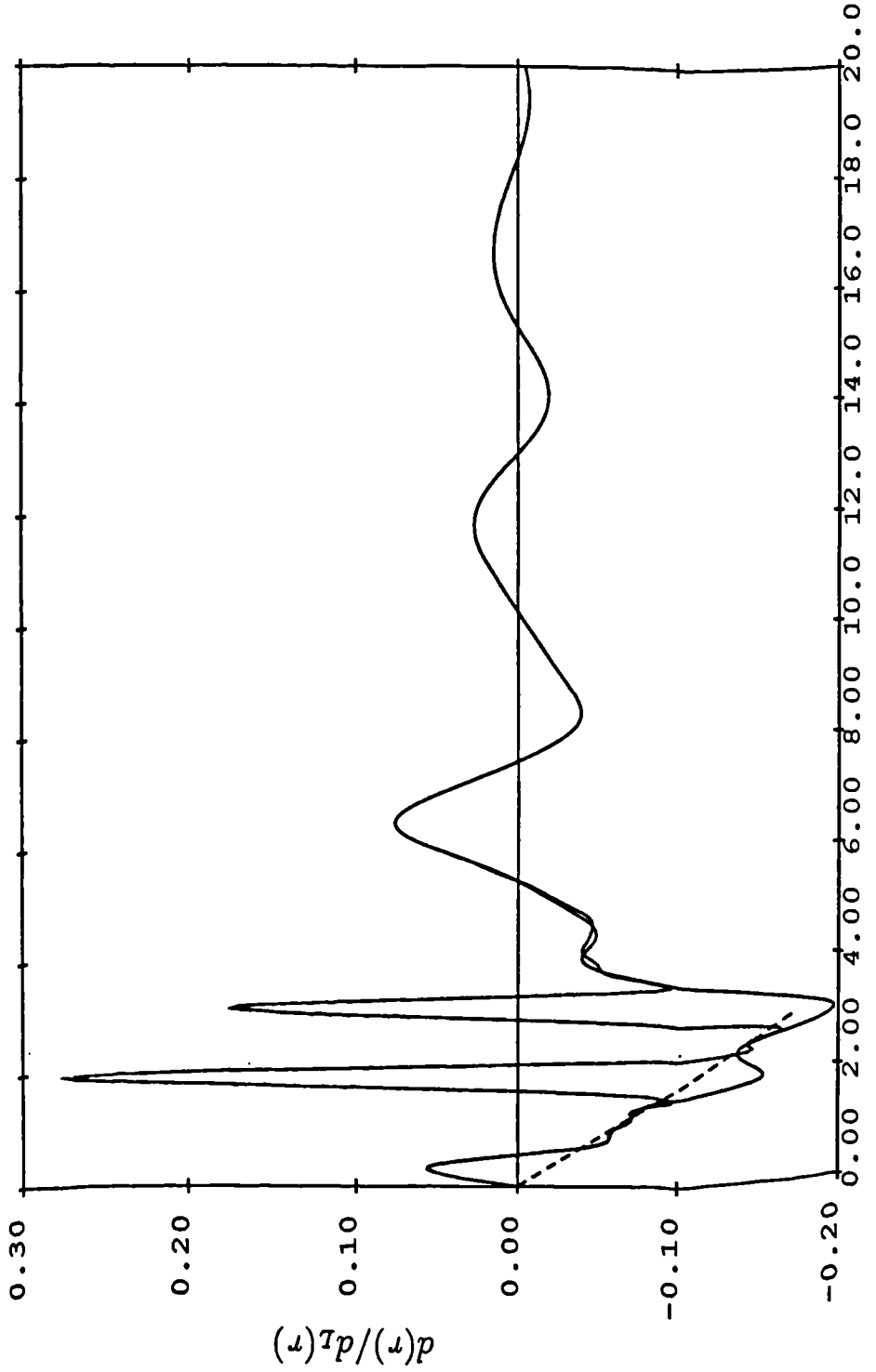

Figure 71: The total (upper) and intermolecular (lower) radial distribution functions for liquid CBr_4 . The density line ($-4\pi r\rho$) is shown dashed.

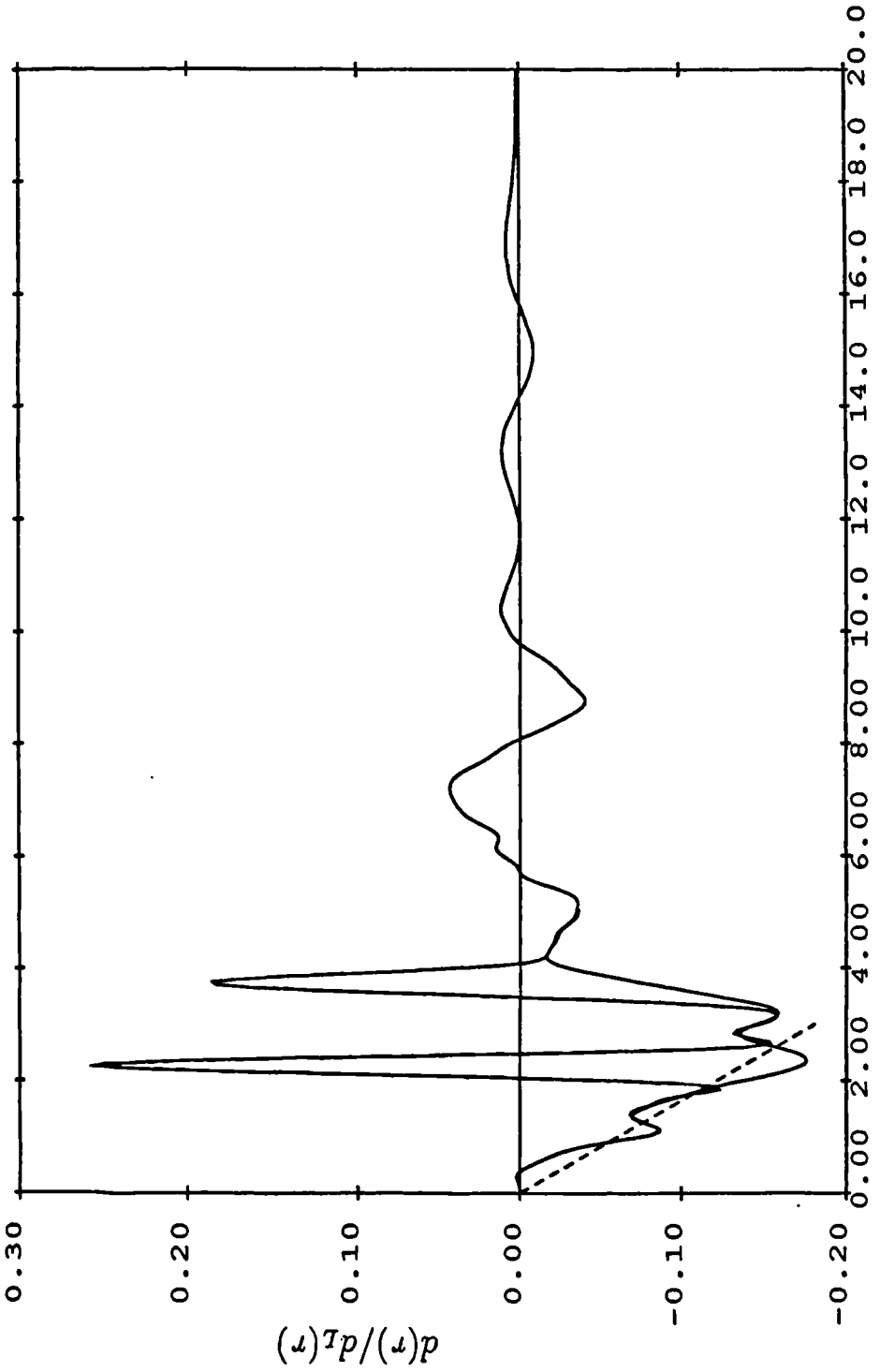

Figure 72: The total (upper) and intermolecular (lower) radial distribution functions for liquid $GeBr_4$. The density line ($-4\pi r\rho$) is shown dashed.

intermediate range order.

To compare the intermolecular radial distribution, $d_L(r)$, to the RISM prediction it was converted to the intermolecular pair-distribution function, $g_L(r)$ using the relationship

$$g_L(r) = \frac{d_L(r)}{4\pi r\rho} + 1 \tag{152}$$

The resultant curves are shown in figures 73 and 74. In both plots the first neighbour peak in the model is displaced to lower-r. The low-r edge of this peak is defined by the Br–Br contact distance, which is in turn defined by r_C. From the plots it can be seen that the leading edge of the peak in both cases is shifted towards lower-r and this indicates that the Br hard core radius used in the model was t0o small. The effect of this is to increase the anisotropy of the molecules in the model and thus to change slightly the correlations predicted. It will also move the first peak towards higher-r, thus bringing better agreement between the predicted and experimental peaks. Examination of the curves shown indicates that for both cases the first peak of the model appears to be more pronounced than the experimental data and that the peak in the $GeBr_4$ data is more pronounced than that in the CBr_4 data. This may be explained as an effect of increasing anisotropy. Increasing the anisotropy of the molecule leads to a more positive location of the nearest neighbour distance, caused by a bromine atom in the adjacent molecule becoming more firmly located in the enlarged hollow between the three bromine atoms which form each side of the molecule. This will in turn lead to a more defined first peak.

The effects of the changed anisotropy in the model are more difficult to assess for the higher peaks, but in general it would appear from the work of Montague *et al.* [90] that there should be an increase in the sharpness of the second peak and an increase in the peak separations. Examining the second peak shows that the

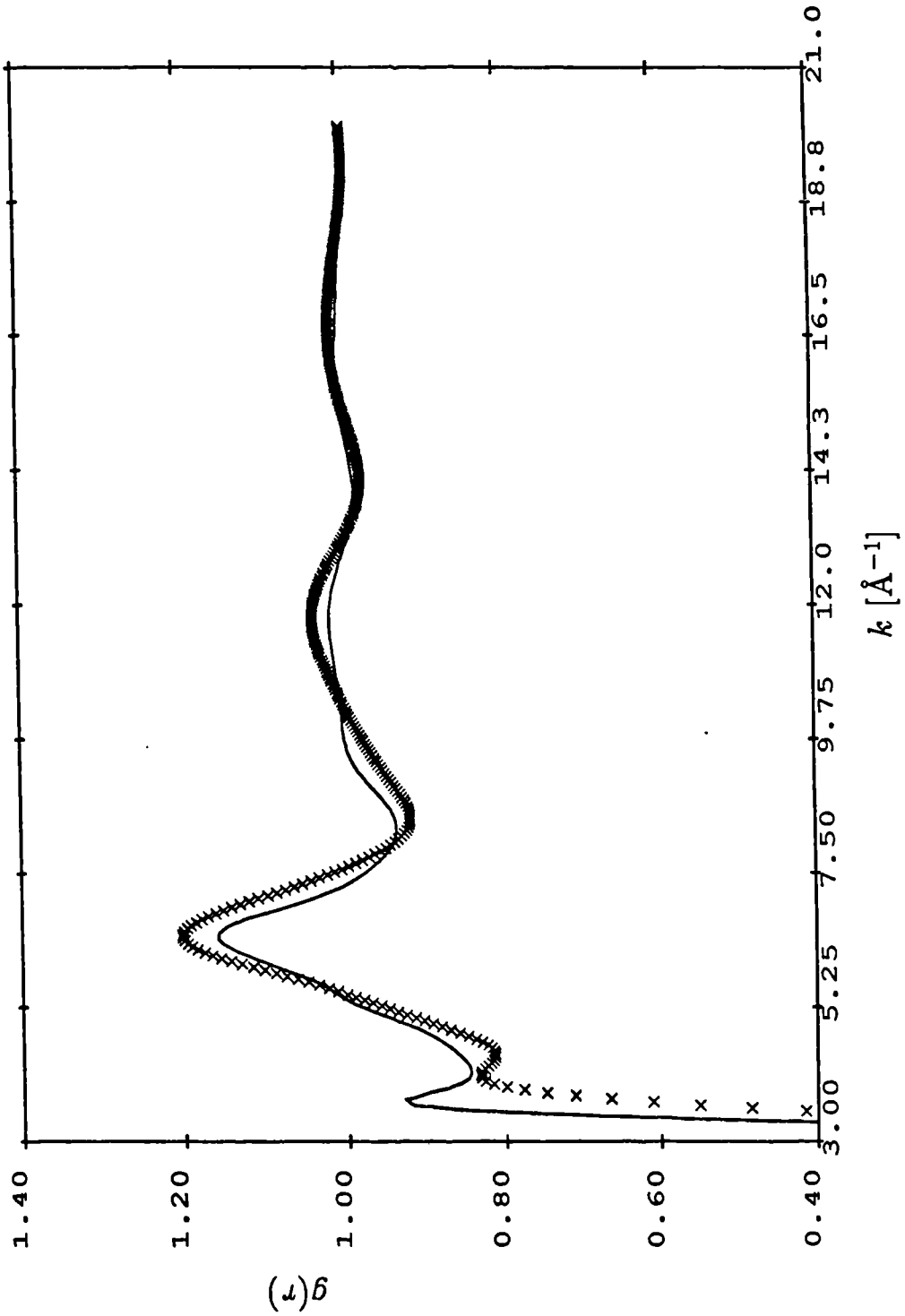

Figure 73: The observed (× × ×) and RISM model (—) intermolecular pair correlation function for liquid CBr_4 .

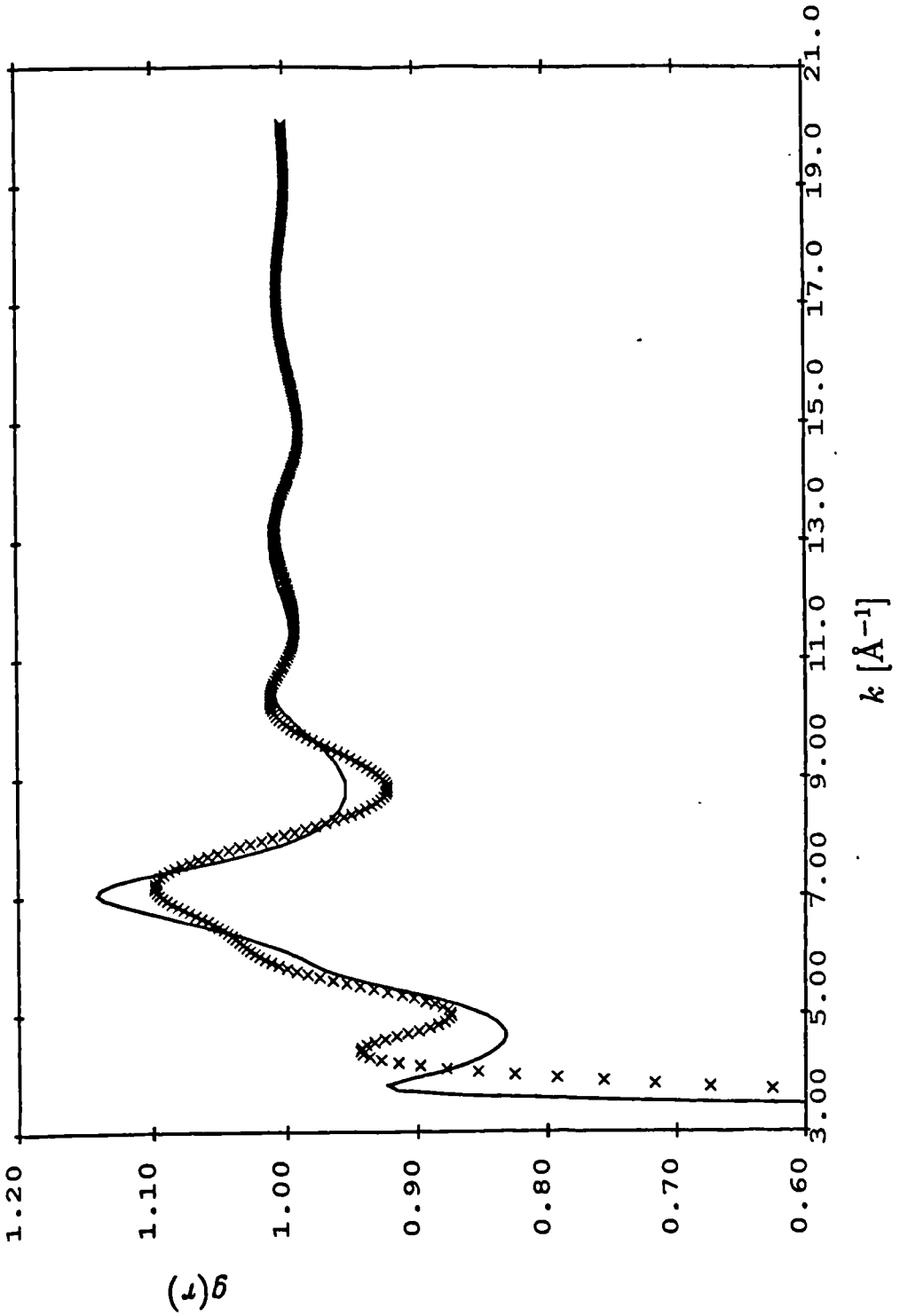

Figure 74: The observed (× × ×) and RISM model (—) intermolecular pair correlation function for liquid $GeBr_4$.

shoulder appearing on the low-r side of the peak in the $GeBr_4$ data is not explained by the model, although a slight shoulder does appear at this point. It is possible that the shoulder in the data has become artificially enhanced during the analysis of the data and further investigation of this possibility should be undertaken. Sharpening of the second neighbour peak in the $GeBr_4$ model does appear to occur if this shoulder is included from the peak shape. In the case of CBr_4 the disparity in height of the second peak makes comparison of the peak shapes more difficult but the model does appear to have a slightly narrower peak shape. Moving to the higher peaks, the peaks in the CBr_4 data are smoother and of greater amplitude than those in the $GeBr_4$ data, which may be indicative of longer range order occurring in the CBr_4 case. In both datasets the RISM model appears to give a reasonable prediction of the general shape of the curves.

6.5 Conclusion

Neutron diffraction data have been collected and analysed for CBr_4 and $GeBr_4$ in the liquid state. The bond lengths deduced from this data ($r_{CBr} = 1.93 \pm 0.02$ Å and $r_{GeBr} = 2.27 \pm 0.02$ Å) are in good agreement with those found by other authors. Predictions of the intermolecular correlations expected in the liquids have been produced using RISM. Unfortunately it would appear that the bromine hard core radius used in these predictions was different from that found in the experiment However making allowance for this indicates that there is a reasonable degree of agreement between the model and the data. It would be interesting to obtain RISM predictions with corrected hard core radii and to perform a comparison study between the two liquids analysed here and those of the tetrachloride series with special attention being placed on the effects of variation in the anisotropy parameter.

Chapter 7

General Conclusions

The following chapter presents a brief summary of the work carried out in this thesis and some suggestions for further work. More detailed conclusions, for the individual parts of this work are included at the ends of the appropriate chapters.

Chapter 3 outlined the results obtained from development work carried out at the SRS, Daresbury. This work involved the use of a technique, first described by Warren and Mavel [40], of removing the Compton component during the collection of X-ray data. The Warren-Mavel (WM) technique involves the observation of the fluorescence produced when an appropriately-selected elemental foil is placed in the path of the diffracted beam. The WM technique was shown to remove at least 90% of the Compton component leaving only a small contribution arising from elastic scattering within the foil. A method has suggested, in the conclusion of chapter 3, which will allow this final component to be eliminated, leaving a Compton-free diffraction pattern and thus removing the major obstacle of correcting the collected spectra for Compton scattering. It is hoped that this technique will be adopted as standard practice in the collection of X-ray diffraction data from liquid and

amorphous samples. The only limitations, aside from those already implicit in sample selection, are the need to select an appropriate incident wavelength and matching foil, and the need for a high incident X-ray flux such as that provided by the SRS.

In chapter 3, the Warren-Mavel technique was applied to a molecular liquid (CCl_4) and in chapter 4 the same technique was applied to an amorphous powder. The sample chosen was amorphous phosphorus (a-P), which being elemental should be one of the simplest amorphous systems. The two samples studied were shown to have marked differences in their intermediate range order which were apparently due to differing degrees of polymerisation during the fabrication of the samples by the heat treatment of white phosphorus. It was shown that none of the many crystal allotropes of phosphorus can conclusively explain the local order present in the samples. Comparisons were also made to a network cluster model produced by Hohl [77]. This model cannot yet describe the sharpness of the features present in the experimental radial distribution functions. Further work being carried out on this model may however lead to its improvement.

A new neutron diffraction study is currently being undertaken on the a-P samples used in this work [107] and these may help to clarify the structure. More importantly they may allow the most exact comparison ever to be made between the neutron and X-ray diffraction patterns of an elemental system, were the observed interference function should be directly comparable. It has been suggested [107] that the results of this comparison may show up any departures from spherical symmetry of the electron density in the component atoms. If this is the case it may for the first time show quantitatively the effects of assuming a free-atom electron-distribution in the analysis of X-ray data. Whether the delocalization of the electron distributions

is evident or not, the results of such a comparison will be of great importance to the question of the complementarity of neutron and X-ray diffraction techniques.

Moving to neutron diffraction chapter 5 presented the results of an experiment performed on liquid antimony pentafluoride, (SbF_5). It was shown that in the liquid state SbF_5 consists of long twisted chains of cis-bridged molecules in which the fluorine-bridge is bent to give an Sb–F–Sb bond angle of 145°. This is similar to one of the two bond angles found in the solid. It had been suggested that the bond angles present in the solid were due to orientations resulting from the crystal packing.The liquid results indicate that this bend is present in the liquid state where such restrictions are not present and thus, it must be caused by some property intrinsic to the fluorine bridge itself. Thus, investigation into the nature of the fluorine bridge in SbF_5 should provide a very informative and rewarding line of investigation.

Chapter 6 briefly described the results of neutron diffraction studies of CBr_4 and $GeBr_4$. The basic CBr and GeBr bond lengths were found to be 1.93 and 2.27 Å respectively. The intermolecular correlations were more ordered in $GeBr_4$ than CBr_4 due to the higher degree of anisotropy present in the $GeBr_4$ molecule. A comparison with the results of RISM models produced for the two samples showed that the RISM model predicted a lower degree of intermolecular order, than that found in either sample.

The tetrahedral molecules (the tetrachlorides and tetrabromides) are also of interest in the study of neutron/X-ray complementarity, as they provide simple well defined two-component molecules. It was originally hoped to carry out X-ray diffraction measurements on one of the two tetrabromide samples. It was not possible to perform such an experiment on CBr_4 as no method of heating the sample

to above its melting point was available on beamline 9.1 at Daresbury where the X-ray work in this thesis was carried out. The very high absorption coefficient of $GeBr_4$ means that very small sample thicknesses are required. This in turn requires either very thin sample cell windows or windows such as aligned Si(111) wafers which will contribute only a very small amount of scattering to the collected pattern. The fabrication of such a cell was not possible during the course of the X-ray experiments and so no X-ray diffraction measurement could be made. The overcoming of these problems and the subsequent analysis and comparison of the neutron and X-ray data sets would still provide much useful information. Also if data could be collected by a third technique, such as EXAFS or AXS it may be possible to separate out the three individual partial pair correlation functions for the samples which would be a major step forward in the analysis of the structures of samples which are not suitable for isotopic substitution or similar techniques.

Bibliography

[1] H. P. Klug and L. E. Alexander. *X-Ray Diffraction Procedures for Polycrystalline and Amorphous Materials.* Wiley-Interscience, 2^{nd} edition, 1974.

[2] E. W. Nuffield. *X-ray Diffraction Methods.* Wiley, 1966.

[3] A. Guinier. *X-ray Diffraction.* W. H. Freeman and Co., 1963.

[4] A. H. Compton and S. K. Allison. *X-rays in Theory and Experiment.* D. Van Nostrand, 2^{nd} edition, 1935.

[5] D. W. L. Hukins. *X-ray Diffraction by Disordered and Ordered Systems.* Pergamon Press, 1981.

[6] N. S. Gingrich. *Rev. Mod. Phys.* **15**, 90 (1943).

[7] K. Furukawa. *Repts. Progr. Phys.* **25**, 395 (1962).

[8] S. Steeb. *Springer Tracts in Modern Physics* **47**, 1 (1968).

[9] A. C. Wright. The structure of amorphous solids by x-ray and neutron diffraction. In *Advances in Structure Research by Diffraction Methods. Vol. 5*, W. Hoppe and R. Mason, editors, Pergamon Press, 1974.

[10] L. Bosio. X-ray diffraction studies of liquids. In *Hydrogen-Bonded Liquids.*, J. C. Dore and J. Teixeira, editors, Kluger Academic Publishers, 1991. NATO ASI Series C. Vol. 329.

[11] S. W. Lovesey. *Theory of Thermal Neutron Scattering from Condensed Matter.* Volume 1: Neutron Scattering, Clarendon Press, 1984.

[12] B. T. M. Willis, editor. *Chemical Applications of Thermal Neutron Scattering.* Oxford University Press, 1973.

[13] P. A. Egelstaff. *An Introduction to the Liquid State.* Academic Press, 1967.

[14] G. E. Bacon. *Neutron Diffraction.* Clarendon Press, 3rd edition, 1975.

[15] G. L. Squires. *Introduction to the Theory of Thermal Neutron Scattering.* Cambridge University Press, 1978.

[16] W. Marshall and S. W. Lovesey. *Theory of Thermal Neutron Scattering.* Clarendon Press, 1971.

[17] R. J. Newport, B. D. Rainford, and R. Cywinski, editors. *Neutron Sacttering at a Pulsed Source.* Adam Hilger, 1988.

[18] J. G. Powles. *Adv. Phys.* **22**, 1 (1973).

[19] J. C. Dore. Structural studies of molecular liquids by neutron and x-ray diffraction. In *Molecular Liquids; Dynamics and Interactions*, W. J. Orville-Thomas A. J. Barnes and J. Yarwood, editors, D. Reidel Publishing Co., 1984. NATO ASI Series C. Vol. 135.

[20] J. C. Dore. Techniques in neutron scattering studies of molecular systems. In *Molecular Liquids; Dynamics and Interactions*, W. J. Orville-Thomas

A. J. Barnes and J. Yarwood, editors, D. Reidel Publishing Co., 1984. NATO ASI Series C. Vol. 135.

[21] L. Blum and A. H. Narten. Diffraction by molecular liquids. In *Advances in Chemical Physics. Vol. 34*, I. Prigogine and S. Rice, editors, Wiley, 1976.

[22] P. Chieux and J. C. Dore. Neutron diffraction techniques. In *Hydrogen-Bonded Liquids.*, J. C. Dore and J. Teixeira, editors, Kluger Academic Publishers, 1991. NATO ASI Series C. Vol. 329.

[23] D. J. Hughes, J. A. Harvey, M. D. Goldburg, and M. J. Stefne. *Phys. Rev.* **90**, 497 (1953).

[24] J. Schwinger and A. E. Teller. *Phys. Rev.* **52**, 286 (1937).

[25] G. Placzek. *Phys. Rev.* **86**, 377 (1952).

[26] D. G. Montague and J. C. Dore. *Molec. Phys.* **57**, 1035 (1986).

[27] C. H. Macgillavry G. D. Rieck, editor. *International Tables of X-Ray Crystallography*, page 201. Volume III, Kynoch, 2^{nd} edition, 1968.

[28] J. A. Ibers and W. C. Hamilton, editors. *International Tables of X-Ray Crystallography*, page 99. Volume IV, Kynoch, 1974.

[29] J. A. Ibers and W. C. Hamilton, editors. *International Tables of X-Ray Crystallography*, page 247. Volume IV, Kynoch, 1974.

[30] D. T. Cromer and J. B. Mann. *J. Chem. Phys.* **47**, 1892 (1967).

[31] D. T. Cromer. *J. Chem. Phys.* **50**, 4857 (1969).

[32] F. Hajdu. *Acta Cryst.* **A27**, 73 (1971).

[33] R. W. James. *Optical Principles of X-ray Diffraction.* Bell, 1948.

[34] P. Debye. *Anna. d. Physik* **46**, 809 (1915).

[35] F. Zernicke and J. Prins. *Zeits f. Physik* **41**, 184 (1927).

[36] P. Debye and H. Menke. *Ergeb. d. Tech. Rontgenk* **11** (1931).

[37] B. E. Warren and N. S. Gingrich. *Phys. Rev.* **46**, 386 (1934).

[38] B. E. Warren. *J. Appl. Phys.* **8**, 645 (1937).

[39] F. R. Elder, A. I. Curewitsch, R. V. Langmuir, and H. C. Pollock. *J. Appl. Phys.* **18**, 810 (1947).

[40] B. E. Warren and G. Mavel. *Rev. Sci. Instr.* **36**, 196 (1965).

[41] E. E. Bray and N. S. Gingrich. *J. Chem. Phys.* **11**, 351 (1943).

[42] A. Eisenstein. *Phys. Rev.* **63**, 304 (1943).

[43] R. W. Grubel and G. T. Clayton. *J. Chem. Phys.* **46**, 639 (1967).

[44] G. Reichelt, J. Weidner, and H. W. Zimmermann. *Ber. Bunsenges Phys. Chem.* **78**, 1050 (1974).

[45] A. H. Narten. *J. Chem. Phys.* **65**, 573 (1976).

[46] Y. Murata and K. Nishikawa. *Bul. Chem. Soc. Jpn.* **51**, 411 (1978).

[47] K. Nishikawa and Y. Murata. *Bul. Chem. Soc. Jpn.* **52**, 293 (1979).

[48] S. Hyodo, N. Tatsuta, and T. Okamoto. *J. Chem. Phys.* **92**, 882 (1989).

[49] L. S. Bartell, L. O. Brockway, and R. H. Schwendeman. *J. Chem. Phys.* **23**, 1854 (1955).

[50] Y. Morino, Y. Nakamura, and T. Iijima. *J. Chem. Phys.* **32**, 643 (1960).

[51] J. R. Granada, G. W. Stanton, and J. H. Clarke. *Molec. Phys.* **37**, 1297 (1979).

[52] J. H. Clarke, J. R. Granada, and J. C. Dore. *Molec. Phys.* **37**, 1263 (1979).

[53] J. B. Van Tricht and J. S. Sjoerdsma. *Molec. Phys.* **59**, 507 (1986).

[54] F. J. Bermejo, E. Enciso, J. Alonso, N. Garcia, and W. S. Howells. *Molec. Phys.* **64**, 1169 (1988).

[55] C. W. Dwiggins Jr and D. A. Parks. *Acta Cryst.* **A27**, 264 (1970).

[56] C. W. Dwiggins Jr. *Acta Cryst.* **A28**, 158 (1971).

[57] G. F. Knoll. *Radiation Detection and Measurement*, page 120. Wiley, 2^{nd} edition, 1989.

[58] H. H. Paalman and C. J. Ping. *J. Appl. Phys.* **33**, 2635 (1962).

[59] C. H. Macgillavry G. D. Rieck, editor. *International Tables of X-Ray Crystallography*, page 157. Volume III, Kynoch, 2^{nd} edition, 1968.

[60] J. B. Van Tricht. *J. Chem. Phys.* **66**, 85 (1977).

[61] A. H. Narten, M. D. Danford, and H. A. Levy. *J. Chem. Phys.* **46**, 4875 (1967).

[62] J. Waser and V. Schomaker. *Rev. Mod. Phys.* **25**, 671 (1953).

[63] J. Dononhue. *The Structures of the Elements.* Wiley, 1974.

[64] K. Krebs and H. U. Gruber. *Z. Naturforsch. Teil A* **22**, 96 (1967).

[65] H. Thurn and B. Krebs. *Acta Cryst. B* **25**, 125 (1969).

[66] G. E. Jellison. *Solid Stata Commun.* **30**, 481 (1979).

[67] H. U. Beyeler and S. Veprek. *Phil. Mag. B* **41**, 327 (1980).

[68] F. Gompf and J. S. Lannin. *J. Phys. Colloq. C6* **42**, 28 (1981).

[69] B. V. Shannabrook and J. S. Lannin. *Phys. Rev. B* **24**, 4771 (1981).

[70] J. S. Lannin, B. V. Shannabrook, and F. Gompf. *J. Non-Crys. Sol.* **49**, 209 (1982).

[71] G. Fasol, M. Cardona, W. Honle, and H. G. von Schnering. *Solid Stata Commun.* **52**, 307 (1984).

[72] D. J. Olego, J. A. Baumann, M. A. Kuck, R. Schachter, C. G. Michel, and P. M. Raccah. *Solid Stata Commun.* **52**, 311 (1984).

[73] D. J. Olego, J. A. Baumann, and R. Schachter. *Solid Stata Commun.* **53**, 905 (1985).

[74] S. R. Elliott, J. C. Dore, and E. Marseglia. *J. Phys. Colloq. C8* **46**, 349 (1985).

[75] E. Belin, C. Senemaud, and A. Szasz. *Phil. Mag. B* **58**, 551 (1988).

[76] R. O. Jones and D. Hohl. *J. Chem. Phys.* **92**, 6710 (1990).

[77] D. Hohl and R. O. Jones. *Phys. Rev. B* (1992). To Be Published.

[78] A. L. Khidir Aljibury and R. L. Redington. *J. Chem. Phys.* **52**, 453 (1969).

[79] I. Beattie, R. Crocombe, A. German, P. Jones, C. Van Schalkwyk, and A. Bukovszy. *J. Chem. Soc. (Dalton Trans)* 1380 (1976).

[80] C. Hoffman, B. E. Holder, and W. L. Jolly. *J. Phys. C (Solid St. Phys.)* **62**, 364 (1958).

[81] I. Beattie, K. M. S. Livingston, G. A. Ozin, and D. J. Reynolds. *J. Chem. Soc. A* 958 (1969).

[82] T. K. Davis and K. C. Moss. *J. Chem. Soc. A* 1054 (1970).

[83] A. J. Edwards and P. Taylor. *Chem. Commun* 1376 (1971).

[84] A. J. Edwards. *J. Chem. Soc.* 3714 (1964).

[85] J. H. Holloway, R. D. Peacock, and R. W. H. Small. *J. Chem. Soc.* 644 (1964).

[86] M. S. Garawi. *Thermal Neutron Scattering by some Molecular Liquids.* PhD thesis, University of Kent at Canterbury, 1987.

[87] V. F. Sears. *Thermal-Neutron Scattering Lengths and Cross Sections for Condensed Matter Research.* Technical Report AECL-8490, Atomic Energy of Canada Ltd., 1984.

[88] S. F. Mughabghab, M. Divadeenam, and N. E. Holden, editors. *Neutron Cross Sections.* Volume 1, Academic Press, 1981.

[89] L. J. Lowden and D. Chandler. *J. Chem. Phys.* **61**, 5228 (1974).

[90] D. G. Montague, M. R. Chowdury, J. C. Dore, and J. Read. *Molec. Phys.* **50**, 1 (1983).

[91] J. S. Sjoerdsma and J. B. van Tricht. *Chem. Phys. Lett.* **117**, 336 (1985).

[92] E. Enciso. Private Communication.

[93] P. Zielinski, R. Fouret, and M. More. *J. Chem. Phys.* **93**, 1948 (1990).

[94] W. Press, H. Grimm, and A. Huller. *Acta Cryst. A* **35**, 881 (1979).

[95] M. More and R. Fouret. *Disc. Faraday Soc.* **69**, 75 (1980).

[96] M. More, J. Lefebvre, B. Hennion, B. M. Powell, and C. M. E. Zeyen. *J. Phys. C (Solid St. Phys.)* **13**, 2833 (1980).

[97] G. Coulon and M. Descamps. *J. Phys. C (Solid St. Phys.)* **13**, 2847 (1980).

[98] G. Dolling, B. M. Powell, and V. F. Sears. *Molec. Phys.* **37**, 1859 (1979).

[99] K. F. Ludwig Jr, W. K. Warburton, Lane Wilson, and A. I. Blienenstock. *J. Chem. Phys.* **87**, 604 (1987).

[100] K. F. Ludwig Jr, Lane Wilson, W. K. Warburton, and A. I. Blienenstock. *J. Chem. Phys.* **87**, 613 (1987).

[101] P. A. Egelstaff, D. I. Page, and J. G. Powles. *Molec. Phys.* **20**, 881 (1971).

[102] G. I. Swan. Private Communication.

[103] W. S. Howells. *Multiply Scattering Corrections for Total Scattering Experiments.* Technical Report NDCN/14/80, A.E.A.R., Jan. 1981.

[104] S. Howells. Private Communication.

[105] J. L. Finney. *Proc. R. Soc. London* **A319**, 495 (1970).

[106] D. Chandler. *Studies in Statistical Mechanics.* Volume III, North-Holland, 1981.

[107] J. C. Dore. Private Communication.